Low Loss Dielectric Mirrors for Optical Cavities Applications

Najwa Sidqi, M.Sc.

Submitted for the degree of Doctor of Philosophy

Helia Photonics Ltd.

Heriot-Watt University
School of Engineering and Physical Sciences

August 2019

The copyright in this thesis is owned by the author. Any quotation from the thesis or use of any of the information contained in it must acknowledge this thesis as the source of the quotation or information.

ABSTRACT

Cavity-based single-photon emitters possess great potential in many quantum applications. Fabry-Perot cavities are an especially good candidate for these applications in order to provide the high-Q cavities necessary for efficient coupling. To assure strong coupling in the cavity, very high reflectance dielectric mirrors are required. Achieving this means overcoming several technical challenges in order to minimize the optical losses in the dielectric layers. This research work explores the potential of several dielectric materials and physical vapour deposition methods to fabricate high reflectance mirrors in the visible region. Single layer material characterisation results showed extinction coefficients below 10^{-5} and a surface roughness below 1 nm for metal oxides deposited by ion assisted and plasma assisted processes. A reflectance superior to 99.9 % was obtained for TiO_2/SiO_2, ZrO_2/SiO_2 and Nb_2O_5/SiO_2 multilayer mirrors deposited using ion assisted E-beam, plasma assisted and microwave assisted sputtering methods. A surface roughness of 0.3 to 0.5 nm was obtained for ZrO_2/SiO_2 and Nb_2O_5/SiO_2 multilayer mirrors deposited using plasma assisted and microwave assisted sputtering methods. Scatter losses of 200 ppm were obtained for TiO_2/SiO_2 deposited using ion assisted E-beam deposition. Micron sized TiO_2/SiO_2 and ZrO_2/SiO_2 mirrors were achieved on curved glass templates by Ion assisted E-beam deposition.

To my Mum

To my Dad

To my siblings
Ichrak, Yousra and Issam

In memory of Grandma

ACKNOWLEDGEMENT

This PhD experience has been full of teachings at both personal and professional levels and I feel so much grown up after completing my thesis. Firstly, I would like to thank my family for their love and encouragements throughout the past three years. I would like to thank my Mum for her unconditional love and her comforting words during the lowest moments. I want to thank my father for teaching me so much resilience and humbleness. I would like to thank my siblings Ichrak, Yousra and Issam for their love and support.

I would like to thank Dr. Caspar Clark, my primary supervisor, for hosting me at Helia Photonics for the past three years and for sharing his knowledge about thin film fabrication and optical materials. I would like to thank him especially for providing so much help and support during my first months in Scoltand. I would like to thank Prof. Gerald Buller, my academic supervisor, for providing so much guidance during my PhD and for shaping my critical thinking as a researcher and improving my scientific rigour. I want to thank both Caspar and Gerald for their patience while reviewing this thesis manuscript and for their invaluable inputs and comments on my research work.

I want to acknowledge the help and support of Helia Photonics staff and thank them for their jovial and kind attitude. I would like to especially acknowledge the help of Dr. Mark Bailey, Dr. Gopala Thalluri, Mr. Dominik Bakalarz and Mrs. Samantha Bocker for providing so much help and attention during my presence at Helia Photonics. I would like to thank Dr. Evgeny Mitrofanov and Dr. Yoann Noblet for aiding with the operation of deposition systems at Helia Photonics and sharing their knowledge about thin film deposition and characterisation. I want to thank all my Scottish pals in the lab: Marlen, Ross. P, Ross. M, Kevin, Peter, Nick, Fraser. I, Fraser. B, John. M and Rory. I would like to thank Mr. Antoine Boudet, my French compatriot at Helia, for his positive spirit and his encouragements. I would like to thank Mr Steve Wood for sharing his knowledge and expertise in optical filters design and fabrication.

I would like to thank Heriot-Watt University and the IPAQs staff for their support during my PhD. I would like to especially thank Mr. Neil Ross for providing help and training on characterisation equipments at the clean room. I would like to thank Dr. Artur Branny (Art) and Mr Guillem Balesteros for their technical assistance while using the AFM system at Heriot-Watt University. I would like to acknowledge the “Single-photon group“ members for their help and support.

I would like to thank Prof. Alexander Tartakovskii for his invaluable inputs on my research work and for hosting me in his group at the University of Sheffield. I would like to thank “Low Dimensional Structures and Devices” group members Mr. Alessandro Catanzaro, Dr. Armando Genco and Mr. Thomas.P Lyons for training me on two-dimensional materials exfoliation and photoluminescence measurements.

I would like to thank Prof. Richard Warburton for hosting me for two months at his group at the University of Basel. I would like to acknowledge the help of Nano-Photonics group members Dr. Benjamin Petrak, Ms. Natasha Tomm, Mr. Daniel Najer, Dr. Tomasz Jakubczyk, Mr. Sigurd Flagan and Dr. Daniel Riedel during my secondment to their group. I would like to thank Dr. Monica Schoenenberger for her assistance and kind help during my secondment at the University of Basel.

I would like to thank Prof. Desmond Gibson for hosting me in his group and for allowing the use of deposition systems at the University of the West of Scotland. I want to thank especially Dr. Lewis Fleming, Dr. Cheng Li and Mr. Martin Hin On Chu for their technical assistance during my secondment at the University of the West of Scotland.

I would like to thank all the Spin-NANO network members and my fellow PhD students. I want to especially thank Dr. Sandrine C. Soubes for her invaluable career advices and Mrs Sally Greenhough for her continuous support during my fellowship.

Finally, I would like to thank the H2020 Marie Skłodowska-Curie commission for providing me with a great training and professional opportunity and for funding this research project.

HERIOT WATT UNIVERSITY

ACADEMIC REGISTRY

Research Thesis Submission

Name:	Najwa Sidqi		
School:	Engineering and Physical Sciences		
Version: *(i.e. First, Resubmission, Final)*	Final submission	Degree Sought:	Doctor of Philosophy

Declaration

In accordance with the appropriate regulations I hereby submit my thesis and I declare that:

1. The thesis embodies the results of my own work and has been composed by myself
2. Where appropriate, I have made acknowledgement of the work of others
3. Where the thesis contains published outputs under Regulation 6 (9.1.2) these are accompanied by a critical review which accurately describes my contribution to the research and, for multi-author outputs, a signed declaration indicating the contribution of each author (complete Inclusion of Published Works Form – see below)
4. The thesis is the correct version for submission and is the same version as any electronic versions submitted*.
5. My thesis for the award referred to, deposited in the Heriot-Watt University Library, should be made available for loan or photocopying and be available via the Institutional Repository, subject to such conditions as the Librarian may require
6. I understand that as a student of the University I am required to abide by the Regulations of the University and to conform to its discipline.
7. Inclusion of published outputs under Regulation 6 (9.1.2) shall not constitute plagiarism.
8. I confirm that the thesis has been verified against plagiarism via an approved plagiarism detection application e.g. Turnitin.

* *Please note that it is the responsibility of the candidate to ensure that the correct version of the thesis is submitted.*

Signature of Candidate:	NAJWA SIDQI	Date:	27/08/2019

Submission

Submitted By *(name in capitals)*:	
Signature of Individual Submitting:	
Date Submitted:	

For Completion in the Student Service Centre (SSC)

Received in the SSC by *(name in capitals)*:			
Method of Submission *(Handed in to SSC; posted through internal/external mail)*:			
E-thesis Submitted (mandatory for final theses)			
Signature:		Date:	

HERIOT WATT UNIVERSITY

ACADEMIC REGISTRY

Inclusion of Published Works

Declaration

This thesis contains one or more multi-author published works. In accordance with Regulation 6 (9.1.2) I hereby declare that the contributions of each author to these publications is as follows:

Citation details	Najwa Sidqi, Caspar Clark, Gerald S. Buller, Gopala Krishna V. V. Thalluri, Jevgenij Mitrofanov, and Yoann Noblet, "Comparative study of dielectric coating materials for micro-cavity applications," Opt. Mater. Express 9, 3452-3468 (2019)
Author 1	Conceptualization, methodology, formal analysis, investigation, data curation, writing-original draft preparation, writing-review & editing, visualization.
Author 2	Conceptualisation, methodology, validation, review and editing, resources, supervision and funding acquisition
Signature:	
Date:	01/08/2019

Citation details	Najwa Sidqi, Caspar Clark, Gerald S. Buller, High reflectance mirrors for micro-cavity applications, SPIE Optics and Photonics, San Diego, August 2019
Author 1	Conceptualization, methodology, formal analysis, investigation, data curation, writing-original draft preparation, writing-review & editing, visualization.
Author 2	Conceptualisation, methodology, validation, review and editing, resources, supervision and funding acquisition
Signature:	
Date:	01/08/2019

Citation details	e. g. Author 1 and Author 2, Title of paper, Title of Journal, X, XX-XX (20XX)
Author 1	Contribution….
Author 2	Contribution….
Signature:	
Date:	

TABLE OF CONTENTS

CHAPTER 1 –INTRODUCTION 1

1.1 Thesis context and motivation 1

1.1.1 H2020 Marie Skłodowska-Curie network Spin-NANO 1

1.1.2 High finesse Fabry-Perot cavities for a new antenna technology 1

1.2 Single-photon technology: development and applications 3

1.3 Single-photon sources 5

1.3.1 Deterministic versus probabilistic sources 5

1.3.2 Transition metal dichalcogenide monolayers 6

1.3.3 Nitrogen-vacancy centres 7

1.4 Microcavities 8

1.4.1 Cavity quantum electrodynamics 9

1.4.2 The Fabry-Perot cavity 10

1.4.3 Finesse and quality factor 10

1.4.4 Purcell factor and small cavity mode volume 15

1.4.5 Plano concave Fabry-Perot cavities 16

1.5 Dielectric distributed Bragg reflectors 16

1.5.1 The quarterwave stack 16

1.5.2 Reflectance, transmittance and absorbance 18

1.5.3 Losses 20

1.6 Summary and thesis plan 21

REFERENCES 22

CHAPTER 2 –SINGLE LAYER DIELECTRIC COATINGS 29

2.1 Deposition methods 29

2.1.1 Thermal evaporation 29

2.1.2 Magnetron sputtering 30

2.1.3 Ion assisted deposition 32
2.1.4 Plasma assisted deposition 33
2.1.5 Other deposition methods 37
2.2 Dielectric materials 38
2.2.1 Selection criteria 38
2.2.2 Studied dielectrics 38
2.3 Optical constants 40
2.3.1 Complex refractive index 40
2.3.2 Refractive index n 45
2.3.3 Extinction coefficient k 49
2.3.4 Summary of optical constants 54
2.4 Surface roughness 54
2.4.1 Light scatter and surface roughness 55
2.4.2 Roughness measurement 55
2.5 Mechanical stress 62
2.5.1 Stoney's formula and curvature method 63
2.5.2 Stress calculation 66
2.6 Summary and discussions 68
REFERENCES 70
CHAPTER 3 –ASSESMENT OF PLANAR MULTILAYER HIGH REFLECTANCE MIRRORS 76
3.1 Design of high reflectance dielectric mirrors 76
3.1.1 Calculation method 76
3.1.2 Reflectance, transmittance and absorptance calculation 77
3.2 Planar mirrors fabrication methods 81
3.2.1 IAD E-beam 81
3.2.2 Plasma assisted DC magnetron sputtering 83
3.2.3 Microwave plasma assisted magnetron sputtering 84
3.3 Optical characterisation 85

3.3.1 Reflectance and transmission measurements 85
3.3.2 Coating derivation and reverse engineering 91
3.3.3 Optical losses 92
3.4 Mirrors roughness and scatter losses 95
3.4.1 Roughness measurements 95
3.4.2 Scatter losses 98
3.4.3 Measurements on superpolished substrates 99
3.4.4 Total integrated scattering 101
3.5 Laser damage 104
3.5.1 Definition 104
3.5.2 LIDT measurements 104
3.6 Planar mirrors assessment summary 110
3.7 Summary and conclusion 110
3.8 Acknowledgements 112
REFERENCES 113
CHAPTER 4 –CONCAVE MULTILAYER DIELECTRIC MIRRORS 116
4.1 Curved mirrors for Fabry-Perot cavities 116
4.1.1 Concave templates fabrication methods 116
4.1.2 Design of curved mirrors 117
4.2 Fabrication of spherical substrates 117
4.2.1 Substrate cleaning and preparation 117
4.2.2 Mesa pattern 118
4.2.3 CO_2 laser ablation 120
4.3 Coating of spherical mirrors 122
4.4 Characterisation of curved mirrors 123
4.4.1 Confocal microscopy 123
4.4.2 Atomic force microscopy 125
4.5 Summary and conclusion 130

4.6 Acknowledgments 130
REFERENCES 132
CHAPTER 5 –CONCLUSION AND FUTURE RESEARCH WORK 134
5.1 Summary 134
5.2 Conclusions 136
5.3 Future research work 138
5.3.1 High reflectance and optical losses measurements 138
5.3.2 Finesse and Q-factor measurements 138
5.3.3 Plasma assisted E-beam TiO_2/SiO_2 mirrors 139
5.3.4 Mechanical stress measurements 139
REFERENCES 140

PUBLICATIONS AND CONFERENCE PRESENTATIONS

Journal articles and conference proceedings

N. Sidqi, C. Clark, G.S. Buller, G.K. Thalluri, J. Mitrofanov, Y. Noblet, *Comparative study of dielectric coating materials for micro-cavity applications*, Opt. Mater. Express 9, 3452-3468 (2019)

N. Sidqi, C. Clark, G.S. Buller, *High reflectance mirrors for micro-cavity applications*, SPIE Optics and Photonics, San Diego, August 2019. Proceeding submitted.

Conference Presentations

N. Sidqi, "Efficient single-photon emitters for quantum information", 8th SU2P symposium, Edinburgh, United Kingdom, April 2017.

N. Sidqi, "Low loss dielectric Bragg reflectors for quantum spin systems ", Photonex Roadshow, invited talk at the 5th anniversary of Fraunhofer CAP UK, Glasgow, United Kingdom, June 2017.

N. Sidqi, "Low loss dielectric Bragg reflectors for quantum spin systems", Spin-NANO meeting with industry, Delft, The Netherlands, June 2017.

N. Sidqi, "Development of dielectric mirrors for an efficient single-photon extraction in spin nanosystems", Spin-NANO Mid-term review, Sheffield, United Kingdom, January 2018.

N. Sidqi, "Low loss dielectric mirrors for quantum applications", Spin-NANO 2nd meeting with industry, Cambridge, United Kingdom, January 2019.

N.Sidqi, "Low loss dielectric mirrors for quantum communication systems", IONS Orlando 2019, Orlando, USA, March 2019.

N. Sidqi, C. Clark, G.S. Buller, "High reflectance mirrors for cavities applications", SPIE Optical engineering+applications symposium, San Diego, USA, August 2019.

Posters

N. Sidqi, C. Clark, G.S. Buller "High efficiency dielectric distributed Bragg mirrors for quantum information systems", 8th SU2P symposium, Edinburgh, United Kingdom, April 2017.

N. Sidqi, C. Clark, G. Thalluri, E. Mitrofanov, G.S. Buller, N. Tomm, D. Najer, B. Petrak, R. Warburton, "Low loss dielectric distributed Bragg reflectors for quantum communication systems", 4th School and conference on spin-based quantum information systems, Konstanz, Germany, September 2018.

N. Sidqi, C. Clark, G. Thalluri, E. Mitrofanov, G.S. Buller, N. Tomm, D. Najer, B. Petrak, R. Warburton, "Low loss dielectric distributed Bragg reflectors for quantum

communication systems", IOP Photon 2018, Birmingham, United Kingdom, September 2018.

N. Sidqi, C. Clark, G. S. Buller, "Supermirrors for unhackable networks", STEM4Brit poster competition, Westminster, United Kingdom, March 2019.

N. Sidqi, C. Clark, G. Thalluri, E. Mitrofanov, G.S. Buller, N. Tomm, D. Najer, B. Petrak, R. Warburton, "Low loss dielectric distributed Bragg reflectors for quantum communication systems", Spin-NANO meeting on Nanophysics, Toulouse, France, March 2019.

CHAPTER 1–INTRODUCTION

Single-photon technology has seen a vast expansion in activity as new applications in quantum communications, quantum-enhanced imaging and quantum information processing are developed. In this first chapter, the context and the aim of the present research work as a H2020 Marie Skłodowska-Curie funded project are reminded in Section 1.1. Single-photon emission and its implementation in many measurement and imaging methods across various disciplines are described in Section 1.2. Examples of single-photon sources in the visible region such as diamond colour centres and transition metal dichalcogenides materials are presented in Section 1.3. Cavity quantum electrodynamics and optical microcavities are introduced in Section 1.4. Dielectric distributed Bragg reflectors are presented in Section 1.5. Finally, the methodology of the present study and the thesis plan are presented in Section 1.6.

1.1 Thesis context and motivation

1.1.1 H2020 Marie Skłodowska-Curie network Spin-NANO

The European Commission has been supporting research and innovation in quantum technologies for the last 15 years by providing the necessary financial means and highly skilled researchers in the field of future and emerging technologies (FET). In order to keep Europe's position as a quantum technologies leader and to help face the growing competition from the United States and Asia, the European Commission has doubled research funds dedicated to quantum sciences in the last 10 years. Target end-applications include secure communication, powerful quantum computers and ultra-precise sensors.

Spin-NANO is one of the innovative training programs funded by the H2020 Marie Skłodowska-Curie actions and aiming to achieve technical and scientific breakthroughs in the field of nano-imaging and quantum information systems.

Some of the main innovation objectives that have been set-up for the network and dividing the network into leading research groups are the realization of spin qubits[1] with all electrical control in material with spinless matrices, the development of applications of spin impurities for quantum computing, quantum networks and nano magnetometry, exploring spin-valley properties in transition metal dichalcogenides(TMDCs)[2-4] and last but not least the development of microcavity and a dielectric antenna technology for efficient photon extraction in spin nanosystems[5, 6] involving Helia Photonics Ltd. and which is the primary research topic of this thesis.

1.1.2 High finesse Fabry-Perot cavities for a new antenna technology

Many photon generation processes have recently demonstrated a great potential as deterministic photon sources in the visible wavelength range such as the emission of a

single quantum dot[7-9], a single nitrogen vacancy centre (colour centre in diamonds)[10-12]or the photoluminescence of two-dimensional materials[13, 14]. These sources emit single photons in the visible wavelength range using an external trigger event. However, this emission process suffers from many limitations that prevent them from being used for quantum networking or quantum computing. Usually, the generated photons are emitted into all directions and show a broad energy distribution. These limitations can be overcome by coupling these photon sources to cavities.

The main research interest of this thesis is the development of microcavities and a new dielectric antenna technology for efficient photon extraction in spin nanosystems. The purpose of this study is to develop low loss dielectric Bragg mirrors (or DBRs) for high finesse tunable microcavities. Figure 1.1 represents the set-up of the studied microcavity. The DBR developed at Helia Photonics Ltd will be integrated in the microcavity setup. The figure below represents the mechanical setup of a Fabry-Perot air gap microcavity as previously illustrated by L.E. Greuter in [15]. The design below represents a highly reflective plano-concave mirror pair separated by a wavelength sized air gap and forming a high finesse resonator. The planar bottom mirror is coated with a DBR coating. Using a three-axis piezo stack allows a sub nanometer precise positioning toward the top mirror. Prior to coating at Helia Photonics Ltd., the top curved mirror substrate is fabricated using CO_2 laser ablation of fused silica (see Chapter 4).

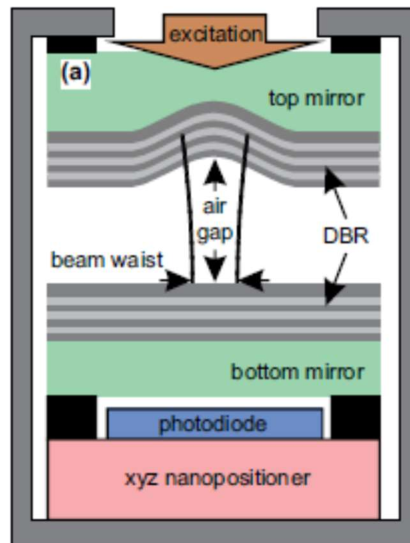

Figure 1.1: *Mechanical setup of a plano-concave Fabry Perot cavity. The top mirror is a quarterwave curved mirror produced by CO_2 laser ablation as described in Chapter 4. The bottom mirror is a plane quarterwave mirror. The mirrors are separated by a wavelength air gap. The bottom mirror is placed on a three-axis piezoelectric nanopositionner. The transmission signal exiting the cavity is collected using a photodiode placed under the bottom mirror, setup extracted from [15].*

Achieving high finesse microcavities can be fulfilled by increasing the reflectivity of the mirrors. Usually consisting of a succession of low and high refractive indices layers. Increasing the refractive index contrast or the number of the layers can lead to an increased reflectance of the DBRs. However, the fabricated DBRs must also fulfil a good mechanical stability and a uniform optical performance. With a target reflectance of up to 99.99%, low loss materials are deposited at Helia Photonics using one of the house-

developed coating technologies. Deposition methods technologies cover the state of the art of many deposition technologies such as Ion assisted electron beam technology, sputtering and thermal evaporation. The main materials investigated are dielectric materials with low optical losses in the visible wavelength range[16].

1.2 Single-photon technology: development and applications

Throughout the centuries, the nature of light has been disputed between scientists and philosophers from a particle nature embraced and developed by Newton in the 17th century to a wave nature first introduced by Descartes in the 17th century later confirmed by the Young's slit experiment in 1803 and supported by Maxwell's equations in 1860[17]. In 1905, light quanta were described by Einstein in the photoelectric effect[18]. The term *photon* was first introduced by Lewis in 1926[19] and defined light as an excitation of a single mode of the quantized electromagnetic field.

Quantum light represents the group of states that cannot be emitted by a classical light source such as discharge lamps. This means that it cannot be described using classical electromagnetism laws but only using quantum mechanics and quantized electromagnetic field. For example, single-photon emission can occur as the emission of one single-photon from a fluorescence process after a source has been electrically or optically excited. The emission of one photon is described by the Jablonski diagram presented in Figure 1.2[20]. The Jablonski diagram illustrates the electronic states of a molecule and the transitions between them.

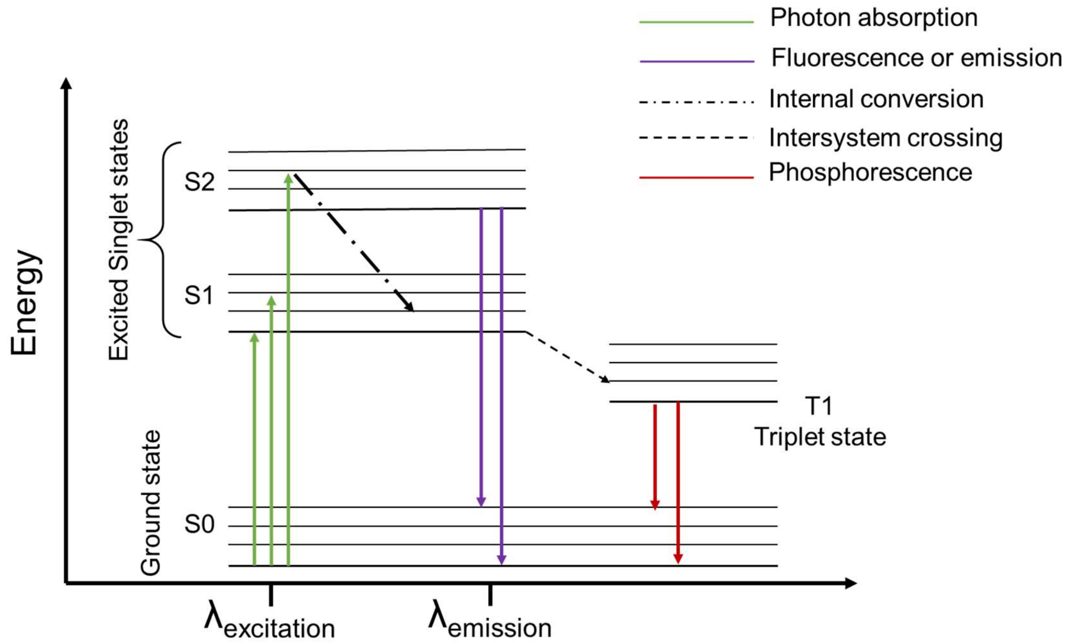

Figure 1.2: *Jablonski diagram showing the electronic states of a molecule and the transition between them. Single-photon emission is represented by the fluorescence or the relaxation from a singlet excited state to the ground state after the absorption of high energy photon at a given wavelength.*

This diagram shows the excitation of a molecule to a singlet state S1 or S2 after the absorption of a high photon energy at a wavelength $\lambda_{excitation}$. The system then relaxes to a ground state S0 resulting in fluorescence or a photon emission at a longer wavelength $\lambda_{emission}$. The absorption and fluorescence transitions are called radiative transitions and are represented by straight arrows in the diagram. Other transitions such as the internal conversion (IC) and intersystem crossing (ISC) represented by tilted arrows are also shown in the Jablonski diagram. An internal conversion is a coupling between an electronically excited state to a lower vibrational electronic state[21]. The internal conversion is a transition to a different spin multiplicity state. Both IC and ISC transitions are called non-radiative transition. The intersystem crossing can be followed by phosphorescence which is a relaxation from a triplet state to a ground state.

Single-photon technology has numerous applications in many scientific fields, including sensing and detection applications[22-25], picosecond circuit analysis (PICA)[26] and medical applications such as diffuse optical tomography[27]. Quantum information and quantum communications technologies have been actively researched in the last years[28-30]. Examples of applications are quantum key distribution introduced by C. Bennett and G. Brassard more than 30 years ago[31]. Quantum repeaters[32] and quantum computation protocols[33] are one of single-photon enabled quantum information applications.

1.3 Single-photon sources

1.3.1 Deterministic versus probabilistic sources

Single-photon sources can be classified into two major categories: probabilistic photon sources and deterministic photon sources. Probabilistic sources are two-photon emission sources where one photon is used to herald the other single-photon emission[34], while deterministic sources permit to produce one single-photon on demand. As counterintuitive as it may seem, probabilistic or photon-pair heralded sources were the first single-photon sources to be developed[35] and are commonly used sources in various quantum information and quantum-enabled measurement applications. Figure 1.3 shows single-photon emission mechanism versus two-photon emission mechanism. Unlike the single-photon emission where a direct energy absorption allows reaching the singlet excited state, the two-photon emission is based on the excitation of a molecule by the absorption of one photon energy to half the energy to reach a virtual state and is completed by the second half photon energy to reach the transition to the singlet state.

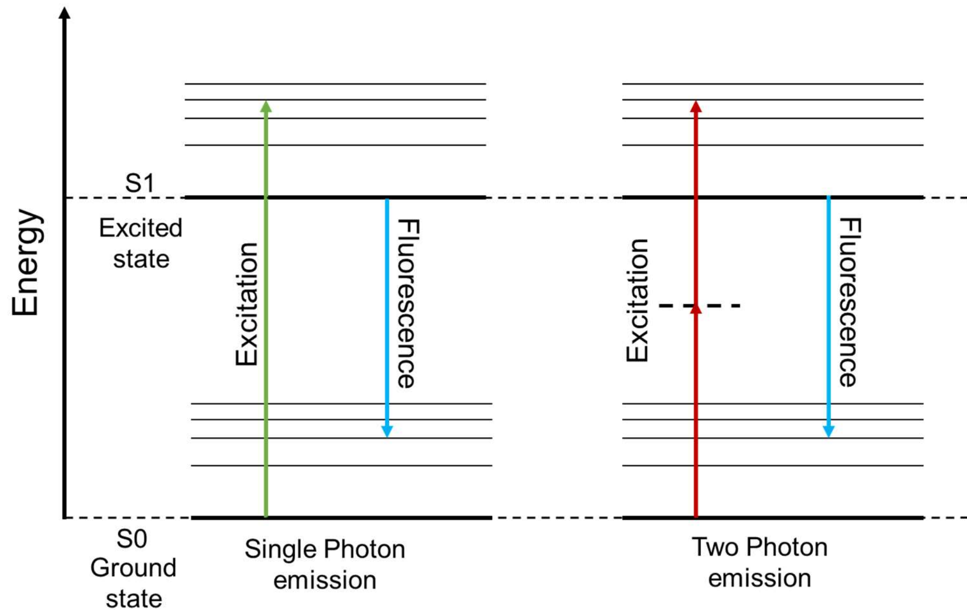

Figure 1.3: *Single-photon emission versus two-photon emission processes.*

Examples of photon-pair heralded sources or probabilistic sources are parametric downconversion based single-photon sources (PDC), offering the highest photon-pair detection rate[36, 37] and sources relying on four-wave mixing in single mode optical fibres, offering the great advantage of generating, encoding, extracting and detecting photon pairs within the same fibre[38]. These heralded photon-pair sources are widely used in quantum communication systems[39].

Examples of deterministic photon sources are discrete quantum systems based on single atoms or ions. They can also be engineered systems such as quantum dots[40] or diamond colour centres[11]. These systems are robust and can emit only one photon in a de-excitation process. When a single-photon is desired, an external power is used to excite

the sources and one photon will be emitted during the relaxation process to a lower energy state. Usually, single-photon sources are coupled to cavities allowing higher emission efficiency into a single spatial mode[41]. An introduction to microcavities as light emitting devices will be provided in Section 1.4 Microcavities.

1.3.2 Transition metal dichalcogenide monolayers

Transition metal dichalcogenide monolayers (TMDs or TMDCs) are one of the most popular and currently most researched light emitting materials thanks to their potential in many device applications[42, 43] and in fundamental research on spin-valley properties[44-46]. TMD monolayers are atomically thin semiconductors composed of one metal atom such as Molybdenum or Tungsten sandwiched between two chalcogen atoms such as Selenium, Sulphur or Tellurium. TMD monolayers are held to the substrate by weak Van der Waals forces. TMD materials are two-dimensional materials with thicknesses of a few Angstroms.

In their bulk form, these materials are indirect bandgap semiconductors. The monolayers of the same material however have a direct band gap which makes them very attractive for many applications such as transistors, emitters and spin-valley physics. Figure 1.4 shows the direct excitonic transitions at high energies at K point[34]. The indirect bandgap becomes larger when the thickness of the material reduces. The bandgap keeps enlarging until it becomes direct for MoS_2 monolayer as represented in Figure1.4. d. The monolayer direct transition allows the photoluminescence (PL) observed in TMDC monolayers.

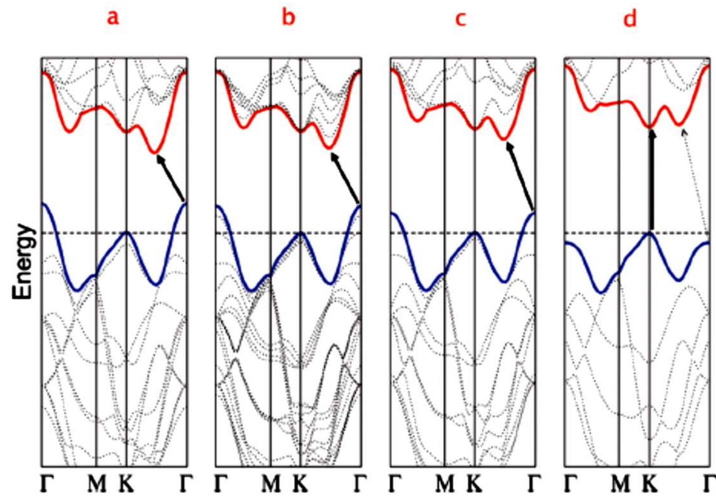

Figure 1.4: *Comparison between band structures calculated for a) a bulk MoS_2, b) a quadrilayer MoS_2, c) a bilayer MoS_2 and d) a monolayer MoS_2 represented in. Energy band diagram extracted from [47].*

As previously stated, TMD crystals are made of many layers, coupled by Van-der-Waals forces. These interactions are very weak and allow monolayers to be fabricated from simple mechanical exfoliation[48] as in the case for graphene monolayers. The dry

exfoliation of the TMDs is followed by a transfer onto a Si/SiO_2 substrate using a viscoelastic stamping method[49].

Figure 1.5 shows a bright-field and a PL image of a WSe_2 monolayer. The translucent area marked by a red dashed circle identifies the monolayer area. The properties of TMD monolayers (direct bandgap) allow using PL imaging to identify the monolayers[50].

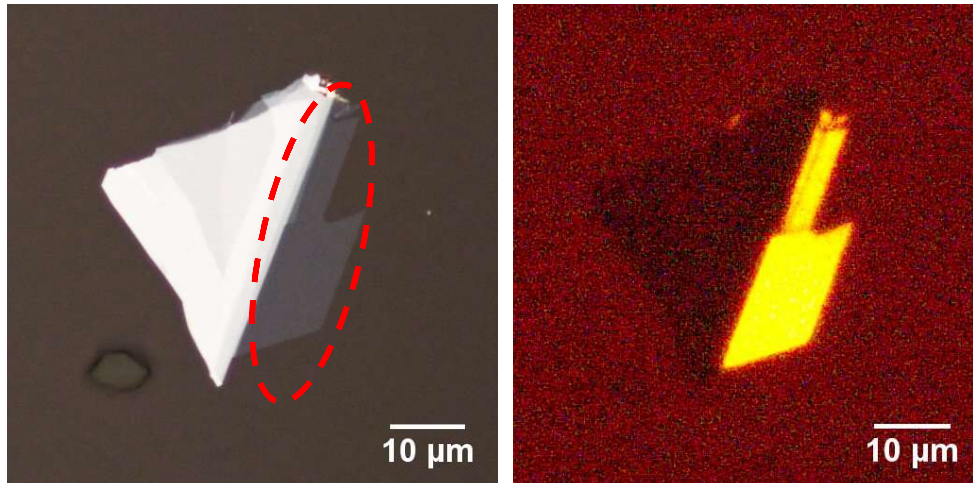

Figure 1.5: *WSe_2 monolayer captured in a bright field (left) versus a PL exposure (right) using the setup described in [50]. The WSe_2 monolayer was exfoliated and captured at the University of Sheffield.*

Many recent studies have reported strong coupling for TMD heterostructures to Fabry-Perot cavities[51-56]. The new light-matter interactions observed such as the formation of excitons-polaritons demonstrated potential for many laser and imaging applications.

1.3.3 Nitrogen-vacancy centres

Nitrogen-vacancy centres or N-V centres, beside two-dimensional materials, are the object of intense research in several quantum applications. Their potential as single-photon sources has been mainly explored for quantum information and communication systems[57] and as solid state spin qubits for quantum processing and quantum metrology devices[58]. N-V centres are a defect point within the diamond lattice (Figure 1.6). One carbon atom is replaced by nitrogen atom pairing with the next vacancy.

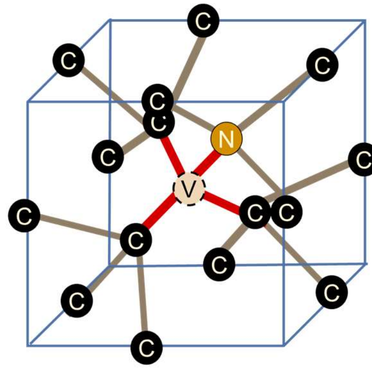

Figure 1.6: *Schematic of Nitrogen-Vacancy centre in a carbon lattice.*

This defect centre is known to exist in both negative and neutral charge states NV^- and NV^0[59] although NV^- remain the main centres used for the previously described applications as the potential of NV^0 centres for quantum applications has not been confirmed yet. N-V centres are also mentioned as colour centres in the literature because diamond impurities result in coloured diamonds.

Despite the abundance of diamond impurities in nature, N-V centres present a particularly interesting feature for communication applications. N-V centres display an emission peak at 637 nm wavelength, also known as the zero phonon line (ZPL) and suitable for optical fibre communication. They are also conveniently excited by many visible lasers due to their bright emission in the red.

Coupling N-V centres to cavities is known to increase the generation and the collection of zero phonon lines by Purcell enhancement later discussed in Section 1.4.4. Many cavity architectures fulfilled this purpose such as photonic crystals[60, 61] and microring resonators[62]. In recent years, many studies using Fabry-Perot cavities have demonstrated strong field confinement and more convenience in using diamond membranes, displaying bulk-like optical properties[63-65].

1.4 Microcavities

Many photon generation processes have recently demonstrated great potential as deterministic photon sources such as the emission of a single quantum dot, a single N-V centre or the fluorescence of a single molecule[66]. These sources emit single-photons using an external trigger event. However, this emission process suffers from many limitations that prevent them from being used for quantum networking or quantum computing. Usually, the generated photons are emitted isotropically and exhibit a broad energy distribution. Hence, the emission process cannot be described by a Hamiltonian evolution and is not reversible. These limitations can be overcome by coupling these photon sources to cavities.

1.4.1 Cavity quantum electrodynamics

A microcavity is an optical resonator of a wavelength-scale dimension. There are two major mechanisms that allow the confinement of light in microcavities. The first mechanism relies on the reflection off a single interface such as a metallic plate or using the total internal reflection at the boundary of two dielectrics. The second mechanism relies on high reflectance Bragg mirrors which are the heart of the Fabry-Perot cavity (see Section 1.4.2). Sometimes a combination of both methods can be used within the same microcavity[67].

Field quantization quantum electrodynamics can be reminded in this case. The cavity eigenmodes can be described by either Laguerre-Gaussian or Hermite-Gaussian modes. The cavity mode function is $\psi_{\text{cav}}(r)$ and its resonance frequency is ω_{cav}. The state vector can be described as a superposition of photon-number states $|n\rangle$ and the energy for n photons is equal to $\hbar\omega_{\text{cav}}\left(n+\frac{1}{2}\right)$. This equal energy spacing allows the cavity to be treated as a harmonic oscillator. The Hamiltonian equation of the cavity can be expressed using the creation and annihilation operators $\hat{a}^{\dagger}$ and $\hat{a}$:

$$H_{\text{cav}} = \hbar\omega_{\text{cav}}\left(\hat{a}^{\dagger}\hat{a}+\frac{1}{2}\right) \tag{1.1}$$

The Hamiltonian equation does not take into account any losses. In a real cavity, the photon number states will decay until thermal equilibrium with the environment is reached. Figure 1.7 illustrates a two-level atom model (also known as Jaynes-Cummings model)[68] of a ground state $|g\rangle$ and an excited state $|x\rangle$.

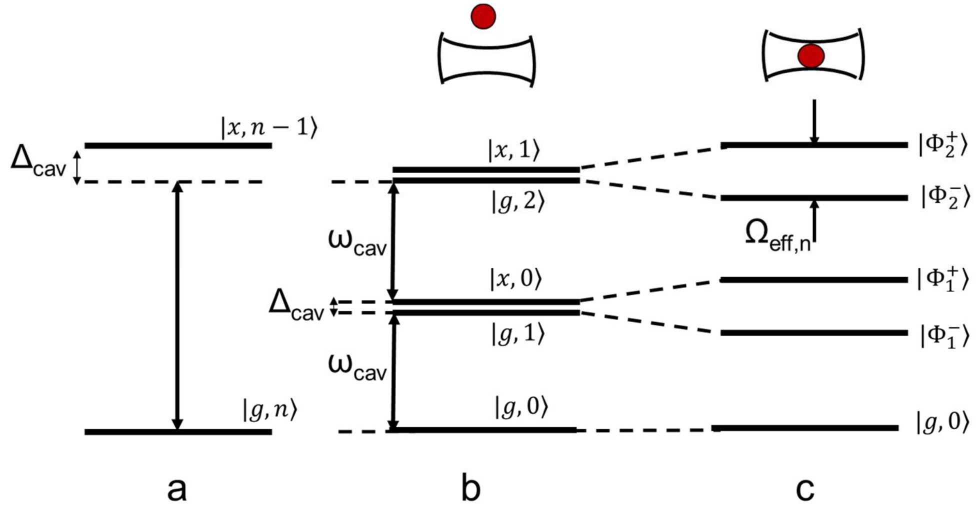

Figure 1.7: *a) Illustration of a two-atom level of a ground state $|g\rangle$ and an excited state $|x\rangle$. b) State doublets split by Δ_{cav} in the case of the atom outside the cavity. c) State doublets split by Rabi frequency $\Omega_{\text{eff,n}}$ in the case of the atom inside the cavity. Diagram reproduced from [69].*

The photon-number states are split into doublets of non-degenerate dressed states with the atom-cavity interaction. The cavity only couples $|g,n\rangle$ and $|x,n-1\rangle$ The ground state $|g,0\rangle$ remains uncoupled to other states and is not subject to any energy shift or splitting. If the cavity mode is resonant with the atomic transition, the population then oscillates with the Rabi frequency. Two corresponding eigenstates are split by $\Omega_{\mathrm{eff,n}}$, the effective Rabi frequency, representing the oscillation frequency of the population between $|g,n\rangle$ and $|x,n-1\rangle$. The cavity field stimulates the emission of an excited atom into the cavity. The photon number will be increased by one during the de-excitation process. The atom is re-excited by absorbing a photon from the cavity field, and so forth[70].

There are various types of cavity systems documented in the literature such as micropillars[71], photonic crystals[72] and microdisk cavities[73]. In this thesis, the principal cavity type studied is the monolithic Fabry-Perot cavity. The structure and the properties of the Fabry-Perot cavity will be discussed in Sections 1.4.2 and 1.4.3.

1.4.2 The Fabry-Perot cavity

The Fabry-Perot microcavity is commonly used in single-photon generation. Initially described by Fabry and Perot in 1899[74], this multiple-beam reflector was composed of an etalon consisting of two flat plates separated by a distance d_s. The plates are aligned and set parallel to each other. An example of Fabry-Perot cavity is shown in Figure 1.8, where the plates are separated by a ring, usually made of quartz. The inner surfaces of the plates are coated to increase their reflectance.

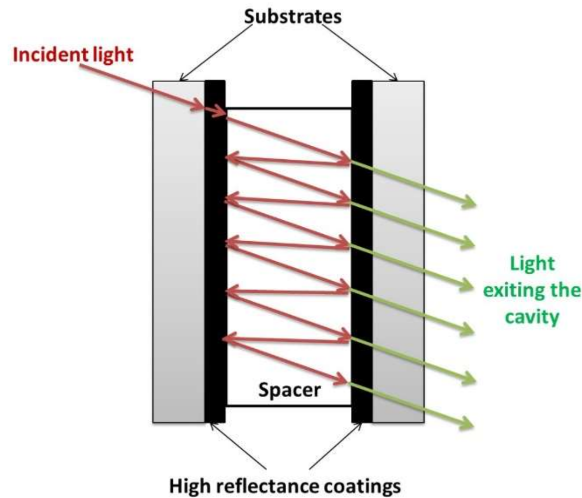

Figure 1.8*: Fabry-Perot etalon composed of two highly reflective coatings separated by a spacer. The diagram shows the internal light reflections between the highly reflecting coatings of the etalon.*

1.4.3 Finesse and quality factor

A microcavity with a total power reflectivity R and a round-trip optical length L is considered for the next calculations. The quality factor or the Q-factor of the cavity is a

dimensionless parameter that characterizes the resonator's bandwidth relatively to its center frequency. Physically, the Q-factor represents the ratio of the energy stored in the cavity over the energy lost or how well photons are confined within the cavity. The Q-factor can be expressed in Equation (1.2) as the ratio of the resonant frequency ω_c of the cavity to its bandwidth $\delta\omega_c$:

$$Q = \frac{\omega_c}{\delta\omega_c} \quad (1.2)$$

The cavity bandwidth $\delta\omega_c$ is calculated at the full width at half maximum (FWHM) linewidth of the Lorentzian spectral line shape of the resonant mode as represented in Figure 1.9. The cavity has also a free spectral range $\Delta\omega_{FSR}$ which represents the frequency spacing of the Gaussian shaped resonance modes. It is given below in Equation (1.3):

$$\Delta\omega_{FSR} = \frac{2\pi c}{2L} \quad (1.3)$$

The free spectral range $\Delta\omega_{FSR}$ and the cavity bandwidth $\delta\omega_c$ are shown in Figure 1.9.

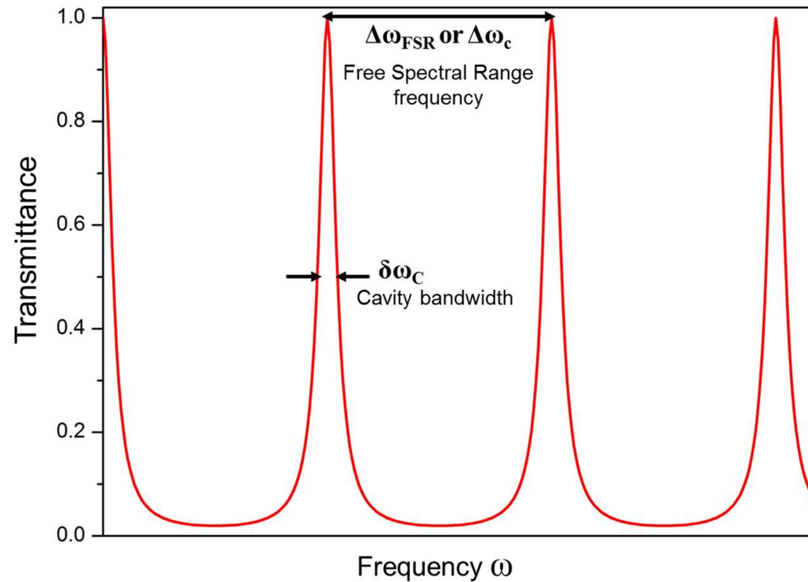

Figure 1.9: *Frequency-dependent transmittance for a Fabry-Perot etalon showing the resonance modes. The free spectral range* $\Delta\omega_{FSR}$ *represents the frequency spacing between two consequent resonant modes while the bandwidth* $\delta\omega_c$ *represents the frequency width at half of the maximum transmittance.*

The *finesse* F of the cavity is defined as the ratio of free spectral range to twice the decay rate k which represents the invert of the duration of an emitted photon in the cavity (see Equation (1.4)). Moreover, $2k$ represents the photon loss rate in the cavity.

$$F = \frac{\Delta\omega_{\mathrm{FSR}}}{2k} \tag{1.4}$$

The finesse of the cavity is also related to the mirror reflectivity R, assuming equal reflectance mirrors, by the following expression:

$$F = \frac{\Delta\omega_c}{\delta\omega_c} = \frac{\pi\sqrt{R}}{1-R} \tag{1.5}$$

The reflectivity dependency of the *finesse* is represented in Figure 1.10 in a logarithmic scale. The finesse varies slowly between 10^3 and 10^4 for a reflectance between 99.7 and 99.98 %. Beyond 99.99 %, the finesse becomes very sensitive to the reflectance value as it can vary by several orders of magnitude. As the reflectance approaches 100 %, the finesse asymptotes infinity (see Equation (1.5)).

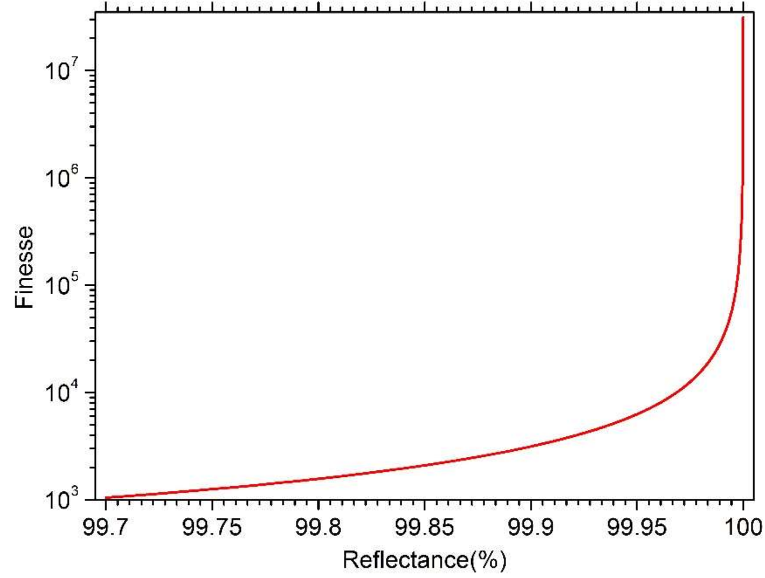

Figure 1.10: *Finesse as a function of cavity reflectance plotted from Equation (1.5).*

In the case of a wavelength scale microcavity, the values of the *finesse* and the Q-factor are very close because the mode frequency separation $\Delta\omega_c$ is similar to the resonant frequency of the cavity ω_c. In the case of a longer cavity, the Q-factor becomes greater than the *finesse*. Considering the reflectance and the transmittance of both surfaces are equal with no phase change, the transmittance of a plane wave for the Fabry-Perot etalon can be described in the following equation:

$$T = \frac{T_s^2}{(1-R_s)^2}\frac{1}{1+\left(\frac{4R_s}{(1-R_s)^2}\right)\sin^2\delta} \tag{1.6}$$

R_s and T_s being the reflectance and the transmittance of the spacer and δ is the phase thickness of the layer as defined in Equation (1.7):

$$\delta = \frac{2\pi n_s d_s \cos v_s}{\lambda} \tag{1.7}$$

n_s and d_s being the respective refractive index and the physical thickness of the spacer while v_s includes the oblique incidence of the light.

The *finesse* F of the interferometer is represented in Equation (1.6) as the ratio: $\frac{4R_s}{(1-R_s)^2}$

Therefore, the transmittance in Equation (1.6) becomes:

$$T = \frac{T_s^2}{(1-R_s)^2} \frac{1}{1+F\sin^2\delta} \tag{1.8}$$

If there is no loss in the reflecting layers, then: $T_s = 1 - R_s$

The transmittance depends now only on the *finesse* F of the cavity and the optical thickness δ :

$$T = \frac{1}{1+F\sin^2\delta} \tag{1.9}$$

The form of this function is shown in Figure 1.10 where the transmittance of the Fabry-Perot interferometer is plotted against δ . For $\delta = m\pi$ and $m = 0, \pm 1, \pm 2, ...$, $\sin^2\delta = 0$ and T is maximum. For halfway m values, $\sin^2\delta = 1$ and T is a minimum. The peaks of the $T(\delta)$ function are called fringes and m represents the fringe order. Figure 1.11 also compares the transmittance profile for three finesse values. The fringes width becomes narrower as F increases.

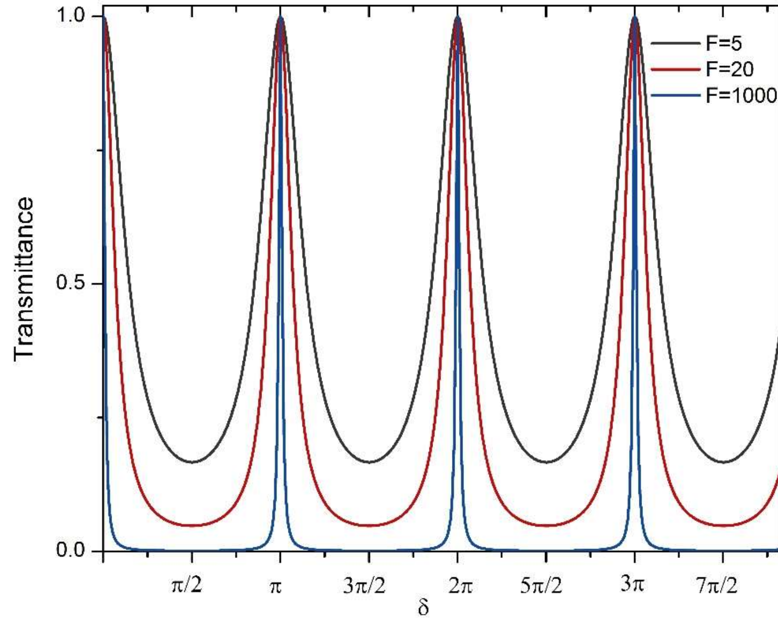

Figure 1.11: *Transmittance of a Fabry-Perot interferometer calculated from Equation (1.9) for three finesse values. The greater is the finesse, the narrower are the resonance modes.*

Practically, the finesse of the interferometer is limited to 25 or 50 in best cases. These limitations are mostly due to manufacturing imperfections of the Fabry-Perot plates. These imperfections are related to the difficulty of producing perfectly flat surfaces. These flatness differences induce local variations to the physical thickness d_s and hence to the optical thickness δ causing the cavity fringes to shift. Using piezo stages to align the reflecting surfaces helps overcoming these issues. The finesse can be also increased to several thousands using plano-concave Fabry-Perot cavities. (See Section 1.4.5).
So far, the absorption has been neglected in Equation (1.9). Now considering A_s the absorptance of each plate, Equation (1.9) becomes:

$$T = \frac{T_s^2}{\left(T_s + A_s\right)^2} \frac{1}{1 + F \sin^2 \delta} \qquad (1.10)$$

Where: $A_s = 1 - R_s - T_s$

The transmittance in Equation (1.10) can be also written as a function of the ratio $\frac{A_s}{T_s}$:

$$T = \frac{1}{\left(1 + \frac{A_s}{T_s}\right)^2} \frac{1}{\left(1 + F \sin^2 \delta\right)} \qquad (1.11)$$

Figure 1.12 represents the transmittance calculated from Equation (1.11) against the finesse for different absorptance A_s values. The transmittance has been also plotted for a silver coating at 550 nm and a gold coating at 1.1 μm[75].

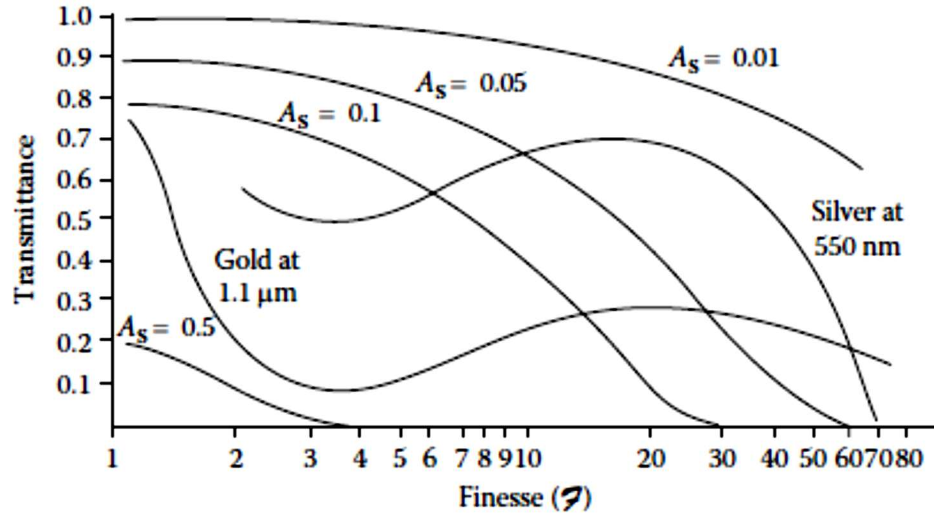

Figure 1.12: *Fabry-Perot Etalon transmittance against finesse F for various absorption values, extracted from[75].*

Figure 1.12 highlights the effect of absorption loss on the transmittance of the Fabry-Perot etalon. For A_s equal to 0.5, the transmittance at a finesse equal to 1 is already limited to 0.2 and drops to zero beyond a finesse equal to 4. By contrast, the transmittance of the Fabry-Perot etalon for A_s equal to 0.01 is almost equal to 1 and drops to 0.7 beyond a finesse equal to 70. The performance of silver, one of the best metals in the infrared and visible region, drops dramatically beyond a finesse value of 20 which makes this material and other metallic coatings inadequate for Fabry-Perot cavities due to high absorption losses. Using dielectric coatings helps overcoming the transmittance drop of Fabry-Perot interferometers. The optical properties of dielectric Bragg reflectors as well as their optical function in Fabry-Perot microcavity will be discussed in Section 1.5 Distributed Bragg Reflectors.

1.4.4 Purcell factor and small cavity mode volume

The deterministic generation of single-photons from atom-cavity systems relies on the Purcell effect[76, 77]. The spontaneous emission rate f, also known as the Purcell factor, is related to the Q-factor, the wavelength λ and the volume of the cavity V as shown in Equation (1.12):

$$f = \frac{3Q\lambda^3}{4\pi^2 V} \qquad (1.12)$$

And the probability of the spontaneous emission β is given in Equation (1.13):

$$\beta = \frac{f}{f+1} \qquad (1.13)$$

The above equation shows the dependency of the photon emission on the volume of the cavity. If the mode volume of the cavity is small enough, the emitter and the cavity couple

so strongly that the probability of emission β becomes close to unity, which means that a deterministic photon emission is possible with an efficiency close to unity.

1.4.5 Plano concave Fabry-Perot cavities

The most common high finesse Fabry-Perot microcavities used in quantum application are half symmetric cavities using one flat dielectric mirror and one curved mirror. Curved mirrors allow confining light in the lateral plane and reducing the cavity losses. Curved mirrors are curved substrates usually made by either focused ion beam milling[78] or CO_2 laser ablation[63] and coated with high reflectance dielectric coatings. The concavity of the mirrors is defined by the radius of curvature. Finesse values above 10 000 have been reported for a radius of curvature between 15 µm and 20 µm for N-V diamond quantum devices[63, 64]. The fabrication and the coating of curved substrates will be detailed in Chapter 4.

1.5 Dielectric distributed Bragg reflectors

The main properties of microcavities such as finesse, the quality factor and the probability of single-photon emission related to the Purcell theory were presented in Section 1.3. The theory of the Fabry-Perot interferometer and the optical signification of the finesse was also explained. Multilayer dielectric mirrors increase the finesse of the cavity by combining very high reflectance and low absorptance. The following section introduces the optical properties and losses of multilayer dielectric coatings.

1.5.1 The quarterwave stack

The basic type of dielectric mirrors used for microcavities is a stack of alternating low and high-index films. The optical thickness of each layer is a quarterwave. While the light reflected within the high-index layers does not sustain any phase shift on reflection, the reflected light within low index layers will keep a phase change of 180 °. The left diagram on Figure 1.13 shows the multiple reflection of a dielectric multilayer coating. The incident light produced by reflection at successive boundaries through the stack reappears at the front surface all in phase. The Fabry-Perot cavity (Figure 1.13, right diagram) consists of a spacer layer that is usually half a wavelength thick, bounded by two high-reflectance coatings. Multiple-beam interference in the spacer or cavity layer causes the transmission of the cavity to be extremely high over a narrow band of wavelengths around that for which the spacer is a multiple of one-half–wavelength thick.

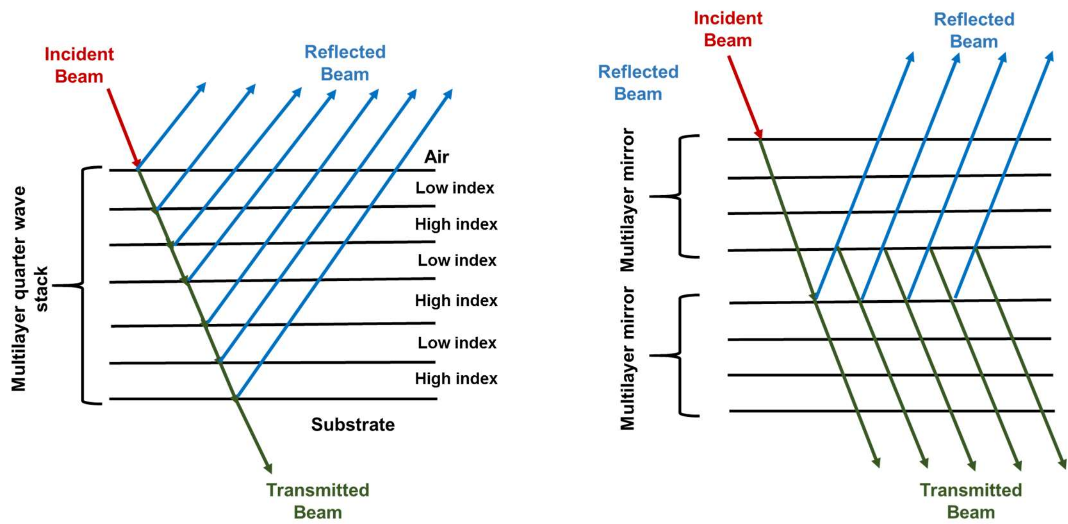

Figure 1.13: *Right: a Fabry-Perot cavity using multilayer high-reflectance coatings. Left: a multilayer dielectric coating consisting of alternating high and low refractive indices. Reproduced from[79].*

The reflectance of a quarterwave multilayer coating can be made as high as desired by increasing the number of alternate low and high index layers. Figure 1.14 shows calculated transmittance and reflectance spectra of a 29-layer TiO_2/SiO_2 high reflectance coating designed at a centre wavelength of 640 nm. At this wavelength, the refractive indices of silicon dioxide and titanium dioxide are 1.45 and 2.27 respectively. The calculation was made using a glass substrate of an index of 1.52. The reflectance remains high over a limited range of wavelength.

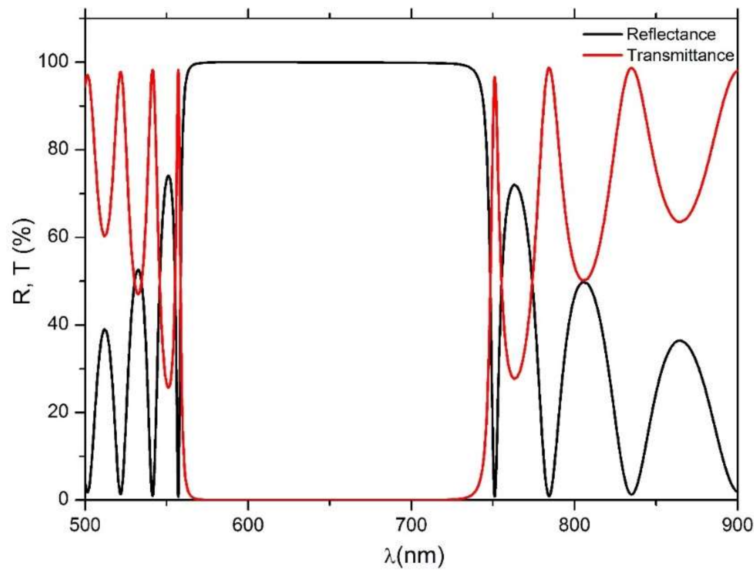

Figure 1.14: *Computed transmittance and reflectance (dashed-line) spectra of multilayer dielectric high-reflectance stack deposited on a transparent substrate (n_{sub}=1.52) using Essential Macleod software. The low index material is SiO_2 (n_L=1.45) and the high index material is TiO_2 (n_H=2.27). The calculation was performed for a stack composed of a total 20 alternating SiO_2 and TiO_2 layers.*

The bandwidth of the maximum reflectance (or minimum transmittance) depends only on the ratio of high and low refractive indices. Both transmittance and reflectance spectra also show a rectangular shape in the passband zone. Outside this zone, the reflectance changes abruptly to low values. This optical behaviour is used to build many thin-film filters such as longwave or shortwave pass filter, bandstop filter or simply to fabricate high reflectance coating mirrors for lasers such as the vertical cavity surface emitting laser structure (VCSEL) illustrated in Figure 1.15.

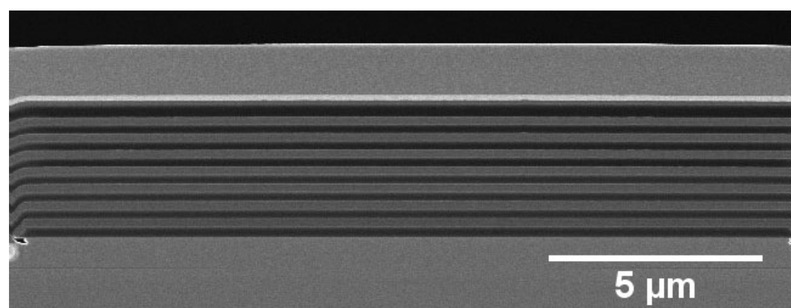

Figure 1.15: *Scanning electron micrograph of high reflectance mirror deposited at Helia Photonics Ltd as a part of a vertical cavity surface emitting laser(VCSEL) showing the alternating layers of low index(grey) and high index(dark) layers.*

1.5.2 Reflectance, transmittance and absorbance

Dielectric coatings of alternate quarterwave high and low index layers allow reaching very high reflectance. This reflectance can be made as high as possible by increasing the number of low/high indices layer pairs. Considering that n_H and n_L are the indices of the

high and low-index layers and if the high-index layers are outermost at both sides of the stack, the reflectance in free space is described by Equation (1.14):

$$R = \left[\frac{1 - \frac{n_{\mathrm{H}}^{2p+2}}{n_{\mathrm{L}}^{2p}.n_{\mathrm{sub}}}}{1 + \frac{n_{\mathrm{H}}^{2p+2}}{n_{\mathrm{L}}^{2p}.n_{\mathrm{sub}}}} \right]^2 \quad (1.14)$$

With n_{sub} and 2p+1 being the refractive index of the substrate and the number of layers of the coating.

The bandwidth of the stopband depends only on the refractive index contrast between the high index layer and the low index layer as expressed in the following equation:

$$\Delta g = \frac{4}{\pi} \arcsin\left(\frac{n_{\mathrm{H}} - n_{\mathrm{L}}}{n_{\mathrm{H}} + n_{\mathrm{L}}} \right) \quad (1.15)$$

The greater the number of the layers, the greater is the reflectance (see Figure 1.16, left diagram). A larger bandwidth is obtained for a greater refractive index contrast as shown in Figure 1.16 on the right diagram. ZnS/ Na_3AlF_6 coating has indeed a greater refractive index contrast than TiO_2/SiO_2 coating.

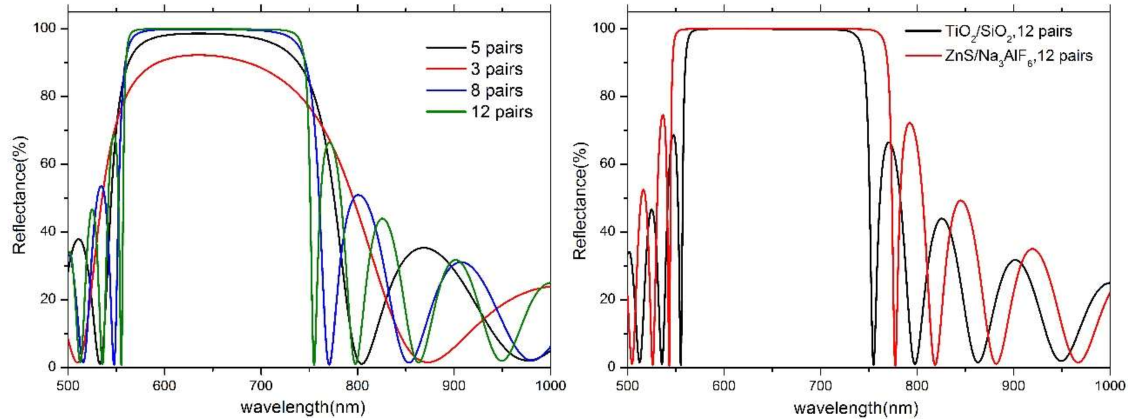

Figure 1.16: *Left, reflectance calculated for a TiO_2/SiO_2 quarterwave multilayer stack for increasing pair numbers. Right, reflectance calculated for 12-pair TiO_2/SiO_2 and ZnS/Na_3AlF_6 quarterwave multilayer stacks.*

If $\frac{n_{\mathrm{H}}^{2p+2}}{n_{\mathrm{L}}^{2p}.n_{\mathrm{sub}}} > 1$, then the reflectance becomes:

$$R \approx 1 - 4\frac{n_{\mathrm{L}}^{2p}.n_{\mathrm{sub}}}{n_{\mathrm{H}}^{2p+2}} \quad (1.16)$$

And the transmittance T is given by Equation (1.17), considering perfect dielectric layers:

$$T \approx 4\frac{n_{\mathrm{L}}^{2p}.n_{\mathrm{sub}}}{n_{\mathrm{H}}^{2p+2}} \quad (1.17)$$

This approximation of the refractive indices shows that the addition of two extra layers reduces the transmittance by $\frac{n_H}{n_L}$. Both transmittance and reflection presented in Equations (1.16) and (1.17) assumed of lossless dielectric material. However, the reflectance achieved by high reflectance coatings is usually limited by absorption losses. The absorptance of the multilayer coating can be calculated using the concept of potential transmittance introduced by Hemingway and Lissberger in 1973[80]. The multilayer stack can be split into subassemblies of single layers. The potential transmittance of the multilayer is equal to the product of the individual single layer transmittances. For the entire multilayer, the absorptance can be written, for an outer layer of a high index, as:

$$A = \frac{2\pi n_0 \left(k_H + k_L\right)}{\left(n_H^2 - n_L^2\right)} \quad (1.18)$$

The absorptance can be expressed in the same manner for a multilayer ending with a low-index material. The final low-index layer will reduce the reflectance and so increase the absorptance:

$$A = \frac{2\pi}{n_0} \frac{n_L^2 k_H + n_H^2 k_L}{n_H^2 - n_L^2} \quad (1.19)$$

Knowing the n and k values of both high and low refractive indices materials, the absorption losses can be estimated for a given pair of high and low refractive indices dielectrics.

1.5.3 Losses

It has been demonstrated in the previous section that the reflectance attainable by a quarterwave stack depends on the number of layers (Equation (1.14)). It was also demonstrated that the addition of another pair of layers allows to decrease the transmittance by a ratio of $\frac{n_H}{n_L}$ (see Equation (1.17)). These equations made the assumption of lossless materials. However, the reflectance of multilayer coatings is practically limited by absorption and scatter losses.

High levels of light absorption can be tolerated in many low power optical instruments, especially using metallic coatings where few percent of incident light will be absorbed. However, in many high power optics applications, precision measurements optics and for instance cavity quantum electrodynamics, very small levels of absorption are enough to cause many thermal aberrations. Absorption in high reflectance cavity mirrors produces heat gradients which are responsible for thermoelastic deformations[81] related to the expansion coefficients of the materials, thermal depolarization[82] where heat gradients induce different polarisations at different point sections of the coating and thermorefractive phase gradients also known as thermal lensing[83], where the absorption of power inside a dielectric material results in a heat gradient changing the optical path length through the medium. The latter is related to the temperature dependence of the refractive index.

Absorption losses are strongly related to the intrinsic electronic properties of the materials. They can be caused by impurities, composition or simply due to the structure of the material. Absorption is related to the extinction coefficient k of the media. Reducing the absorption of high reflectance mirrors requires using materials with very low extinction coefficient. Estimating absorption for dielectric materials will be presented in Chapter 2. An estimation of the absorption for multilayer dielectric mirrors can be calculated for a pair of low-high indices quarterwave stack using Equations (1.18) and (1.19). Many techniques allow to measure accurately very small absorption losses such as the photothermal deflection technique[84] and the photothermal common path interferometry[85].

Scattering in high reflectance mirrors is caused by many factors such as surface roughness [86], irregularities and impurities in the stack layers. The scattered field from isolated local defects can be estimated using the Mie theory[87]. Scatter losses are unlikely to cause heating or distortion like absorption losses. An estimation of scatter from surface roughness for dielectric materials and dielectric mirrors will be provided in Chapters 2 and 3.

Rough surfaces are also responsible for electromagnetic wave scattering which is relevant to telecommunication and sensing applications. One classical approach to wave scattering is the Kirchhoff Approximation given the incident electromagnetic wave is smaller than the radius of curvature of the surface [88, 89].

1.6 Summary and thesis plan

Fabry-Perot cavities represent the state of the art for strong light-matter coupling for several quantum devices and applications. High finesse cavities can be achieved using multilayer dielectric coatings. Dielectric Bragg reflectors are a good alternative to metal coatings allowing very high reflectivity and maintaining zero transmittance. However, the quality of fabrication of these coatings is continuously challenged by stringent demands of quantum applications, for example by devices which require near-zero optical losses. This thesis addresses the optical losses of multilayer dielectric coatings. In Chapter 2, a methodology for low losses dielectric materials grown using various physical vapour deposition techniques is presented. The design, the fabrication and the characterisation of planar multilayer coatings are presented in Chapter 3. Curved mirrors fabrication and characterisation are explained in Chapter 4.

REFERENCES

[1] T. F. Watson *et al.*, "A programmable two-qubit quantum processor in silicon," *Nature,* vol. 555, p. 633, 2018.

[2] T. P. Lyons *et al.*, "The valley Zeeman effect in inter- and intra-valley trions in monolayer WSe2," *Nature Communications,* vol. 10, no. 1, p. 2330, 2019.

[3] R. Pisoni *et al.*, "Interactions and Magnetotransport through Spin-Valley Coupled Landau Levels in Monolayer MoS2," *Physical Review Letters,* vol. 121, no. 24, p. 247701, 2018.

[4] M. Manca *et al.*, "Enabling valley selective exciton scattering in monolayer WSe2 through upconversion," *Nature Communications,* Article vol. 8, p. 14927, 2017.

[5] R. Daniel *et al.*, "Deterministic enhancement of coherent photon generation from Nitrogen-Vacancy center in Ultrapure diamond," *Physical Review X,* vol. 7, no. 3, p. 031040, 2017.

[6] D. Riedel *et al.*, "Low-Loss Broadband Antenna for Efficient Photon Collection from a Coherent Spin in Diamond," *Physical Review Applied,* vol. 2, no. 6, p. 064011, 2014.

[7] H. Thyrrestrup *et al.*, "Quantum Optics with Near-Lifetime-Limited Quantum-Dot Transitions in a Nanophotonic Waveguide," *Nano Letters,* vol. 18, no. 3, pp. 1801-1806, 2018.

[8] T. Kaldewey, A. V. Kuhlmann, S. R. Valentin, A. Ludwig, A. D. Wieck, and R. J. Warburton, "Far-field nanoscopy on a semiconductor quantum dot via a rapid-adiabatic-passage-based switch," *Nature Photonics,* vol. 12, no. 2, pp. 68-72, 2018.

[9] L. Greuter, S. Starosielec, A. V. Kuhlmann, and R. J. Warburton, "Towards high-cooperativity strong coupling of a quantum dot in a tunable microcavity," *Physical Review B,* vol. 92, no. 4, p. 045302, 2015.

[10] R. Albrecht, A. Bommer, C. Deutsch, J. Reichel, and C. Becher, "Coupling of a single nitrogen-vacancy center in diamond to a fiber-based microcavity," *Physical review letters,* vol. 110, no. 24, p. 243602, 2013.

[11] M. W. Doherty, N. B. Manson, P. Delaney, F. Jelezko, J. Wrachtrup, and L. C. L. Hollenberg, "The nitrogen-vacancy colour centre in diamond," *Physics Reports,* vol. 528, no. 1, pp. 1-45, 2013.

[12] S. Prawer, *Quantum information processing with diamond : principles and applications / edited by Steven Prawer and Igor Aharonovich* (Quantum Information Processing with Diamond). Cambridge, UK: Cambridge, England : Woodhead Publishing, 2014.

[13] E. M. Alexeev *et al.*, "Imaging of Interlayer Coupling in van der Waals Heterostructures Using a Bright-Field Optical Microscope," *Nano Letters,* vol. 17, no. 9, pp. 5342-5349, 2017.

[14] C. Palacios-Berraquero *et al.*, "Large-scale quantum-emitter arrays in atomically thin semiconductors," *Nature Communications,* Article vol. 8, p. 15093, 2017.

[15] L. E. Greuter, "self-assembled quantum dots in a fully tunable microcavity," Doctor of Philosophy, Departement Physik, University of Basel, Basel, 2015.

[16] N. Sidqi, C. Clark, G. S. Buller, G. K. V. V. Thalluri, J. Mitrofanov, and Y. Noblet, "Comparative study of dielectric coating materials for micro-cavity applications," *Opt. Mater. Express,* vol. 9, no. 8, pp. 3452-3468, 2019.

[17] J. C. Maxwell, "On physical lines of force," *The London, Edinburgh and Dublin Philosophical Magazine and Journal of science,* vol. 4th series, no. March, April, pp. 161-175, 282-291, 338-349, 13-24, 85-95, 1861.

[18] A. Einstein, "Über einen die Erzeugung und Verwandlung des Lichtes betreffenden heuristischen Gesichtspunkt," *Annalen der Physik,* vol. 322, no. 6, pp. 132-148, 1905.

[19] G. N. Lewis, "The Conservation of Photons," *Nature,* vol. 118, p. 874, 1926.

[20] A. Jablonski, "Efficiency of Anti-Stokes Fluorescence in Dyes," *Nature,* vol. 131, p. 839, 1933.

[21] M. Bixon and J. Jortner, "Intramolecular Radiationless Transitions," *The Journal of Chemical Physics,* vol. 48, no. 2, pp. 715-726, 1968.

[22] J. S. Santos, I. M. Raimundo, C. M. B. Cordeiro, C. R. Biazoli, C. A. J. Gouveia, and P. A. S. Jorge, "Characterisation of a Nafion film by optical fibre Fabry–Perot interferometry for humidity sensing," *Sensors & Actuators: B. Chemical,* vol. 196, no. C, pp. 99-105, 2014.

[23] L.Kubetsky, "Multielement Electronic Device," 1931.

[24] T. Bondo, M. Hennrich, T. Legero, G. Rempe, and A. Kuhn, "Time-resolved and state-selective detection of single freely falling atoms," *Optics Communications,* vol. 264, no. 2, pp. 271-277, 2006.

[25] T. McIlrath, R. Hudson, A. Aikin, and T. Wilkerson, "Two-photon lidar technique for remote sensing of atomic oxygen," *Appl. Opt.,* no. 18, p. 316, 1979.

[26] J. Kash, J. Tsang, D. Knebel, and D. Vallett, "ISTFA98: Proceedings of the 24th international symposium for testing and failure analysis," 1998,

[27] J. Tsang, J. Kash, and D. Vallett, "Picosecond imaging circuit analysis," *IBM J. RES. DEV,* vol. 44, no. 4, pp. 583-603, 2000.

[28] E. Togan *et al.*, "Quantum entanglement between an optical photon and a solid-state spin qubit," *Nature,* vol. 466, no. 7307, p. 730, 2010.

[29] H. Bernien *et al.*, "Heralded entanglement between solid-state qubits separated by three metres," *Nature,* vol. 497, no. 7447, p. 86, 2013.

[30] L. M. Duan, M. D. Lukin, J. I. Cirac, and P. Zoller, "Long-distance quantum communication with atomic ensembles and linear optics," *Nature,* Article vol. 414, p. 413, 2001.

[31] C. Bennett and G. Brassard, in *Proceedings of IEEE international conference on computers, Systems and Signal processing*, Bangalore, India, 1984,

[32] H. J. Briegel, W. Dur, S. J. van Enk, J. I. Cirac, and P. Zoller, *The physics of quantum information*. Springer, Berlin, 2000.

[33] C. H. Bennett, G. Brassard, C. Crépeau, R. Jozsa, A. Peres, and W. K. Wooters, "Teleporting an unknown quantum state via dual classical and Einstein-Podolsky-Rosen channels," *Phys. Rev. lett.,* no. 70, 1993.

[34] M. Göppert-Mayer, "Über elementarakte mit zwei quantensprüngen," *Annalen der Physik,* vol. 401, no. 3, pp. 273-294, 1931.

[35] M. A. Nielsen and I. L. Chuang, "quantum computation and quantum informartion," *Cambridge University Press,* 2010.

[36] D. Magde and H. Mahr, "Study in Ammonium Dihydrogen Phosphate of Spontaneous Parametric interaction Tunable from 4400 to 16 000A," *Phys. Rev. lett.,* no. 18, pp. 905-907, 1967.

[37] D. C. Burnham and D. L. Weinberg, "Observation of Simultaneity in Parametric Production of optical photon pairs," *Phys. Rev. Lett.,* no. 25, pp. 84-87, 1970.

[38] J. Chen, X. Li, and P. Kumar, "Two-Photon-State generation via Four wave mixing in optical fibres," *Phy.Rev.A 72 033801,* 2005.

[39] X. Li, J. Chen, P. Voss, J. Sharping, and P. Kumar, "All-Fiber Photon source for quantum communications: Improved generation of correlated photons," *Phys. Rev. lett. 12, 3737-3744,* 2004.

[40] P. Michler, *Quantum Dots for Quantum Information Technologies edited by Peter Michler*. Cham : Springer International Publishing : Imprint: Springer, 2017.

[41] S. Haroche and D. Kleppner, "Cavity quantum electrodynamics," *Physics Today,* vol. 42, no. 1, pp. 24-30, 1989.

[42] F. K. Perkins, A. L. Friedman, E. Cobas, P. M. Campbell, G. G. Jernigan, and B. T. Jonker, "Chemical vapor sensing with monolayer MoS2," *Nano Letters,* vol. 13, no. 2, pp. 668-673, 2013.

[43] Y. F. Lin *et al.*, "Origin of noise in layered MoTe2 transistors and its possible use for environmental sensors," *Advanced Materials,* vol. 27, no. 42, pp. 6612-6619, 2015.

[44] X. Xiaodong, Y. Wang, X. Di, and F. H. Tony, "Spin and pseudospins in layered transition metal dichalcogenides," *Nature Physics,* vol. 10, no. 5, p. 343, 2014.

[45] Z. Gong *et al.*, "Magnetoelectric effects and valley-controlled spin quantum gates in transition metal dichalcogenide bilayers," *Nature Communications,* Article vol. 4, p. 2053, 2013.

[46] S. Dufferwiel *et al.*, "Valley coherent exciton-polaritons in a monolayer semiconductor," (in eng), *Nature communications,* vol. 9, no. 1, pp. 4797-4797, 2018.

[47] A. Splendiani *et al.*, "Emerging Photoluminescence in Monolayer MoS2," *Nano Letters,* vol. 10(4), pp. 1271-1275, 2010.

[48] J. Wang, G. Li, and L. Li, "Synthesis Strategies about 2D Materials," in *Two-dimensional Materials - Synthesis, Characterization and Potential Applications*: InTech, 2016, p. 3.

[49] A. Castellanos-Gomez *et al.*, "Deterministic transfer of two-dimensional materials by all-dry viscoelastic stamping," *2D materials,* vol. 1, no. 1, 2014.

[50] E. M. Alexeev, A. Catanzaro, O. V. Skrypka, and A. I. Tartakovskii, "Imaging of interlayer coupling in van der Waals heterostructures using a bright-field optical microscope," *Arxiv,* 2016.

[51] S. Dufferwiel *et al.*, "Exciton–polaritons in van der Waals heterostructures embedded in tunable microcavities," *Nature Communications,* vol. 6, no. 1, 2015.

[52] R. T. Grant *et al.*, "Efficient radiative pumping of polaritons in a strongly coupled microcavity by a fluorescent molecular dye," *Advanced Optical Materials,* vol. 4, no. 10, pp. 1615-1623, 2016.

[53] D. Coles, R. Grant, D. Lidzey, C. Clark, and P. Lagoudakis, "Imaging the polariton relaxation bottleneck in strongly coupled organic semiconductor microcavities," *Physical Review B (Condensed Matter and Materials Physics),* vol. 88, no. 12, 2013.

[54] D. M. Coles *et al.*, "Organic semiconductors: Vibrationally assisted polariton-relaxation processes in strongly coupled organic-semiconductor microcavities," *Advanced Functional Materials,* vol. 21, no. 19, pp. 3690-3690, 2011.

[55] S. K. Rajendran *et al.*, "Ultrafast dynamics of cavity polaritons in an organic semicondutor microcavity," in *International Conference on Fibre Optics and Photonics*, Chennai, 2012: Optical Society of America, in OSA Technical Digest (online), pp. 1, 3

[56] T. Cookson *et al.*, "A yellow polariton condensate in a dye filled microcavity," *Advanced Optical Materials,* vol. 5, no. 18, p. 1700203, 2017.

[57] I. Aharonovich and S. Prawer, "Promising directions in diamond technologies for quantum information processing (QIP) and sensing," in *Quantum Information Processing with Diamond*: Woodhead Publishing, 2014, pp. 307-317.

[58] S. Prawer, *Quantum information processing with diamond : principles and applications* (Quantum Information Processing with Diamond). Cambridge, UK: Cambridge, England : Woodhead Publishing, 2014.

[59] J. H. N. Loubser and J. A. v. Wyk, "Electron spin resonance in the study of diamond," *Reports on Progress in Physics,* vol. 41, no. 8, pp. 1201-1248, 1978.

[60] J. Riedrich-Möller *et al.*, "Nanoimplantation and Purcell enhancement of single nitrogen-vacancy centers in photonic crystal cavities in diamond," *Applied Physics Letters,* vol. 106, no. 22, 2015.

[61] L. Li *et al.*, "Coherent spin control of a nanocavity-enhanced qubit in diamond," *Nature Communications,* Article vol. 6, p. 6173, 2015.

[62] F. Andrei, E. B. Paul, S. Charles, C. F. Kai-Mei, and G. B. Raymond, "Resonant enhancement of the zero-phonon emission from a colour centre in a diamond cavity," *Nature Photonics,* vol. 5, no. 5, p. 301, 2011.

[63] D. Riedel *et al.*, "Deterministic enhancement of coherent photon generation from a Nitrogen-Vacancy center in ultrapure diamond," *Physical Review X,* vol. 7, no. 3, p. 031040, 2017.

[64] S. Bogdanovic *et al.*, "Design and low-temperature characterization of a tunable microcavity for diamond-based quantum networks," *Applied Physics Letters,* vol. 110, no. 17, 2017.

[65] S. Bogdanovic, "Diamond-based Fabry-Perot microcavities for quantum networks," PhD Doctoral thesis, Delft University of Technology, Delft, Netherlands, 2017.

[66] C. Brunel, B. Lounis, P. Tamarat, and M. Orrit, " Triggered Source of Single Photons Based on controlled single molecule fluorescence," *Phy. Rev. lett. ,* no. 83, pp. 2722-2725, 1999.

[67] A. V. Kavokin, J. J. Baumberg, G. Malpuech, and F. P. Laussy, *Microcavities*. Oxford university Press, 2007.

[68] B. W. Shore and P. L. Knight, "The Jaynes-Cummings model," *J. Mod. Opt,* no. 40, p. 1195, 1993.

[69] G. S. Solomon, C. Santori, and A. Kuhn, "Single emitters in isolated quantum systems," in *Single-photon generation and detection : experimental methods in the physical sciences*. Amsterdam: Academic Press, 2013, p. 473.

[70] G. S. Solomon, S. Santori, and A. Kuhn, "Single Emitters in Isolated quantum systems," in *Single-photon generation and detection : experimental methods in the physical sciences* Amsterdam: Academic Press, 2013, p. 473.

[71] M. Lermer *et al.*, "High beta lasing in micropillar cavities with adiabatic layer design," *Applied Physics Letters,* vol. 102, no. 5, p. 052114, 2013.

[72] M. D. Settle, R. J. P. Engelen, M. Salib, A. Michaeli, L. Kuipers, and T. F. Krauss, *Opt. Express,* vol. 15, no. 1, pp. 219-226, 2007.

[73] L. Wang *et al.*, "High-Q chaotic lithium niobate microdisk cavity," *Opt. Lett.,* vol. 43, no. 12, p. 2917, 2018.

[74] C. Fabry and A. Perot, "Theorie et applications d'une nouvelle méthode de spectroscopie interférentielle," *Annales des Chimie et des Physique,* vol. 7th series, no. 16, pp. 115-144, 1899.

[75] H. A. Macleod, "Multilayer high-reflectance coatings," in *Thin-film optical filters*: CRC Press, 2010, p. 215.

[76] E. M. Purcell, "Spontaneous Emission Probabilities at Radio Frequencies," *Phys. Rev.,* no. 69, p. 681, 1946.

[77] R. J. Barbour *et al.*, "A tunable microcavity," *Journal of Applied Physics,* vol. 110, no. 5, p. 053107, 2011.

[78] S. Schwarz *et al.*, "Two-dimensional metal-chalcogenide films in tunable optical microcavities," *Nano letters,* vol. 14, no. 12, p. 7003, 2014.

[79] H. A. Macleod, "Introduction," in *Thin-film optical filters*: CRC Press, 2010, pp. 7-8.

[80] D. J. Hemingway and P. H. Lissberger, *Optica Acta: International Journal of Optics,* vol. 20, no. 2, pp. 85-96, 1973.

[81] D. Iesan and A. Scalia, *Thermoelastic deformations*. Kluwer, 1996.

[82] Y. Aoyagi, T. Taira, and I. Shoji, "Thermal analysis simulation using depolarization loss in solid-state microchip laser," *SICE 2003 Annual Conference,* vol. 2, pp. 2195-2200, 2003.

[83] V. Mitrofanov *et al.*, "Technology for the next gravitational wave detectors," *Science China Physics, Mechanics & Astronomy,* vol. 58, no. 12, pp. 1-26, 2015.

[84] J. Sancho-Parramon, J. Ferré-Borrull, S. Bosch, A. Krasilnikova, and J. Bulir, "New calibration method for UV–VIS photothermal deflection spectroscopy set-up," *Applied Surface Science,* vol. 253(1), pp. 158-162, 2006.

[85] L. Anghinolfi *et al.*, "Optical properties of uniform, porous, amorphous Ta2O5 coatings on silica: temperature effects," *Journal of Physics D: Applied Physics,* vol. 46(45), p. 455301, 2013.

[86] A. A. Maradudin, *Light Scattering and Nanoscale Surface Roughness*. New York: Springer, 2007.

[87] H. Wolfram and T. Wriedt, *The Mie Theory: Basics and Applications*. Berlin: Springer, 2012.

[88] A. Voronovich, "The Kirchhoff and Related Approximations," in *Light Scattering and Nanoscale Surface Roughness*, A. Voronovich Ed., J. L. David, Ed., 2007, ch. 2, pp. 35-60.

[89] R. Papa and J. Lennon, "Conditions for the validity of physical optics in rough surface scattering," *IEEE Transactions on Antennas and Propagation,* vol. 36, pp. 647-650, 1988.

CHAPTER 2–SINGLE LAYER DIELECTRIC COATINGS

As already discussed in Chapter 1, many optical and structural parameters such as the refractive index n, the extinction coefficient k and the surface roughness influence the optical properties and losses of multilayer dielectric mirrors. This chapter describes the fabrication methods and the dielectric materials selected for high reflectance mirrors. The optical constants and the surface roughness of single layer dielectric materials are also presented. Absorption and scatter losses are studied for single layer coatings. The residual stress for single layer dielectrics is also presented.

The content of this chapter is partially adapted from:

Najwa Sidqi, Caspar Clark, Gerald S. Buller, Gopala Krishna V. V. Thalluri, Jevgenij Mitrofanov, and Yoann Noblet, "Comparative study of dielectric coating materials for micro-cavity applications," Opt. Mater. Express 9, 3452-3468 (2019)

2.1 Deposition methods

There are various deposition methods used to produce high reflectance dielectric mirrors. However, the properties expected from the fabricated coatings play a very decisive role in the choice of the fabrication method. Some of these properties include coating uniformity and adhesion to substrate, intrinsic stress, growth defects and material packing density. Fabrication cost and process length are also very important factors in the choice of the deposition method. The deposition processes mainly used to fabricate high reflectance mirrors are physical vapour deposition (PVD) processes. For industrial and production scale applications, we can distinguish between two principal deposition categories: thermal evaporation and energetic processes involving a high kinetic energy of the evaporated material. Thermal evaporation and energetic processes are presented in the following.

2.1.1 Thermal evaporation

Thermal evaporation is commonly used for thin film fabrication. The source material is placed in a boat and is heated either by a resistor-based heating or by an incident electron beam, bringing the material to an evaporation or sublimation point. The vapour is produced in an even stream of particles inducing fine variations of the thickness (see Figure 2.1). The vapour condenses on the substrate forming a thin film coating.

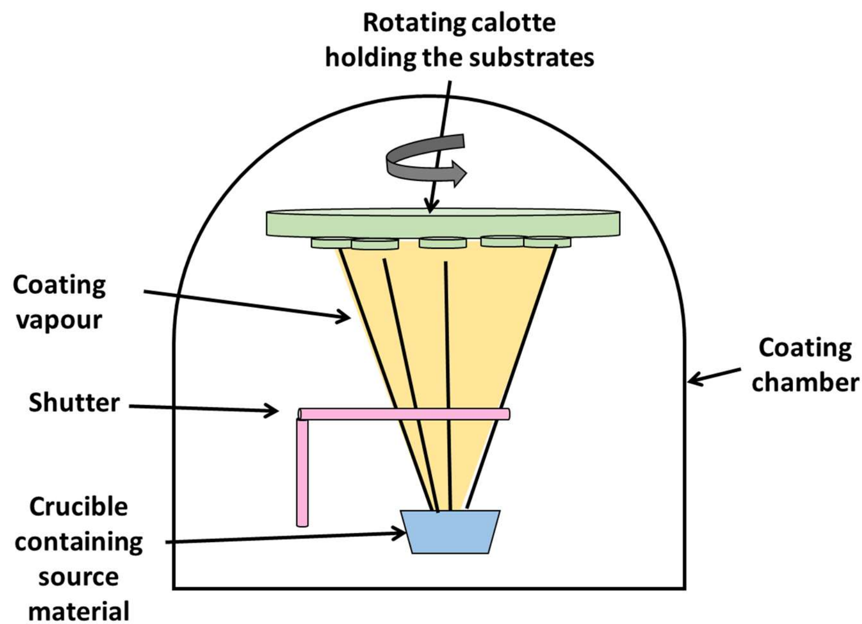

Figure 2.1: *Schematic of a thermal evaporation process. The source material is placed in a crucible and heated using an electron beam or a heating resistance. The material evaporates in an even vapour stream directed toward a rotating calotte holding the substrate.*

Thermal evaporation is a quick and accessible process. Few process parameters are involved and this method allows the evaporation of a wide range of materials including sulphides, fluorides, oxides and nitrides. Sometimes heating the substrate is used to enhance the final performances of the coating but the substrate temperature can be dictated by the coating properties and the final application. However, thermally evaporated coatings have a characterising columnar structure that causes instability and drift in their optical properties[1]. This is one of the main reasons that pushed to use energetic processes. Energetic deposition methods provide a higher kinetic energy allowing the disruption of the columnar structure of thermally evaporated coating. For instance, during E-beam evaporation, some atoms hang on the surface of the substrate and trap voids in the coating structure. Using ion assisted deposition, the incident ions bombard the surface of the substrate and allow the displacement of any overhanging atoms, leaving the voids open to be filled by the evaporated material. A better oxidation of the deposited film is allowed inducing a higher refractive index of thin film coatings.

2.1.2 Magnetron sputtering

One commonly known energetic process, even predating thermal evaporation is sputtering. In sputtering process, the momentum transfer from the incident ions allows the displacement and the ejection of atoms and molecules from the target into the partial pressure. This momentum and the kinetic energy involved become higher each time a new particle arrives to disrupt the columnar structure and the voids in the coating. Using a metallic target is conventional in sputtering processes. The bombarding ions are provided by a DC discharge near the target. This discharge is confined by crossed magnetic and electric fields in the case of magnetron sputtering. Magnetron sputtering

main advantage over conventional sputtering is the long electrons path so that discharge can be maintained at a lower pressure (10^{-2} mbar). A DC planar magnetron sputtering configuration is presented in Figure 2.2. One of the drawbacks of this configuration is the concentration of discharges between the poles' region leading to a higher target erosion in this area. This problem can be critical for a lot of oxide processes such as silicon dioxide due to oxide build up on the less eroded areas. The oxide patches formed on the target surface have high capacitance and break down in arcing discharges. Arcing discharges cause the ejection of molten material later embedded in the thin film structure. Other magnetron sputtering methods like mid-frequency sputtering (MF) or dual magnetron overcomes the build-up of charges in the eroded regions of the target. An even more advanced process which allows the covering of the target with insulating materials is radio frequency sputtering (RF) which permits for discharging to occur at very high frequencies. Using a pulsed DC power supply also permit to avoid the accumulation of electrical charges next to the target.

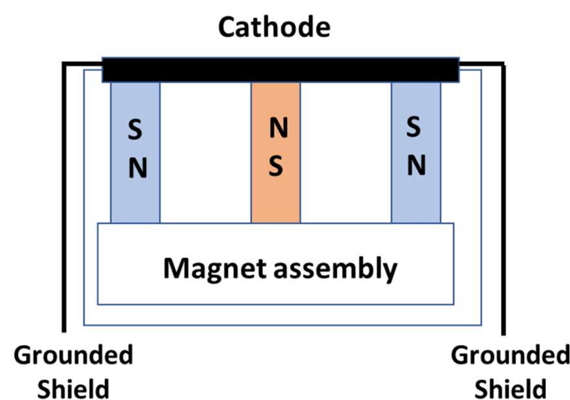

Figure 2.2: *Single planar magnetron configuration. The cathode or the target is connected to a negative supply. The positive supply is formed by the grounded shields and the coating chamber. Electrons leaving the cathode move outward turning into a cycloidal path due to magnetic field. The magnets polarity is arranged so the outer poles are opposite to inner one, reproduced from [2].*

Other methods of sputtering include ion beam sputtering (IBS). An ion gun allows producing ion discharges directed toward the target (Figure 2.3). This technique provides a higher film purity, especially for high reflectance multilayer coatings applications, where less than 1 ppm optical losses have been achieved using this method[3]. This technique, although slow, permits the production of high purity and dense films, especially for division wavelength multiplexing filters in the 90s[4]. As represented in Figure 2.3, an ion gun can be also added to classical thermal evaporation (called ion assisted deposition or IAD) in order to achieve higher film density. IBS and IAD do not however operate at similar energy levels. For IAD deposition, the incident ion energy ranges between 1 to 20 eV while ion beam energy can reach up to 1 keV.

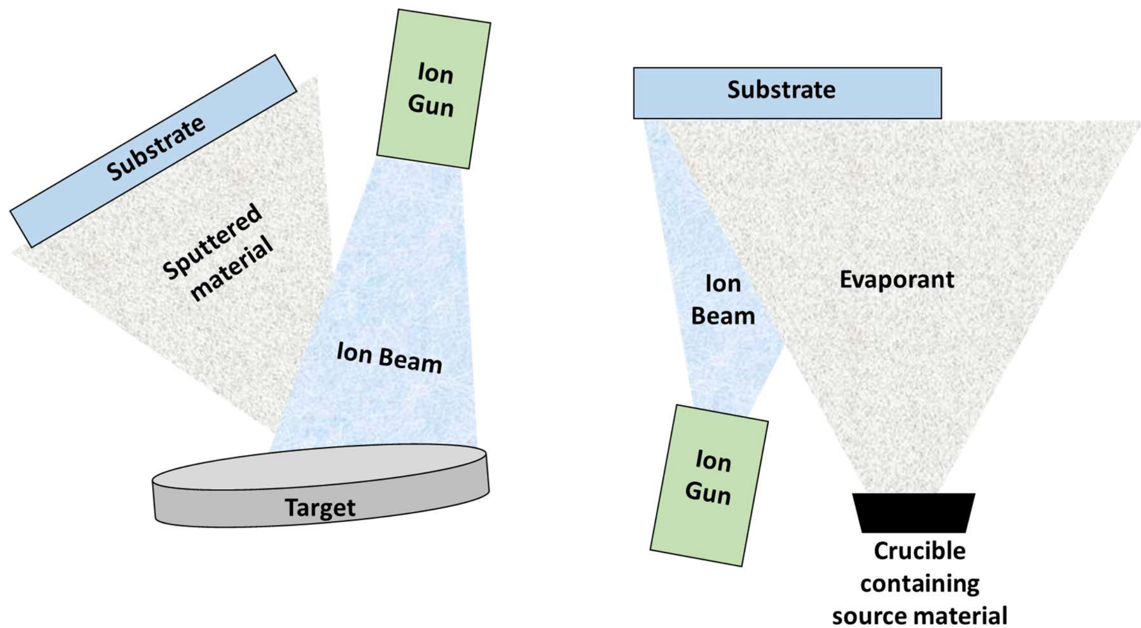

Figure 2.3: *Ion beam sputtering schematic (left) and Ion-assisted thermal evaporation (right)[5].*

Despite all its advantages, IBS has the significant disadvantage of its low deposition rate and therefore its high production cost. With a typical layer deposition rate of a few Angstroms per minute, the growth of a quarterwave multilayer stack for the visible region can take several days. Another major drawback of IBS is being limited to a range of materials, typically metal oxides, adding to the post processing of the deposited coatings by annealing due to the substochiometric composition of the coatings. Furthermore, the deposited films suffer from high compressive stress which is critical for applications coupling atomically thin TMD layers or diamond membranes to Fabry-Perot cavities.

2.1.3 Ion assisted deposition

The porous nature of E-beam and thermally evaporated coatings is very critical for multilayer dielectric mirrors as the optical properties of the coatings can alter in the presence of changes in temperature or humidity. For high reflectance coatings, the shift in refractive indices also causes a shift in the centre wavelength of the filter. Material porosity not only causes poor environment endurance but also low mechanical durability. Furthermore, most E-beam processes require heating the substrates and introduce stress in the substrates and the coating. Ion Assisted Deposition or IAD helps improve the mechanical and the environmental durability of the coatings. The ion energy bombardment results in a higher film density allowing higher refractive indices.

There are several types of ion sources or guns used in ion assisted deposition. The most common sources are Kaufman and end-Hall sources[6]. While the Kaufman ion source is used for inert gas ions, end-Hall sources are used for reactive gas ions. An example of end-Hall ion source and the ion beam generation process from this source are provided in Figure 2.4. The ion gun represented is a gridless source provided with a single thermionic tungsten filament. The design of this ion source takes its name from the ion beam leaving the source at the end axis of the magnetic field. The lines represented within the anode-cathode region are equipotential lines. A significant voltage drop inside the ion source is

perceived by ions, accelerating them away from the source. The cathode provides electrons to sustain the plasma discharge. The glowing ion source illustrated on the right of Figure 2.4 is a Veeco Commonwealth MKII source.

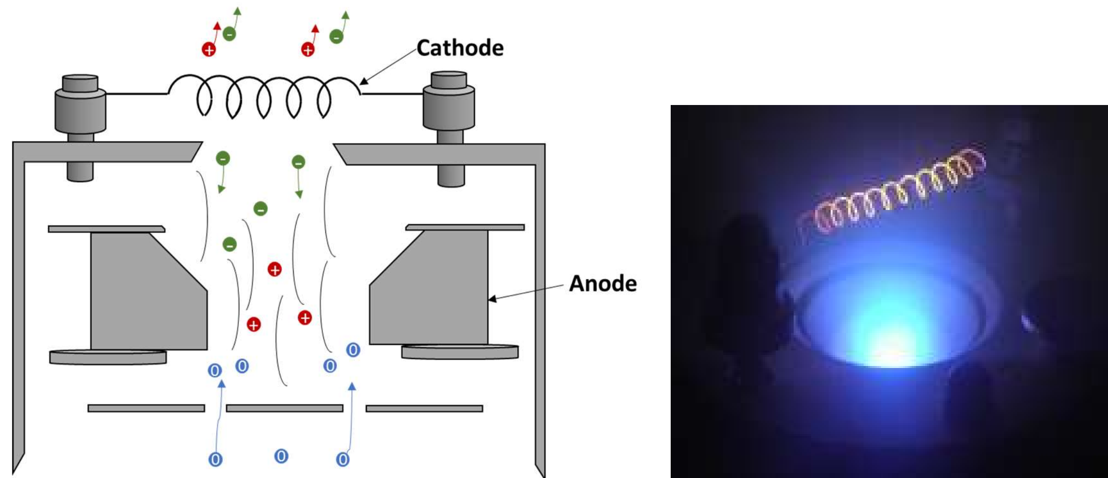

Figure 2.4: *Schematic of a gridless end-Hall ion source and glowing plasma from a Veeco commonwealth MKII ion source.*

Several dielectric oxides investigated in this thesis have been deposited using the ion source above. The deposition conditions and the characterisation of these coatings are given in Section 2.2.

2.1.4 Plasma assisted deposition

Several plasma assisted deposition methods have been explored in this thesis, including plasma assisted DC magnetron sputtering (Plasma-Coat^{TM}), microwave plasma assisted magnetron sputtering (Microdyn®) and plasma assisted E-beam deposition. A birds-eye schematic of the Plasma-Coat^{TM} coating system is presented in Figure 2.5. This system possesses two slots available for two six-inch circular metallic targets. Each target is mounted on top of a planar magnetron.

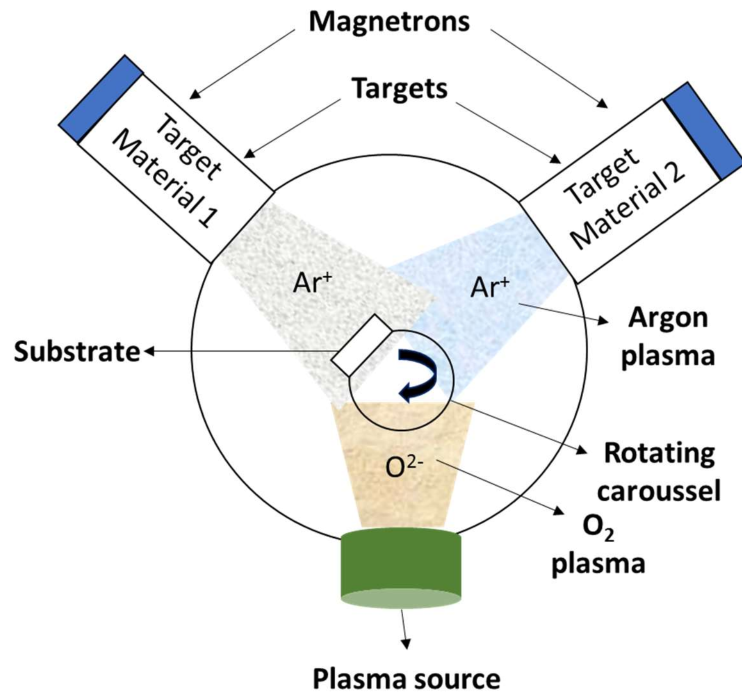

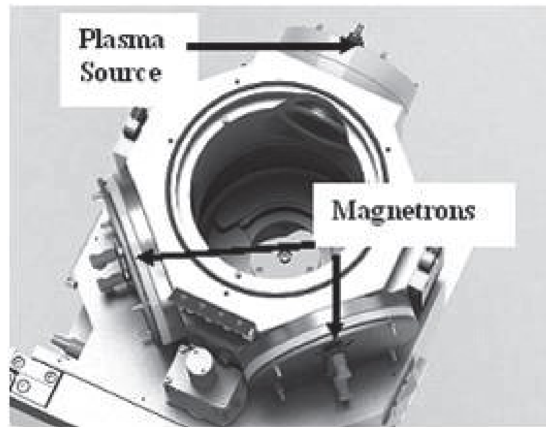

Figure 2.5: *Schematic of the Plasma-Coat^{TM} coating system and top view of a two-magnetron deposition chamber with a plasma source, photo credit to the Institute of Thin Films, Sensors and Imaging, University of the West of Scotland.*

Once power is applied to the magnetron, a cathodic discharge from the metallic target surface ionizes the argon process gas atoms forming positively charged argon ions. The ions are then accelerated towards the metallic target surface and through kinetic transfer of momentum, eject metallic particles from the target surface. The ejected target particles traject toward the centre of the chamber and deposit on the substrate surface, forming a thin film. The magnetic field from the magnetron confines secondary electrons emitted from the target surface during sputtering near the surface and allows more plasma ionization with a faster deposition rate. A hollow plasma source cathode is fitted to the opposite end of the chamber. For thin film metal oxides, oxygen is fed into the system to form an oxygen plasma. As the substrate mounted on the rotating carousel sweeps through the plasma, the deposited metallic film becomes oxidised forming a metal oxide.

Similar high plasma ion densities would only be achievable at higher gas pressures in which the sputtered flux would be impeded and redirected by intervening gas particles resulting in the inability to deposit thin films on the substrate surface. Bombarding the

deposited thin film material with plasma oxygen also results in a higher packing density. The coating optical constants, its packing density and stoichiometry depend on process parameters such as plasma and magnetron powers and inert and reactive gases flows. Examples of thin film oxides and multilayer high reflectance coatings produced using PlasmaCoat system are provided in Section 2.2 and in Chapter 3.

Another type of plasma assisted magnetron sputtering system called Microdyn® is presented in Figure 2.6. This system utilizes an octagonally shaped chamber, where electrically conductive targets are arranged around the periphery of the chamber. The substrates to be coated are held on a cylindrical rotating drum concentric within the chamber.

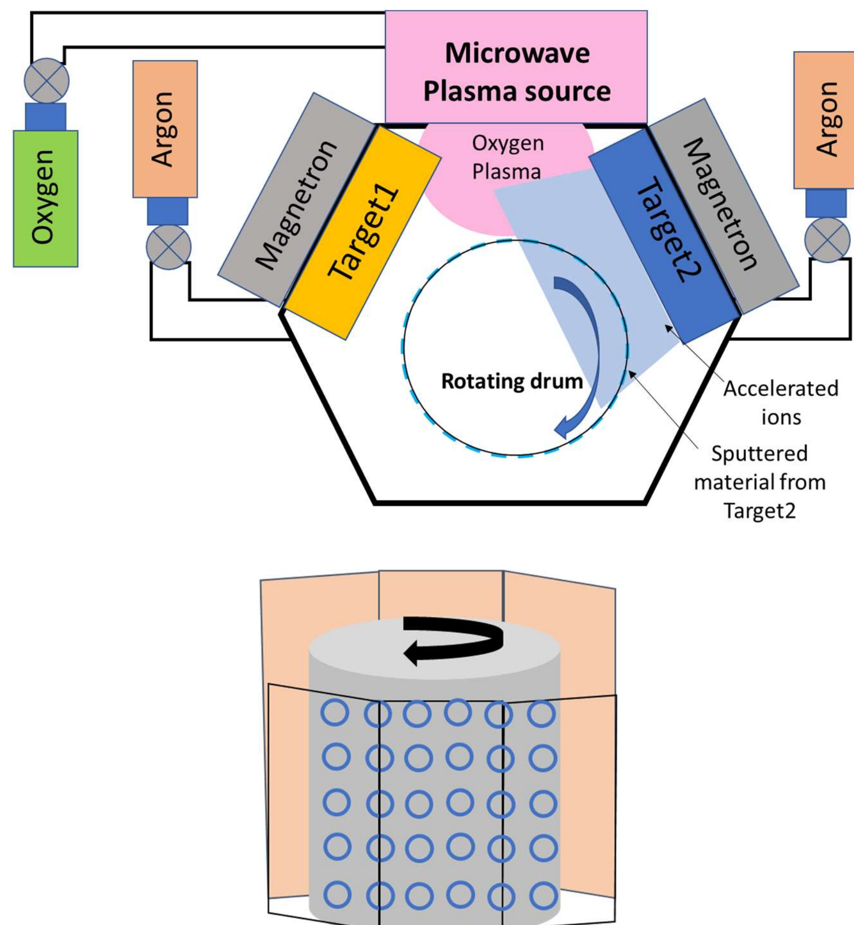

Figure 2.6: *Schematic of the Microdyn® coating system and design of the rotating drum.*

The deposition of metallic thin film coatings mechanism is similar to the one described for the PlasmaCoat. In order to produce thin film metal oxides, a small amount of oxygen is also introduced into the system. Microwaves are utilized to ionize the plasma. The oxygen ions then react with the metallic layers resulting in thin film metal oxides. Because the sputtered target atoms are ejected with a large amount of energy, the coatings produced have a higher packing density than evaporated ones. Unlike PlasmaCoat where only one magnetron can be switched on at once, the Microdyn system allows both magnetrons to be active simultaneously. This feature is particularly interesting in the case of co-sputtering two materials. Co-sputtering two materials (a high index and low index) simultaneously allows the deposition of a mixed layer with a controllable intermediate

index. In this study, the Microdyn system is used to produce a multilayer Nb_2O_5/SiO_2 high reflectance coating. The design and the spectral data of the coatings will be presented in Section 2.2 and Chapter 3.

A third type of plasma source from Thin Film Solutions is represented in Figure 2.7 and is used in combination with E-beam deposition. The plasma source is composed of LaB_6 cathode heated up via a water-cooled induction coil. The induction coil is heated by an RF heater at a power of 2.7 kW allowing the cathode to reach temperatures above 1500 °C.

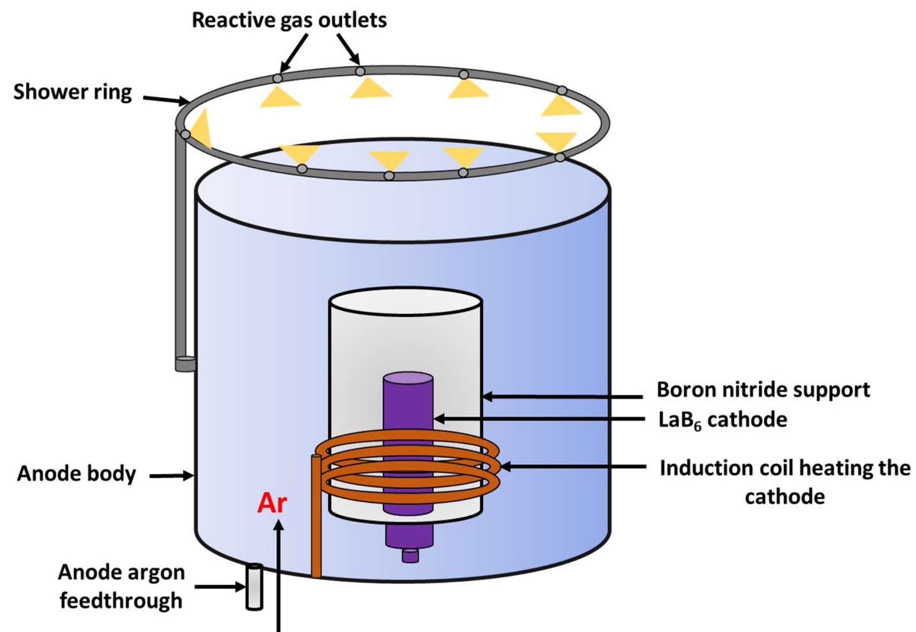

Figure 2.7: *Construction principle of a Thin Film Solutions plasma source.*

The emitted electrons from the cathode move towards the anode in a spiral path due to the oscillating RF field created by the induction coil. Argon atoms are introduced through the plasma source which the electron collide with, leaving the argon atoms ionised. The extraction coil surrounding the anode creates a DC electromagnetic field constraining the anode. Both RF and DC magnetic fields help extending the flight path of the electrons and therefore increasing the probability of argon ionisation. An oxygen ring shower gas inlet placed on the top of the plasma source allow a reactive deposition. The cathode is protected from oxygen by the surrounding argon gas/plasma. Boron nitride ceramics are used to isolate the anode and cathode and contain the plasma within the centre of the source. The plasma source in operation during an E-beam deposition is represented on the right of Figure 2.8. Part of the plasma is extracted out of the opening of the source into the vacuum chamber. The extracted part of the plasma is the charge carrier, which is used to add energy to the evaporated material from the E-beam source.

Figure 2.8: *RF heated LaB_6 cathode on the left and plasma source in operation during an E-beam deposition. Photos credit to Thin Film Solutions.*

The principle of charge carrier flows is outlined in Figure 2.9. As a result of the discharge voltage U_D between the anode and the cathode, a discharge current I_D flows between both electrodes. The positive charge carrier flow to the cathode is represented by the red arrow while the negative charge carrier flow to the anode is represented by the blue arrow. A fraction of emitted electrons (current I-) and ions (current I_+) move towards the chamber wall. If the anode takes a positive potential against ground, the positive charge carrier will be accelerated towards the chamber walls and respectively onto the substrates being coated. The energy of the ions hitting the deposited film on the substrate is an essential parameter in the layer growth process.

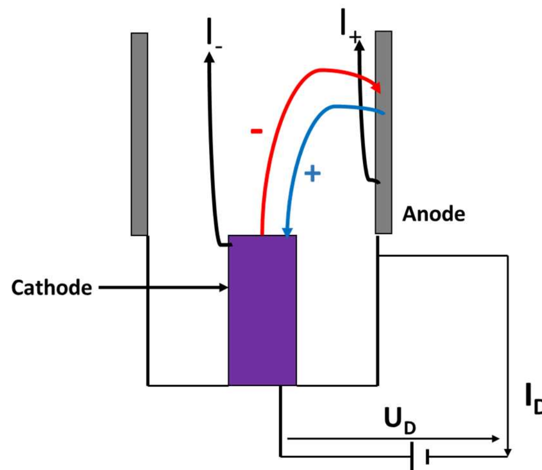

Figure 2.9: *Charge carrier flows in the plasma source.*

This plasma source is used to grow E-beam evaporated multilayer TiO_2/SiO_2 coatings on both curved and planar substrates. The design and spectral data of the grown high reflectance layers are presented in Section 2.2 and Chapter 3.

2.1.5 Other deposition methods

evaporation and sputtering processes as part of PVD processes have been so far introduced. Multilayer thin films can be also grown using chemical vapour deposition processes (CVD). There is a debate in the literature about the definition of CVD, but it can be briefly described as the deposition of thin films using gaseous precursors. CVD allows growing thin films in different environments such as a liquid phase environment

or a plasma enhanced one, also known as PECVD. Metal-organic precursors are used in the case of MOCVD. Molecular beam epitaxy (MBE) is a common deposition method used in the fabrication of semiconductor devices and dielectric Bragg reflectors. The deposition of quarterwave stacks for optical cavities can be fulfilled by changing the composition of the materials such as for $Al_xGa_{1-x}As$[7].

2.2 Dielectric materials

Many single dielectric materials have been investigated in this thesis. These materials have been deposited using the PVD methods described in Section 2.1. Dielectric materials for high reflectance coatings have been selected among a wide a range of materials and represent the state of the art of dielectrics in the visible wavelength range. In this section, the selection criteria of dielectric materials, the deposition methods and the fabrication processes of thin film coatings are described.

2.2.1 Selection criteria

The studied materials have been selected according to several parameters such as their optical properties (refractive index n and region of transparency), the availability of the deposition method in the thin film form, the toxicity of the materials and their availability. Other relevant parameters such as the chemical and mechanical properties of the coatings (compatibility with other materials, stoichiometry and built-in stresses) have been also important factors in the choice of the dielectric materials to be used in high reflectance coatings for Fabry-Perot cavities.

2.2.2 Studied dielectrics

High index dielectric materials frequently used for high reflectance mirrors in the visible region are tantalum pentoxide (Ta_2O_5)[8] and titanium dioxide (TiO_2)[9]. They have been highly developed and characterised for high finesse microcavities[8, 10-12] as they have very low optical losses[13]. Combined with silicon dioxide (SiO_2) as a low index dielectric material, these two oxides materials are widely quoted in the literature and are two of the most commonly used high index materials for the fabrication of cavities for diamond-based quantum emitters[12]. Another high index dielectric material commonly used in high reflectance mirrors for microcavities is niobium pentoxide(Nb_2O_5)[9, 14-17] which was developed for strongly coupled organic semiconductor and TMD heterostructures microcavities. Mixing high index pure oxide materials with a proportion of silicon dioxide has demonstrated reduced absorption and scatter losses in combinations such as ZrO_2-SiO_2, Nb_2O_5-SiO_2 and TiO_2-SiO_2 films[18, 19]. It was previously demonstrated that adding SiO_2 in high index films prevents crystallisation of the high index layers. The mixed film structure remains amorphous as well. Adding a proportion of SiO_2 in the previously cited high index materials increases the annealing temperature of the coating without crystallisation and reduces the internal stress of the coating. Zinc

sulphide and cryolite (Na_3AlF_6) form a common combination in multilayer dielectric mirrors[20-22]. The contrast of the refractive indices of these materials allows achieving a high optical performance. Easy to evaporate even at low temperature, these materials however possess some disadvantages such as poorer environmental resistance to moisture and to contaminations[23]. Zinc sulphide is also a very soft material. It can be however substituted by zinc selenide which offers a higher toughness[24]. Magnesium fluoride presents a low refractive index but can suffer from high intrinsic tensile stress[25].

Tables 2-1 and 2-2 summarise the deposited materials, the deposition methods and the process parameters for each single layer coating. The thicknesses of the coatings are reported in Table 2-3. The thin film materials have been deposited on Corning™ 2947-75 mm × 25 mm plain 1 mm thick microscope slides, made from soda lime glass. For silicon dioxide coatings, 1 mm thick and 25 mm diameter SF11 witnesses were substituted to microscope slides to allow a greater refractive index contrast to the substrate during the transmission measurement. The coatings have been evaporated and sputtered from 99.99 % purity targets and crucibles provided by Scotech Ltd. Experiments have been performed at the process pressures indicated in Tables 2-1 and 2-2.

Material	**Method**	**Source material**	**Process pressure(mbar)**	**Deposition rate(Å/s)**	**Backfill gas (sccm)**	**Substrate heating(°C)**
MgF_2	T.evaporation	MgF_2 pellets	2.1×10^{-5} to 6.7×10^{-5}	1	none	100
	E-beam		4.2×10^{-5}	8	none	160
LiF	T.evaporation	LiF_2 pellets	5×10^{-5}	1	none	130
Na_3AlF_6	T.evaporation	Na_3AlF_6 pellets	1.3×10^{-5} to 3.7×10^{-6}	1	none	100
	E-beam		2.3×10^{-5}	10	none	160
SiO_2	RF sputtering	Si target	8×10^{-3}	0.34	Ar:20 / O_2:6	none
	P-DC sputtering	Si target	9.5×10^{-3}	0.6	Ar:77 / O_2:45	120
	E-beam	SiO_2 pellets	5.8×10^{-5}	3	none	160
	IAD E-beam	SiO_2 pellets	9×10^{-5}	2	none	50
	Plasmacoat	Si target	5×10^{-3}	5	Ar:20 / O_2:8	none
	Microdyn	Si target	9.3×10^{-4}	1.1	Ar:120 / O_2:50	none

Table 2-1: *Source materials and process conditions for thin film low index dielectric coatings. This table presents the main variable parameters of the process.*

Material	Method	Source material	Process pressure(mbar)	Deposition rate(Å/s)	Backfill gas (sccm)	Substrate heating(°C)
TiO_2	IAD E-beam	TiO_2 pellets	1.8×10^{-4}	1	O_2: 35	none
Ta_2O_5	P-DC sputtering	Ta target	8.8×10^{-3}	1.9	Ar:77 / O_2:45	120
$LaTiO_3$	Reactive E-beam	$LaTiO_3$ pellets	1.3×10^{-2}	3	O_2:10	160
HfO_2	E-beam	Hf pellets	1.2×10^{-4}	1.2	O_2:50	none
	IAD E-beam	Hf pellets	1.8×10^{-4}	1.4	O_2:50	none
	PIAD E-beam	Hf pellets	1.9×10^{-4}	1.4	O_2:50	none
Nb_2O_5	PIAD E-beam	Nb pellets	4.4×10^{-4}	1.5	O_2:50	none
	RF sputtering	Nb target	8×10^{-3}	0.3	Ar:20 / O_2:4	none
	Plasmacoat	Nb target	5×10^{-3}	0.5	Ar:17 / O_2:18	none
	Microdyn	Nb target	1.3×10^{-3}	1.8	Ar:120 / O_2:70	none
ZrO_2	P-DC sputtering	Zr target	8.8×10^{-3}	0.6	Ar:77 / O_2:15	120
	E-beam	Zr tablets	2×10^{-4}	1.2	O_2:50	none
	IAD E-beam	Zr tablets	2×10^{-4}	0.8	O_2:50	none
	PIAD E-beam	Zr tablets	2×10^{-4}	2	O_2:50	none
	Plasmacoat	Zr target	5×10^{-3}	0.5	Ar:17 / O_2:8	none
ZnS	T.evaporation	ZnS tablets	5×10^{-5} to 2×10^{-5}	1	none	100
ZnSe	T.evaporation	ZnSe granules	6×10^{-5} to 4.8×10^{-6}	1	none	100

Table 2-2: *Source materials and process conditions for thin film high index dielectric coatings. This table presents the main variable parameters of the process.*

2.3 Optical constants

2.3.1 Complex refractive index

Optical characterisation of thin film coatings consists a very important preliminary study for multilayer high reflectance coatings. Designing dielectric mirrors requires knowledge of the optical constants of high and low index materials. It is also a decisive step to determine suitable dielectrics for low loss mirrors. In this thesis, we rely on optical spectroscopy to measure the optical constants of fabricated thin film coatings.

The refractive index n and the extinction coefficient k of the dielectric coating represent the real and imaginary components of the complex refractive index η deduced from Maxwell's equations in an isotropic media[26, 27] according to Equation (2.1):

$$\eta = n + ik \quad (2.1)$$

Values of the refractive index n, the extinction coefficient k and the thicknesses of the coatings have been extracted from the fitted transmission and reflectance data using the Optichar module of the optilayer software, version 5.82[28].

The transmission and reflectance spectra of all the thin film coatings were measured in the wavelength range of 350 nm to 2200 nm using Perkin Elmer Lambda 900 spectrophotometer. Figure 2.10 illustrates two examples of reflectance and transmission spectra of 500 nm thick IAD E-beam SiO_2 and ZrO_2 coatings on SF11 substrate and microscope slide respectively.

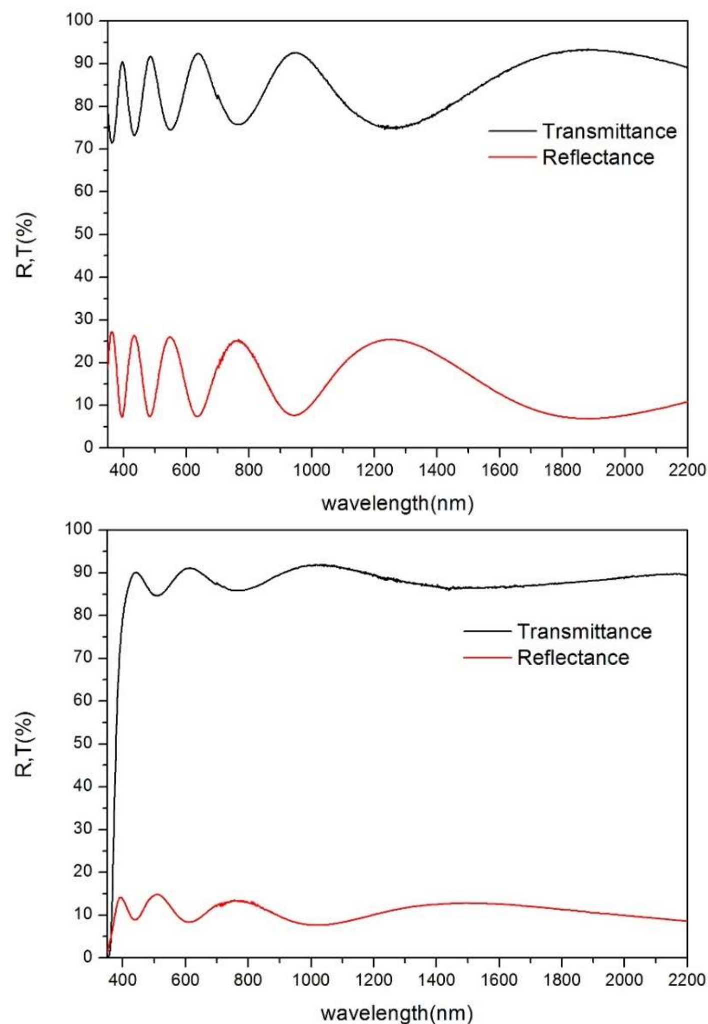

Figure 2.10: *Top graph, reflectance and transmission spectra of ion assisted E-beam ZrO_2 sample on microscope slide in the range of 350 nm to 2200 nm. Bottom graph, reflectance and transmission spectra of ion assisted E-beam SiO_2 sample on SF11 in the range of 350 nm to 2200 nm.*

The transmission and reflectance spectra show a succession of minima and maxima points. For a high index material, the maxima points are called halfwaves and the minima points are called quarterwaves. These points allow the calculation of a model for the optical spectra and to extract some useful data such as the thickness of the film, its optical constants and the homogeneity of the coating. The ripples shown by the transmission and reflectance spectra of silicon dioxide are less prominent than the ripples of the zirconium dioxide spectra. The amplitude of the ripples depends on the contrast between the

substrate and the thin film coating refractive indices. Silicon dioxide has a refractive index of 1.45 in this wavelength range which is close to the refractive index of the substrate of around 1.65. The model calculated for zirconium dioxide single layer is more accurate in this case because the quarterwaves and the halfwaves are more prominent. Therefore, low index dielectric coatings should not be deposited on a substrate having a closer refractive index to the grown material index. An example of a fitted transmittance spectrum of thermally evaporated zinc sulphide coating on microscope slide in the data range of 500 nm to 1000 nm is provided in Figure 2.11. For both transmitance and reflectance spectra, the fitting range has been restricted to a wavelength range from 500 nm to 1000 nm in order to obtain an accurate fit of the optical constants in the visible region.

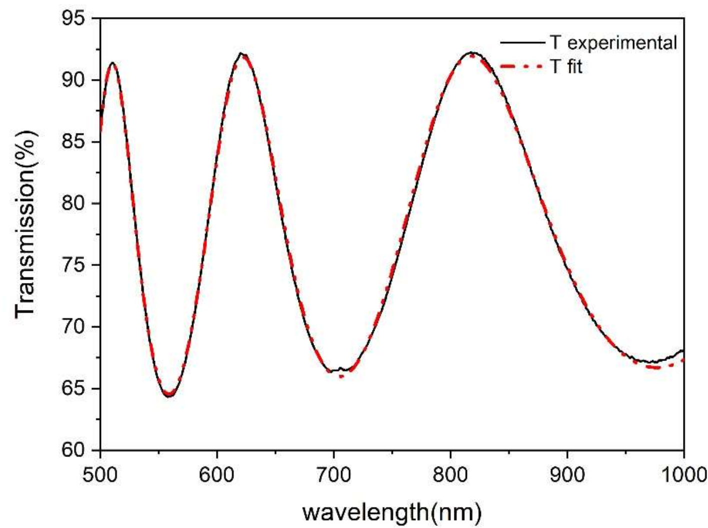

Figure 2.11: *Experimental transmission spectrum of thermally evaporated ZnS layer deposited on microscope slide represented in a black solid line versus model fit represented in a red dashed line.*

The refractive index n and the extinction coefficient k of the coatings are respectively fitted by the Cauchy model or normal dispersion and the exponential model described in Equation (2.2):

$$n(\lambda) = n_\infty + \frac{A}{\lambda^2} + \frac{B}{\lambda^4} \; ; \; \mathrm{k}(\lambda) = \mathrm{B}_0 \exp\left(-\frac{B_1}{\lambda} - B_2 \lambda \right) \qquad (2.2)$$

Where n_∞, A , B , B_0, B_1 *and* B_2 are the fitting coefficients of the model.

The Cauchy formula is suitable for materials with a normal dispersion, meaning materials with a monotonous decreasing refractive index for increasing wavelength values.

The measured data are transferred to the Optilayer module. The substrate models were used in the fitting module to identify any coating inhomogeneities. The thin-film model can be described by a vector of model parameters X. The coordinates of the vector X are the parameters describing the wavelength dependency of both refractive index and extinction coefficient, the coating thickness and the bulk homogeneity. The closeness between experimental and model data is represented by the discrepancy function *DF* expressed in Equation (2.3):

$$DF(X) = \sum_{j=1}^{n} \left[\frac{S(X;\lambda_j) - \hat{S}(\lambda_j)}{\Delta_j} \right]^2 \quad (2.3)$$

Where S is the spectral characteristic of the model, in this case transmittance and reflectance, $\hat{S}$ is the experimentally determined spectral characteristic, λ_j is the wavelength grid in the experimental spectral range, Δ_j are measurement tolerances (typically 0.1%). X is the model vector and its parameters describe the wavelength dependency of both refractive index and extinction coefficient and the coating thickness. The fitting is repeated until the discrepancy function *DF* is minimized[29] based on a needle optimization method[30]. This technique was first developed in the 80s to be implemented in the Russian BESM mainframe and relies on strong and complex algorithms. A physical interpretation of the needle method was presented in [31]. The optical coating is considered as an interference structure which spectral performance is related to the interference effects of the incident light wave at the boundaries of the coating. These interference effects are determined between the amplitude and the phase of the reflected wave. The numerical correspondence between the spectral characteristic of the model S (either reflectance or transmittance) and the measured characteristic $\hat{s}$ is provided by the discrepancy function *DF*. When *DF* is optimised with respect to the film thickness the reflected wave phase are changed. If *DF* is optimised with respect to the film refractive index, the reflected wave amplitude is also changed. The mathematical fitting process is stopped when *DF* cannot be further minimised. A value of *DF* of 1 means the deviation of model data from the experimental ones is about 1 % across the spectral region of interest. The value of *DF* is compared to measurement accuracy of the spectrophotometer. Thin film inhomogeneity is checked by manually inputting small linear gradients in film refractive index. According to Perkin Elmer Lambda 900 spectrophotometer specification data, the photometric accuracies for transmittance and reflectance are of 0.05 %. The fitting was therefore limited to discrepancy values above 0.1 in order to avoid overfitting data. Film thicknesses extracted from fitted transmission spectra and discrepancies of the models are summarised in Table 2-3. The discrepancy obtained for the fitted spectral data is about 0.1 to 0.3 for most of the single layer coatings except for IAD E-beam titanium dioxide and thermally evaporated zinc selenide with discrepancy values of 0.5 and 0.8 respectively. These higher discrepancies are caused by higher inhomogeneities in the coating.

Material	Deposition method	Film thickness(nm)	Discrepancy
Ta_2O_5	P-DC Sputtering	475	0.3
TiO_2	IAD E-beam	466	0.5
$LaTiO_3$	Reactive E-beam	508	0.3
Nb_2O_5	PIAD E-beam	592	0.3
	RF sputtering	592	0.2
	Plasmacoat	578	0.1
	Microdyn	498	0.1
HfO_2	E-beam	210	0.2
	IAD E-beam	283	0.3
	PIAD E-beam	200	0.3
ZrO_2	P-DC sputtering	480	0.2
	E-beam	436	0.1
	IAD E-beam	436	0.2
	PIAD E-beam	503	0.1
	Plasmacoat	675	0.2
ZnS	T. evaporation	527	0.3
ZnSe	T. evaporation	510	0.8
SiO_2	E-beam	310	0.1
	IAD E-beam	500	0.1
	P-DC Sputtering	391	0.2
	RF Sputtering	500	0.1
	Plasmacoat	652	0.1
	Microdyn	482	0.1
LiF	T. evaporation	455	0.1
MgF_2	T. evaporation	530	0.1
	E-beam	478	0.1
Cryolite	T. evaporation	499	0.1
	E-beam	489	0.2

Table 2-3: *Coatings Thicknesses and discrepancy values for the studied dielectric materials.*

2.3.2 Refractive index n

The refractive index values for silicon dioxide single layers deposited using process conditions of Table 2-1 between 500 nm and 1000 nm are presented in Figure 2.12. The refractive index of the single layers is compared to glass silicon dioxide refractive index reported in Palik's optical constants handbook[32].

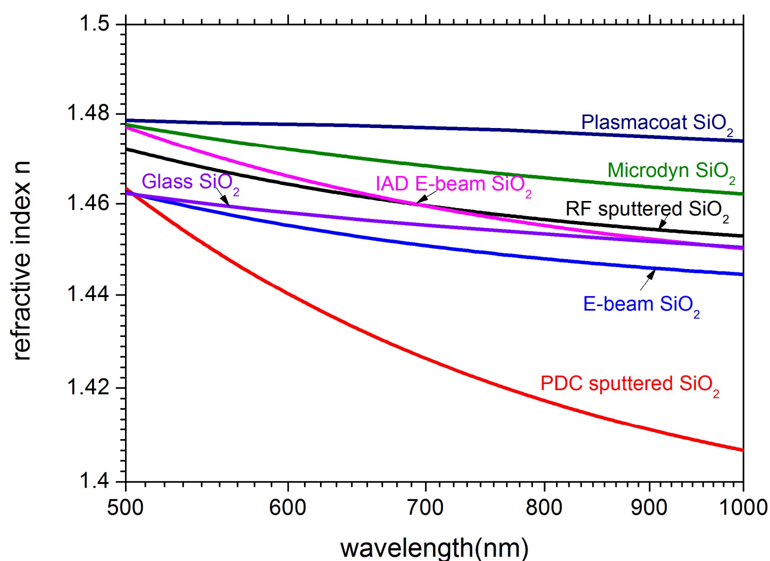

Figure 2.12: *Refractive index spectra of various silicon dioxide thin film layers deposited using PVD methods described in Table 2-1. Thicknesses of the coatings are provided in Table 2-3. The refractive indices of silicon dioxide are compared to glass silicon dioxide data reported in Palik's handbook of optical constants [32].*

Single layers deposited using IAD E-beam, Microdyn and Plasmacoat systems and RF sputtering refractive indices are higher in magnitude to the refractive index reported in Palik's handbook. A refractive index higher than the glass index indicates a substochiometric composition of the silicon dioxide. Silica coating deposited using Plasmacoat system has the highest refractive index of all deposited silicon dioxide layers. The refractive index varies between 1.478 at 500 nm and 1.476 at 1000 nm. These data are in accordance with refractive index values for Plasmacoat silicon dioxide reported in [33]. RF sputtered and IAD E-beam deposited silicon dioxides refractive indices are very close, especially in the centre of the visible region and exhibit values varying between 1.47 at 500 nm and 1.45 at 1000 nm. P-DC sputtered silicon dioxide presents the lowest refractive index of all deposited silicas and has also the largest variation of refractive index between 500 nm and 1000 nm ranging from 1.47 at 500 nm to 1.41 at 1000 nm. The lower refractive of RF sputtered silica may be related to a low packing density of the coating.

The refractive index variation between 500 nm and 1000 nm for thermally evaporated fluorides (lithium fluoride, magnesium fluoride and cryolite) are presented in Figure 2.13. Magnesium fluoride and cryolite have refractive indices of 1.385 and 1.399 at 500 nm respectively which show little change over this spectral band. Lithium fluoride refractive index varies between 1.390 at 500 nm and 1.382 at 1000 nm.

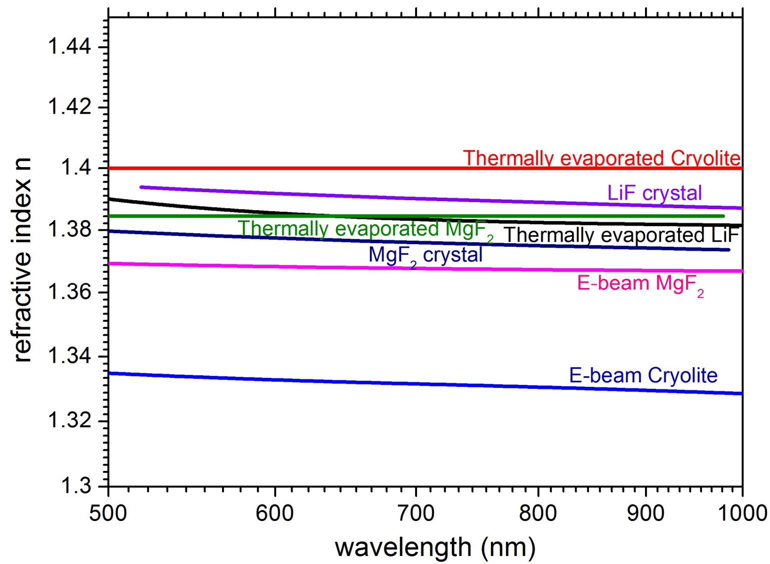

Figure 2.13: *Refractive index spectra of fluoride thin film layers deposited using PVD methods described in Table 2-1. Thicknesses of the coatings are provided in Table 2-3. The refractive indices of lithium fluoride and magnesium fluoride are compared to the crystal optical data from [34] and [35].*

The refractive indices of E-beam magnesium fluoride and cryolite coatings are lower to thermally evaporated coatings. E-beam cryolite has the lowest refractive index of all the evaporated fluorides. Indeed, the optical properties of cryolite strongly depend on the temperature of the source evaporation. E-beam cryolite is evaporated at a rate of 10 Å/s, which can lead to the dissociation of the material and the modification of the chemical composition of the coating[22, 36].

The effect of the deposition method on the optical constants of the coatings has been also studied for high index dielectric materials as shown in Figure 2.14 for zirconium dioxide.

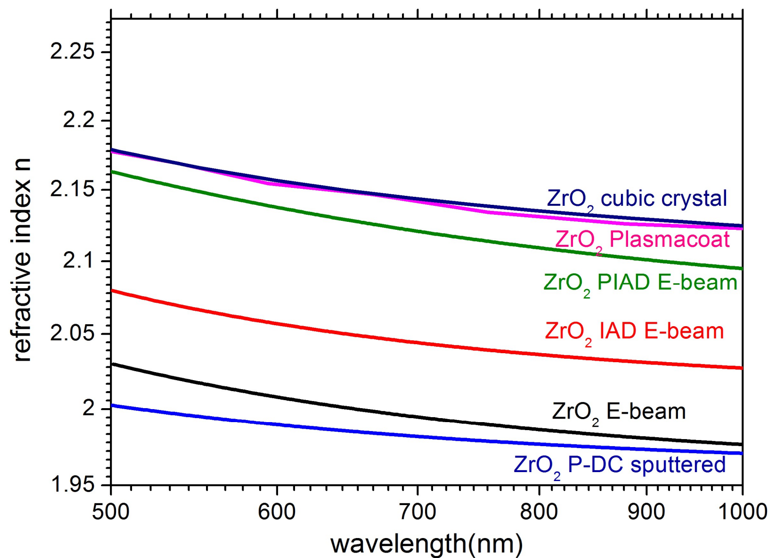

Figure 2.14: *Refractive index spectra of zirconium dioxide thin film layers deposited using PVD methods described in Table 2-2. Thicknesses of the coatings are provided in Table 2-3. The refractive index is compared to the refractive index of cubic zirconia stabilized with yttria and extracted from [37].*

Overall, zirconium dioxide has a small refractive index dispersion between 500 nm and 1000 nm which is particularly interesting for designing broadband filters. Pulsed-DC sputtered zirconia has the lowest refractive index of all the studied deposition methods. A low refractive index may be either related to a low packing density of the coating or to a substochiometric composition of the coating. E-beam evaporated zirconia refractive index is the second lowest refractive index presented in Figure 2.14. Under low substrate temperature (unheated substrate), the coating grows with significant void volume resulting in a low packing density. When vented to air, the refractive index of the E-beam evaporated coating is subject to changes[38]. An improvement of the refractive index of zirconia using ion and plasma sources can be noticed in Figure 2.14. Plasmacoat zirconium dioxide has the closest refractive index to cubic zirconia stabilized with yttria reported in [37] due to the efficiency of oxidation of zirconium coating using plasma assisted reactive magnetron sputtering[39].

Niobium pentoxide refractive index has been determined for coatings deposited using E-beam and few sputtering methods (Figure 2.15). RF sputtered niobia has the lowest refractive index in the four deposition methods which can be caused by a low oxidation of the coating. Microdyn niobium pentoxide has the highest refractive index in the studied wavelength range followed by PIAD E-beam niobia and Plasmacoat niobia. The high index of Microdyn niobia can be explained by the high surface reaction of the deposition process and the high oxidation of the material using microwave plasma assisted magnetron sputtering. Microdyn niobia refractive index is also comparable in magnitude to IAD E-beam deposited titania (Figure 2.17), one of the highest achievable refractive indices for metal oxides in the visible region.

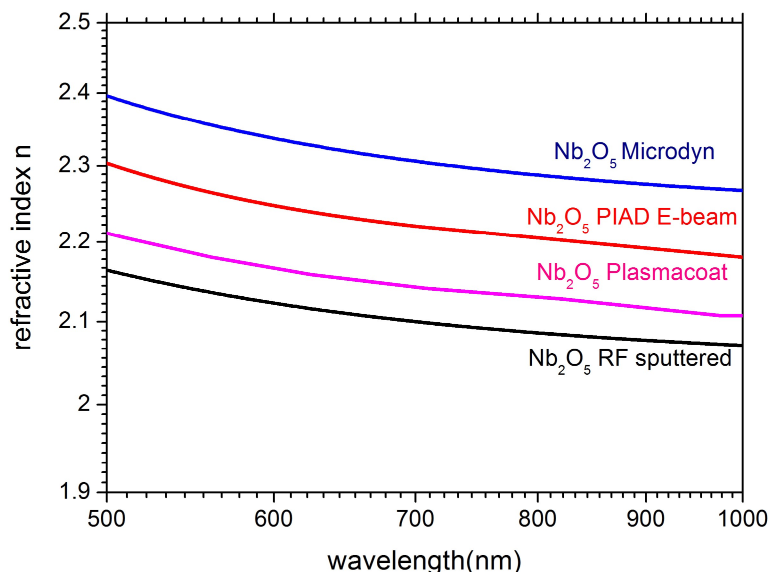

Figure 2.15: *Refractive index as a function of wavelength for several niobia thin film layers produced using PVD processes described in Table 2-2. Thicknesses of the coatings are provided in Table 2-3.*

The refractive index of hafnia using E-beam evaporation and IAD and PIAD E-beam is presented in Figure 2.16. Like zirconium dioxide and niobium pentoxide, hafnium dioxide displays an improvement of the refractive index using an ion gun or a plasma source. Under low energy evaporation and in the absence of substrate heating as is the

case for these coatings, hafnium dioxide films grow with a porous structure and a low packing density. Once the machine is vented, the coating is very vulnerable to air humidity and causes changes in the refractive index of the coating. IAD and PIAD deposition help closing the voids in the coating microstructure and increasing the packing density resulting in a higher refractive index. It is however difficult to get close to bulk material refractive index.

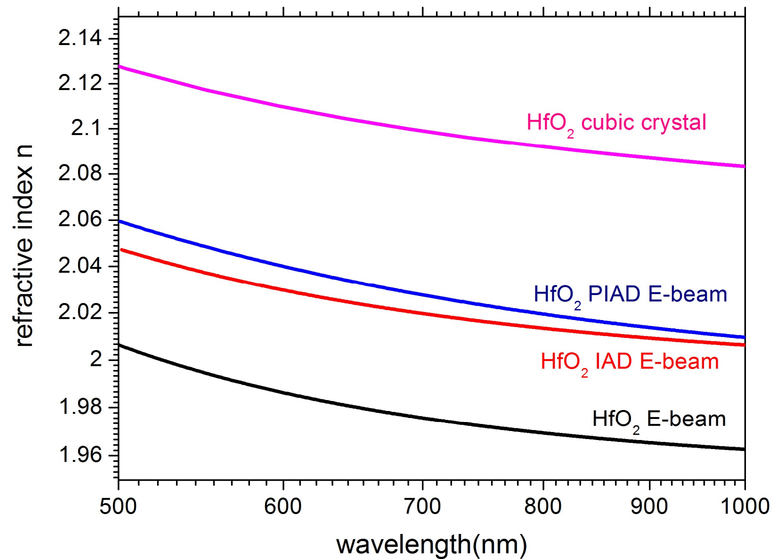

Figure 2.16: *Refractive index wavelength dependency for hafnium dioxide thin film layers deposited using three different E-beam processes described in Table 2-2. Thicknesses of the coatings are provided in Table 2-3. The refractive index is compared to the refractive index of cubic hafnia stabilized with yttria and extracted from [40].*

The last studied high index materials are presented in Figure 2.17. Thermally evaporated zinc sulphide and zinc selenide have the highest refractive indices of the studied materials. Their refractive indices are also close to bulk values reported in [41] and [42]. Although zinc sulphide is subject to dissociation during evaporation, nearly stochiometric coatings are still formed as zinc and sulphur recombine near the substrate. The refractive index of zinc sulphide depends also on the substrate temperature[43]. IAD E-beam deposited titanium dioxide has the third highest refractive index with a refractive index of 2.4 at 500 nm wavelength. This result is even more outstanding as the grown film was evaporated from a titanium dioxide crucible. Titanium oxides usually decompose into suboxides and lose oxygen which can lead to substochiometric compositions. A refractive index of 2.42 at 500 nm wavelength has been previously reported in[44] for reactive ion assisted E-beam deposited titania from a titanium crucible. The refractive index distribution of pulsed DC reactive magnetron sputtering agrees with optical data reported in [45, 46] for tantalum pentoxide layers grown in similar process conditions and within the same physical thickness range. E-beam deposited lanthanum titanate shows a low refractive index dispersion. The coating refractive index varies between 2.09 at 500 nm and 2.05 at 1000 nm.

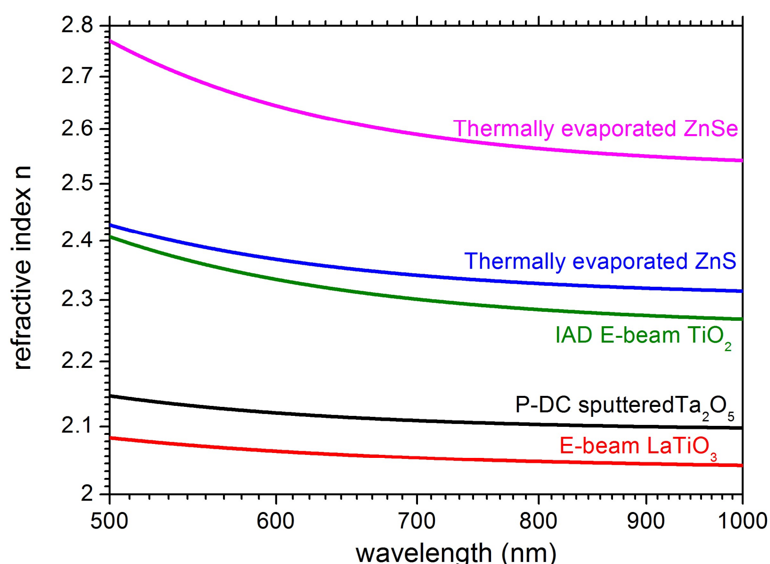

Figure 2.17: *Refractive index wavelength dependency for high index thin film layers deposited using deposition methods described in Table 2-2. Thicknesses of the coatings are provided in Table 2-3.*

2.3.3 Extinction coefficient k

The extinction coefficient k values for thin film silica grown using various evaporation and sputtering methods are presented in Figure 2.18. Generally, fully oxidized silicon dioxide coatings are transparent over the range below 250 nm to at least 3.5 µm. P-DC and RF sputtered silicon dioxide have the highest absorption amongst the deposited coatings which can be related to an unbalanced argon to oxygen ratio during the sputtering processes. E-beam silica has the third highest absorption. When starting from a silicon dioxide source, a little dissociation of the material occurs resulting in an oxygen loss which is not necessary solveable by providing a background pressure of oxygen. The use of an ion gun reduces the absorption of the coating in this case. A lower absorption of silicon dioxide deposited using Microdyn system is also expected considering the high oxidation of the coating using reactive microwave assisted magnetron sputtering. However, a high absorption is observed which can be caused by a target contamination.

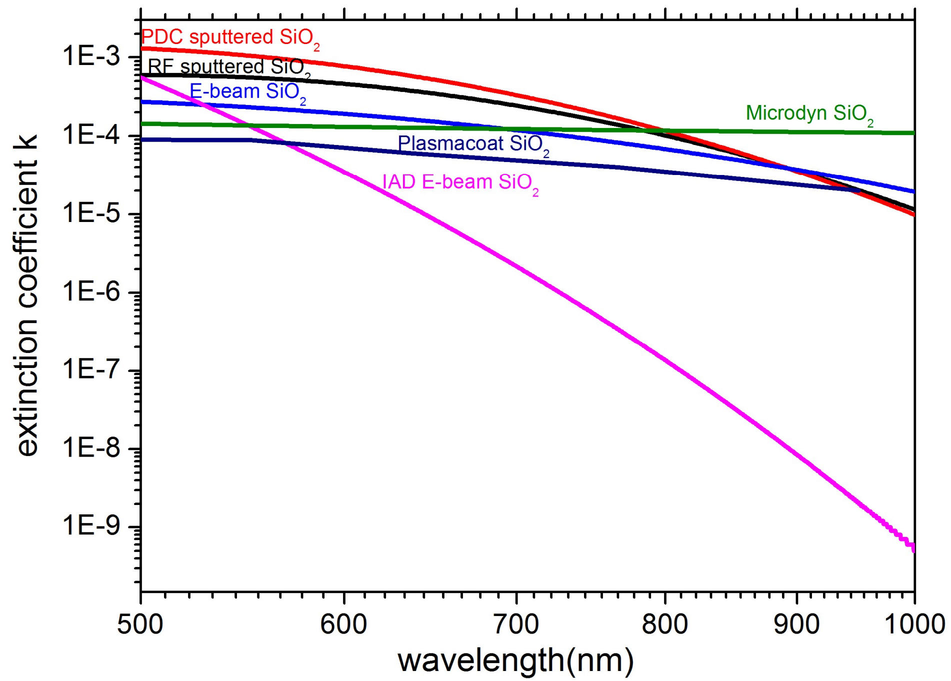

Figure 2.18: *Extinction coefficient spectra calculated from fitted transmission data of various silica single layers produced using PVD processes described in Table 2-1. Thicknesses of the coatings are provided in Table 2-3.*

Fitted transmission data indicate that thermally evaporated lithium fluoride and magnesium fluoride and E-beam cryolite are transparent between 500 nm and 1000 nm. The extinction coefficient of thermally evaporated cryolite and E-beam magnesium fluoride is given in Figure 2.19.

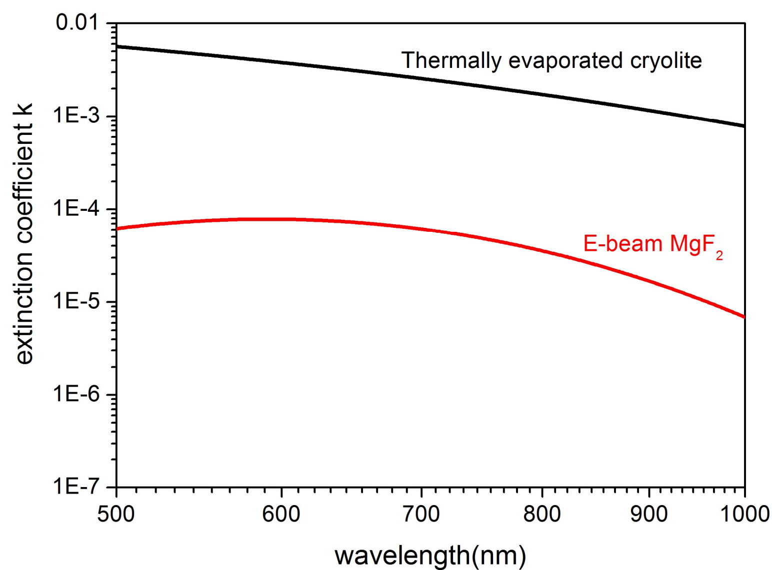

Figure 2.19: *Extinction coefficient k calculated from fitted transmission data of cryolite and magnesium fluoride layers produced using PVD processes described in Table 2-1. Thicknesses of the coatings are provided in Table 2-3.*

Thermally evaporated cryolite k coefficient varies between 0.007 at 500 nm to nearly 0.001 at 1000 nm. The optical properties of cryolite are very dependent on the process temperature and pressure. High absorption can be caused by the modification of the chemical composition of the material caused by the dissociation of the alumina and the fluoride in the cryolite. The absorption of E-beam magnesium fluoride extinction

coefficient varies between 6×10^{-4} at 500 nm and 7×10^{-5} at 1000 nm. The absorption of E-beam evaporated magnesium fluoride can be related to the high evaporation rate of the deposition process (8 Å/s). It has been reported previously that magnesium fluoride k coefficient is higher for higher evaporation rates[47].

Figure 2.20 represents the extinction coefficient of zirconia using PVD methods previously presented. While IAD E-beam deposition increases the refractive index in comparison to E-beam and P-DC sputtered coatings (Figure 2.14), the absorption is however increased which is problematic for low loss dielectric mirrors and laser applications. The absorption is somewhat equivalent for E-Beam, Plasmacoat and P-DC sputtered coatings with an extinction coefficient around 2×10^{-4} at 550 nm. PIAD E-beam coating has the lowest absorption with a k value below 10^{-5} beyond 550 nm.

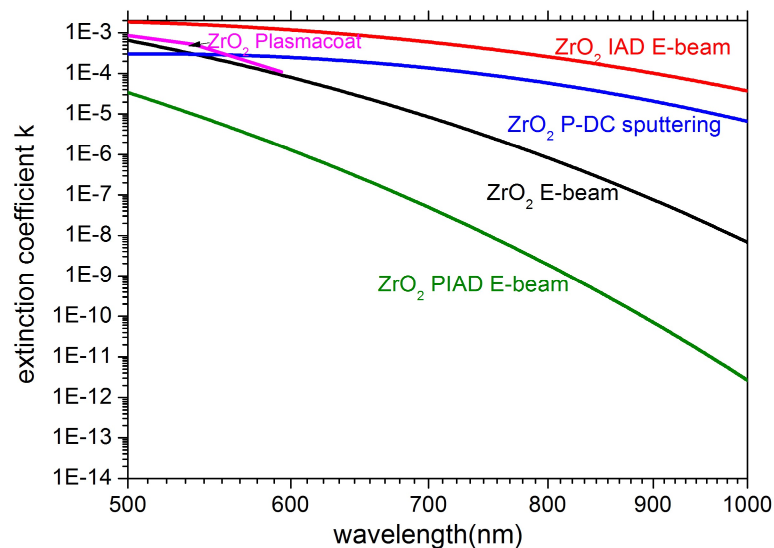

Figure 2.20: *Extinction coefficient k calculated from fitted transmission data of zirconia single layers produced using PVD processes described in Table 2-2. Thicknesses of the coatings are provided in Table 2-3.*

The extinction coefficient values for hafnium dioxide using three E-beam methods are presented in Figure 2.21. The decrease of absorption using IAD and PIAD can be explained by the improvement of hafnium dioxide microstructure and packing density. The oxidization of hafnium is also improved using IAD E-beam and consequently reduces the absorption of the coating.

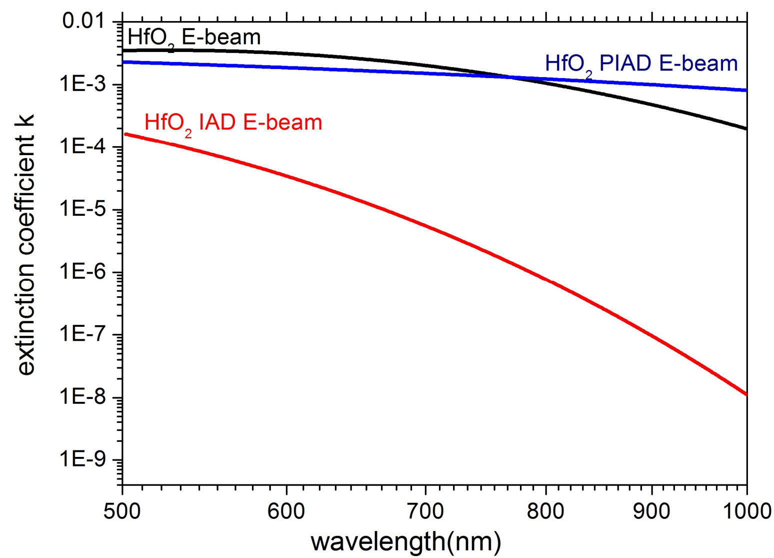

Figure 2.21: *Extinction coefficient k calculated from fitted transmission data of hafnia single layers produced using PVD processes described in Table 2-2. Thicknesses of the coatings are provided in Table 2-3.*

The extinction coefficient distribution for sputtered and E-beam deposited niobia is presented in Figure 2.22. Overall, PIAD E-beam deposited has the lowest absorption. The highest absorption is noted for RF sputtered niobium dioxide for which the lowest refractive index was also reported. This can be justified by a low oxidation of the coating. Microdyn coating is also characterized by a high absorption despite having the highest refractive index. This high absorption can be explained by many inclusions noted on the surface of the coating. The coating surface also presents many pinhole defects as presented in Figure 2.23.

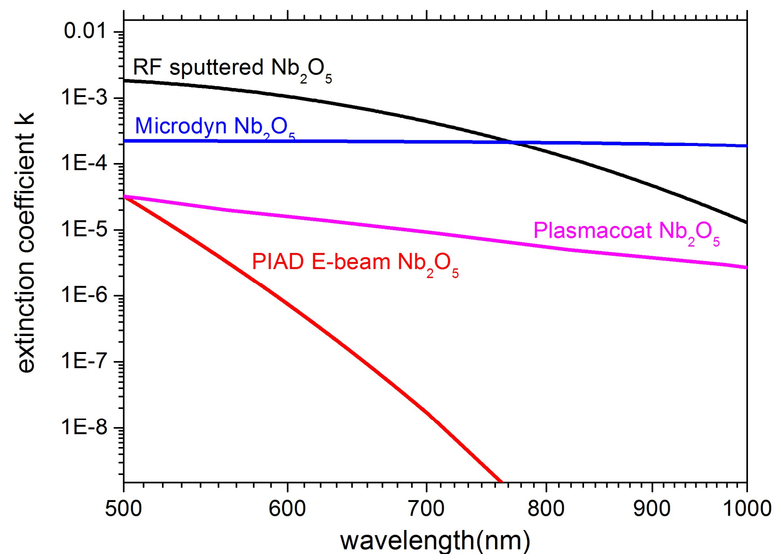

Figure 2.22: *Extinction coefficient k calculated from fitted transmission data of niobia single layers produced using PVD processes described in Table 2-2. Thicknesses of the coatings are provided in Table 2-3.*

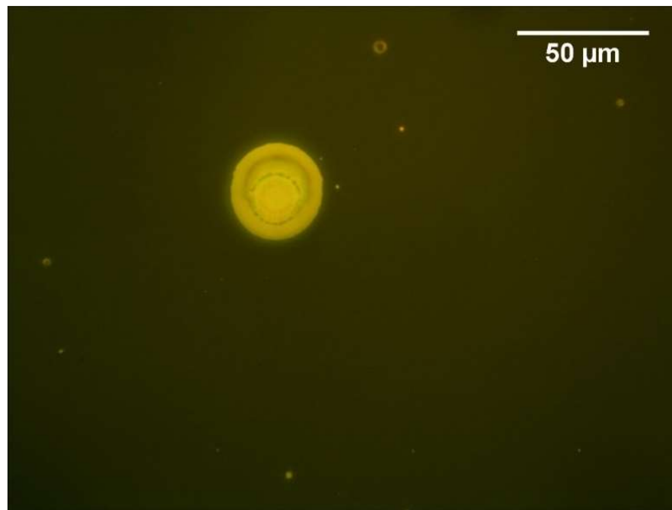

Figure 2.23: *Pinhole defects reported for single layer niobia coating deposited using microwave assisted reactive magnetron sputtering.*

Pinholes in thin film coatings may be caused by surface contaminants deposited on the substrate during the sputtering process. These contaminants consist of dust particles and debris deposited on the target and the shields of the chamber.

The extinction coefficients of thermally evaporated zinc sulphide and zinc selenide are shown in Figure 2.24. At 500 nm wavelength, the extinction coefficient k is equal to 10^{-2}. At a substrate temperature equal to 100 °C, zinc selenide high absorption is caused by a low crystallinity causing a shift of the absorption to longer wavelengths[48]. The microstructure of zinc selenide coatings will be described in Section 2.4.2. The extinction coefficient of zinc sulphide is about one order of magnitude lower than zinc selenide and follows a similar distribution. Indeed, both zinc selenide and zinc sulphide are II-VI semiconductors and have similar optical and structural properties.

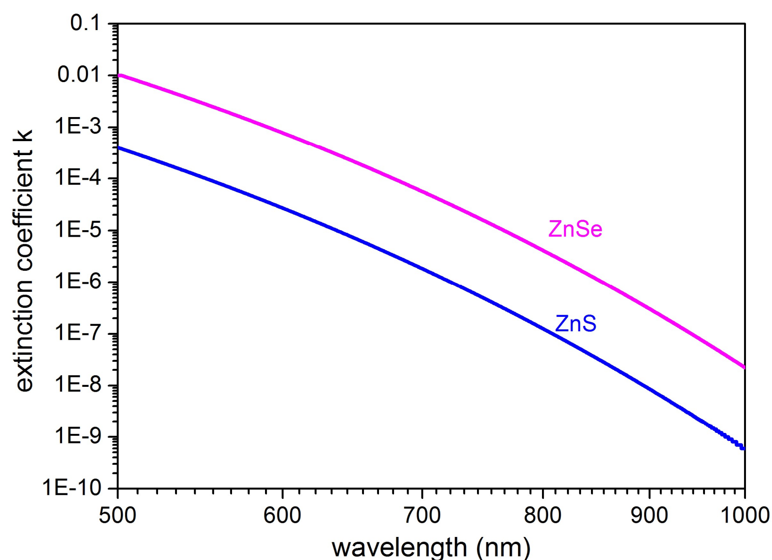

Figure 2.24: *Extinction coefficient k calculated from fitted transmission data of thermally evaporated zinc selenide and zinc sulphide layers produced using PVD processes described in Table 2-2. Thicknesses of the coatings are provided in Table 2-3.*

2.3.4 *Summary of optical constants*

A summary of refractive indices and extinction coefficients at 500 nm and 1000 nm wavelength is presented in Table 2-4. The refractive index values of the studied materials are compared to bulk indices reported in the literature. In Table 2-4, extinction coefficients below 10^{-5} are noted as $<10^{-5}$ due to the limitation of the spectral resolution.

Material	Fabrication method	n_{1000}	n_{500}	k_{1000}	k_{500}	n_{b1000}	n_{b500}
Ta_2O_5	P-DC sputtering	2.10	2.15	$<10^{-5}$	$<10^{-5}$		
TiO_2	IAD E-beam	2.27	2.40	$<10^{-5}$	$<10^{-5}$	2.4856[49]	2.7114[49]
$LaTiO_3$	E-beam	2.04	2.08	$<10^{-5}$	$<10^{-5}$		
Nb_2O_5	PIAD E-beam	2.23	2.31	$<10^{-5}$	$<10^{-5}$		
	RF sputtering	2.08	2.12	2×10^{-4}	2×10^{-3}		
	Plasmacoat	2.20	2.1	$<10^{-5}$	$<10^{-5}$		
	Microdyn	2.39	2.27	2×10^{-4}	4×10^{-4}		
HfO_2	E-beam	1.98	2.01	1×10^{-3}	3×10^{-3}	2.0833[40]	2.1277[40]
	IAD E-beam	2.02	2.05	$<10^{-5}$	$<10^{-5}$		
	PIAD E-beam	2.02	2.06	1×10^{-3}	2×10^{-3}		
ZrO_2	P-DC sputtering	1.98	2.01	$<10^{-5}$	8×10^{-5}	2.1248[37]	2.1788[37]
	E-beam	1.98	2.02	$<10^{-5}$	6×10^{-4}		
	IAD E-beam	2.02	2.08	2×10^{-3}	8×10^{-3}		
	PIAD E-beam	2.09	2.16	$<10^{-5}$	3×10^{-5}		
	Plasmacoat	2.15	2.19	2×10^{-3}	3×10^{-3}		
ZnS	T.evaporation	2.31	2.43	$<10^{-5}$	4×10^{-4}	2.2925[41]	2.4199[41]
ZnSe	T.evaporation	2.54	2.77	$<10^{-5}$	2×10^{-2}	2.4783[42]	2.7326[42]
SiO_2	E-beam	1.46	1.47	1×10^{-3}	1.5×10^{-3}	1.4502[32]	1.4619[32]
	IAD E-beam	1.45	1.47	$<10^{-5}$	4×10^{-5}		
	RF sputtering	1.45	1.47	6×10^{-5}	1.2×10^{-4}		
	P-DC sputtering	1.45	1.47	$<10^{-5}$	6×10^{-4}		
	Plasmacoat	1.47	1.47	5×10^{-5}	1×10^{-4}		
	Microdyn	1.46	1.47	1.1×10^{-4}	1.4×10^{-4}		
LiF	T.evaporation	1.38	1.39	$<10^{-5}$	$<10^{-5}$	1.3871[34]	1.3944[34]
MgF_2	T.evaporation	1.38	1.38	$<10^{-5}$	$<10^{-5}$	1.3736[35]	1.3798[35]
	E-beam	1.36	1.37	$<10^{-5}$	6×10^{-5}		
Cryolite	T.evaporation	1.40	1.40	7×10^{-4}	5×10^{-3}		
	E-beam	1.32	1.33	$<10^{-5}$	$<10^{-5}$		

Table 2-4: *Summary of the optical constants results for the studied dielectric coatings at 500 nm and 1000 nm compared to bulk material refractive index n_b from the literature at the respective wavelength values.*

2.4 Surface roughness

As previously discussed in Section 1.4.3, surface roughness contributes to optical losses (scatter). Dielectric materials used for high reflectance mirrors must therefore have very smooth surfaces. In this section, light scatter caused by surface roughness is briefly presented. The roughness measurement data of single layer coatings previously characterised are provided in Section 2.4.

2.4.1 *Light scatter and surface roughness*

Scattering in optical surfaces is strongly related to the surface state with respect to incident light. There are several theories and models allowing the calculation of scattering from surface roughness. Most analytic models for light scattering from surface roughness are based on Maxwell equations. The most notable theories in light scattering calculation are the Kirchhoff theory[50, 51], the Rayleigh-Rice theory[51] and the Beckmann approximation[52]. A modelling of different scattering regimes of surface roughness has been proposed in [51]. The relationship between light scattering, the incident wavelength and the root mean square roughness r for single layer coatings is described in Equation (2.4)[53], assuming normal incidence of the light on the surface:

$$S = \left(\frac{4\pi r}{\lambda}\right)^2 \quad (2.4)$$

Scatter dependency of surface roughness is represented in Figure 2.25 at 500 nm, 640 nm and 1000 nm wavelengths. For low loss high reflectance mirrors in the UV-visible region, it is very important to aim for very low roughness materials (below 1 nm), especially as the roughness tends to increase for multilayer coatings.

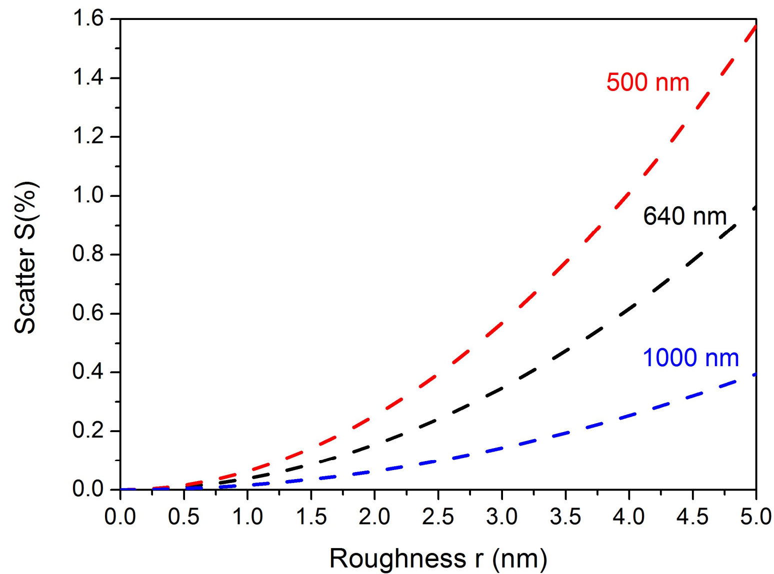

Figure 2.25: *Scatter calculated from surface roughness using Equation (2.4) at 500 nm, 640 nm and 1000 nm wavelengths.*

2.4.2 *Roughness measurement*

The surface roughness of the deposited materials on microscope slides was evaluated using Atomic Force Microscopy (AFM). All measurements have been performed at Heriot-Watt University using Veeco Dimension 3100 system in Tapping mode. In this mode, the cantilever of the AFM taps along the coating surface. It is more appropriate to

soft dielectrics and prevents damaging the coatings. It is also sufficient to measure the roughness of the dielectric samples prepared for this study. AFM scans have been performed at a frequency of 0.25 Hz using a sampling of 256 × 256 lines and a Bruker n-doped silicon AFM probe. The root mean square roughness r of the studied samples is presented in Table 2-5. The roughness has been calculated from raw scanning data using the statistical quantities function of Gwyddion software, version 2.51[54]. An estimation of scatter in percent at 500 nm and 1000 nm wavelengths is provided in the same table. The scatter S has been calculated from the rms roughness, r, using Equation (2.4).

Material	Deposition method	r, roughness (nm)	Scatter (1000 nm) (%)	Scatter (500 nm) (%)
Ta_2O_5	P-DC sputtering	1.2 ± 0.2	0.02	0.09
TiO_2	IAD E-beam	0.8 ± 0.2	0.01	0.04
$LaTiO_3$	E-beam	3.3 ± 0.4	0.17	0.70
HfO_2	E-beam	2.6 ± 0.2	0.11	0.43
	IAD E-beam	3.7 ± 0.2	0.20	0.86
	PIAD E-beam	3.0 ± 0.2	0.14	0.57
Nb_2O_5	PIAD E-beam	1.4 ± 0.3	0.03	0.12
	RF sputtering	2.9 ± 0.3	0.13	0.53
ZrO_2	P-DC sputtering	1.5 ± 0.3	0.04	0.14
	E-beam	3.1 ± 0.8	0.15	0.61
	IAD E-beam	1.5 ± 0.3	0.04	0.14
ZnS	T. evaporation	6.8 ± 0.3	0.73	2.92
ZnSe	T. evaporation	1.5 ± 0.3	0.04	0.14
SiO_2	E-beam	1.7 ± 0.2	0.05	0.18
	IAD E-beam	1.2 ± 0.1	0.02	0.09
	RF sputtering	1.7 ± 0.2	0.05	0.18
	P-DC sputtering	1.7 ± 0.4	0.05	0.18
LiF	T. evaporation	4.3 ± 0.2	0.29	1.17
MgF_2	T. evaporation	2.9 ± 0.5	0.13	0.53
	E-beam	3.0 ± 1.1	0.14	0.57
Na_3AlF_6	T. evaporation	1.9 ± 0.6	0.06	0.23
	E-beam	2.0 ± 0.4	0.06	0.25
Micro-slide/SF11	/	1.0 ± 0.2	0.02	0.06

Table 2-5: *Summary of the root mean square r roughness values of the studied dielectric coatings and the estimated scatter at 500 nm and 1000 nm from Equation (2.5).*

It can be concluded from the results presented in Table 2-5 that surface roughness varies between grown materials and also between deposition methods for the same material. While most of the thin film coatings deposited on microscope slides show a roughness in the range of 1 nm to 2 nm, other coatings such as thermally evaporated zinc sulphide, lithium fluoride, magnesium fluoride and E-beam evaporated lanthanum titanate and hafnium dioxide exhibit a significantly greater roughness. Considering the case of the lowest surface roughness obtained for E-beam titanium dioxide, the estimated scatter varies between 0.04 % or 400 ppm at 500 nm and 0.01 % or 100 ppm at 1000 nm. By contrast, a surface roughness of 6.8 nm for thermally evaporated zinc sulphide induces a scatter of almost 3 % at 500 nm. This estimation is not reasonable as it does not agree with the halfwave transmittance loss with respect to the substrate of 0.2 ± 0.05 % (Figure 2.26). This deviation between the scatter estimated from surface roughness and the optical transmission data is most likely explained by a variation of the rms roughness of the zinc sulphide coating across the large sample area. It is also difficult to perform both rms roughness and transmission measurements in the same spot. Furthermore, the roughness measurement was performed on a few µm² area whereas transmission measurement is

made on many mm² area. Other measurements, such as total integrated scattering, are a possible route to verify the scatter values presented in Table 2-5.

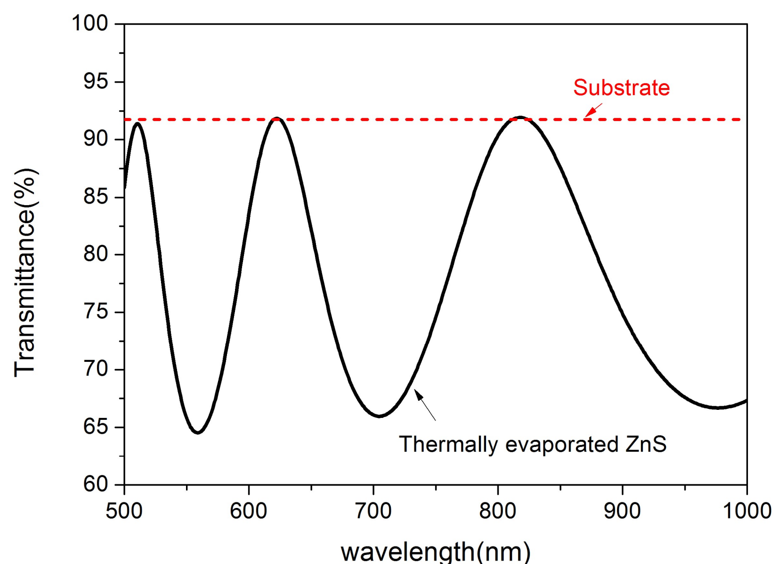

Figure 2.26: *Halfwaves of thermally evaporated zinc sulphide laying on the substrate transmittance.*

AFM two-dimensional height profiles of silicon dioxide layers of equivalent thickness are shown in Figure 2.27. Overall, the silicon dioxide layers present similar roughness values. IAD E-beam silicon dioxide has however a slightly smaller surface roughness. The height profile scans also highlight the difference in the growth mode and the coating morphology between the various deposited coatings. For RF sputtered silicon dioxide (2.27.a), the film grains are clearly distinguishable and have a round shape. The grain size ranges between 30 to 50 nm. Both E-beam and IAD E-beam (2.27.c and 2.27.d) exhibit a very dense structure with a grain size around 20 nm. P-DC sputtered silicon dioxide presents a structure with larger grains (around 100 to 150 nm). The latter can be explained by a very low deposition rate (0.6 Å/s for P-DC sputtering to 2 to 3 Å/s for E-beam and IAD E-beam) allowing the grains to expand and resulting in a flatter structure. Indeed, a lower deposition rate during film growth reduces the initial cluster size representing the number of atoms arriving per time unit. With a deposition rate of 2 to 3 Å/s, the cluster formed is 3 to 4 times bigger[55] for E-beam processes. This is not however the case for RF sputtered silicon dioxide which was deposited at 0.34 Å/s. The growth mode difference between E-beam and P-DC sputtered silicas can be also related to the energy difference between both deposition methods. The difference noted in the growth mode between RF sputtering and P-DC sputtering may be related to the higher frequency of RF sputtering. This is not however enough to explain the difference of surface morphologies between RF and P-DC sputtered silica layers as other process parameters can influence the growth mode of the coating such as the substrate temperature (a heating at 120 °C has been used in the case of P-DC sputtered silica) and the inert and reactive gases flows.

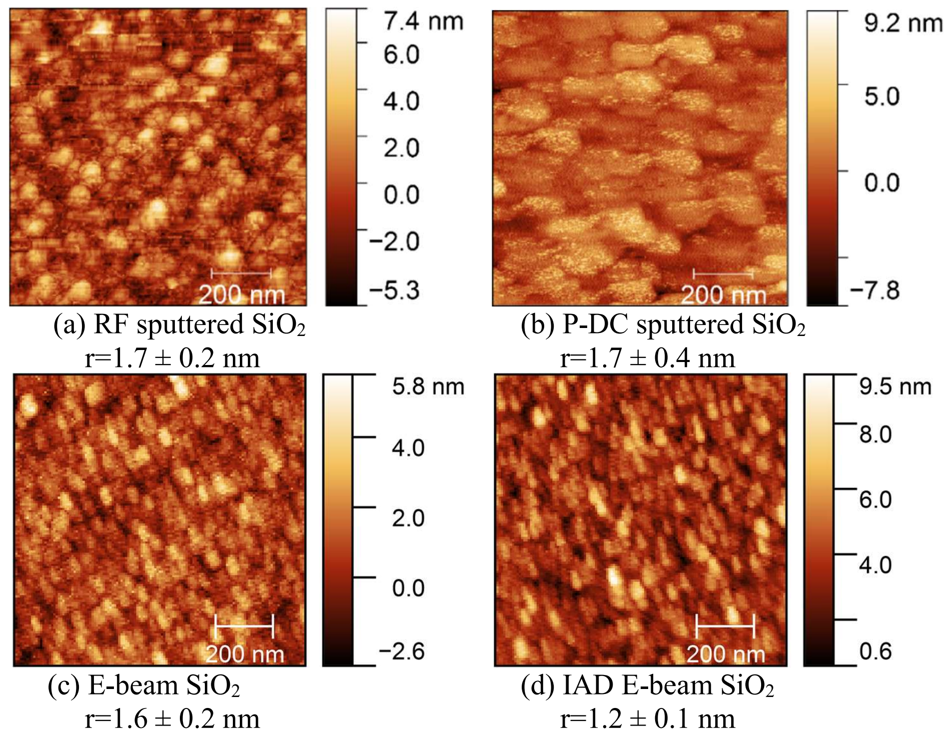

Figure 2.27: *Comparison between AFM scans for silicon dioxide single layer produced by various physical vapour deposition methods. The AFM scans have been performed in tapping mode on 1 μm × 1 μm area at a speed of 0.25 Hz using 256 samples/line.*

The surface morphology of cryolite and magnesium fluoride deposited using E-beam and thermal evaporation is presented in Figure 2.28. Thermally evaporated magnesium fluoride and cryolite present a similar surface morphology with a flatter surface for thermally evaporated cryolite resulting in a lower surface roughness. The same observation can be made for E-beam evaporated materials. In both cases cryolite thin films are smoother than magnesium fluoride.

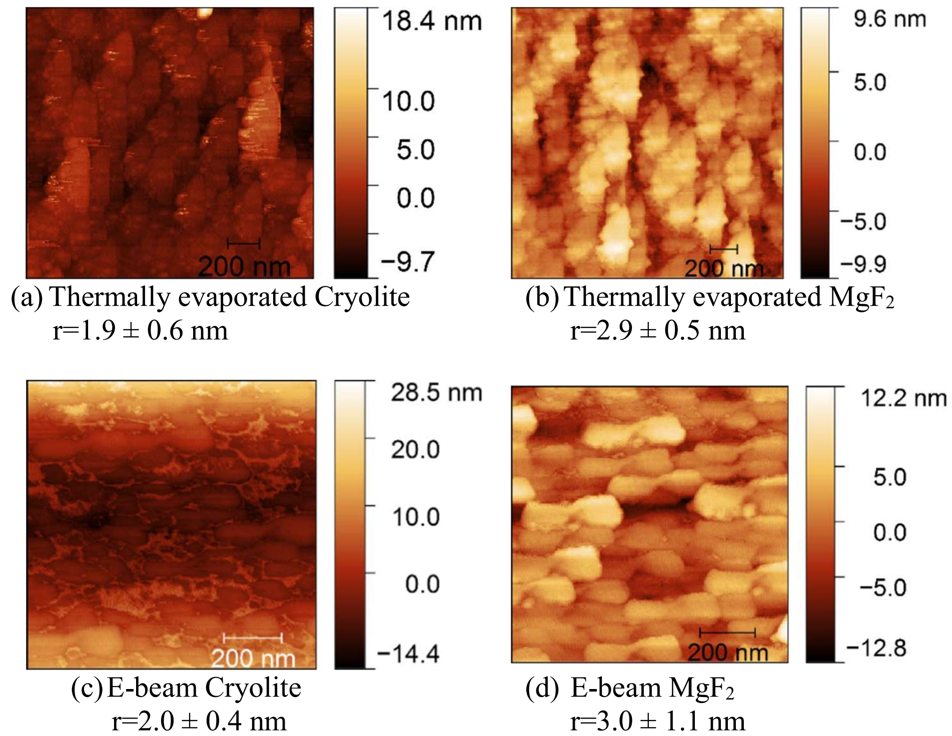

(a) Thermally evaporated Cryolite r=1.9 ± 0.6 nm

(b) Thermally evaporated MgF_2 r=2.9 ± 0.5 nm

(c) E-beam Cryolite r=2.0 ± 0.4 nm

(d) E-beam MgF_2 r=3.0 ± 1.1 nm

Figure 2.28: *Comparison between AFM scans for single layer cryolite and magnesium fluoride produced using E-beam and thermal evaporation. The AFM scans have been performed in tapping mode at a speed of 0.25 Hz using 256 samples/line. The coating thickness is of 500 nm approximately.*

In order to study the difference in the growth mode between the two depositions methods, comparative three-dimensional scans of thermally evaporated and E-beam grown magnesium fluorides are presented in Figure 2.29. E-beam magnesium fluoride grows in a joined islands mode, also known as Stranski-Krastanow mode[56] while thermally evaporated grows as larger islands in Frank and Vander Merwe model[57].

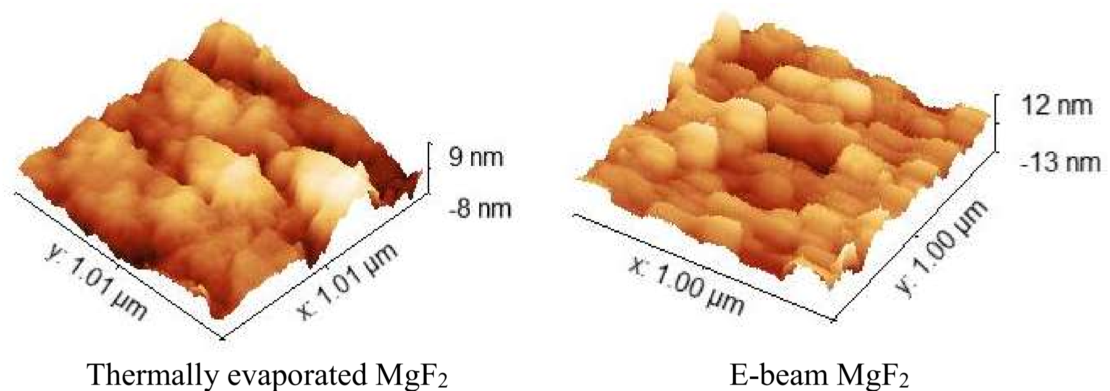

Thermally evaporated MgF_2 E-beam MgF_2

Figure 2.29: *Comparison between AFM 3D profile for single layer magnesium fluoride produced using E-beam and thermal evaporation. The AFM scans have been performed in tapping mode on 1 µm × 1 µm at a speed of 0.25 Hz using 256 samples/line.*

The microstructures of thermally evaporated zinc selenide and zinc sulphide are presented in Figure 2.30. Zinc selenide shows a dense and flat microstructure with a grain size between 10 and 15 nm (Figure 2.30.a) which is in accordance with values reported in [48]

for thermally grown zinc selenide at 100 °C. It has been also reported in [58, 59] that the grain size was related to the absorption of the coating. The zinc selenide AFM scan also reveals some structure defects within the coating. These impurities are caused by material spitting during thermal evaporation. Similar defects have been also reported in [60, 61]. The defects trapped in the coating can also explain the high absorption demonstrated by zinc selenide coating in Figure 2.24. The surface of zinc sulphide appears rougher with a uniform round shape grains ranging from 30 to 50 nm (Figure 2.30.b). Similar defects to zinc selenide can be distinguished within the zinc sulphide coating but are less prominent due to a rougher surface profile.

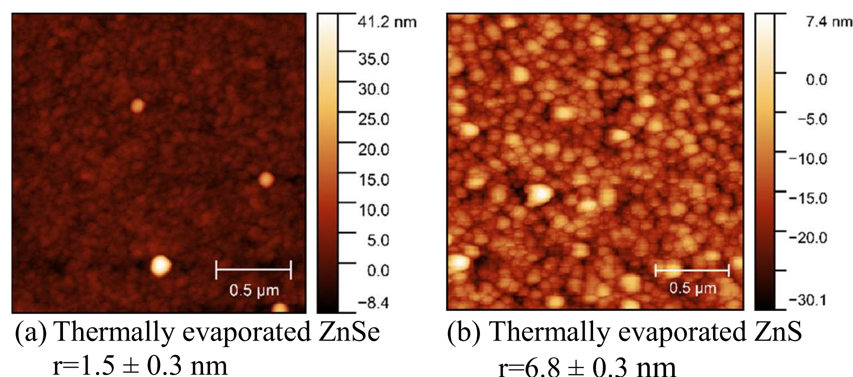

(a) Thermally evaporated ZnSe
r=1.5 ± 0.3 nm

(b) Thermally evaporated ZnS
r=6.8 ± 0.3 nm

Figure 2.30: *AFM scans for thermally evaporated single layer zinc selenide, zinc sulphide. The AFM scans have been performed in tapping mode 2 μm × 2 μm at a speed of 0.25 Hz using 256 samples/line. The coating thickness is of 500 nm approximately.*

For zirconium dioxide layers, a low surface roughness is noted for both IAD E-beam and P-DC sputtered layers. The surface morphology of P-DC sputtered zirconium dioxide (Figure 2.31.b) is particularly interesting as it has been already observed for P-DC sputtered silicon dioxide (Figure 2.27.b). For IAD E-beam zirconia, the surface presents a dense morphology with a grain size of 10 nm to 20 nm (Figure 2.31.a).

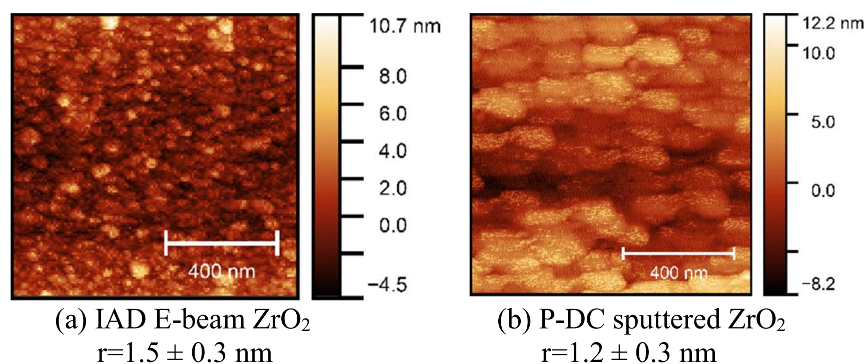

(a) IAD E-beam ZrO_2
r=1.5 ± 0.3 nm

(b) P-DC sputtered ZrO_2
r=1.2 ± 0.3 nm

Figure 2.31: *Comparison between AFM scans for single layer zirconia produced using IAD E-beam and P-DC sputtering. The AFM scans have been performed in tapping mode at a speed of 0.25 Hz using 256 samples/line on 1 μm × 1 μm scan areas.*

The difference in surface roughness, coating morphology and growth mode for hafnium dioxide deposited using different deposition methods is shown in Figure 2.32. For instance, E-beam hafnium dioxide presents a monolayer growth mode (Figure 2.32.a). The coating does not however cover the substrate evenly resulting in a porous coating which explains the high absorption of the coating (Figure 2.21). IAD E-beam hafnia coating shows a Volmer-Weber growth mode where isolated islands are formed on the substrate and join in some areas of the coating (Figure 2.32.b). This growth mode causes

a higher roughness for the coating. In Figure 2.32.c, PIAD E-beam hafnia presents an even layer of coating with some distinguishable islands on the surface and has therefore a lower surface roughness than IAD E-beam hafnia.

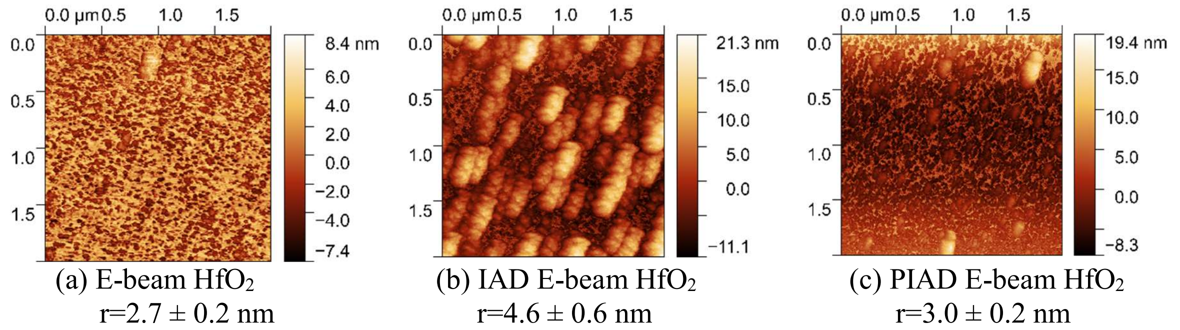

(a) E-beam HfO_2 r=2.7 ± 0.2 nm (b) IAD E-beam HfO_2 r=4.6 ± 0.6 nm (c) PIAD E-beam HfO_2 r=3.0 ± 0.2 nm

Figure 2.32: *Comparison between AFM scans for single layer hafnia produced using three E-beam processes. The AFM scans have been performed in tapping mode at a speed of 0.25 Hz using 256 samples/line on 2 µm × 2 µm scan areas.*

A comparison between AFM scans for niobia coatings deposited using PIAD E-beam and RF sputtering processes is provided in Figure 2.33. In Figure 2.33.a, PIAD E-beam niobia presents a flat smooth surface and the coating height is even. RF sputtered niobia has a grainy morphology similar to RF sputtered silica (Figure 2.27.a) with a higher surface roughness due to a grainy microstructure.

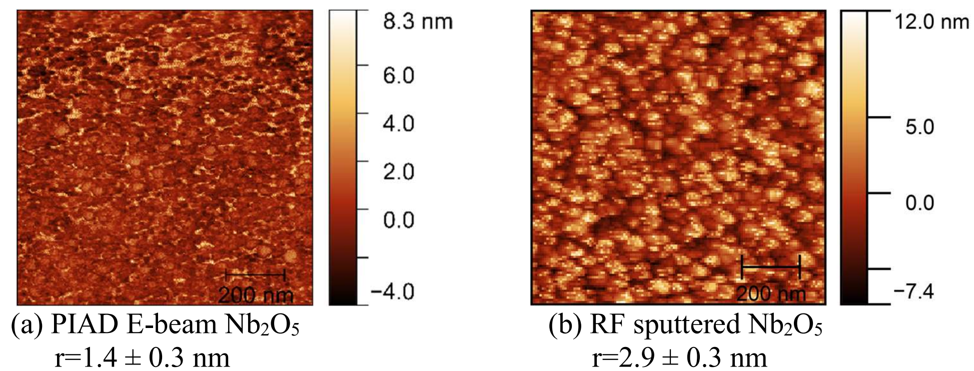

(a) PIAD E-beam Nb_2O_5 r=1.4 ± 0.3 nm (b) RF sputtered Nb_2O_5 r=2.9 ± 0.3 nm

Figure 2.33: *Comparison between AFM scans for single layer niobia produced using PIAD E-beam and RF sputtering processes. The AFM scans have been performed in tapping mode at a speed of 0.25 Hz using 256 samples/line on 1 µm × 1 µm scan areas.*

AFM scans for the last studied high index materials are shown in Figure 2.34. P-DC sputtered tantala presents a low surface roughness with a mixed surface of flat and grainy morphology (Figure 2.34.a). IAD E-beam titania has an evenly flat surface forming in one single layer (Figure 2.34.b). This coating has in fact the lowest roughness of all the presented single layer coatings. E-beam lanthanum titanate has a flat surface with several craters resulting in a higher surface roughness (Figure 2.34.c).

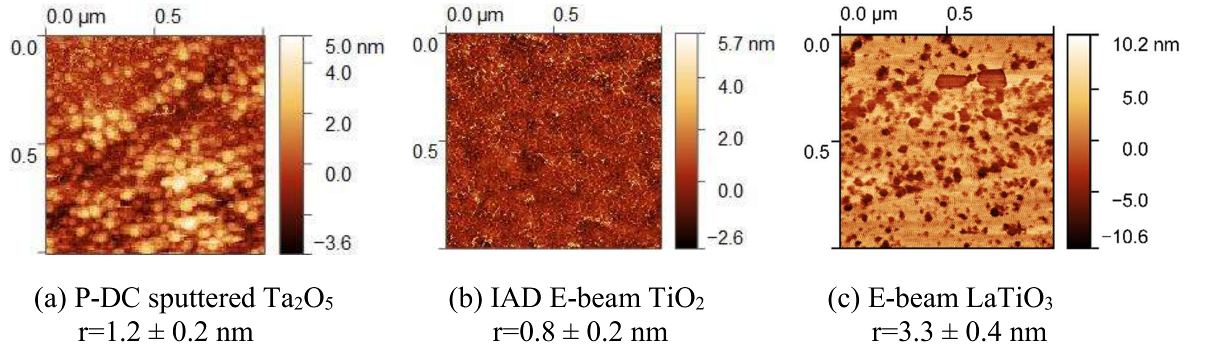

(a) P-DC sputtered Ta_2O_5
r=1.2 ± 0.2 nm

(b) IAD E-beam TiO_2
r=0.8 ± 0.2 nm

(c) E-beam $LaTiO_3$
r=3.3 ± 0.4 nm

Figure 2.34: *AFM scans of titanium dioxide, tantalum pentoxide and lanthanum titanate. The AFM scans have been performed in tapping mode on 1 µm × 1 µm area at a speed of 0.25 Hz using 256 samples/line.*

2.5 Mechanical stress

The mechanical behaviour of multilayer coatings consists a very important characterisation aspect in the durability of Fabry-Perot cavities. Indeed, intrinsic compressive or tensile stresses alter the structure of multilayer coatings leading to modified light-matter interactions within the cavity.

The total stress σ_{tot} in a thin film can be described as the sum of three types of stresses according to Equation (2.6).

$$\sigma_{\mathrm{tot}} = \sigma_{\mathrm{ext}} + \sigma_{\mathrm{th}} + \sigma_{\mathrm{i}} \qquad (2.5)$$

Where σ_{ext} , σ_{th} and σ_{i} represent the external stress, the thermal stress and the internal stress in the deposited layer, respectively.

In this study, external stress is neglected as the studied samples are not submitted to any external strain source. Thermal stress is created by temperature fluctuations during the deposition and can be calculated if the temperature gradient, the thermal expansion of the material and the Young's modulus are known using the following expression:

$$\sigma_{\mathrm{th}} = E_{\mathrm{s}}(\alpha_{\mathrm{f}} - \alpha_{\mathrm{s}})(T_{\mathrm{f}} - T_{0}) \qquad (2.6)$$

Where E_s represents the Young's modulus of the coating, α_f and α_s are the expansion coefficients of the film and the substrate. T_f and T_0 are the initial and final temperatures of the deposition process.

Thermal fluctuations during deposition are negligible and heating and cooling processes were gradual. Thermal stress contribution to the overall mechanical stress will be therefore neglected. Internal stresses represent the remaining stress in the coating at the end of the process. Measurement method and values of internal stress using the curvature method are presented in the next section.

2.5.1 Stoney's formula and curvature method

The curvature method is the oldest and most common measurement method of internal stress. It was presented by Stoney more than a century ago to calculate internal stress for electrodeposited metallic thin films[62]. This method is applied to silicon cantilevers clamped on one end. The cantilever can be subject to either a tension or a compression stress due to a force applied by the coating (Figure 2.35).

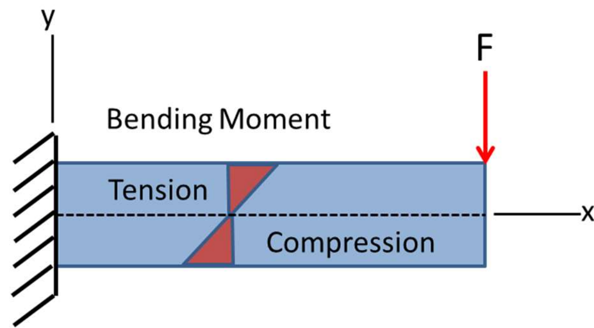

Figure 2.35: *Orientation of compression and tension stresses on a clamped silicon stress.*

The elastic behaviour of the cantilever is given by Equation (2.8):

$$-\nabla.\sigma = f \qquad (2.7)$$

σ being the stress tensor and f is the force vector

In the present study, the coatings were deposited on silicon cantilever substrates. The substrate was clamped from one end only allowing the coating to freely bend during and after the deposition process. The stress of the coating results in a deflection of the substrate (Figure 2.36).

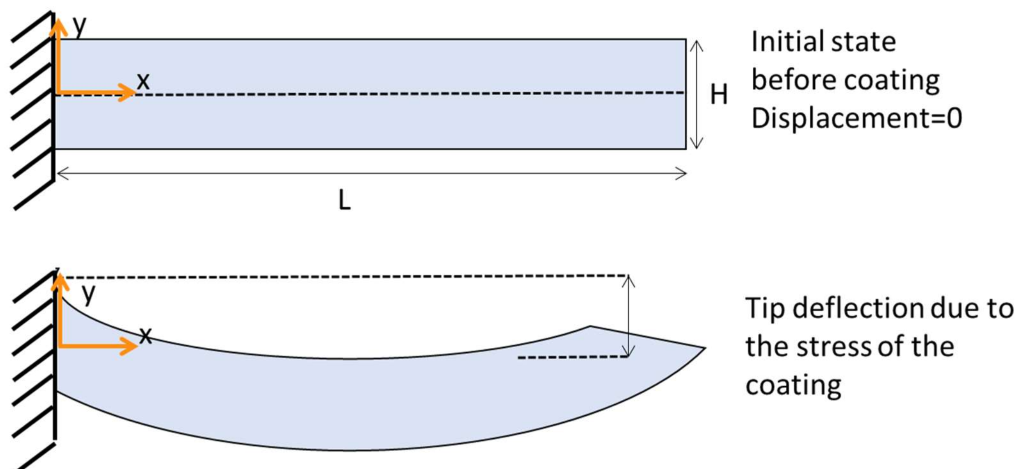

Figure 2.36: *Top: Initial state of the clamped silicon cantilever. Bottom: Deflection of the beam due to the stress of the coating.*

The stress of the coating is related to the bending moment of the cantilever by the following equation:

$$\sigma = -\frac{My}{I_c} \tag{2.8}$$

Where M is the bending moment of the cantilever, y the distance from the beam's neutral axis to the point of interest along the height of the cross section and I_c is the centroidal moment of inertia.

The measurement of internal stresses through the bending of the silicon cantilever relies on Equation (2.9) which connects the internal stress to the curvature radii variation before and after coating[63]:

$$\sigma = \frac{E_s}{6(1-\nu_s)} \frac{h_s^2}{h_f} \left(\frac{1}{R} - \frac{1}{R_0} \right) \tag{2.9}$$

Where E_s and ν_s are the Young's modulus and the Poisson's ratio of the substrate. h_s and h_f are the respective thicknesses of the substrate and the film. R and R_0 are the curvature radii of the substrate after and before deposition.

There are, however, several conditions for the application of the above formula to calculate internal stresses of thin film coatings: the thicknesses of the substrate and the coating should be smaller than the lateral dimensions; and the coating must have a smaller thickness than the substrate. The Stoney formula also assumes that both substrate and coating are homogenous, isotropic and linearly elastic. The equation only applies in the case of spherical deformations and in the case of infinitesimal deformations and rotations. In order to meet the above conditions, several test strips (or cantilevers) have been prepared using Valley Design P-type CZ Silicon (100) 2" diameter and 100 μm thick polished silicon wafers. The wafers were cleaved to 3.5 cm long and 0.5 cm wide strips. The cantilevers were carefully fixed on a microscope slide using Kapton tape positioned at 0.5 cm from the end of the strip (Figure 2.37). This set-up allows the cantilever to bend freely during the coating process.

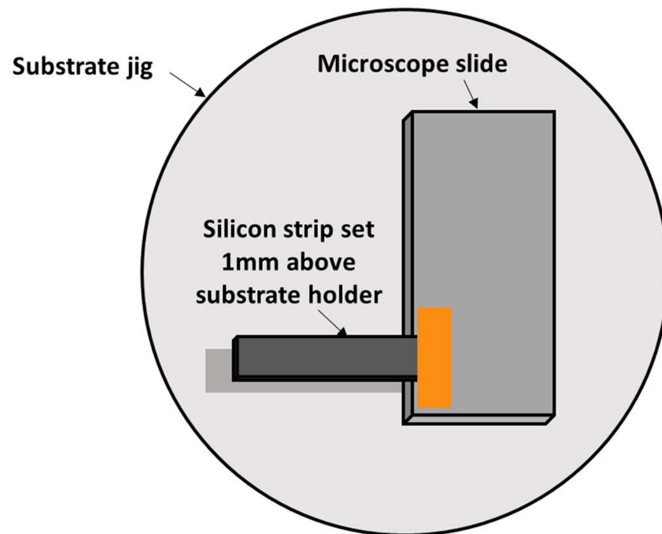

Figure 2.37: *Top-view of silicon strip clamped on a microscope slide and mounted on a circular jig.*

The curvature method consists of measuring the variation between the radii of curvature before and after deposition. Figure 2.38 represents a bespoke curvature measurement apparatus used to determine the internal stress for dielectric single layers. A 640 nm wavelength, a diode laser is shined on the silicon cantilever and the reflected spot position is marked on a screen set at 2.3 m from the sample. The sample is placed accurately on the holder and the laser position is also accurately set.

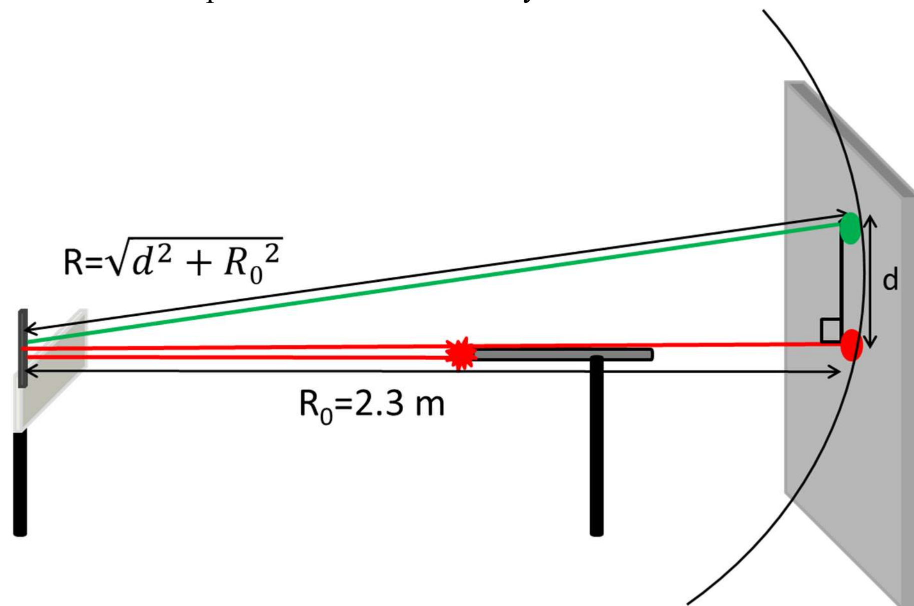

Figure 2.38: *Bespoke curvature measurement apparatus.*

The radius of curvature before coating R_0 was estimated as 2.3 m. Before coating, a laser source is shined on a given position of the silicon strip. The reflected laser spot on the screen is marked down (red spot on Figure 2.38). After coating, the laser was shined again on the same position and the reflected spot is marked down again (green spot). The deviation between the red and the green spots allows the estimation of the new radius of curvature R using Equation (2.10):

$$R = \sqrt{d^2 + R_0^2} \quad (2.10)$$

Where d is the deviation between the red and the green spots or the laser positions before and after coating.

2.5.2 Stress calculation

The radii of curvature variations are reported for three positions on the silicon cantilever (Figure 2.39). This method allows evaluating the deflection of the cantilever over its total length. Position 3 is a very sensitive measuring point as it is the closest point to the clamped end of the cantilever.

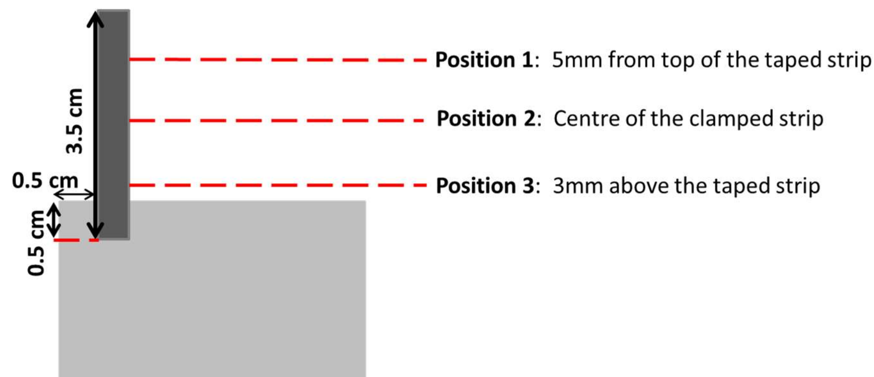

Figure 2.39: *Dimensions of silicon strip mounted on glass substrate showing the laser spots measurements positions. Position 1 is at 5 mm below the free end of the strip. Position 2 is at the middle of the strip. Position 3 is at 3 mm above the clamped end of the strip.*

Beam deviations for the previously defined positions are reported in Table 2-6. The studied thin film coatings have been deposited in the same process conditions stated in Tables 2-1 and 2-2.

Material	Fabrication method	Thickness(nm)	d_1(cm)	d_2(cm)	d_3(cm)
TiO_2	IAD E-beam	470.6	1.2	0.9	0.9
Ta_2O_5	P-DC sputtering	519	-1.4	-0.9	-0.4
$LaTiO_3$	E-beam	333.5	-0.3	1.8	-0.1
ZrO_2	RF sputtering	592.1	2.9	1.9	1.2
	IAD E-beam	435.8	2.7	2.6	2.3
	PIAD E-beam	502.8	3.7	2.2	1
Nb_2O_5	RF sputtering	592.1	2.9	1.9	1.2
ZnS	T.evaporation	576	-3	-2.8	-2.4
ZnSe	T.evaporation	553	0.6	2.2	3.3
SiO_2	E-beam	454	-8.2	-7	-6.3
	IAD E-beam	463.7	-5.6	-3.4	-1.1
	RF sputtering	460.1	0.2	0.4	0.9
	P-DC sputtering	391	-16	-15.9	-15.6
LiF	T.evaporation	455	-4.2	-4.1	-4.4
MgF_2	T.evaporation	396	0.7	0.4	0
Cryolite	T.evaporation	457	-5.7	-5.8	-5.7

Table 2-6: *Tip deflection calculated using the curvature apparatus described in Figure 2.38. d_1, d_2 and d_3 correspond to tip deflections for Positions 1, 2 and 3 respectively.*

Knowing the thickness of the coating and the radii of curvature before and after deposition, the internal stress of the studied dielectrics can be calculated. Young's modulus and Poisson's ratio for Si(100) are 130 GPa and 0.28 respectively[64]. Results of internal stress values are represented in Table 2-7.

Material	Fabrication method	Thickness (nm)	σ_1(kPa)	σ_2(kPa)	σ_3(kPa)
TiO_2	IAD E-beam	470.6	3.5	1.9	1.9
Ta_2O_5	P-DC sputtering	519	4.3	1.8	0.4
$LaTiO_3$	E-beam	367	-24.4	31.8	-6.1
ZrO_2	RF sputtering	592.1	2.9	1.9	1.2
	IAD E-beam	435.8	19.1	17.7	14.0
	PIAD E-beam	502.8	31.1	11.0	2.3
Nb_2O_5	RF sputtering	16.2	7.0	2.8	16.2
ZnS	T.evaporation	576	-17.8	-15.5	-11.4
ZnSe	T.evaporation	553	0.7	10.0	22.5
SiO_2	E-beam	454	-168.9	-123.1	-99.7
	IAD E-beam	463.7	-77.2	-28.5	-2.9
	RF sputtering	460.1	0.1	0.4	2.0
	P-DC sputtering	391	-744.7	-735.4	-708.1
LiF	T.evaporation	455	44.2	42.2	48.6
MgF_2	T.evaporation	396	1.4	0.5	0.0
Cryolite	T.evaporation	457	-81.1	-84.0	-81.12

Table 2-7: *Stress calculated for dielectric single films using Stoney's equation.*

Overall, the calculated stress values are very low, and the stress is homogeneous over the length of the cantilever. Few interesting facts can be deduced from the stress results on the mechanical behaviour of silicon dioxide coatings. E-beam silicon dioxide displays a compressive behaviour which is slightly improved by IAD. The porous structure of E-beam evaporated silicon dioxide absorbs water molecules when the sample is moved from vacuum to air which causes the coating to become more compressive[65, 66]. The decrease of intrinsic compressive stress for IAD E-beam silicon dioxide can be hence justified by the improvement of the coating porosity and its density. P-DC sputtered silica has a more pronounced compressive behaviour with the highest stress value reported for the studied coatings. P-DC sputtered silica was also found to have the highest absorption of all deposited silica layers which may mean that this compressive behaviour is related to the growth mechanism of the P-DC sputtered silica. A model proposed by Davis in [67] explains the formation of compressive intrinsic stresses in dense coatings is caused by atoms implanted below the surface of the film by knock-on processes in accordance with the model proposed by Windischmann[68].

In a multilayer coating, a materials pair with opposite stress values would be conveniently selected in order to end with a neutral stress and conserve the initial figure of the substrate. For instance, IAD E-beam silicon dioxide should be paired with a tensile coating such as IAD E-beam titanium dioxide or IAD E-beam zirconium dioxide. Thermally evaporated zinc sulphide and lithium fluoride also form a convenient pair in terms of mechanical stress compensation.

It is important to note that the stress of the material strongly depends on the thickness of the coating according to Stoney's equation. A higher stress value is therefore expected for a thinner coating on the same substrate. This mechanical study only provides a first

indication of the stress values and the mechanical properties of thin film coatings. A stress study is required for multilayer mirrors to establish their mechanical behaviour.

2.6 Summary and discussions

The fabrication methods for a selection of dielectric materials representing the state of the art of optical materials for Fabry-Perot microcavities in the UV-visible region have been presented. An optical and structural characterisation has been conducted on the selected dielectrics in order to identify the optimum high index/low index pair for low loss dielectric mirrors. In some cases, several fabrication methods have been investigated for the same material. This approach not only led to very interesting findings about the optical properties and the morphology of the investigated materials but also to some generic conclusions on specific fabrication methods. A methodology of extracting the optical constants n and k for thin film coatings based on spectral data was also proposed. Surface roughness obtained from AFM topography allowed a first estimation of potential scatter losses for single layer coatings. Using the curvature method and a bespoke stress apparatus, the internal stress of single layer thin film coatings has been calculated using Stoney's equation. Overall, the studied materials showed very low stress values.

The study of dielectric layers grown by various deposition processes has shown very mixed results and proved that the choice of suitable materials for low loss cavities is made of many technical compromises. While some materials like thermally evaporated magnesium fluoride, lithium fluoride, lanthanum titanate are transparent in the studied wavelength range and have a low refractive index, their surface roughness is not acceptable for the desired application as the scatter losses of the coating will be too high. Other materials such as zinc selenide have a very high refractive index and a low surface roughness but suffer from a very high absorption in the UV-visible wavelength range.

A good compromise between optical properties and surface roughness has been found for PIAD E-beam niobium pentoxide, P-DC sputtered tantalum pentoxide, IAD E-beam titanium dioxide and zirconium dioxide as high index dielectrics and IAD E-Beam silicon dioxide as low index dielectric. Considering the IAD E-beam deposited TiO_2/SiO_2 combination at 640 nm, a reflectance of 99.99 % is attainable for an 11-pair stack ending with a titanium dioxide layer. Other combinations such as P-DC sputtered Ta_2O_5/SiO_2, and IAD E-bean deposited ZrO_2/SiO_2 will require three extra pairs to achieve 99.99 % reflectance at the same wavelength due to a smaller contrast between the high and the low refractive indices. Nevertheless, the deposition of a full stack is still feasible within a single day of growth, with the given deposition rates and process base pressure. With a mirror reflectance of 99.99 %, we can expect a cavity finesse of around 32 000 (Equation (1.5)), which fulfils the requirements of most microcavity applications. A further experimental study will be made to determine the absorption and scatter losses for multilayer stacks and will be presented in the next chapter.

High reflectivity mirrors for microcavity applications usually call for a surface roughness between 0.2 nm and 0.3 nm in order to reduce the scatter losses[69]. However, E-beam deposited TiO_2, Ta_2O_5, ZrO_2, Nb_2O_5 and SiO_2 have a surface roughness between 1 nm and 1.5 nm. Considering a multilayer stack of a similar surface roughness, the total

estimated scatter varies between 0.02 % and 0.1 % at 640 nm wavelength, which reduces the reflectance of the multilayer stack down to 99.9 %. Consequently, the finesse of the cavity is reduced to about 3200. The scatter of the coatings can be considerably improved in this case by using superpolished substrates as previously demonstrated in [70] for E-beam evaporated Ta_2O_5/SiO_2 multilayer high reflectance coatings.

REFERENCES

[1] I. M. Reid, H. A. Macleod, E. Henderson, and M. J. Carter, "Proc International Conference on Ion Plating and Allied Techniques (IPAT 79)," in *The ion plating of optical thin films for the infrared*, London, 1979,

[2] H. A. Macleod, "Production methods and thin-film materials," in *Thin-film optical filters*: CRC Press, 2010, pp. 502-503.

[3] G. Rempe, R. J. Thompson, H. J. Kimble, and R. Lalezari, "Measurement of ultralow losses in an optical interferometer," *Opt. Lett.,* vol. 17, no. 5, pp. 363-365, 1992.

[4] J. N. Damask and H. A. Haus, "Wavelength-division multiplexing using channel-dropping filters," *Journal of Lightwave Technology,* vol. 11(3), pp. 424-428, 1993.

[5] H. A. Macleod, "Production methods and Thin-film materials," in *Thin-film optical filters*: CRC Press, 2010, pp. 508-511.

[6] H. R. Kaufman, R. S. Robinson, and R. I. Seddon, "End-Hall ion source," *Journal of Vacuum Science & Technology A,* vol. 5, no. 4, pp. 2081-2084, 1987.

[7] D. Najer *et al.*, "A gated quantum dot far in the strong-coupling regime of cavity-QED at optical frequencies," *arXiv.org,* 2018.

[8] S. Reid and I. Martin, "Development of mirror coatings for gravitational wave detectors," *Coatings,* vol. 6, no. 4, p. 61, 2016.

[9] S. K. Rajendran *et al.*, "Ultrafast dynamics of cavity polaritons in an organic semicondutor microcavity," ed, 2012, pp. 1-3.

[10] L. C. Flatten, A. A. P. Trichet, and J. M. Smith, "Spectral engineering of coupled open-access microcavities," *Laser & Photonics Reviews,* vol. 10, no. 2, pp. 257-263, 2016.

[11] R. J. Barbour *et al.*, "A tunable microcavity," *Journal of Applied Physics,* vol. 110, no. 5, p. 053107, 2011.

[12] L. Greuter *et al.*, "A small mode volume tunable microcavity: Development and characterization," *Applied Physics Letters,* vol. 105, no. 12, 2014.

[13] D. Vander-Hyde, C. Amra, M. Lequime, F. Magaña-Sandoval, J. R. Smith, and M. Zerrad, "Optical scatter of quantum noise filter cavity optics," *Classical and Quantum Gravity,* vol. 32, no. 13, p. 135019, 2015.

[14] S. Dufferwiel *et al.*, "Exciton–polaritons in van der Waals heterostructures embedded in tunable microcavities," *Nature Communications,* vol. 6, no. 1, 2015.

[15] D. M. Coles, P. Michetti, C. Clark, A. Adawi, and D. G. Lidzey, "Temperature dependence of the upper-branch polariton population in an organic semiconductor microcavity," *Phys. Rev. B,* vol. 84, no. 20, 2011.

[16] D. M. Coles *et al.*, "Vibrationally Assisted Polariton-Relaxation Processes in Strongly Coupled Organic-Semiconductor Microcavities," *Advanced Functional Materials,* vol. 21, no. 19, pp. 3691-3696, 2011.

[17] R. T. Grant *et al.*, "Efficient Radiative Pumping of Polaritons in a Strongly Coupled Microcavity by a Fluorescent Molecular Dye," 2016.

[18] S. Chao, W.-H. Wang, and C.-C. Lee, "Low-loss dielectric mirror with ion-beam-sputtered TiO2–SiO2 mixed films," *Applied Optics,* vol. 40, no. 13, pp. 2177-2182, 2001.

[19] A. Melninkaitis *et al.*, "Characterization of zirconia- and niobia-silica mixture coatings produced by ion-beam sputtering," *Applied Optics,* vol. 50, no. 9, pp. C188-C196, 2011.

[20] A. E. Ennos, "Stresses Developed in Optical Film Coatings," *Applied Optics,* vol. 5, no. 1, pp. 51-61, 1966.

[21] M. Banning, "Practical Methods of Making and Using Multilayer Filters," *Journal of the Optical Society of America,* vol. 37, no. 10, pp. 792-797, 1947/10/01 1947.

[22] R. P. Netterfield, "Refractive indices of zinc sulfide and cryolite in multilayer stacks," *Applied Optics,* vol. 15, no. 8, pp. 1969-1973, 1976.

[23] C. C. Lee, "Moisture adsorption and optical instability in thin film coatings, PhD Dissertation, University of Arizona," 1983.

[24] W. Heitmann, "Extrem hochreflektierende dielektrische Spiegelschichten mit Zincselenid Zeitschrift für Angewandte Physik," vol. 21, pp. 503–508, 1966.

[25] J. F. Hall, "Optical properties of magnesium fluoride films in the ultraviolet," *Journal of the Optical Society of America,* vol. 47, pp. 662–665, 1957.

[26] J. C. Maxwell, "On physical lines of force," *The London, Edinburgh and Dublin Philosophical Magazine and Journal of science,* vol. 4th series, no. March, April, pp. 161-175, 282-291, 338-349, 13-24, 85-95, 1861.

[27] H. A. Macleod, "Maxwell's equations and plane electromagnetic waves," in *Thin-film optical filters*: CRC Press, 2010, pp. 13-16.

[28] M. K. Trubetskov and A. V. Tikhonravov, "OptiLayer Thin film Software," ed: OptiLayer GmbH.

[29] A. V. Tikhonravov *et al.*, "Optical parameters of oxide films typically used in optical coating production," *Applied Optics,* vol. 50, no. 9, pp. C75-C85, 2011.

[30] A. V. Tikhonravov and M. K. Trubetskov, "Development of the needle optimization technique and new features of OptiLayer design software," in *International Symposium on Optical Interference Coatings*, 1994, vol. 2253: SPIE,

[31] A. V. Tikhonravov, M. K. Trubetskov, and G. W. DeBell, "Application of the needle optimization technique to the design of optical coatings," *Applied Optics,* vol. 35, no. 28, pp. 5493-5508, 1996/10/01 1996.

[32] H. R. Philipp, "Silicon Dioxide (SiO2) (Glass)," in *Handbook of Optical Constants of Solids*, E. D. Palik Ed. Boston: Academic Press, 1985, pp. 749-763.

[33] D. Gibson, J. Martin, F. Placido, and D. Child, "Magnetron sputtering system for small batch high throughput production," in *55th Annual Technical Conference Proceedings*, Santa Clara, CA, USA, 2012: Society of Vacuum Coaters,

[34] E. D. Palik and W. R. Hunter, "Lithium Fluoride (LiF)," in *Handbook of Optical Constants of Solids*, E. D. Palik Ed. Boston: Academic Press, 1985, pp. 675-693.

[35] M. J. Dodge, "Refractive properties of magnesium fluoride," *Applied Optics,* vol. 23, no. 12, pp. 1980-1985, 1984.

[36] H. K. Pulker and C. Zaminer, "Composition and structure of vapour-deposited cryolite films," *Thin Solid Films,* vol. 5, no. 5, pp. 421-428, 1970.

[37] D. L. Wood and K. Nassau, "Refractive index of cubic zirconia stabilized with yttria," *Applied Optics,* vol. 21, no. 16, pp. 2978-2981, 1982.

[38] E. Ritter, "Optical film materials and their applications," *Applied Optics,* vol. 15, no. 10, pp. 2318-2327, 1976.

[39] D. Gibson, J. Martin, F. Placido, D. E. D. T. M. Childs, and D. Ristau, "Small Batch High Throughput Plasma Activated Magnetron Sputtering System," in *Optical Interference Coatings*, Whistler, 2013/06/16 2013: Optical Society of America, in OSA Technical Digest (online), p. ThB.8

[40] D. L. Wood, K. Nassau, T. Y. Kometani, and D. L. Nash, "Optical properties of cubic hafnia stabilized with yttria," *Applied Optics,* vol. 29, no. 4, pp. 604-607, 1990.

[41] C. A. Klein, "Room-temperature dispersion equations for cubic zinc sulfide," *Applied Optics,* vol. 25, no. 12, pp. 1873-1875, 1986.

[42] B. Tatian, "Fitting refractive-index data with the Sellmeier dispersion formula," *Applied Optics,* vol. 23, no. 24, pp. 4477-4485, 1984.

[43] D. Kurbatov, A. Opanasyuk, and H. Khlyap, "Substrate-temperature effect on the microstructural and optical properties of ZnS thin films obtained by close-spaced vacuum sublimation," *physica status solidi (a),* vol. 206, no. 7, pp. 1549-1557, 2009.

[44] J. Bellum, E. Field, D. Kletecka, and L. Finis, "Reactive ion-assisted deposition of e-beam evaporated titanium for high refractive index TiO2 layers and laser damage resistant, broad bandwidth, high-.(Report)," *Applied Optics,* vol. 53, no. 4, p. A205, 2014.

[45] K. Zhang, R. E. D. T. M. Faber, and D. Ristau, "Plasma assisted pulsed DC magnetron sputtering system for optical thin film coatings," in *Optical Interference Coatings*, Whistler, 2013: Optical Society of America, in OSA Technical Digest (online), p. ThB.6

[46] O. D. Vol'pyan, P. P. Yakovlev, B. B. Meshkov, and Y. A. Obod, "Optical properties of Ta2O5 films obtained by reactive magnetron sputtering," *J. Opt. Technol.,* vol. 70, no. 9, pp. 669-672, 2003.

[47] G. Hass and J. B. Ramsey, "Vacuum deposition of dielectric and semiconductor films by a CO2 lLaser," *Applied Optics,* vol. 8, no. 6, pp. 1115-1118, 1969.

[48] S. Chaliha, M. N. Borah, P. C. Sarmah, and A. Rahman, "Effect of substrate temperature on structural properties of thermally evaporated ZnSe thin films of different thickness.," *Journal of Physics: Conference Series,* vol. 114, no. 1, 2008.

[49] J. R. DeVore, "Refractive indices of rutile and sphalerite," *Journal of the Optical Society of America,* vol. 41, no. 6, pp. 416-419, 1951.

[50] A. A. Maradudin, *Light scattering and nanoscale surface roughness*. New York: New York : Springer, 2007.

[51] S. Schröder, A. Duparré, L. Coriand, A. Tünnermann, D. H. Penalver, and J. E. Harvey, "Modeling of light scattering in different regimes of surface roughness," *Opt. Express,* vol. 19, no. 10, p. 9820, 2011.

[52] P. Beckmann and A. Spizzichino, *The scattering of electromagnetic waves from rough surfaces*. Pergamon Press: Oxford; printed in Poland (in English), 1963.

[53] J. M. Elson, J. P. Rahn, and J. M. Bennett, "Relationship of the total integrated scattering from multilayer-coated optics to angle of incidence, polarization, correlation length, and roughness cross-correlation properties," *Applied Optics,* vol. 22, no. 20, pp. 3207-3219, 1983.

[54] D. Nečas and P. Klapetek, "Gwyddion, Free SPM data analysis software," ed.

[55] G. Dennler, A. Houdayer, P. Raynaud, I. Seguy, Y. Segui, and M. Wertheimer, "Growth modes of SiOx films deposited by evaporation and plasma-enhanced chemical vapor deposition on polymeric substrates," *Plasmas And Polymers,* vol. 8, no. 1, pp. 43-59, 2003.

[56] A. Baskaran and P. Smereka, "Mechanisms of Stranski-Krastanov growth," *Journal of Applied Physics,* vol. 111, no. 4, 2012.

[57] E. Alfonso, J. Olaya, and G. Cubillos, "Thin Film Growth Through Sputtering Technique and Its Applications," in *Crystallization - Science and Technology*, 2012.

[58] M. R. A. Bhuiyan, A. H. Miah, and J. Begum, *Substrate Temperature Effect on the Structural and Optical Properties of ZnSe Thin Films*. 2012, pp. 233-240.

[59] A. Kathalingam, T. Mahalingam, and C. Sanjeeviraja, "Optical and structural study of electrodeposited zinc selenide thin films.," *Materials Chemistry and Physics,* vol. 106, no. 2, pp. 215-221, 2007.

[60] V. Mittal, N. P. Sessions, J. S. Wilkinson, and G. S. Murugan, "Optical quality ZnSe films and low loss waveguides on Si substrates for mid-infrared applications," *Opt. Mater. Express,* vol. 7, no. 3, pp. 712-725, 2017.

[61] M. Özkan, N. Ekem, M. Z. Balbag, and S. Pat, "ZnSe nanocrystalline thin films deposition on Si substrate by thermionic vacuum arc," *Proceedings of the Institution of Mechanical Engineers, Part L: Journal of Materials: Design and Applications,* vol. 226, no. 2, pp. 103-108, 2012.

[62] G. G. Stoney, "The Tension of Metallic Films Deposited by Electrolysis," *Proceedings of the Royal Society of London. Series A, Containing Papers of a Mathematical and Physical Character (1905-1934),* vol. 82, no. 553, pp. 172-175, 1909.

[63] G. C. A. M. Janssen, M. M. Abdalla, F. van Keulen, B. R. Pujada, and B. van Venrooy, "Celebrating the 100th anniversary of the Stoney equation for film stress: Developments from polycrystalline steel strips to single crystal silicon wafers," *Thin Solid Films,* vol. 517, no. 6, pp. 1858-1867, 2009.

[64] J. J. Wortman and R. A. Evans, "Young's Modulus, Shear Modulus, and Poisson's Ratio in Silicon and Germanium," *Journal of Applied Physics,* vol. 36, no. 1, pp. 153-156, 1965.

[65] Y. Pauleau, "Generation and evolution of residual stresses in physical vapour-deposited thin films," *Vacuum,* vol. 61, no. 2, pp. 175-181, 2001.

[66] M. Fang, D. Hu, and J. Shao, "Evolution of stress in evaporated silicon dioxide thin films," *Chin. Opt. Lett.,* vol. 8, no. 1, pp. 119-122, 2010.

[67] C. A. Davis, "A simple model for the formation of compressive stress in thin films by ion bombardment," *Thin Solid Films,* vol. 226, no. 1, pp. 30-34, 1993.

[68] H. Windischmann, "Intrinsic stress in sputter-deposited thin films," *Critical Reviews in Solid State and Materials Sciences,* vol. 17, no. 6, pp. 547-596, 1992.

[69] T. Klaassen, M. P. van Exter, and J. P. Woerdman, "Characterization of scattering in an optical Fabry-Perot resonator," *Applied optics,* vol. 46, no. 22, p. 5210, 2007.

[70] S. E. Watkins, J. P. Black, and B. J. Pond, "Optical scatter characteristics of high-reflectance dielectric coatings and fused-silica substrates," *Applied Optics,* vol. 32, no. 28, pp. 5511-5518, 1993.

CHAPTER 3–ASSESMENT OF PLANAR MULTILAYER HIGH REFLECTANCE MIRRORS

The optical and structural characterisation of high reflectance mirrors designed at a reference wavelength of 640 nm is described in this chapter. The optical performances of planar mirrors are estimated with the aid of proprietary thin film analysis software. High index/low index quarterwave combinations such as TiO_2/SiO_2, ZrO_2/SiO_2 and Nb_2O_5/SiO_2 are presented. High reflectance mirrors were deposited using IAD E-beam evaporation, microwave assisted magnetron sputtering and plasma assisted DC magnetron sputtering. Transmittance, reflectance and optical losses of the mirrors were measured using optical spectrometry. The coating roughness was measured using atomic force microscopy. Total integrated scattering and laser-induced damage study are presented for IAD E-beam TiO_2/SiO_2, Plasmacoat ZrO_2/SiO_2 and Nb_2O_5/SiO_2 and Microdyn Nb_2O_5/SiO_2 mirrors.

The content of this chapter is partially adapted from:

Najwa Sidqi, Caspar Clark, Gerald S. Buller, "High reflectance mirrors for micro-cavity applications", SPIE Optics and Photonics, San Diego, August 2019

3.1 Design of high reflectance dielectric mirrors

3.1.1 Calculation method

Before designing a high reflectance mirror, it is necessary to establish several key parameters such as the coating materials, the substrate material, the required centre wavelength of the filter, the design type and the target reflectance specification. Knowledge of the coating materials and the substrate's optical constants at the reference wavelength is usually required. A suitable design for high reflectance mirrors required for the application was conceived based on the specifications indicated in Table 3-1. The proposed design was based on quarterwave dielectric Bragg reflector stack composed of alternating high index and low index materials grown on a glass substrate. The target reflectance value was ≥ 99.99 % at a centre wavelength of 640 nm.

Optical coating	Substrate Material	Design type	Centre wavelength	Coating Material	Reflectance
High reflectance mirror	Glass substrate (Microscope slide, Fused Silica, Quartz)	Quarterwave Bragg reflector	640 nm	Dielectric coating composed of high and low index materials	>99.99 %

***Table 3-1**: Specification table for a high reflectance mirror to be designed at a centre wavelength of 640 nm.*

The design of high reflectance mirrors was performed using Essential Macleod software provided by Thin Film Center[1]. Essential Macleod is a program allowing the design and the calculation of optical performances of optical structures composed of thin film multilayer stacks. This interface allows creating a design for high reflectance mirrors according to the given specifications. The reference wavelength determines the refractive index and the extinction coefficient of the studied materials. The material physical thicknesses are calculated from the product of the optical thickness of the coating by the reference wavelength divided by the refractive index. High reflectance mirrors were designed using the formula tool described in Figure 3.1. High and low index materials are entered in the window using H and L symbols. For example, $(HL)^5$ H formula creates a 5-pair TiO_2/SiO_2 with an additional TiO_2 top layer in contact with the incident light.

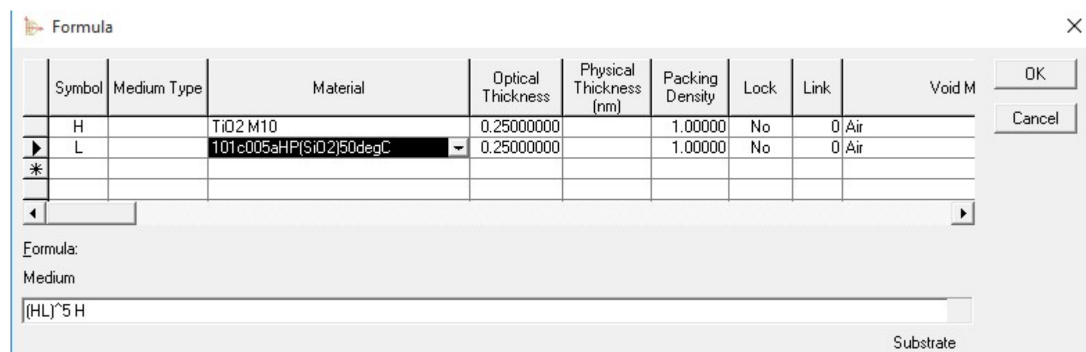

Figure 3.1: *Formula window allowing the repetition of material layers according to a given design.* $(HL)^5$ *H formula creates a 5-pair* TiO_2/SiO_2 *with an additional* TiO_2 *top layer in contact with the incident light.*

The mirrors' transmittance and reflectance were calculated and plotted using the Performance menu of Essential Macleod. The wavelength range was set from 500 nm to 1000 nm.

3.1.2 Reflectance, transmittance and absorptance calculation

A higher reflectance is achieved for a multilayer mirror by increasing the number of quarterwave layers. However, the order of high index and low index layers in the mirror design influences the reflectance magnitude. Reflectance spectra of IAD E-beam TiO_2/SiO_2 coating calculated at a reference wavelength of 640 nm using $(HL)^{14}$ H and $(LH)^{14}$ L formulae are presented in Figure 3.2. The $(HL)^{14}$ H formula gives a 14-pair stack with high index layers placed outermost of the stack while $(LH)^{14}$ L formula gives 14-pair stack with low index layers placed outermost. In Figure 3.2.b, a maximum reflectance of 99.9975 % is obtained at 640 nm for $(LH)^{14}$ L design formula against a reflectance of 99.9995 % at the same wavelength for $(HL)^{14}$ H design formula. A reflectance difference of 0.002 % between the two coating designs is very significant to Fabry-Perot cavities as the finesse can be increased by several order of magnitudes. The mirror reflectance curve also appears broader using the $(HL)^{14}$ H design formula.

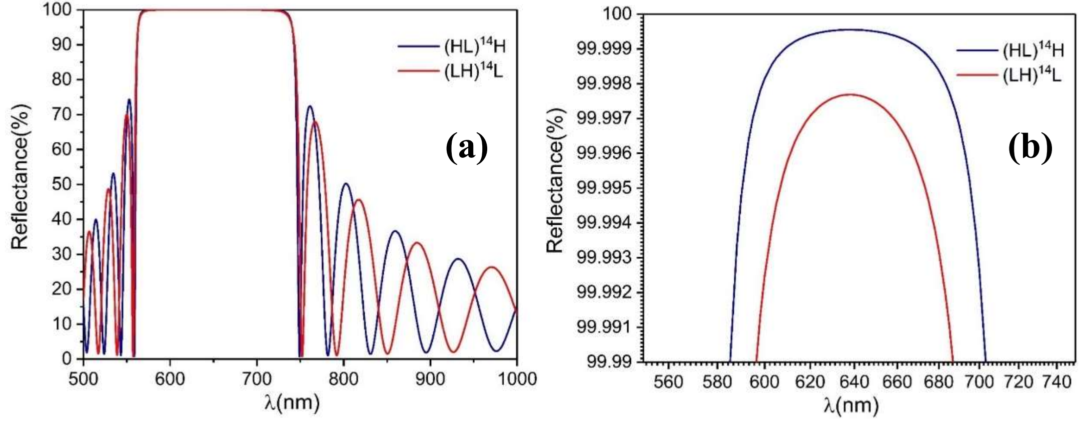

Figure 3.2: *(a) Computed reflectance at a reference wavelength of 640 nm using the optical constants of IAD E-beam evaporated TiO_2 and SiO_2 for two designs. The blue line curve represents reflectance magnitude calculated using $(HL)^{14}H$ formula with high index layers outermost. The red line curve represents reflectance magnitude calculated using $(LH)^{14}L$ formula with low index layers outermost. (b) Zoomed vertical and wavelength axis for IAD E-beam TiO_2/SiO_2 reflectance for $(HL)^{14}H$ and $(LH)^{14}L$ designs.*

With high index layers being at the outermost of the coating, the reflectance of the multilayer quarterwave stack is expressed in Equation (3.1)[2]:

$$R = \left[\frac{1 - \dfrac{n_{\mathrm{H}}^{2p+2}}{n_{\mathrm{L}}^{2p}.n_{\mathrm{sub}}}}{1 + \dfrac{n_{\mathrm{H}}^{2p+2}}{n_{\mathrm{L}}^{2p}.n_{\mathrm{sub}}}} \right]^2 \qquad (3.1)$$

Where n_{sub} is the refractive index of the substrate, n_{H} the high index, n_{L} the low index and 2p+1 the number of layers in the stack.

Transmittance is also reduced by an order of magnitude for IAD E-beam TiO_2/SiO_2 mirror when placing high index layers outermost (Figure 3.3). The transmittance for a 14-pair stack with high index layers outermost ($(HL)^{14}$ H) is approximately equal to 4×10^{-4} at 640 nm and to 3×10^{-3} at the same wavelength with low index layers outermost ($(LH)^{14}$ L).

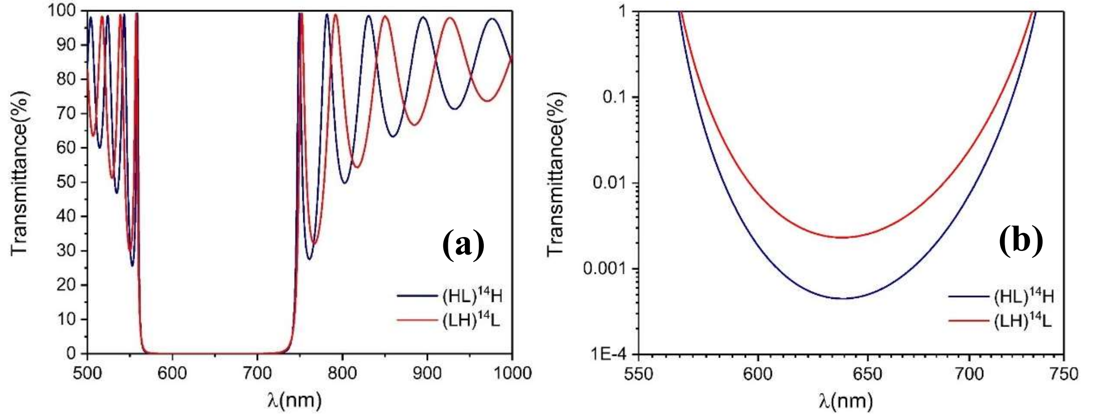

Figure 3.3: *(a) Computed transmittance at a reference wavelength of 640 nm using the optical constants of IAD E-beam evaporated TiO_2 and SiO_2 for two designs. The blue line curve represents reflectance magnitude calculated using $(HL)^{14}H$ formula with high index layers outermost. The red line curve represents transmittance magnitude calculated using $(LH)^{14}L$ formula with low index layers outermost. (b) Zoomed vertical and wavelength axis for TiO_2/SiO_2 IAD E-beam evaporated transmittance for $(HL)^{14}H$ and $(LH)^{14}L$ designs.*

The absorptance of multilayer mirrors can be calculated using the concept of potential transmittance introduced by Hemingway and Lissberger in 1973[3](See section 1.4.2, Chapter 1). The absorptance of the stack is reminded in the following:

For high index layers outermost, the multilayer absorptance can be written as:

$$A = \frac{2\pi n_0 \left(k_{\mathrm{H}} + k_{\mathrm{L}}\right)}{n_{\mathrm{H}}^2 - n_{\mathrm{L}}^2} \qquad (3.2)$$

Where n_0 is the medium refractive index, which is air in this case (n_0 =1).

The absorptance can be expressed in the same manner for a multilayer mirror ending with a low index material. The final low index layer will reduce the reflectance and consequently increase the absorptance:

$$A = \frac{2\pi}{n_0} \frac{n_{\mathrm{L}}^2 k_{\mathrm{H}} + n_{\mathrm{H}}^2 k_{\mathrm{L}}}{n_{\mathrm{H}}^2 - n_{\mathrm{L}}^2} \qquad (3.3)$$

A calculation example using the optical constants of niobium pentoxide and silicon dioxide deposited using plasma assisted DC magnetron (Plasmacoat) is provided in Figure 3.4. Absorption losses are calculated for a 10-pair quarterwave stack for high index($(HL)^{10}$ H) and low index layers ($(LH)^{10}$ L) outermost. The absorptance is roughly 0.1 % at 640 nm for low index layers outermost and of 0.02 % for high index layers outermost.

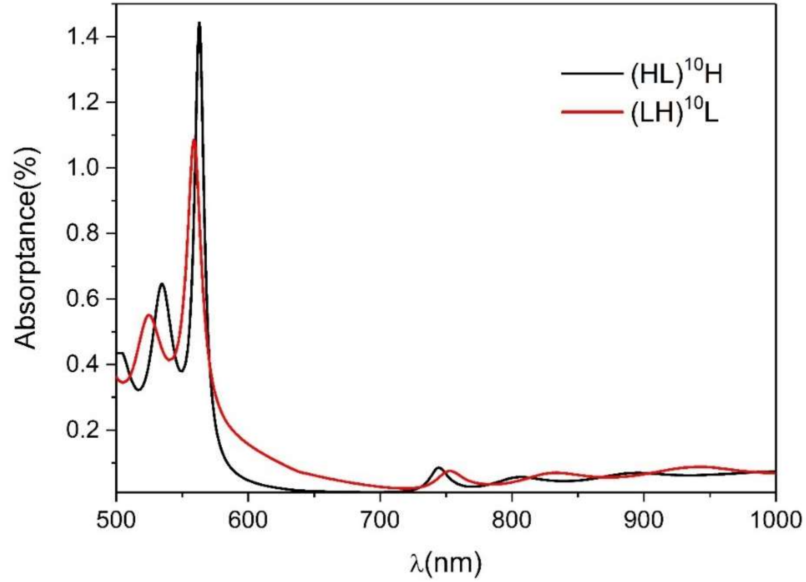

Figure 3.4: *Simulated absorptance for Nb_2O_5/SiO_2 deposited using Plasmacoat system. The black line curve represents absorptance magnitude calculated using $(HL)^{10}$ H formula where the high index layers are outermost. The red line curve represents absorptance calculated for $(LH)^{10}$ L structure where the low index layers are outermost.*

The bandwidth of the mirror stopband Δg depends only on the refractive index contrast between the high index layer and the low index layer as expressed in the following equation:

$$\Delta g = \frac{4}{\pi}\arcsin\left(\frac{n_{\mathrm{H}} - n_{\mathrm{L}}}{n_{\mathrm{H}} + n_{\mathrm{L}}}\right) \qquad (3.4)$$

Figure 3.5 shows the calculated reflectance spectra for 14-pair stacks ending with high index layers outermost, based on fitted optical constants presented in Chapter 2. A reflectance above 99.99 % is expected using the proposed stack design for the studied dielectric materials combinations. The purple line curve representing simulated reflectance for Nb_2O_5/SiO_2 mirror deposited using microwave assisted magnetron sputtering (Microdyn) has the broadest bandwidth (around 220 nm) due to a higher contrast between the low and the high index materials ($n_{\mathrm{H}} = 2.36$ and $n_{\mathrm{L}} = 1.45$ at 640 nm). By contrast, ZrO_2/SiO_2 mirror deposited by plasma assisted DC magnetron sputtering (Plasmacoat) have the narrowest bandwidth (150 nm approximately) because of the low contrast between the zirconia index ($n_{\mathrm{H}} = 2.15$) and the silica index ($n_{\mathrm{L}} = 1.47$).

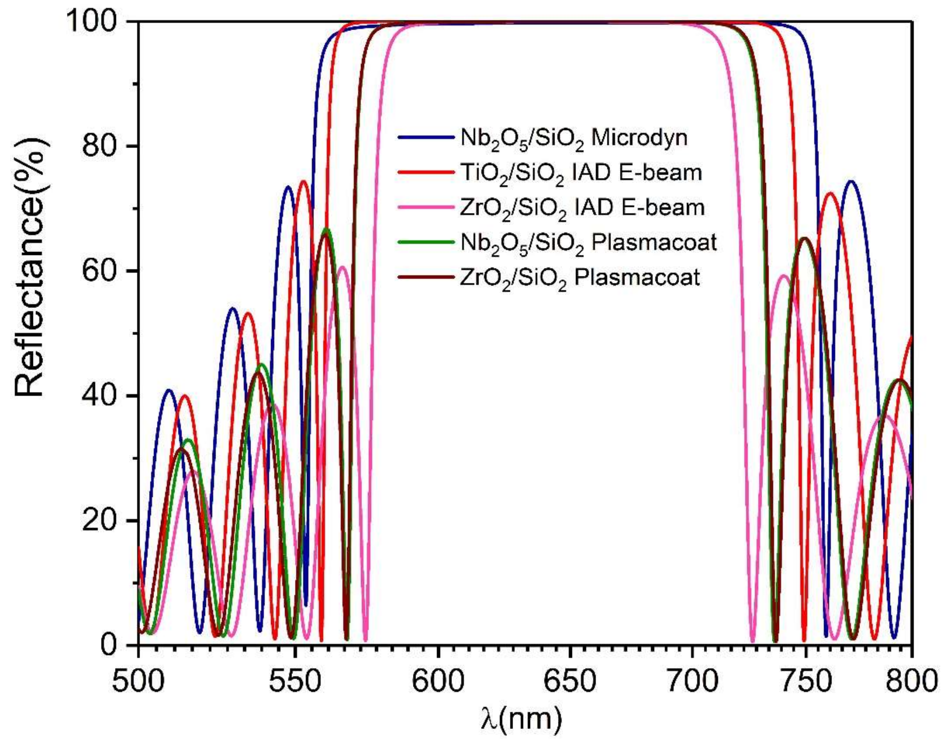

Figure 3.5: *Simulated reflectance spectra using Essential Macleod for several dielectric mirrors using optical constants data of single layer coatings presented in Chapter 2. The filters design is $(HL)^{14}H$ where high index layers are outermost of the coating. The reference wavelength is 640 nm. The purple line curve representing simulated reflectance for Microdyn Nb_2O_5/SiO_2 mirror has the largest bandwidth of the coatings due to a higher contrast between the Microdyn niobia and silica layers.*

3.2 Planar mirrors fabrication methods

Multilayer dielectric mirrors were deposited using IAD E-beam, plasma assisted DC magnetron sputtering (Plasmacoat) and microwave assisted magnetron sputtering (Microdyn). The process parameters and experimental plan are presented in Sections 3.2.1 to 3.2.3.

3.2.1 IAD E-beam

ZrO_2/SiO_2 and TiO_2/SiO_2 multilayer mirrors were deposited using IAD E-beam on Corning™ 2947-75×25 plain 1 mm thick microscope slides made from soda lime glass. Dielectric materials were evaporated from source materials of 99.99 % purity provided by Scotech limited. Process conditions are summarised in Table 3-2. Sample designs and optical constants of high index and low index layers at 640 nm are provided in Table 3-3. At 640 nm wavelength, the quarterwave thicknesses of SiO_2, TiO_2 and ZrO_2 are of 108 nm, 78 nm and 70 nm respectively.

Material	Source material	Process Pressure (mbar)	Deposition rate (Å/s)	Backfill gas (sccm)	Substrate Heating(°C)
TiO_2	TiO_2 pellets	1.8×10^{-4}	1	O_2: 35	110
ZrO_2	Zr tablets	1.7×10^{-4}	2	O_2: 50	110
SiO_2	SiO_2 pellets	9.6×10^{-5}	2	none	110

Table 3-2: *Deposition parameters of TiO_2, SiO_2 and ZrO_2 by IAD E-beam evaporation used for high reflectance mirrors.*

Sample design	Number of layers	n_H (640 nm)	n_L (640 nm)	k_H (640 nm)	k_L (640 nm)
$(HL)^5$ H	11				
$(HL)^{10}$ H	21	TiO_2: 2.31	1.48	TiO_2: $<10^{-5}$	$<10^{-5}$
$(HL)^{14}$ H	29	ZrO_2: 2.05		ZrO_2: $<10^{-5}$	
$(HL)^{15}$ H	31				

Table 3-3: *IAD E-beam coating designs and optical constants of TiO_2, ZrO_2 and SiO_2 at 640 nm.*

Reflectance and transmittance of IAD E-beam ZrO_2/SiO_2 and TiO_2/SiO_2 mirrors centred at 640 nm reference wavelength were calculated for coating designs presented in Table 3-3 using Essential Macleod software. Simulated spectra are presented in Figures 3.6 and 3.7.

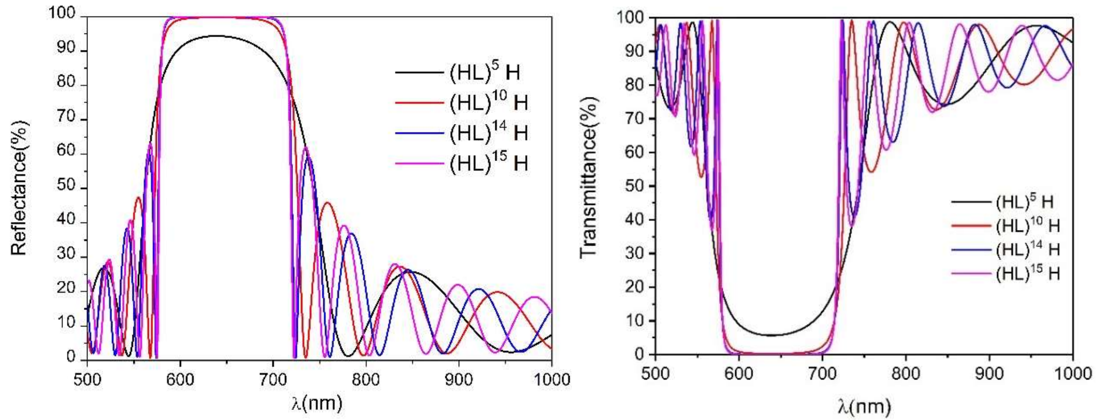

Figure 3.6: *Simulated reflectance and transmittance spectra at 640 nm for IAD E-beam ZrO_2/SiO_2 with increasing coating pairs.*

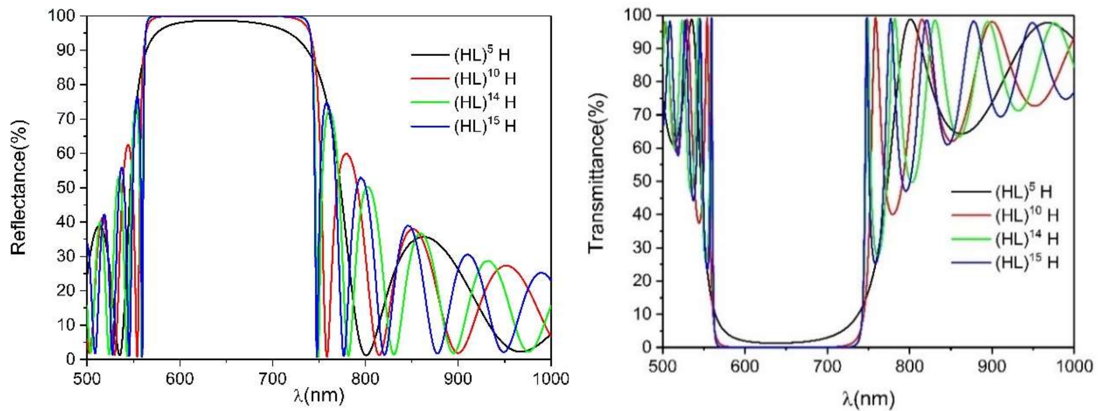

Figure 3.7: *Simulated reflectance and transmittance spectra at 640 nm for IAD E-beam TiO_2/SiO_2 with increasing coating pairs.*

3.2.2 Plasma assisted DC magnetron sputtering

ZrO_2/SiO_2 and Nb_2O_5/SiO_2 multilayer mirrors were deposited using plasma assisted magnetron sputtering system (Plasmacoat system at the University of the West of Scotland) on 20 mm diameter circular fused silica JGS-1 substrates provided by Changchun Qianhao Photoelectric Co Ltd.. The coatings are sputtered from source materials of 99.99 % purity sources. Process conditions are summarised in Table 3-4. Sample designs and optical constants of high index and low index layers at 640 nm wavelength are provided in Table 3-5. The quarterwave thickness of SiO_2 at 640 nm is of 109 nm and of 75 nm for Nb_2O_5 and ZrO_2 at the same wavelength.

Material	Source material	Process pressure(mbar)	Deposition rate(nm/s)	Process gas (sccm)	Magnetron /Plasma Powers(W)
Nb_2O_5	Nb metal target		0.05	Ar: 17 / O_2: 18	900/100
ZrO_2	Zr metal target	$\approx 5\times10^{-3}$	0.56	Ar: 17 / O_2: 8	900/100
SiO_2	Si metal target		0.52	Ar: 20 /O_2: 8	1000/80

Table 3-4: *Deposition parameters of Nb_2O_5, SiO_2 and ZrO_2 by Plasma assisted DC magnetron sputtering*

Sample design	Number of layers	n_H (640 nm)	n_L (640 nm)	k_H (640 nm)	k_L (640 nm)
$(HL)^5$ H	11				
$(HL)^9$ H	19	Nb_2O_5: 2.16	1.47	Nb_2O_5: 4×10^{-5}	6.10^{-5}
$(HL)^{12}$ H	25	ZrO_2: 2.15		ZrO_2: $<10^{-5}$	
$(HL)^{14}$ H	29				

Table 3-5: *Plasmacoat coating designs and optical constants of Nb_2O_5, SiO_2 and ZrO_2 at 640 nm.*

Reflectance and transmittance for Plasmacoat ZrO_2/SiO_2 and Nb_2O_5/SiO_2 mirrors were calculated using Essential Macleod at 640 nm reference wavelength for designs indicated in Table 3-5. Simulation results are presented in Figures 3.8 and 3.9.

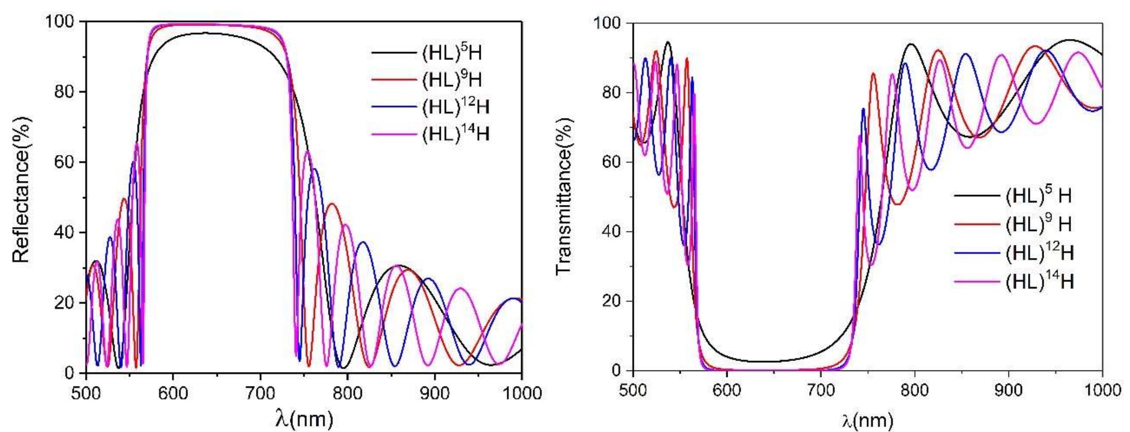

Figure 3.8: *Simulated reflectance and transmittance spectra at 640 nm for Plasmacoat ZrO_2/SiO_2 with increasing coating pairs.*

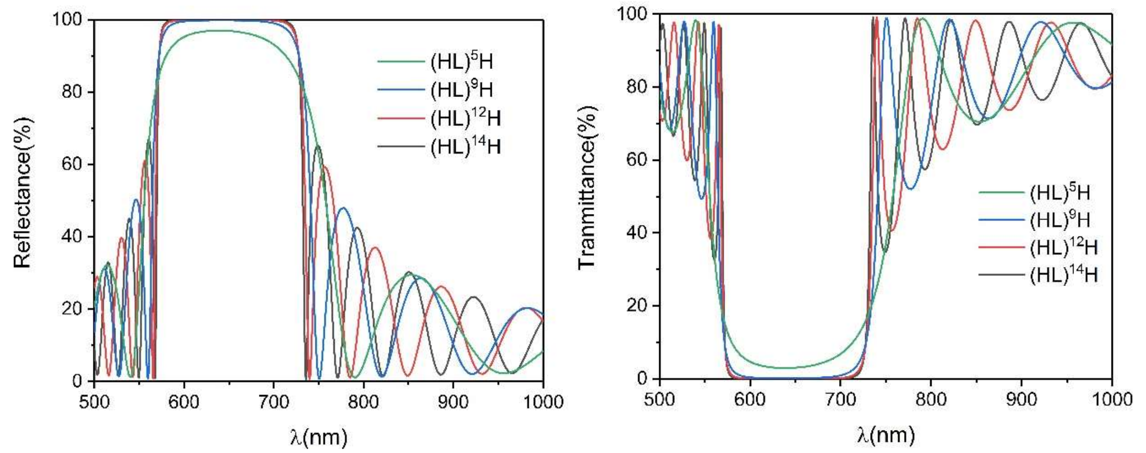

Figure 3.9: *Simulated reflectance and transmittance spectra at 640 nm for Plasmacoat Nb_2O_5/SiO_2 with increasing coating pairs.*

3.2.3 Microwave plasma assisted magnetron sputtering

Nb_2O_5/SiO_2 multilayer mirror was deposited using microwave assisted magnetron sputtering (Microdyn system at the University of the West of Scotland) on 20 mm diameter circular fused silica JGS-1 substrates provided by Changchun Qianhao Photoelectric Co Ltd. Process conditions are summarised in Table 3-6. The mirror design and optical constants of niobia and silica at 640 nm are provided in Table 3-7. At a wavelength of 640 nm, the quarterwave thicknesses of SiO_2 and Nb_2O_5 are of 111 nm and 68 nm respectively. Reflectance and transmittance calculated at 640 nm using Essential Macleod for a 14-pair stack are presented in Figure 3.13.

Material	Source material	Process Pressure(mbar)	Deposition rate(Å/s)	Process Gas (sccm)	Plasma Power(kW)
Nb_2O_5	Nb metal target	10^{-3}	1.8	Ar:120/O_2:71	900/100
SiO_2	Si metal target	7×10^{-4}	1.1	Ar:120/O_2:50	1000/80

Table 3-6: *Deposition parameters of Nb_2O_5 and SiO_2 by microwave assisted magnetron sputtering.*

Sample design	Number of layers	n_H (640 nm)	n_L (640 nm)	k_H (640 nm)	k_L (640 nm)
$(HL)^{14}$ H	29	2.36	1.45	$<10^{-5}$	10^{-3}

Table 3-7: *Microdyn coating design and optical constants of Nb_2O_5 and SiO_2 at 640 nm.*

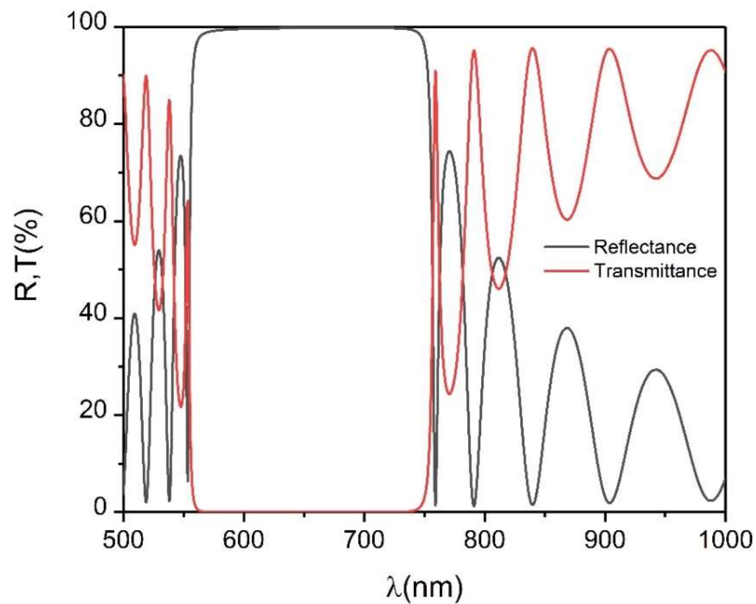

Figure 3.10: *Simulated reflectance and transmittance spectra for a $(HL)^{14}H$ Nb_2O_5/SiO_2 using optical constants from Nb_2O_5 and SiO_2 coatings deposited using Microdyn system.*

3.3 Optical characterisation

3.3.1 Reflectance and transmission measurements

Reflectance and transmittance measurements were performed using a Perkin Elmer Lambda 900 spectrophotometer. Reflectance was measured at near normal incidence using a relative method[4]. A background correction was performed using two high reflectance glass IR gold standard mirrors (R > 99 % beyond 600 nm). The gold mirrors were first placed on a 6 ° reflectance accessory stage to acquire a 0 % and 100 % reflectance baseline. One of the gold mirrors was afterwards replaced by the sample to be measured. The reflectance scans were performed from 2200 nm to 350 nm. Transmittance was measured at normal incidence from 2200 nm to 350 nm after a 0 % and 100 % transmittance baseline correction. Reflectance and transmittance measurements for high reflectance mirrors are presented in graphs from Figure 3.11 to Figure 3.15.

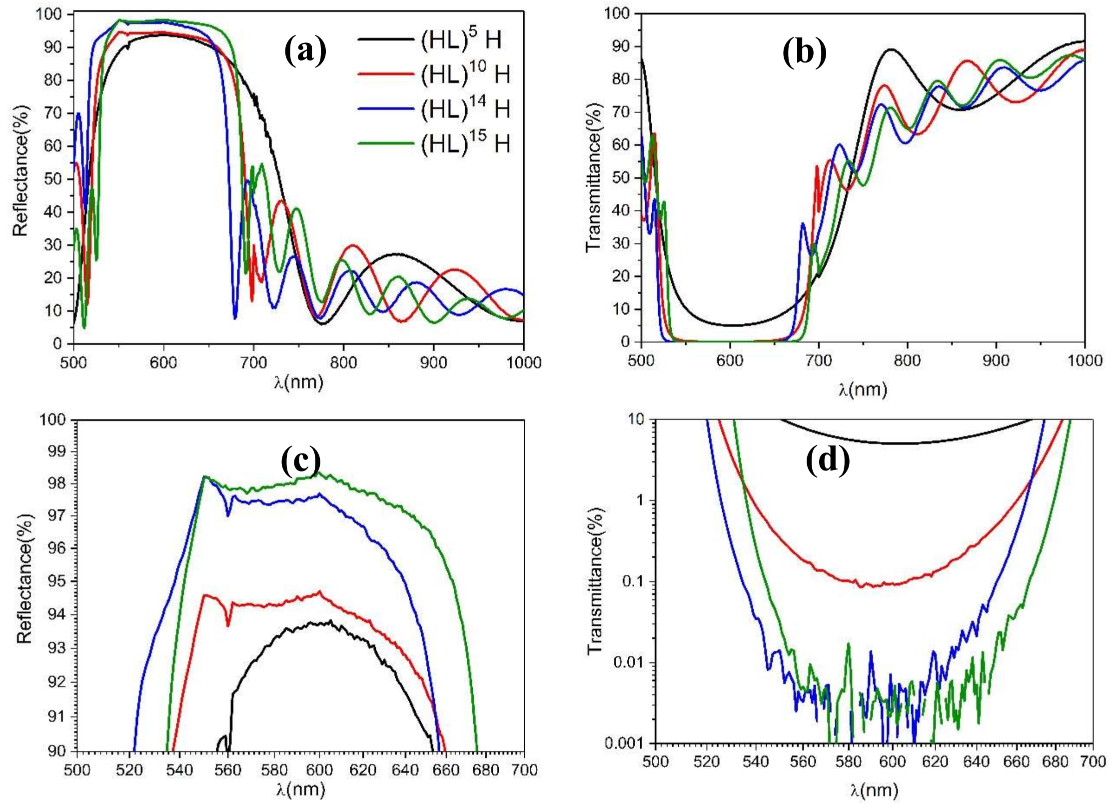

Figure 3.11: *(a) Measured reflectance and (b) transmittance spectra for IAD E-beam ZrO_2/SiO_2 with various coating pairs. (c) Zoomed reflectance and (d) transmittance are presented around the centre wavelength.*

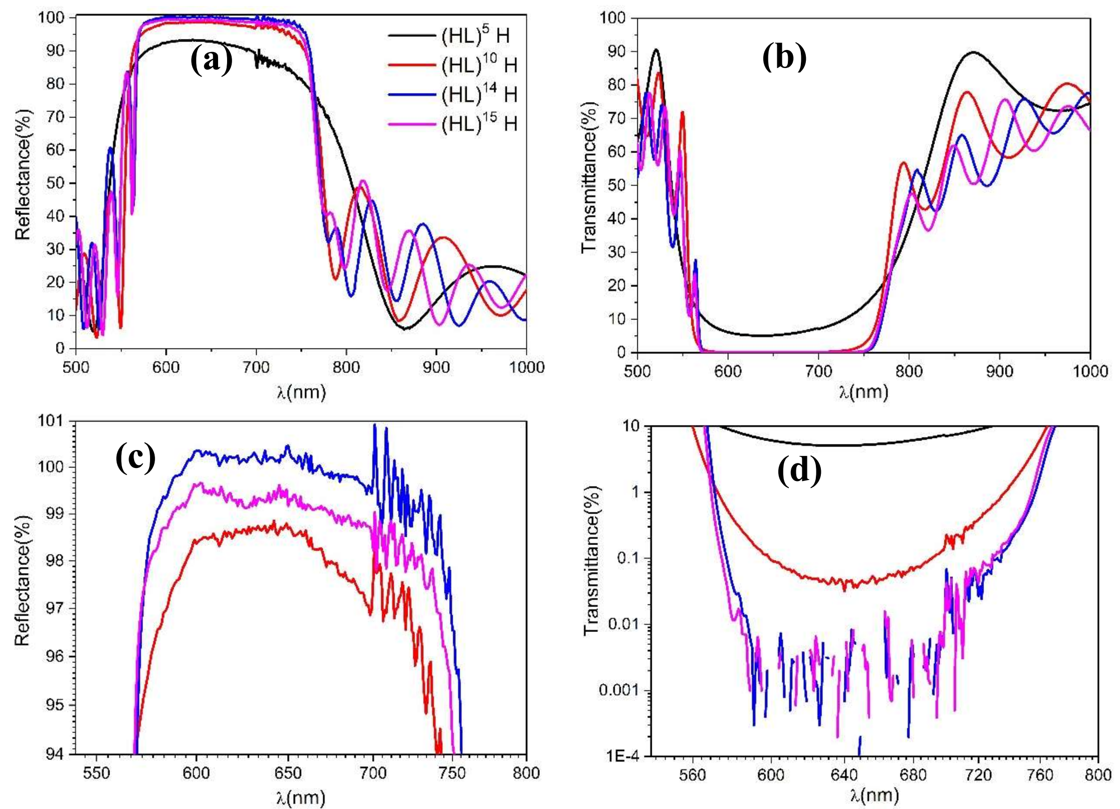

Figure 3.12: *(a) Measured reflectance and (b) transmittance spectra for IAD E-beam TiO_2/SiO_2 with various coating pairs. (c) Zoomed reflectance and (d) transmittance are presented around the centre wavelength.*

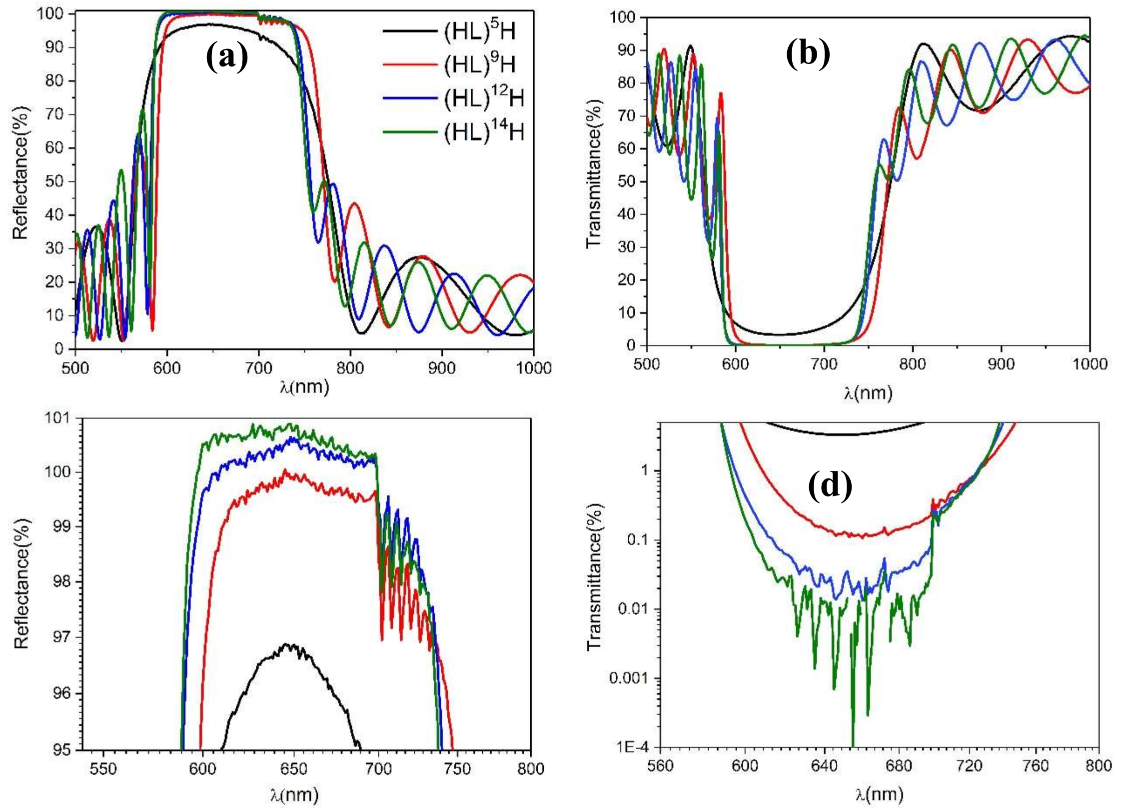

Figure 3.13: *(a) Measured reflectance and (b) transmittance spectra for Plasmacoat ZrO_2/SiO_2 with increasing coating pairs. (c) Zoomed reflectance and (d) transmittance are presented around the centre wavelength.*

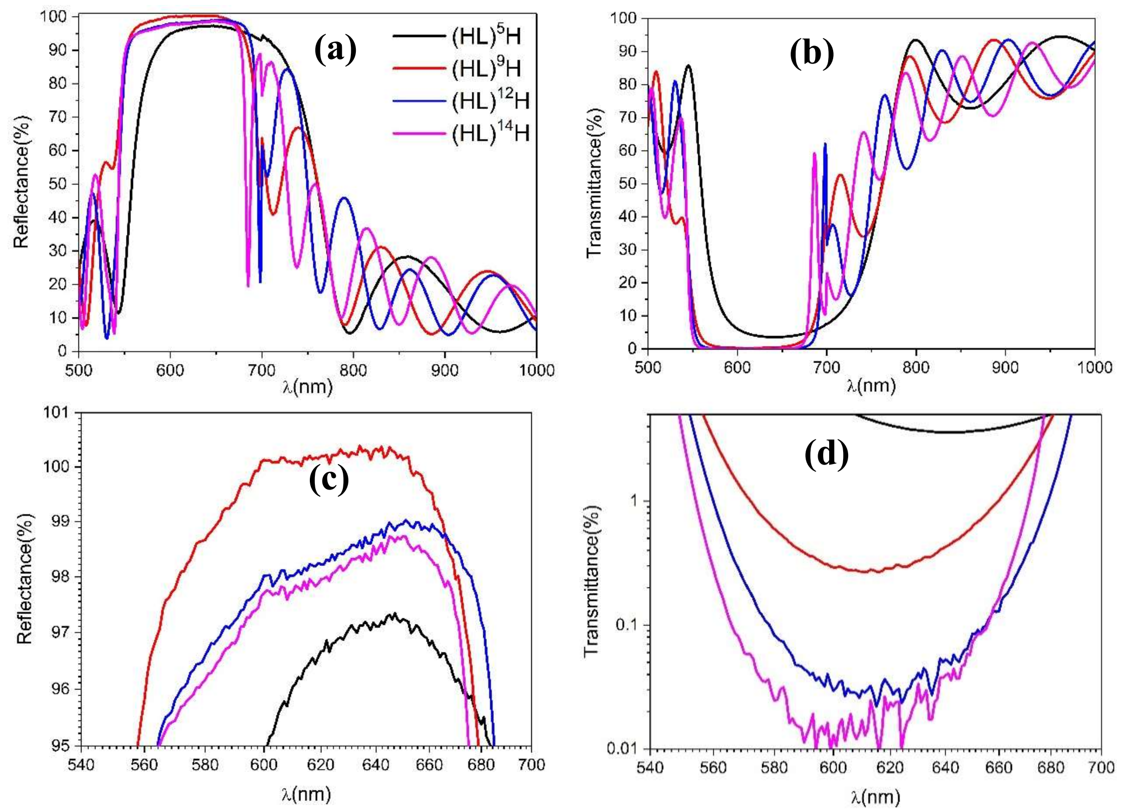

Figure 3.14: *(a) Measured reflectance and (b)transmittance spectra for Plasmacoat Nb_2O_5/SiO_2 with increasing coating pairs. (c) Zoomed reflectance and (d) transmittance around the centre wavelength.*

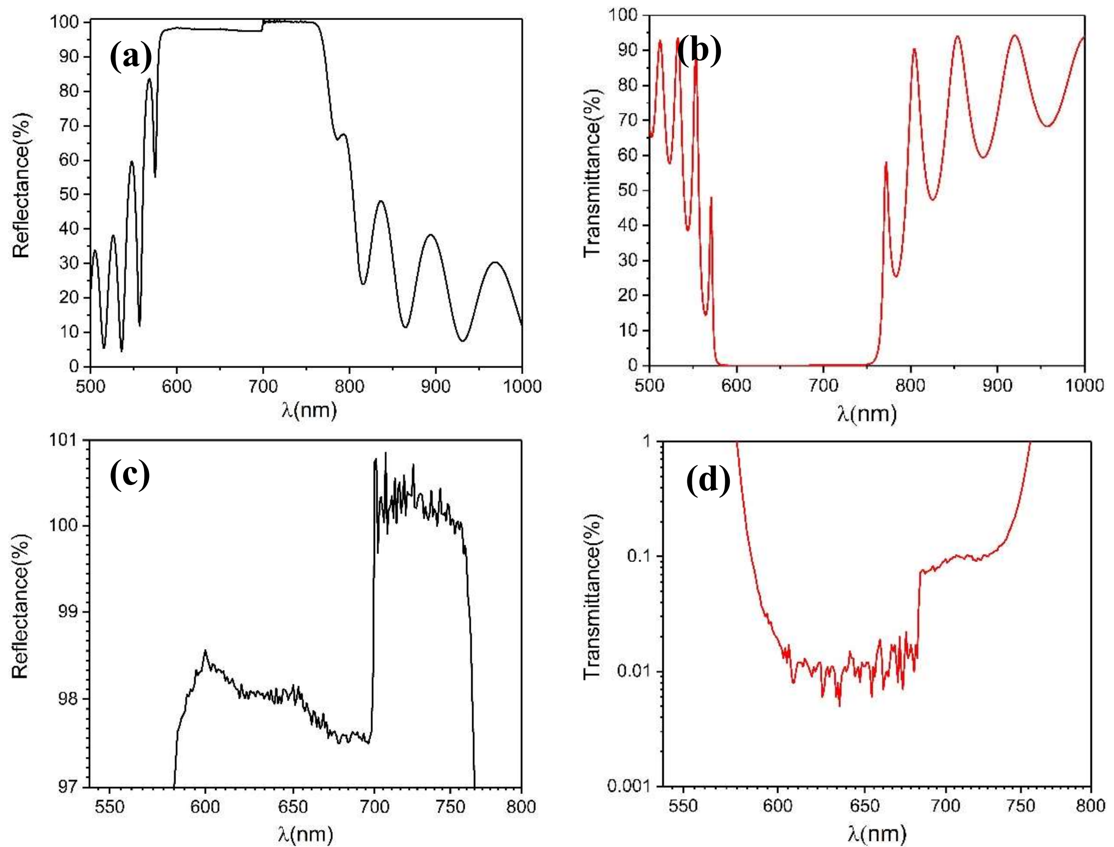

Figure 3.15: *(a) Measured reflectance and (b) transmittance spectra for $HL^{14}H$ Microdyn Nb_2O_5/SiO_2 mirror. (c) Zoomed reflectance and (d) transmittance around the centre wavelength.*

Reflectance and transmittance spectra show that deposited mirrors are centred at 640 to 650 nm which complies with the design wavelength except for IAD E-beam ZrO_2/SiO_2 mirror. The latest shows a shift of the centre wavelength to 600 nm, either caused by a shift of the physical thickness or the refractive index of the coating materials. The reflectance magnitude for 15-pair IAD E-beam ZrO_2/SiO_2 is of 98.5 % at 600 nm (Figure 3.11.c) and the corresponding transmittance is below 0.01 % (Figure 3.11.d), which indicates high absorption and/or scattering losses.

The Perkin Elmer Lambda 900 spectrophotometer employs two grating monochromators. One grating is used for the ultraviolet-visible range from 170 nm to 700 nm and another grating for the near-infrared range from 700 nm to 3300 nm. The grating change is synchronized with the photodetector change during the spectral scan. However, the change of grating during reflectance and transmittance measurements can cause a discontinuity of the scan which was more notable for some of the mirrors used in this study (Figure 3.13.c, Figure 3.13.d, Figure 3.15.c, Figure 3.15.d). The mechanical change of the grating causes a dip in either transmittance or reflectance spectra. In the case of Microdyn Nb_2O_5/SiO_2 mirror, the reflectance drops by nearly 2 % at 700 nm (Figure 3.15.c) and the corresponding transmittance drops by one order of magnitude (Figure 3.15.d). The grating change is accompanied in some cases by a noisy signal around 700 nm for the high reflectance measurements (Figure 3.12.c and Figure 3.13.c). It can be noted from reflectance measurements presented in Figures 3.11 to 3.15 that reflectance spectra become very noisy beyond 99.5 % and transmittance spectra below 0.1 %. Reflectance and transmittance value beyond these ranges reach the signal-to-noise ratio

(SNR) limit of the spectrophotometer. High reflectance measurements are also less accurate than transmittance measurements. For many of the deposited mirrors, the measured reflectance magnitude exceeds 100 %, which does not obviously represent the real reflectance value of the mirrors. These over 100 % values can be explained by the uncertainty of the 100 % reflectance baseline correction performed before the sample measurement. For the studied mirrors, direct spectroscopy does not allow to determine which of the mirrors or the deposition methods is the best because the measurements are not accurate enough.

A more precise method to measure very high reflectance is cavity ring down spectroscopy (CRDS)[5, 6]. This method consists of deducing the reflectance of the coating from the total optical losses of the mirror. An example of CRDS setup is shown in Figure 3.16. A cavity setup is build using two highly reflective mirrors (R>99.9 %). A laser pulse is introduced to the cavity. Typical laser pulse durations vary between 40 and 500 ns and the laser repetition frequencies between 0.1 to 100 kHz[7]. The light pulse is reflected back and forth between the mirrors leading to a loss of light through the mirrors at each round trip.

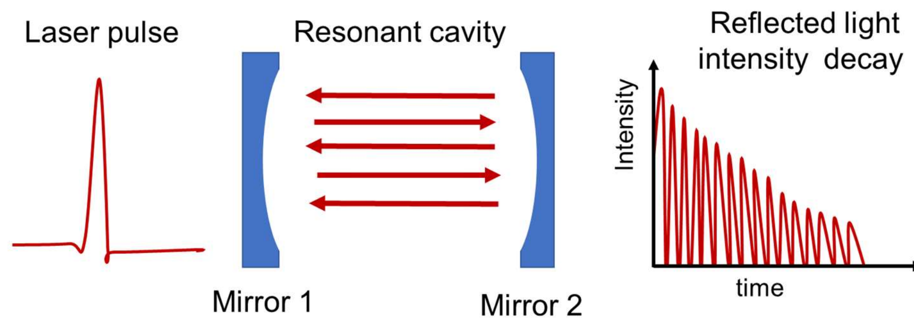

Figure 3.16: *Cavity ring down spectroscopy setup allowing the measurement of the total optical losses of a high reflectance mirror. A laser pulse is sent through a cavity formed by two high reflectance mirrors. The light round trips between the mirrors lead to a decay of light intensity. The light decay defines the cavity losses. The reflectance is deduced from the total losses.*

The exponential decay of light intensity *I* as a function of time, *t*, due to mirror optical losses is expressed in the following equation[8]:

$$I = I_0 \exp\left[-\frac{\tau t c}{2L}\right] \qquad (3.5)$$

Where I_0 is the initial light intensity, *c* is the speed of light, *L* is the length of the cavity, τ is the total of cavity losses. For ultra-low loss resonators, the decay time is of the order of few nanoseconds.

The light signal can be detected using a photomultiplier tube (PMT) and recorded using an oscilloscope. The decay time, also known as ring-down time, is determined using the time dependency of light intensity expressed in Equation (3.5). Cavity ring down

spectroscopy allows measuring optical losses in the range of few hundred ppms, it is hence frequently used in the measurement of low absorption coefficients in gas sensing applications[9-11].

The measurement of a high reflectance using a CRDS setup is practically achieved in a three-measurements setup using three high reflectance mirrors M1, M2 and Mx (Figure 3.17)[12]. M1 and M2 have known reflectance values (R >99.99 %) and Mx is the unknown reflectance sample. The first step consists in calibrating the cavity with M1 and M2 using the method described in Figure 3.19. The first cavity loss L_A is deduced from the calibration step. Then, one of the known mirrors, M_2 for example, is replaced by Mx. The new cavity loss L_B is measured. M2 is put back in the cavity and M1 is replaced with M_x. The last cavity loss L_C is measured.

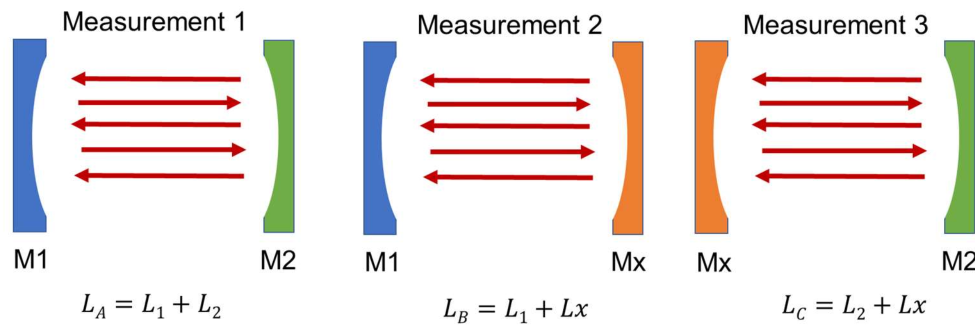

Figure 3.17: *High reflectance measurement for an unknown mirror Mx using a three-mirror cavity ring down spectroscopy setup. Three high reflectance mirrors are used including two mirrors with a known reflectance value. The third mirror is the sample to be measured. The cavity setup allows three cavity loss measurements by interchanging the mirrors position. The reflectance of the unknown mirror is deduced from three cavity losses measurements.*

The optical loss L_x of the unknown mirror can be deduced from the following equation:

$$L_x = \frac{1}{2}(L_B + L_C - L_A) \tag{3.6}$$

The reflectance R_x of the unknown mirror is hence:

$$R_x = 1 - L_x = 1 - \left[\frac{1}{2}(L_B + L_C - L_A)\right] \tag{3.7}$$

The CRDS setup in Figure 3.17 gives a rigorous method for high reflectance measurement. If M1 and M2 have identical losses, only two cavity measurements are required to determine the reflectance of the unknown mirror. Equation (3.6) therefore becomes:

$$L_x = L_B - \frac{1}{2}L_A \tag{3.8}$$

The reflectance of Mx is therefore:

$$R_x = 1 - L_x = 1 - \left(L_B - \frac{1}{2}L_A\right) \tag{3.9}$$

CRDS allows measuring optical losses in the range of 100 ppm to 1000 ppm. The reflectance can be therefore determined with up to 0.001% accuracy while direct spectroscopy allows at best a 0.1 % accuracy[13].

While CRDS allows measuring very low optical losses and consequently very high reflectance values, it is however unsuitable for mirrors with a reflectance below 99.5 %. Direct spectroscopy described in the beginning of this section is more appropriate. A measurement method presented in [13] combines cavity ring down spectroscopy with spectrophotometry to allow the measurement of mirrors with reflectance higher than 99 % with 0.001 % accuracy and mirrors with reflectance below 99 % with 0.3 % accuracy at the same time.

3.3.2 Coating derivation and reverse engineering

Several high reflectance mirrors were grown using various evaporation and sputtering methods and used different materials combinations. However, some of the studied mirrors failed to fulfil the required performance such as the case of IAD E-beam ZrO_2/SiO_2 mirror (Figure 3.15) where the maximum reflectance for a 14-pair stack was limited to 98 %. In the case of IAD E-beam TiO_2/SiO_2 mirror, a blueshift was noticed for the reference wavelength. A design derivation is required to understand why some mirrors failed the initial specifications. Coating derivation is also performed for reverse engineering purposes. The actual coating structure and optical coatings must be determined if the measured reflectance and transmittance spectra do not match the initial coating design.

Whilst calculating reflectance and transmittance from a given mirror design is straightforward, design derivation has a more complicated path as there is no single solution in establishing the design from the spectroscopic analysis. Because of the numerous variables in the coating design such as the optical constants of the coating, the optical and physical thicknesses and the material absorptions, many solutions can be found that may not be realistic. However, design calculations can be performed using the reverse engineering feature of the Essential Macleod software.

An example of coating derivation is presented in Figure 3.18 for a 14-pair ZrO_2/SiO_2 mirror. In Figures 3.18.a and 3.18.b, measured reflectance and transmittance are plotted against simulated performances from Figure 3.8. A slight shift of the mirror stopband to the UV range is noted. The amplitude of the mirror ripples is inferior to the amplitude predicted by the design. Using the reverse engineering tool of Essential Macleod, the design is readjusted to reflectance and transmittance measurements (Figures 3.18.c and 3.18.d). Three main parameters were adjusted in this calculation. The first adjusted parameter is the thickness of the coatings. In this case, thickness can be readjusted layer by layer to obtain a satisfactory design derivation. The second parameter is the coating density. The packing density refinement was applied to both refractive index and extinction coefficient of the dielectric layers. The third and final adjusted parameter is the inhomogeneity of the coating layers. Considering the present design contains 29 layers,

same material layers (high index or low index) had their thickness, density and inhomogeneity changed in the same way.

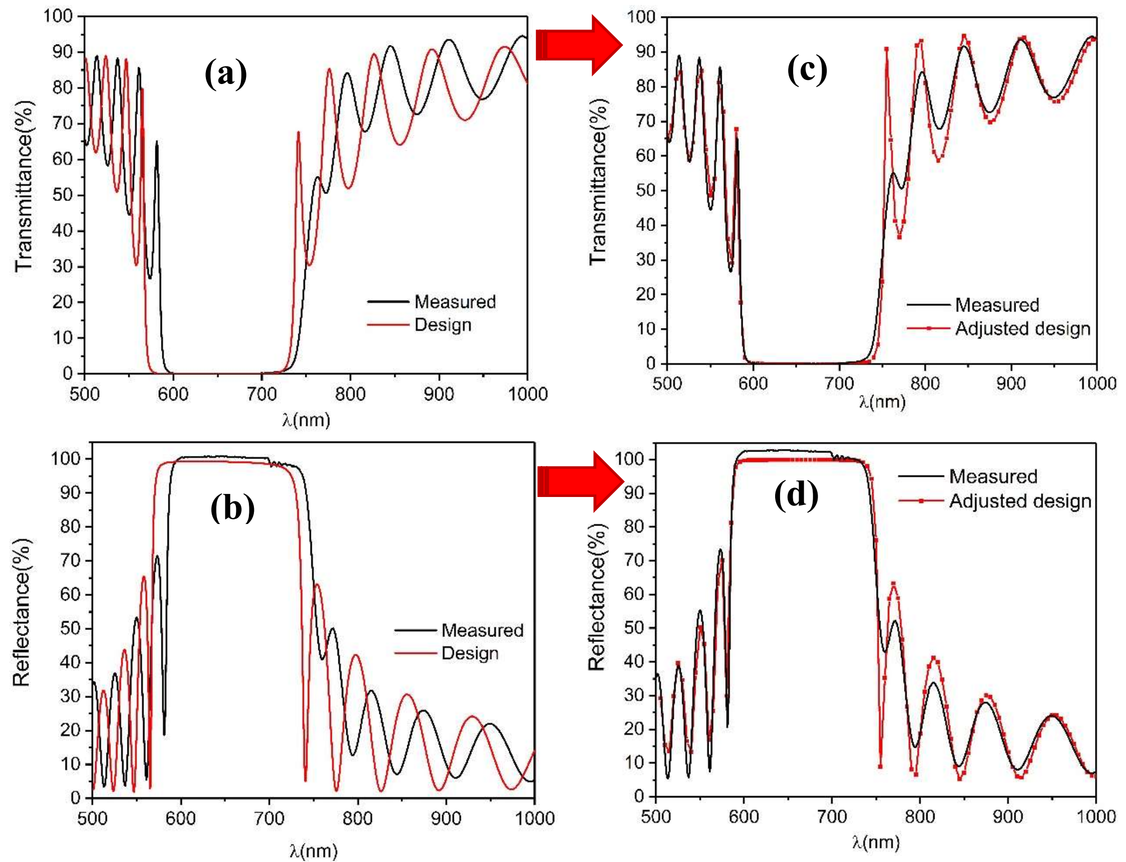

Figure 3.18: *(a) Measured reflectance and (b) measured transmittance for Plasmacoat $(HL)^{14}H$ ZrO_2/SiO_2 mirror versus Macleod simulated spectra. Using the reverse engineer tool of Essential Macleod, the initial design is adjusted to the measured reflectance and transmittance in (c) and (d).*

The new design derivation is obtained by adjusting the refractive indices of zirconia and silica layers to 2.12 and 1.46 respectively. The initial refractive indices values for zirconia and silica were of 2.15 and 1.47 at 640 nm wavelength. The thicknesses of zirconia and silica were also adjusted to 120 nm and 72 nm instead of 109 nm and 75 nm. The layers extinction coefficients were not altered during the design derivation. While the new design allows a good fit of the calculated performance to the measured one, some of the mirror ripples are not perfectly fitted because the adjustment process applies a constant change to same material layers. A better refinement may be obtained by readjusting slightly the layers thickness and optical constants independently. However, this operation can lead to several design solutions that do not represent the actual behaviour of the coating or the deposition method.

3.3.3 Optical losses

The total optical losses of the studied mirrors can be determined by few means. CRDS for instance can be used to measure accurately small optical losses of high reflectance mirrors. Total optical losses L can be also directly calculated from reflectance R and transmittance T measurements using the following formula:

$$L = 1 - R - T \tag{3.10}$$

The total optical losses were calculated from transmittance and reflectance spectra and the results are presented for studied high reflectance mirrors. The highest optical losses are obtained for IAD E-beam ZrO_2/SiO_2 with approximately 4 % losses at 600 nm followed by Plasmacoat Nb_2O_5/SiO_2 with nearly 2 % losses at 640 nm wavelength. The total losses become very noisy below 1 % due to the noise in the reflectance and the transmittance measurements. Determining losses from spectral reflectance and transmittance measurements lacks accuracy, especially when reflectance exceeds 100 %. Furthermore, this method does not establish whether losses are due to absorption or to scattering. Absorption and scatter losses should be therefore measured separately.

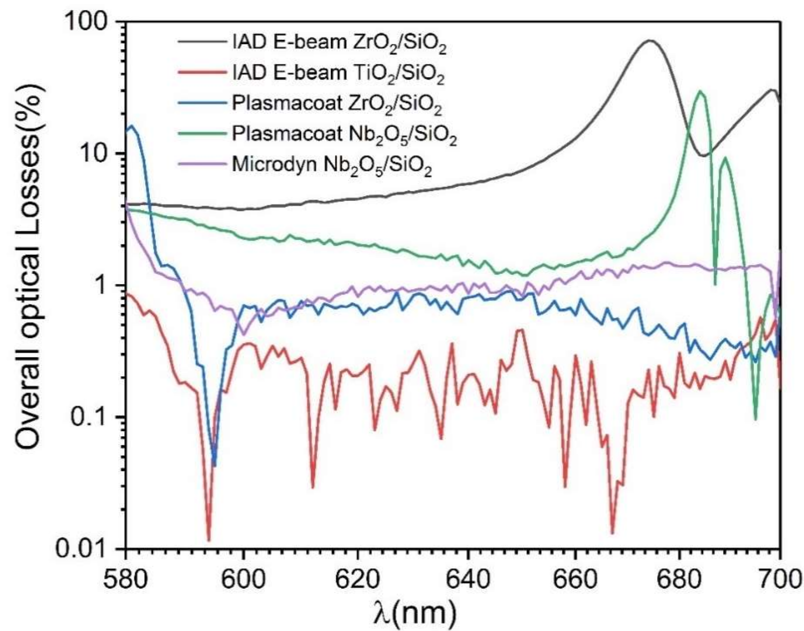

Figure 3.19: *Overall optical losses around 640 nm deduced from transmittance and reflectance data of studied $(HL)^{14}$ H mirrors.*

Absorption in high reflectance cavity mirrors produces heat gradients which are responsible for thermoelastic deformations[14], thermal depolarization[15] and thermorefractive phase gradients [16]. Absorption measurements are also relevant to low laser damage threshold mirrors as absorption induces damage in the coating[17].

Many techniques allow an accurate measurement of very small absorption losses such as the photothermal common path interferometry[18], a lock-in detection method that can be applied to a CCD sensor[19] and the photothermal deflection spectroscopy[20, 21]. In the latter, the absorbed light energy is converted to heat by non-radiative recombination, which generates periodic temperature fluctuations. Since the refractive index is temperature dependent, the thermal fluctuations cause a periodic refractive index change. Absorption losses are caused by defects and contaminants within the coating structure. Contaminants are made of water or oxygen particles ejected during the evaporation process. The purity level of material sources also dictates absorption losses in the coatings. Flaking material on the chamber shields can also deposit on the coating surface during the layer processing and cause absorption. For sputtering systems such as Microdyn and Plasmacoat, contaminants may be caused by debris due to oxides build-up

on the target surface and the chamber walls. Examples of surface contaminants and defects are provided in Figure 3.20 and 3.21 for 14-pair Plasmacoat ZrO_2/SiO_2 and Nb_2O_5/SiO_2 mirrors and 14-pair Microdyn Nb_2O_5/SiO_2 mirror. These surface defects not only cause absorption but also scatter losses that reduce significantly the reflectance of the coating.

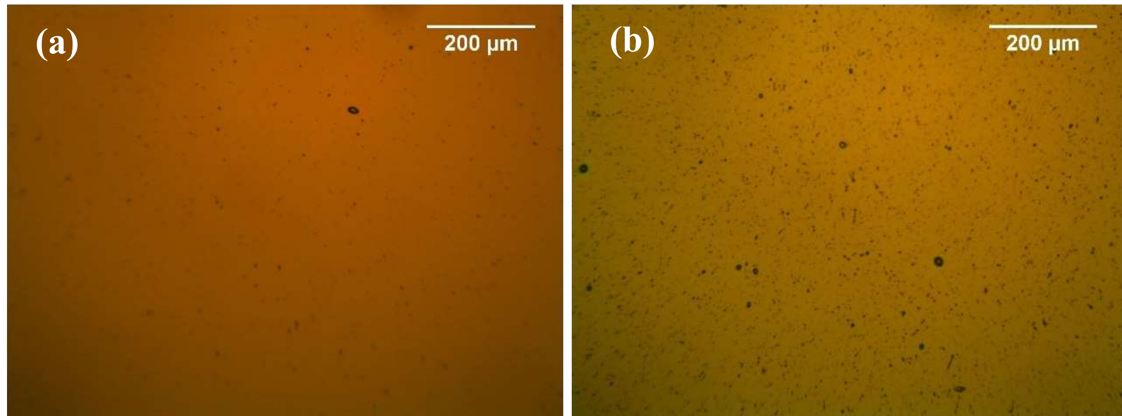

Figure 3.20: *(a) Optical image of multilayer $(HL)^{14}H$ ZrO_2/SiO_2 and (b) $(HL)^{14}H$ Nb_2O_5/SiO_2 deposited using Plasmacoat system.*

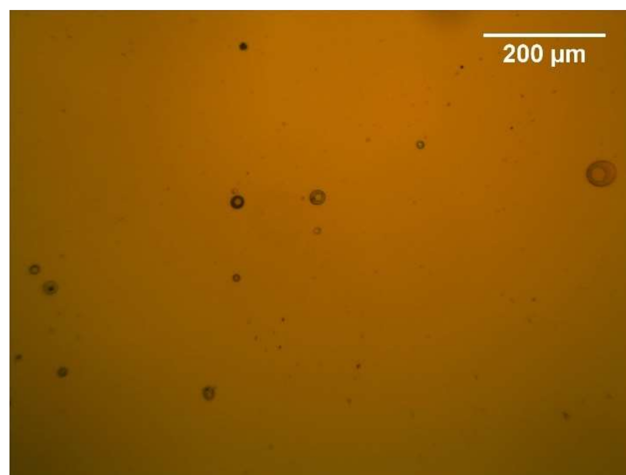

Figure 3.21: *Optical image of multilayer $(HL)^{14}H$ Nb_2O_5/SiO_2 deposited using Microdyn system.*

Scattering in high quality reflectance mirrors is caused by many factors such as surface roughness[22], irregularities and impurities in the stack layers. Scatter losses not only reduce the optical power but also degrade the signal-to-noise ratio and alter the quality of the signal readout during the experiment. Local defects and particles on the surface of the coating produce a range of scattering effects. These effects depend on the impurities size and compositions. The scattered field from isolated local defects can be estimated using Mie theory (Mie, 1908)[23]. Scatter losses are unlikely to cause heating or distortion like absorption losses. Scattering may also introduce spurious phase or displacement noise in precision interferometry. Scattering can be measured by resolving the bidirectional reflectance distribution function (BRDF) as a function of scattering angle[24]. Scatter losses can be also directly determined from total integrated scattering measurements or estimated from the coating surface roughness. Both approaches will be discussed in Section 3.4.

3.4 Mirrors roughness and scatter losses

3.4.1 Roughness measurements

The evolution of roughness with increasing coating layers is studied for ZrO_2/SiO_2 and Nb_2O_5/SiO_2 mirrors deposited by IAD E-beam using atomic force microscopy. AFM scans were performed on an area of 0.5 µm × 0.5 µm using a scan speed of 0.5 Hz and a sampling matrix of 512 × 512. AFM scans for IAD E-beam ZrO_2/SiO_2 multilayer coatings are presented in Figure 3.22. The roughness of the coatings is determined from the root mean square roughness values, r. Measurement results show that the rms roughness of multilayer IAD ZrO_2/SiO_2 increase with increasing pairs of the coatings due to the nuclei and columnar growth of the coating. $(HL)^5$ H coating has rounded grains of 30 nm to 40 nm with some voids in the structure of the coating (Figure 3.22 a). While increasing the coating layers, smaller grains of 10 to 20 nm form between larger grains and fill the voids in the structure (Figure 3.22 b) leading to a grain coalescence (Figures 3.22 c and 3.22.d) resulting in a high surface roughness.

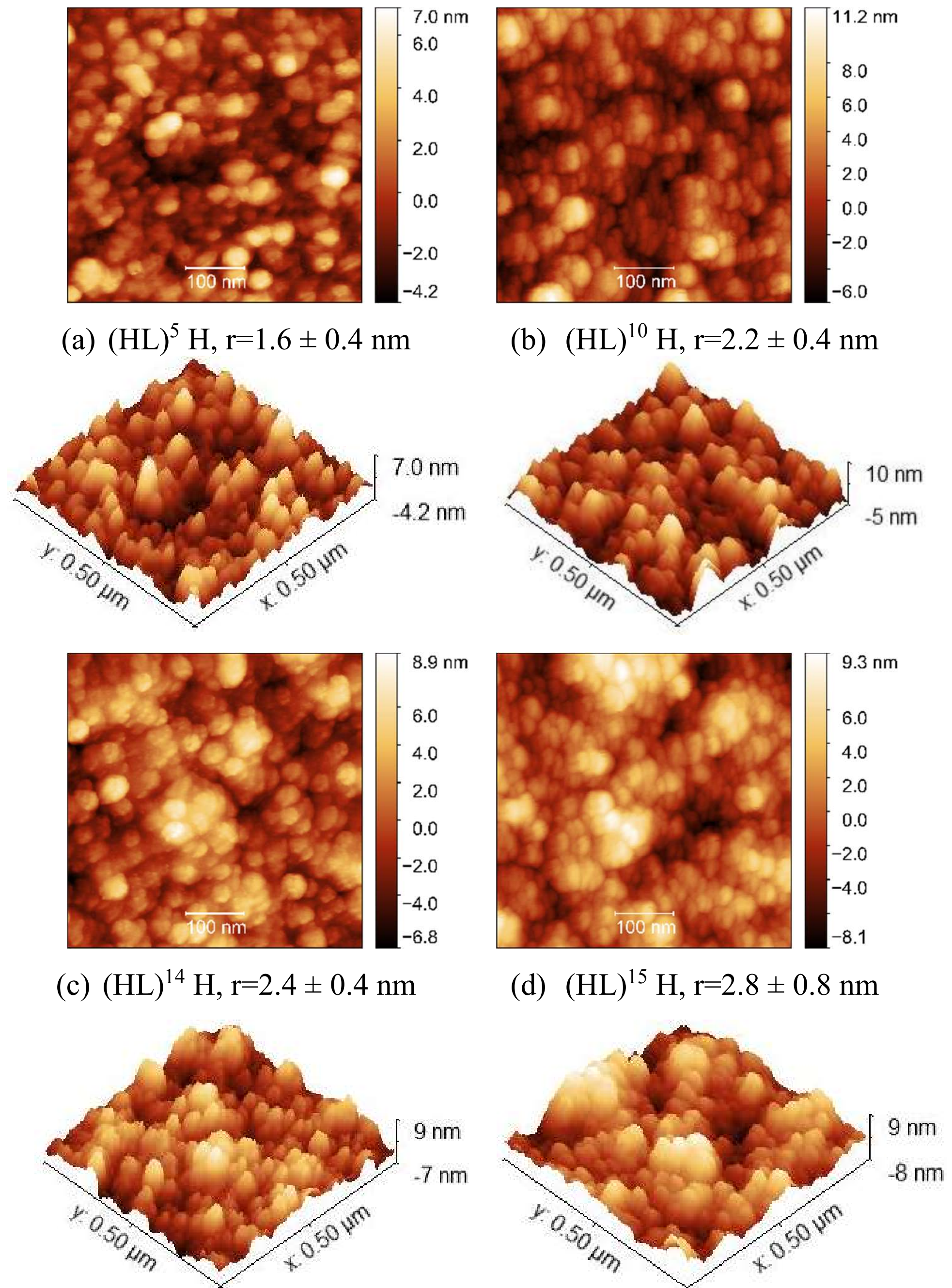

Figure 3.22: *Two dimensional and three-dimensional AFM measurements for IAD E-beam ZrO_2/SiO_2 coatings with increasing pairs. AFM scans were performed on an area of 0.5 µm × 0.5 µm using a scan speed of 0.99 Hz and a sampling matrix of 512 × 512.*

AFM scans for IAD E-beam TiO_2/SiO_2 mirrors are shown in Figure 3.23. The studied coatings show generally smaller grain size than ZrO_2/SiO_2 coatings deposited by the same method (between 10 to 20 nm). Surface roughness also increases by increasing the coating layers leading to grain coalescence previously observed for IAD E-beam ZrO_2/SiO_2 (Figures 3.23.b, 3.23.c and 3.23.d).

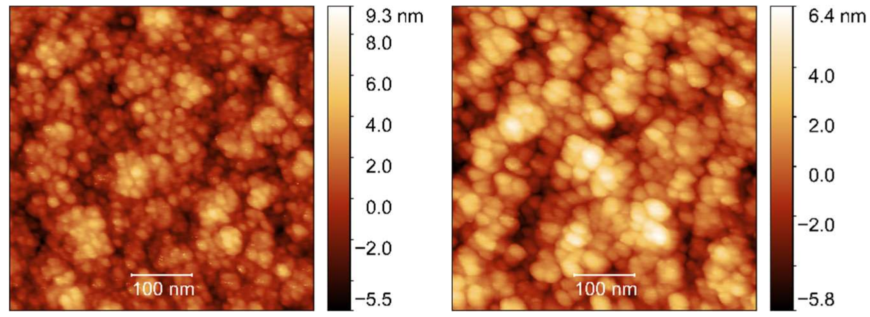

(a) $(HL)^5$ H, r=1.6 ± 0.6 nm (b) $(HL)^{10}$ H, r=2.0 ± 0.3 nm

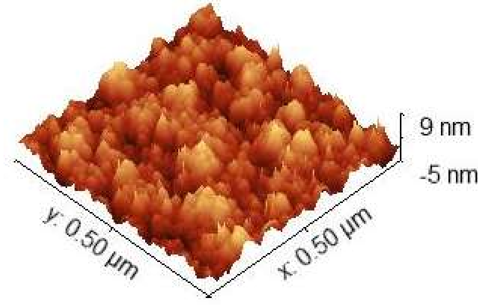

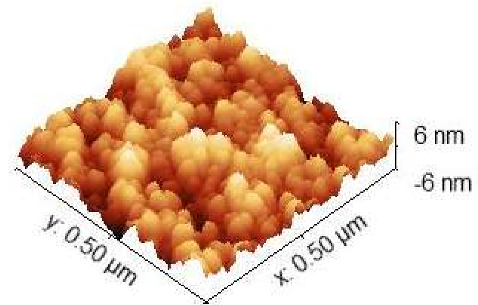

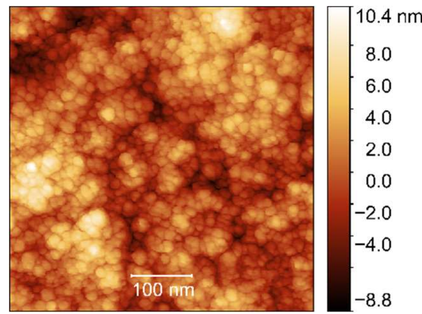

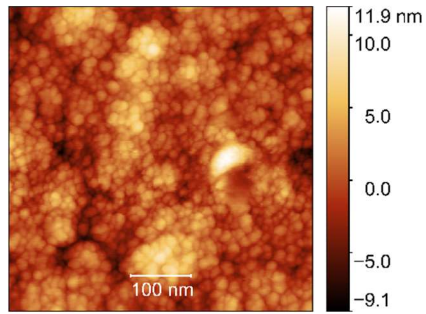

(c) $(HL)^{14}$ H, r=2.7 ± 0.5 nm (d) $(HL)^{15}$ H, r=2.5 ± 0.5 nm

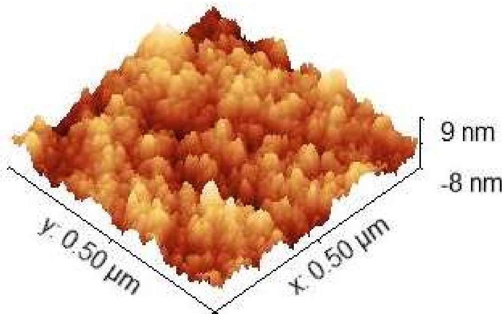

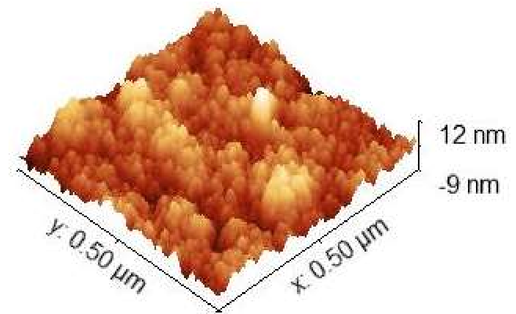

Figure 3.23: *Two dimensional and three-dimensional AFM measurements for IAD E-beam TiO_2/SiO_2 coatings with increasing pairs. AFM scans were performed on an area of 0.5 µm × 0.5 µm using a scan speed of 0.99 Hz and a sampling matrix of 512 × 512.*

The previous AFM results demonstrate that the top layer roughness is correlated to the roughness introduced by the previously deposited layer[25]. The rms roughness for IAD E-beam TiO_2/SiO_2 and ZrO_2/SiO_2 mirrors from Figures 3.22 and 3.23 is plotted against pair numbers in Figure 3.24.

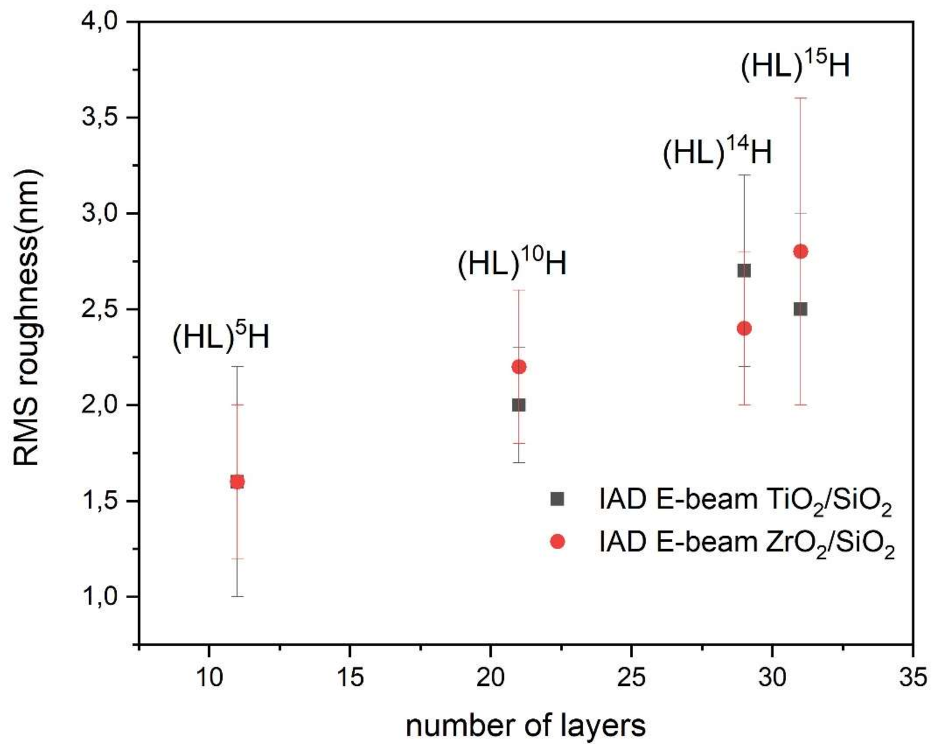

Figure 3.24: *RMS roughness values for AFM scans presented in Figures 3.22 and 3.23 for IAD E-beam ZrO_2/SiO_2 and TiO_2/SiO_2 with coating increasing pairs.*

3.4.2 Scatter losses

Scatter losses at 640 nm wavelength were estimated from the root mean square roughness at 640 nm for multilayer coatings using Equation (2.5) given in Section 2.4.1. Scatter losses for IAD E-beam TiO_2/SiO_2 and ZrO_2/SiO_2 mirrors are shown in Figure 3.25.

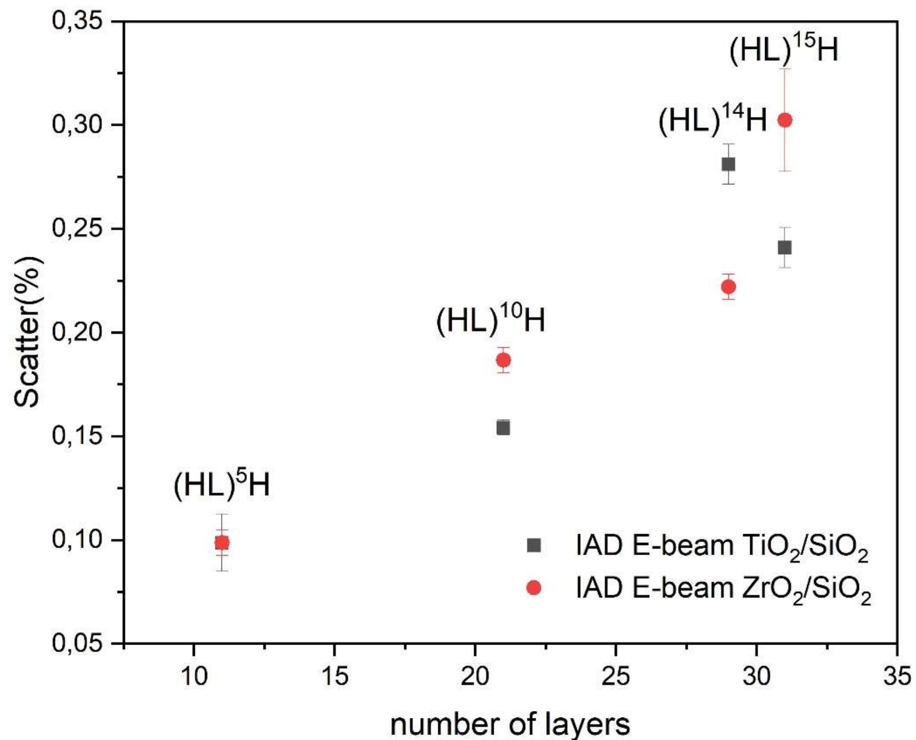

Figure 3.25: *Scatter calculated from RMS roughness values presented in Figures 3.24.*

Considering the estimated scatter for a 15-pair IAD E-beam ZrO_2/SiO_2 mirror, the maximum reflectance of the mirror is limited to 99.6 % or 99.7 %. A reflectance of 98.6 % and a transmittance below 0.1 % were previously reported for the same mirror at its reference wavelength. An absorptance of nearly 1 % can be therefore deduced for the coating.

3.4.3 Measurements on superpolished substrates

IAD E-beam TiO_2/SiO_2, Plasmacoat Nb_2O_5/SiO_2 and ZrO_2/SiO_2 and Microdyn Nb_2O_5/SiO_2 mirrors were deposited on superpolished etalons provided by Shenzhen Brilliant Optics co Ltd. The substrates are made of plane circular UV grade fused silica and have 25 ± 0.3 mm diameter and 8 ± 0.2 mm thickness. AFM measurement of the superpolished substrate indicate a root-mean-square roughness of 0.3 ± 0.05 nm. Two dimensional and three-dimensional AFM profiles of the deposited mirrors are shown in Figure 3.26. The roughness of IAD E-beam TiO_2/SiO_2 is of 1.8 ± 0.5 nm. This value agrees with roughness data presented in Figure 3.25 for IAD E-beam TiO_2/SiO_2 multilayer coatings grown on microscope slides. The microstructure of the coating is also similar to $(HL)^5H$ TiO_2/SiO_2 multilayer sample presented in Figure 3.23.a. This result indicates that the quality of the substrate did not influence the final roughness of the IAD E-beam TiO_2/SiO_2 mirror. The Plasmacoat Nb_2O_5/SiO_2 mirror has a roughness of 2.0 ± 0.5 nm, explained by the island growth mode. Smooth surfaces are obtained for Microdyn Nb_2O_5/SiO_2 and Plasmacoat ZrO_2/SiO_2 mirrors with a roughness of 0.3 ± 0.02 nm and 0.5 ± 0.02 nm respectively. Considering the previous roughness values, the scatter losses are estimated to 0.1 ± 0.01 % and 0.15 ± 0.01 % for IAD E-beam TiO_2/SiO_2 and Plasmacoat Nb_2O_5/SiO_2 mirrors at 640 nm reference wavelength. The estimated scatter losses for Microdyn Nb_2O_5/SiO_2 and Plasmacoat ZrO_2/SiO_2 mirrors are of 0.003 % and 0.009 % or 30 ppm and 90 ppm respectively.

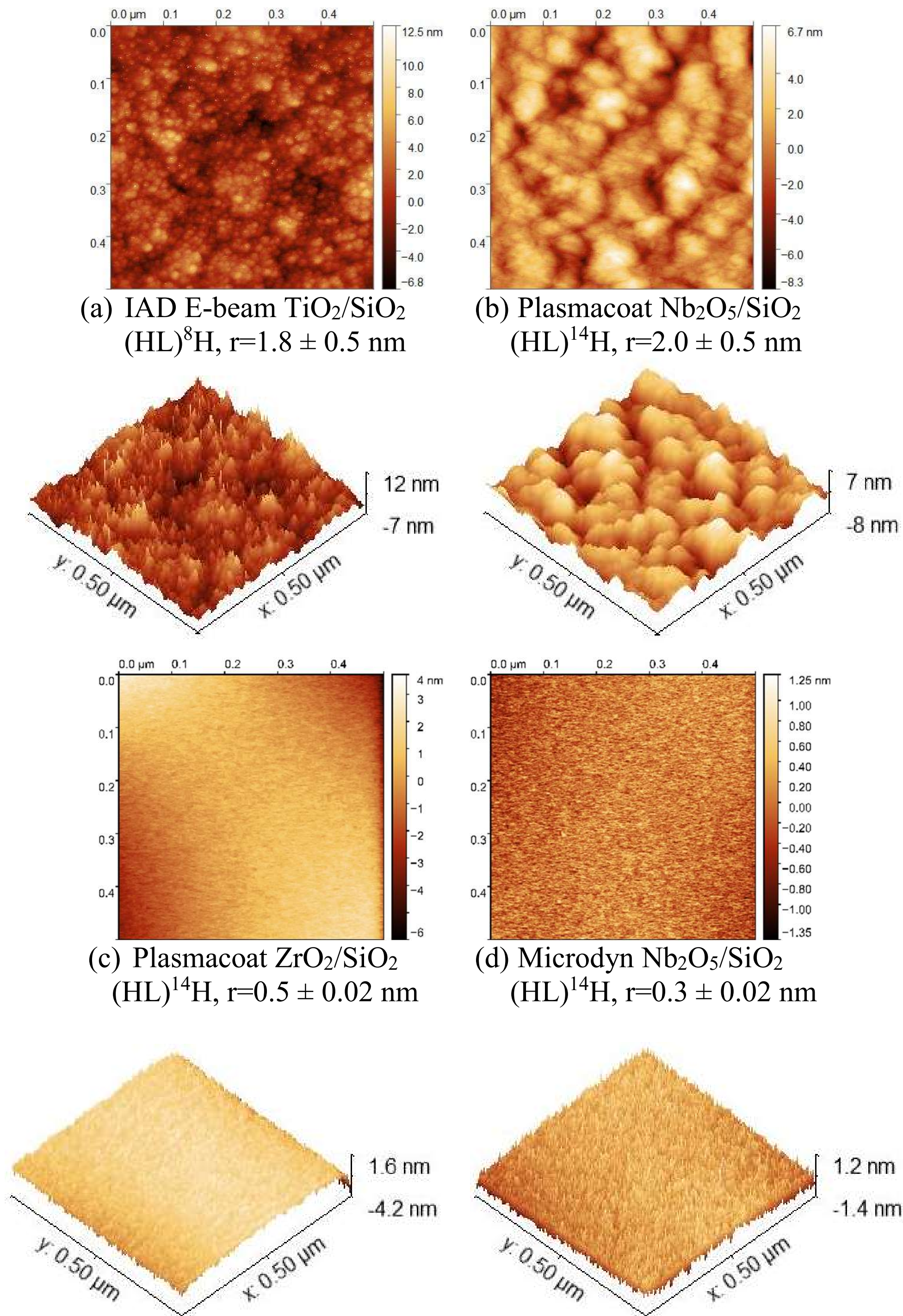

Figure 3.26: *Two dimensional and three-dimensional AFM measurements for IAD E-beam TiO_2/SiO_2, Plasmacoat Nb_2O_5/SiO_2 and ZrO_2/SiO_2 and Microdyn Nb_2O_5/SiO_2 mirrors. AFM scans were performed on an area of 0.5 µm × 0.5 µm using a scan speed of 0.99 Hz and a sampling matrix of 512 × 512.*

3.4.4 Total integrated scattering

Total Integrated Scattering (TIS) is a surface quality measure indicating how much light is randomly deviating in space from a laser beam specular reflectance or transmittance. Total scattering is defined according to ISO 13696 standard term, as the ratio of the total power generated by all contributions of scattered light into the forward or backward half-spaces or both, to the incident beam power radiation. Backward and forward spaces are presented in Figure 3.27. The light fraction scattered in the backward half-space is called backward scattering and the light fraction scattered in the forward half-space is called forward scattering.

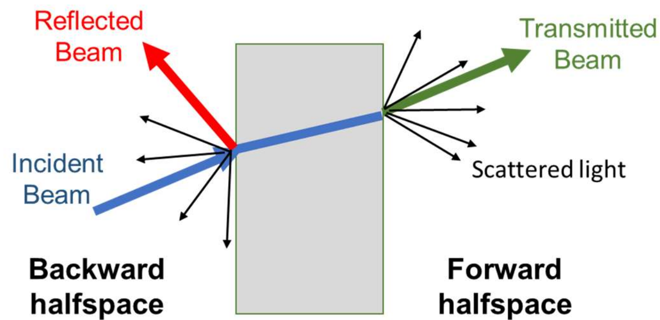

Figure 3.27: *Scattered radiation in the forward and/or the backward half-space, reproduced from[26].*

According to ISO 13696 standard, the total integrated light scattering can be determined from either forward scattering or backward scattering. The TIS losses can be calculated using the following equation[27]:

$$TIS(\%) = \frac{U_{\mathrm{sample}} - U_{\mathrm{F}}}{U_{\mathrm{S}}} \times 100 \quad (3.11)$$

Where U_{sample} is the *TIS* signal measured from the sample, U_{F} the unloaded sphere signal or the background signal and U_{S} is the diffuse reflectance standard signal.

The transmitted and reflected beams were subtracted from the integrating sphere. This setup used a Nd:YAG Ekspla NL-202/SH/TH laser. The central wavelength of the laser was of 532 nm. Measurements were performed at 1.5 ° angle of incidence. The laser pulse frequency was of 1 kHz and the pulse duration is of 9 ns. The beam diameter in target plane was of 3.9 mm for forward scattering. TIS measurements setup is presented in Figure 3.28. The measurement setup consists of an Ulbricht integrating sphere. The light scattered from the sample in a wide angular range (from 4.73 ° to 88.20 °) is collected and directed to the detector after several reflections on the internal surface of the sphere. For this purpose, the inner sphere surface is coated with barium sulphate, a highly diffusive reflecting material. The sphere spectral region is from 0.35 µm to 1.4 µm. The scattered signal is detected using a Hamamatsu H5784-20 photomultiplier mounted on the top of the sphere. The photomultiplier is sensitive from 300 nm to 900 nm wavelength and the sensitive area diameter is of 8 mm. The TIS apparatus is mounted in a hermetic and opaque chamber in order to avoid undesirable light that could influence the

measurements. Only three windows mounted at a Brewster angle are left as inputs for the incident, the specularly reflected and the transmitted beams[28].

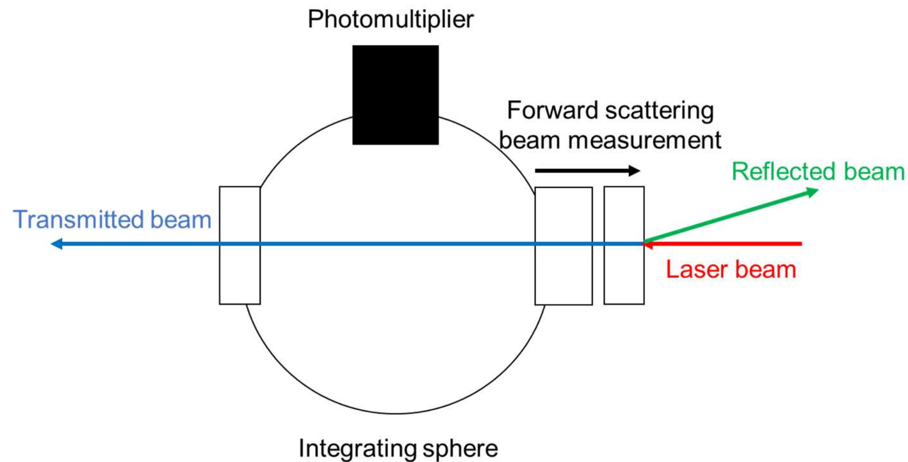

***Figure 3.28**: TIS measurement configuration for forward (FW) scattering (the surface with the coating is the first surface) using an Ulbricht sphere according to ISO 13696[29].*

Total integrated scattering was measured on high reflectance mirrors presented in Figure 3.26 by Lidaris Ltd[26]. Samples were handled in an ISO 14644-1 class cleanroom and cleaned using ethanol prior to scattering measurements. Surface dust was blown-off using a compressed air gun. The unloaded sphere signal is $(4.8 \pm 0.3) \times 10^{-4}$. The total number of measured sites is 605. The sites were equally spaced by 500 µm. Ten measurements were averaged per one test site in order to reduce the influence of laser fluctuations on the TIS signal. A Standa 8MT173 motorized translation stage is employed to move the measured mirror in X and Y directions.

The transmitted and reflected beams were removed from the integrating sphere and the measurement chamber. The TIS losses maps for high reflectance mirrors deposited on superpolished substrates are shown in Figure 3.29. The TIS maps were realised at a wavelength of 532 nm by dividing one-inch aperture into the grid of 605 cells. The beam diameter $1/e^2$ in target plane was used to investigate each cell and was set to 3.9 mm for forward scattering measurements. The spatial resolution of the measurement is limited by the distance between neighbouring cells which is equal to 500 µm.

A saturation of the scatter signal (red colour) is noted on the edges of the tested mirrors which can be explained by contamination while handling the samples by the edges. The similarity between TIS losses maps for Plasmacoat Nb_2O_5/SiO_2 and ZrO_2/SiO_2 indicates scatter is related to the deposition process and to the position of the samples inside the coating chamber.

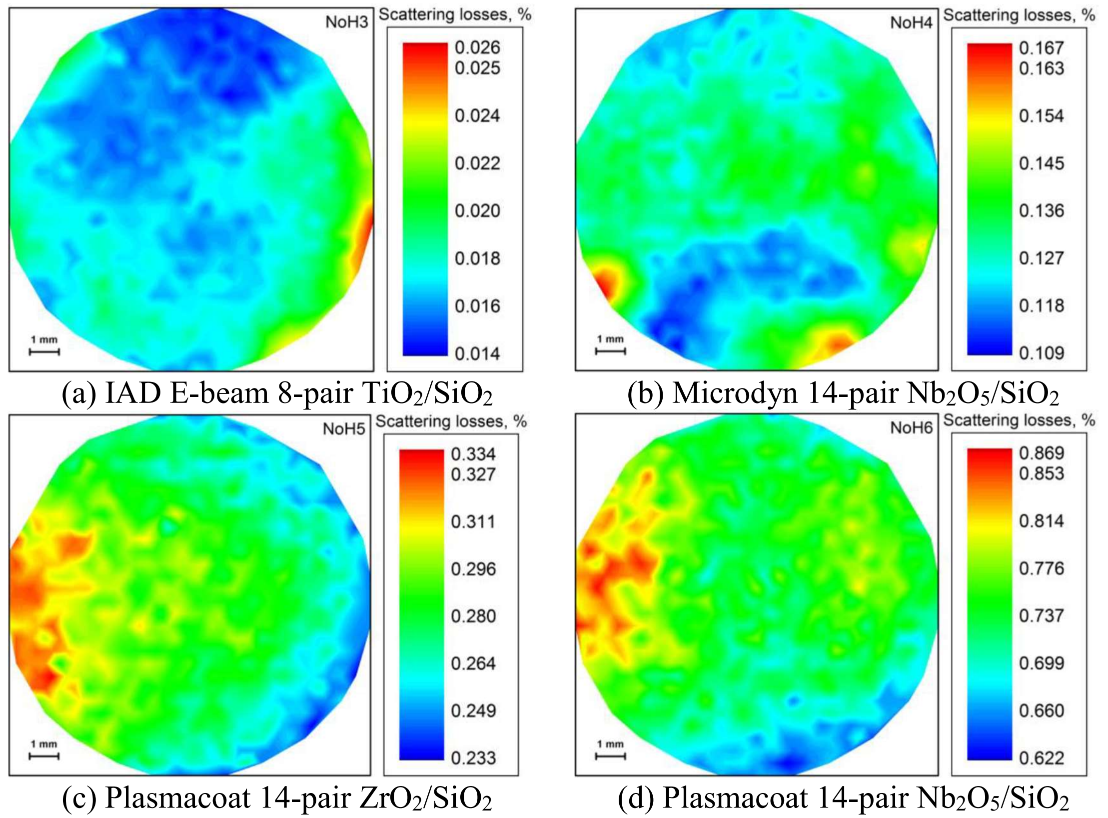

(a) IAD E-beam 8-pair TiO_2/SiO_2 (b) Microdyn 14-pair Nb_2O_5/SiO_2

(c) Plasmacoat 14-pair ZrO_2/SiO_2 (d) Plasmacoat 14-pair Nb_2O_5/SiO_2

Figure 3.29: *Forward total integrated scattering losses maps at 532 nm wavelength for high reflectance mirrors on superpolished substrates.*

Surface defects such as scratches, coating spatters and contaminants induce higher scattering than the intrinsic scatter levels of the coating and the substrate. The ISO/DIS 13696 standard therefore proposes a data reduction method in order to remove the contributions of the surface defects and contaminations[29]. Data reduction is executed using three iterative steps. The mean scatter value M is first calculated. Then, the standard deviation σ of data set is determined. Finally, scatter values in the range (M-2σ) and (M+2σ) are selected. The first two data reduction steps are repeated until there is no significant change in the mean value or its standard deviation. The final mean value obtained is called an optimised mean value and represent the scatter value with the highest probability in the data set. The optimised mean value and its standard deviation for each mirror are presented in Figure 3.30. Low scattering losses are obtained for IAD E-beam TiO_2/SiO_2 mirror and are approximately equal to 200 ppm. The scatter losses for Microdyn Nb_2O_5/SiO_2 are of 0.15 %. The highest scatter losses are obtained for Plasmacoat ZrO_2/SiO_2 and Nb_2O_5/SiO_2 mirrors and are approximately of 0.3 % and 0.8 % approximately. The latest values are nearly hundred times higher than estimated scatter from surface roughness measured using AFM. This great disparity can be explained by the multiple surface defects, craters and contaminants noted on Plasmacoat ZrO_2/SiO_2(Figure 3.20) and Microdyn Nb_2O_5/SiO_2(Figure 3.21) mirrors.

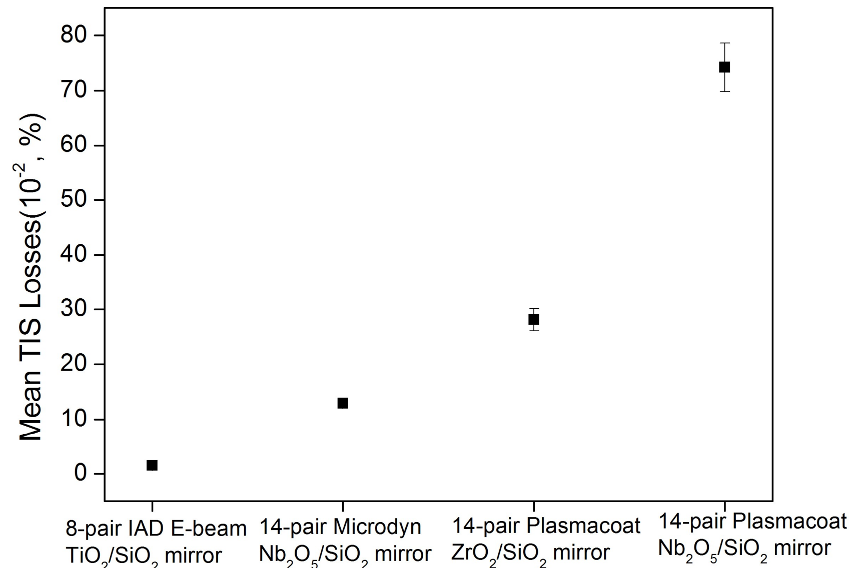

Figure 3.30: *TIS mean optimised value for high reflectance mirrors grown on superpolished substrates.*

3.5 Laser damage

3.5.1 Definition

Laser damage is a critical parameter for high power lasers systems and their applications. According to the ISO 21254-1:2011 standard terms and definitions sections[30], laser-induced damage is defined as any permanent laser radiation induced change in the characteristics of the surface/bulk of the specimen which can be observed by an inspection technique and at a sensitivity related to the intended operation of the product concerned. The laser-induced damage threshold (LIDT) is defined as the highest quantity of laser radiation incident upon the optical component for which the extrapolated probability of damage is zero[30]. Laser damage in optical coatings may be triggered by various light-matter interactions. Very often, optical absorption in thin film coatings couple thermal energy under laser irradiation causing heating in the coating structure. In the case of overheating or mechanical disruption, a catastrophic failure, known as Laser-Induced Damage (LID) may occur. For multilayer high reflectance coatings in the visible to mid-infrared region, deposition processes are already optimised to reduce absorption in single dielectric layers. In this case, laser damage is ruled by nodular defects embedded in the dielectric layers[31, 32]. Beside thermal heating and intrinsic defects, damage may be also induced by direct electronic excitation for short pulse laser[33].

3.5.2 LIDT measurements

LID of high reflectance mirrors grown on superpolished substrates was investigated by following a standard S-on-1 test procedure[34]. This procedure uses a series of pulses with constant laser energy density on each unexposed site with a short and constant time interval between two successive pulses, where the length of the time interval between the pulses of a series is given by the reciprocal of the pulse repetition rate of the laser source.

The present LID tests used an InnoLas SpitLight Hybrid Q-switched Nd:YAG laser with a central wavelength of 532 nm. Measurements were performed at normal incidence. The pulse repetition frequency was of 100 Hz and the pulse duration was of 5.4 ± 0.3 ns. The pulse to pulse energy stability is of 2.7 %. The laser has a near Gaussian spatial beam profile and its beam diameter is of 210.3 ± 10.0 µm. The laser source and its parameters are monitored using a beam diagnostic system. The spatial and temporal profile and the radiation energy of the laser are recorded using the diagnostic system (Figure 3.31).

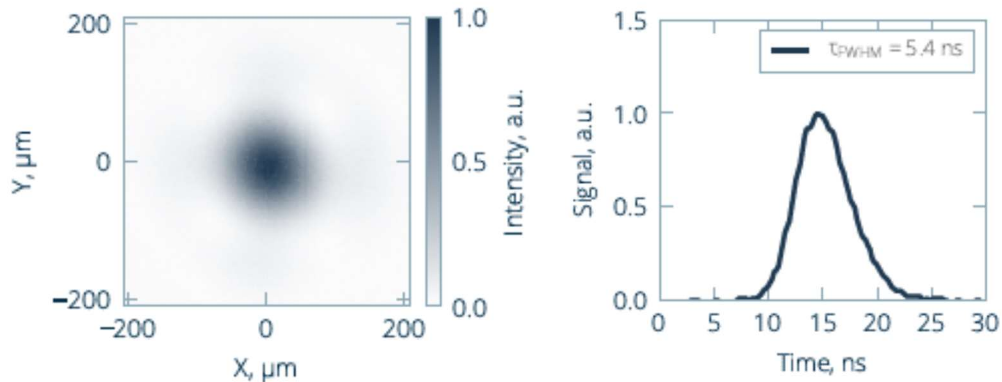

Figure 3.31: *Beam and pulse profiles for the laser source used for LIDT measurements.*

The LID measurement setup is presented in Figure 3.32. The laser radiation is focused on a specific spot of the coating surface with a high energy density using an optical imaging system or a focusing system. A variable attenuator placed between the laser source and the focusing system allows the tuning of the laser fluence in the target plane. The laser fluence describes the energy delivered per unit area and is expressed in J/cm^2.The test site on the sample is moved on the mirror surface using a positioning system. The sample positioning unit is controlled by a computer which also operates the measurement process. After the laser irradiation, the mirror is inspected using a damage detection unit, in this case a Normarski interference contrast microscope. The resulting raw data of the LID test are composed of a set of fluence values corresponding to damage states.

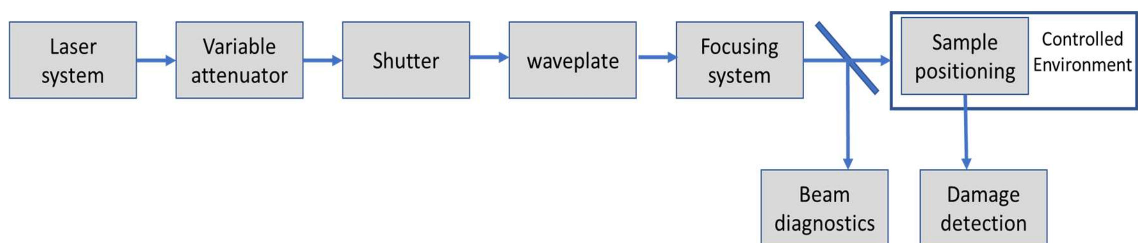

Figure 3.32: *Laser Induced Damage (LID) measurement test set-up.*

An example of damage probability plots is presented in Figure 3.33 for IAD E-beam (HL)^{8}H TiO_2/SiO_2 mirror for 1- on -1, 10- on -1, 100- on -1 and 1000- on -1 testing procedures. The 1- on -1 test uses one laser radiation on each test site of the mirror sample, the 10- on -1 test uses 10 pulses on each test site and so on. The full 1- on -1 test procedure consists of multiple irradiation cycles of different energies (Figure 3.33), covering a range of both low fluences with no damage and high fluences causing damage. LIDT values were determined by fitting experimental damage probability data with a

model derived for a Poisson damage process assuming degenerate defect ensemble. The LIDT value represent the highest laser fluence for which the extrapolated probability of damage is zero as presented by the red line in Figure 3.33. Cross-shaped points represent the number of pulses applied per test at a specific laser fluence. The pink highlighted area represents the 95 % confidence interval [M-2σ, M+2σ] or the deviation from the LIDT measured mean value M by two times its standard deviation σ. The number of tested sites on the sample is 400. Test sites are spaced by 900 µm.

For IAD E-beam TiO_2/SiO_2 mirror, no damage event was detected with a maximum laser fluence of 4.37 ± 0.87 J/cm^2 for a 1- on -1 testing mode or a single shot irradiation. The LIDT value shifts to lower fluences for multiple-shot irradiations. The LIDT values are similar for 1- on -100 and 1- on -1000 and are equal to 0.83 ± 0.17 J/cm^2.

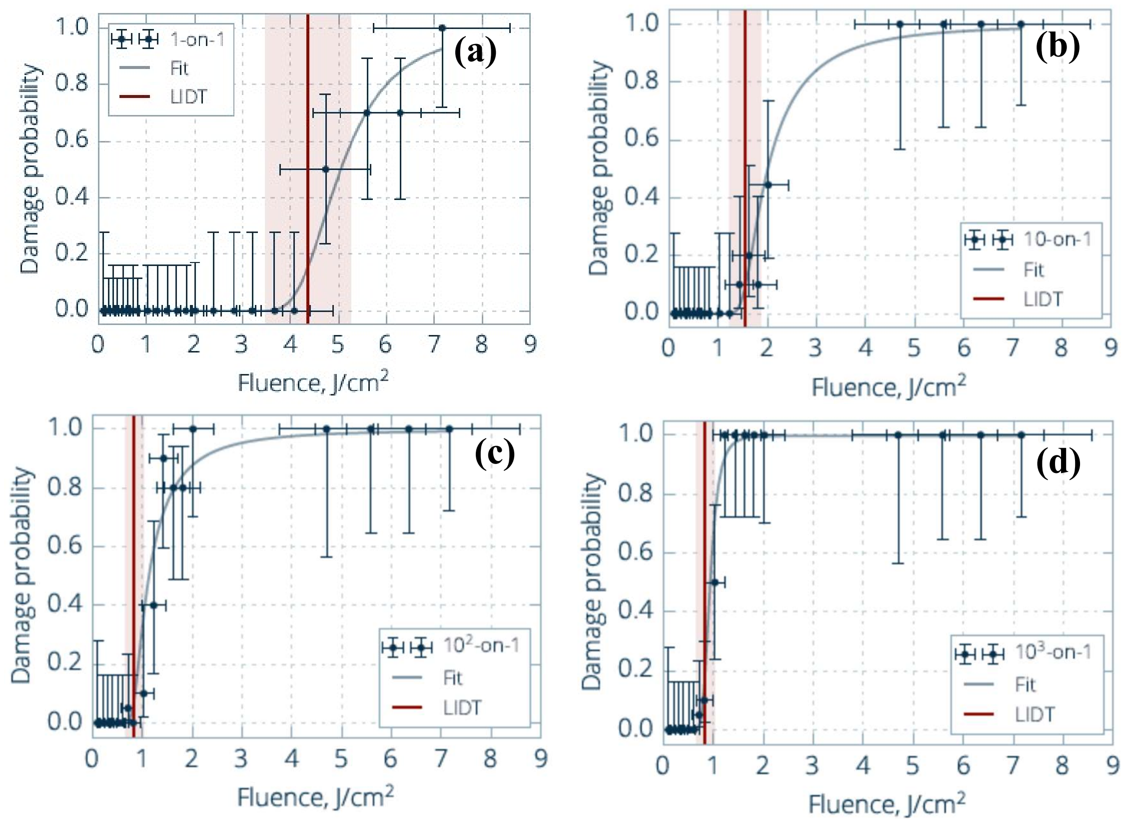

Figure 3.33: *Damage probability plots for IAD E-beam (HL)^{8}H TiO_2/SiO_2 mirror. (a) 1- on -1 (b) 10- on -1 (c) 100- on -1 (d) 1000- on -1*

LID tests were performed on high reflectance mirrors grown on superpolished substrates presented in Figure 3.29 using the same test procedure as per IAD E-beam TiO_2/SiO_2 mirror. Damage curves for IAD E-beam TiO_2/SiO_2, Microdyn Nb_2O_5/SiO_2 and Plasmacoat ZrO_2/SiO_2 and Nb_2O_5/SiO_2 mirrors are shown in Figure 3.34. The curves represent the S-on-1 laser-induced damage threshold as a function of the number of pulses per site (1, 10, 100 and 1000 pulses) using a pulse repetition frequency of 100 Hz. LIDT values are extracted for each mirror from damage probability plots as per Figure 3.33.

The lowest LIDT values are reported for Microdyn and Plasmacoat Nb_2O_5/SiO_2 mirrors (Figures 3.34.b and 3.34.d) which can be explained by the high defect density already

reported in Section 3.3.3 for these mirrors. The LIDT values for the latest samples are however slightly reduced by multiple shot tests in comparison to damage curves presented in Figures 3.34.a and 3.34.c for IAD E-beam TiO_2/SiO_2 and Plasmacoat ZrO_2/SiO_2 mirrors. For instance, the LIDT varies from 4.37 ± 0.87 J/cm^2 for IAD E-beam TiO_2/SiO_2 mirror on a 1- on -1 test to 1.54 ± 0.31 J/cm^2 on 10- on -1 test, while the LIDT varies only from 1.39 ± 0.27 J/cm^2 on a 1- on -1 test to 1.13 ± 0.22 J/cm^2 on 10- on -1 test for Microdyn Nb_2O_5/SiO_2 mirror.

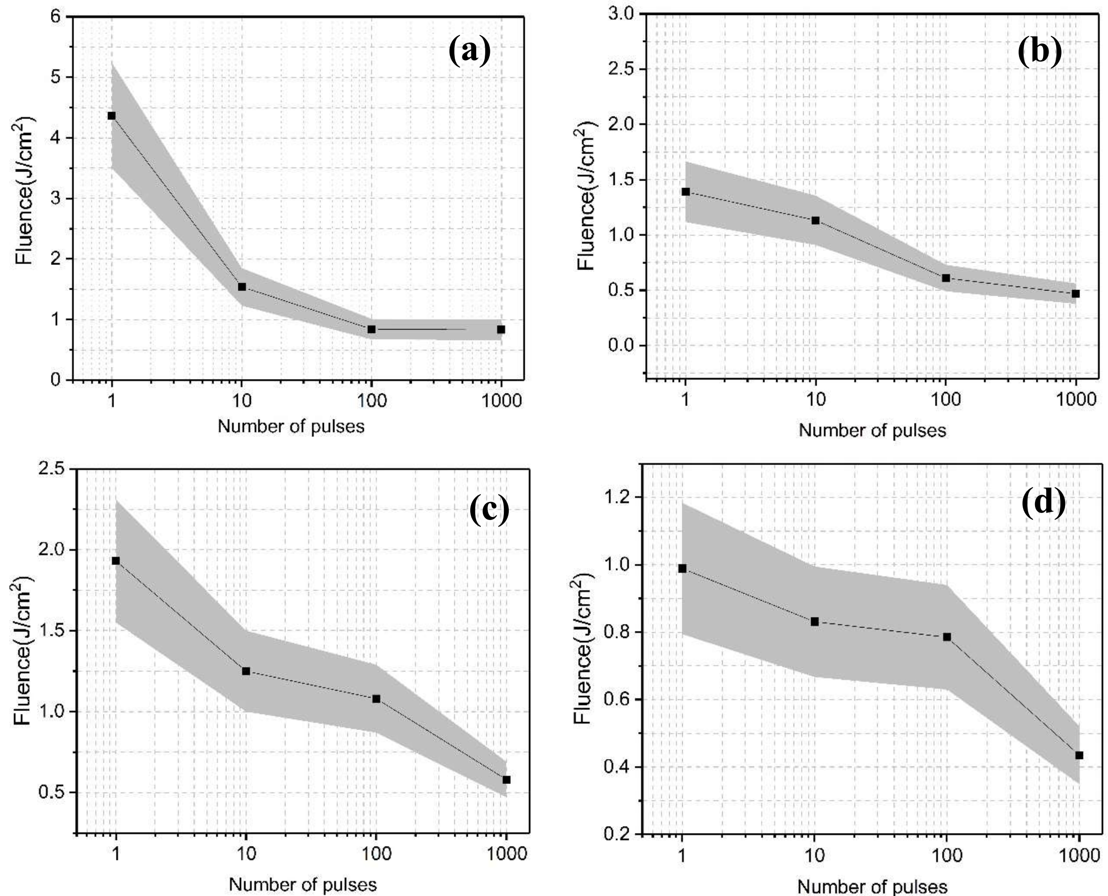

Figure 3.34: *Characteristic damage curve (laser threshold) for HR coatings grown on superpolished substrates. a) IAD E-beam $(HL)^8H$ TiO_2/SiO_2 mirror. b) Microdyn $(HL)^{14}H$ Nb_2O_5/SiO_2 mirror. c) Plasmacoat $(HL)^{14}H$ ZrO_2/SiO_2 mirror. d) Plasmacoat $(HL)^{14}H$ Nb_2O_5/SiO_2 mirror. The gray filled area represents the 95 % confidence interval [M- 2σ, M+2σ] or the deviation from the measured mean value M by two times its standard deviation σ.*

Typical damage morphologies for the studied mirrors are presented in Figure 3.35. In Figure 3.35.a1, a damage occurred on IAD E-beam TiO_2/SiO_2 mirror after the irradiation laser fluence exceeded the LIDT values (0.816 J/cm^2 after 602 pulses). This type of damage starts at a localised intrinsic defect site[31]. A larger damage is obtained with a fluence of 1.66 J/cm^2 after 66 pulses (Figure 3.35.a2). A similar damage morphology is reported in Figure 3.35.b1 for Microdyn Nb_2O_5/SiO_2 mirror after the 1000th- on -1 pulse on a surface defect at a fluence of 0.590 J/cm^2 exceeding the damage threshold of 0.5 J/cm^2. A higher fluence of 1.19 J/cm^2 after the 40th pulse induced a delamination of the coating in the laser irradiation area for the same mirror. This damage morphology is

typically caused by mechanical stress in the coating induced by heating in the irradiated area. Another defect induced damage is reported in Figure 3.35.c for Plasmacoat ZrO_2/SiO_2 mirror. This damage is characterised by a crater morphology and is caused by defects and inclusions in the coating. Defects on the surface of the coating possess a greater absorption than the surrounding material. They consequently heat up faster than the rest of the material under laser irradiation. The defects explode and remove the material covering the substrate. Finally, a typical absorption induced melting is presented in Figure 3.35.d for the Plasmacoat Nb_2O_5/SiO_2 mirror. The high density of defects on the mirror surface caused an overheating of the coating under until reaching the melting point of the coating.

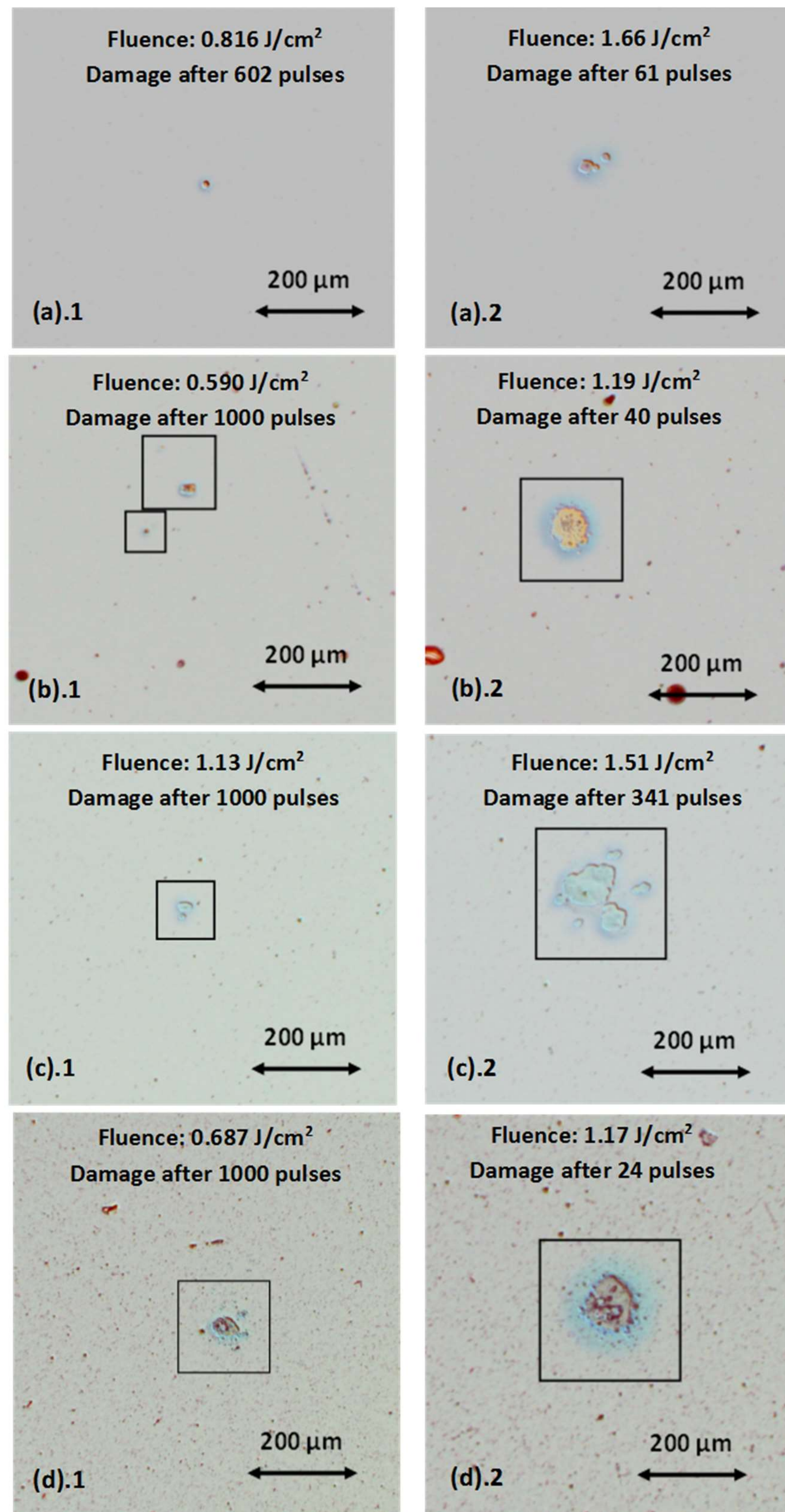

Figure 3.35: *Laser damage morphology for high reflectance mirrors on superpolished substrates. (a) IAD E-beam* $(HL)^8H$ TiO_2/SiO_2 *mirror. (b) Microdyn* $(HL)^{14}H$ Nb_2O_5/SiO_2 *mirror. (c) Plasmacoat* $(HL)^{14}H$ ZrO_2/SiO_2 *mirror. (d) Plasmacoat* $(HL)^{14}H$ Nb_2O_5/SiO_2 *mirror.*

3.6 Planar mirrors assessment summary

Planar mirrors were grown on superpolished etalons using IAD E-beam and sputtering methods. Surface roughness was measured using atomic force microscopy. Total integrated scattering was determined from forward scattering losses using an Ulbricht sphere. Absorptance was deduced from optical spectrometry measurements. Laser-induced damage threshold values were obtained by an S-on-1 test procedure explained in Section 3.5.2. A summary of planar mirrors assessment is provided in Table 3-8. According to results presented in Table 3-8, multilayer TiO_2/SiO_2 mirror deposited by IAD E-beam represents the lowest optical loss despite a high surface roughness. This conclusion must be verified for a $(HL)^{14}H$ structure to confirm the performance of the coating. Absorptance losses should be also measured using a more accurate method as discussed in Section 3.3.3.

Coating Design/material	Deposition method	rms roughness(nm)	TIS (%)	LIDT* (J/cm^2)	Absorptance @640 nm (%)
$(HL)^8H$ TiO_2/SiO_2	IAD E-beam	1.8 ± 0.5	0.02	4.37 ± 0.87	0.1
$(HL)^{14}H$ ZrO_2/SiO_2	Plasmacoat	0.3 ± 0.02	0.3	1.93 ± 0.38	0.4
$(HL)^{14}H$ Nb_2O_5/SiO_2	Plasmacoat	2.0 ± 0.5	0.8	0.989 ± 0.195	0.2
$(HL)^{14}H$ Nb_2O_5/SiO_2	Microdyn	0.5 ± 0.02	0.2	1.391 ± 0.274	0.8

Table 3-8: *Assessment summary for high reflectance mirrors grown on superpolished substrates. *The LIDT values were determined from the 1- on -1 laser test.*

3.7 Summary and conclusion

Design calculations for multilayer mirrors were performed using Essential Macleod software. TiO_2/SiO_2, ZrO_2/SiO_2 and Nb_2O_5/SiO_2 mirrors were grown using IAD E-beam, plasma assisted magnetron sputtering and microwave assisted magnetron sputtering deposition methods. Reflectance and transmittance measurements of deposited mirrors using optical spectroscopy are not sufficiently accurate for high reflectance mirrors. A three-measurement cavity ring down spectroscopy experiment was presented to determine the reflectance and the optical losses of the mirrors with a higher accuracy. Total optical losses were deduced from transmittance and reflectance spectral measurement. The optical losses determined by this method are subject to high error measurements. High defect density caused by debris and contaminants ejected during the sputtering process was observed for Plasmacoat ZrO_2/SiO_2 and Nb_2O_5/SiO_2 and Microdyn Nb_2O_5/SiO_2. The observed defects contribute to both absorption and scatter losses. A process quality check will be performed to reduce the defects density of the coatings. An example of design derivation method by Essential Macleod was proposed to adjust calculated reflectance and transmission data for Plasmacoat ZrO_2/SiO_2 mirror to measured values. This method does not however lead to a single analytical solution.

Additional coating runs will be necessary to verify the solution proposed by the design derivation method.

The effect of increasing layers on surface roughness in a dielectric Bragg stack was studied for IAD E-beam TiO_2/SiO_2 and ZrO_2/SiO_2 mirrors grown on microscope slides using atomic force microscopy. AFM scans indicate that surface roughness from one layer to another are correlated and showed a grain coalescence with increasing layer stack. The surface roughness of IAD E-beam TiO_2/SiO_2 and ZrO_2/SiO_2 mirrors was approximately of 2 nm which is too high for low loss high finesse cavities. The surface roughness was evaluated for IAD E-beam TiO_2/SiO_2, Plasmacoat Nb_2O_5/SiO_2 and ZrO_2/SiO_2 and Microdyn Nb_2O_5/SiO_2 mirrors deposited on superpolished substrates. The rms roughness of IAD E-beam TiO_2/SiO_2 was of 1.8 ± 0.5 nm which agrees with the roughness values on microscope slides. Use of superpolished substrates did not influence the microstructure of the mirror. Plasmacoat Nb_2O_5/SiO_2 mirror roughness was of 2.0 ± 0.5 nm. This high surface roughness is explained by an island growth mode of the coating. Smooth surfaces were obtained for Microdyn Nb_2O_5/SiO_2 and Plasmacoat ZrO_2/SiO_2 mirrors with a rms roughness of 0.3 ± 0.02 nm and 0.5 ± 0.02 nm respectively. Roughness measurement allowed a first estimation of scatter losses at the reference wavelength. Scatter losses were estimated for Microdyn Nb_2O_5/SiO_2 and Plasmacoat ZrO_2/SiO_2 mirrors to 30 ppm and 90 ppm at 640 nm respectively. Total integrated scatter measurements were performed on IAD E-beam TiO_2/SiO_2, Plasmacoat Nb_2O_5/SiO_2 and ZrO_2/SiO_2 and Microdyn Nb_2O_5/SiO_2 mirrors grown on superpolished substrates using a normal incidence Ulbricht sphere setup. Low scattering losses were obtained for IAD E-beam TiO_2/SiO_2 mirror and are approximately equal to 200 ppm. The scatter losses for Microdyn Nb_2O_5/SiO_2 mirror are of 0.15 % approximately. The highest scatter losses are obtained for Plasmacoat ZrO_2/SiO_2 and Nb_2O_5/SiO_2 mirrors and are approximately of 0.3 % to 0.8 %. The latest values are much higher than estimated scatter by roughness measurements. This disparity can be explained by the multiple surface defects, craters and contaminants noted on Plasmacoat ZrO_2/SiO_2 and Microdyn Nb_2O_5/SiO_2 mirrors. In general, scatter values are too high for the present application and further process optimisation is required to reduce the roughness and the defect density of the coatings.

A laser-induced damage study was performed on IAD E-beam TiO_2/SiO_2, Plasmacoat Nb_2O_5/SiO_2 and ZrO_2/SiO_2 and Microdyn Nb_2O_5/SiO_2 mirrors deposited on superpolished substrates using an S-on-1 test procedure. Laser-induced damage thresholds were determined by fitting experimental damage probability data with a Poisson derived model. The lowest LIDT values were reported for Microdyn and Plasmacoat Nb_2O_5/SiO_2 mirrors which can be explained by the high defect density of the coating. Typical damage morphologies were presented for the studied mirrors. Reported damage morphologies were induced by coating defects and occurred after the applied laser fluence exceeded the damage threshold. Typical morphologies included pin-point damage in the case of IAD E-beam TiO_2/SiO_2 at 1.66 J/cm^2 after 66 pulses and after the 1000th- on -1 pulse using a fluence of 0.590 J/cm^2. Other defect induced damages include

a coating delamination for Microdyn Nb_2O_5/SiO_2 mirror at fluence of 1.19 J/cm^2 after the 40th- on -1 pulse. A crater damage was reported for Plasmacoat ZrO_2/SiO_2 mirror and was induced by coating surface overheating. Finally, a typical absorption induced melting damage was reported for Plasmacoat Nb_2O_5/SiO_2 mirror after the 24th pulse at a fluence of 1.17 J/cm^2.

3.8 Acknowledgements

Total integrated scattering measurements and laser-induced damage tests were kindly performed by Mrs L. Vigricaite and Mrs L. Mažulė in LIDARIS Ltd. (Vilnius, Lithuania). Microdyn and Plasmacoat high reflectance mirrors were deposited at the University of the West of Scotland (Paisley, United Kingdom) using coating systems at the Institute of Thin Films, Sensors and Imaging. The mirror coatings were realised with technical assistance of Dr L. Fleming and Dr C. Li.

REFERENCES

[1] T. F. C. Inc. "Essential Macleod Software version 10.5.528." https://www.thinfilmcenter.com/essential.php (accessed.

[2] H. A. Macleod, "Multilayer high-reflectance coatings," in *Thin-film optical filters*: CRC Press, 2010, p. 216.

[3] D. J. Hemingway and P. H. Lissberger, *Optica Acta: International Journal of Optics,* vol. 20, no. 2, pp. 85-96, 1973.

[4] J. C. Zwinkels, M. Noël, and C. X. Dodd, "Procedures and standards for accurate spectrophotometric measurements of specular reflectance," *Applied Optics,* vol. 33, no. 34, pp. 7933-7944, 1994.

[5] G. Rempe, R. J. Thompson, H. J. Kimble, and R. Lalezari, "Measurement of ultralow losses in an optical interferometer," *Opt. Lett.,* vol. 17, no. 5, pp. 363-365, 1992.

[6] A. Duparré and D. Ristau, "Optical Interference Coatings 2010 Measurement Problem," *Applied Optics,* vol. 50, no. 9, pp. C172-C177, 2011.

[7] A. B. S. Alquaity, E.-t. Es-sebbar, and A. Farooq, "Sensitive and ultra-fast species detection using pulsed cavity ringdown spectroscopy," *Opt. Express,* vol. 23, no. 6, pp. 7217-7226, 2015.

[8] D. Z. Anderson, J. C. Frisch, and C. S. Masser, "Mirror reflectometer based on optical cavity decay time," *Applied Optics,* vol. 23, no. 8, pp. 1238-1245, 1984.

[9] D. Munzke, M. Böhm, and O. Reich, "Gaseous Oxygen Detection Using Hollow-Core Fiber-Based Linear Cavity Ring-Down Spectroscopy," *Journal of Lightwave Technology,* vol. 33, no. 12, pp. 2524-2529, 2015.

[10] M.-K. Oh, Y.-H. Lee, S.-C. Choi, D.-K. Ko, and J.-M. Lee, "Detection of methane and ethane by continuous-wave cavity ring-down spectroscopy near 1.67 µm," *J. Opt. Soc. Korea,* vol. 12, no. 1, pp. 1-6, 2008.

[11] P. A. Y. Fiadzomor, D. M. Baker, A. M. Keen, R. B. Grant, and A. J. Orr-Ewing, "Pressure broadening of H2O absorption Lines in the 1.3 µm region measured by continuous wave-cavity ring-down spectroscopy: Application in the trace detection of water vapor in N2, SiH4, CF4, and PH3," *Appl. Spectrosc.,* vol. 62, no. 12, pp. 1354-1362, 2008.

[12] C. Cook, T. Karam, I. Stevenson, and S. Vandendriessche. "Webinar: High Reflectivity Mirrors for Laser Applications." https://www.edmundoptics.com/resources/trending-in-optics/high-reflectivity-mirrors/ (accessed.

[13] H. Zu, B. Li, Y. Han, and L. Gao, "Combined cavity ring-down and spectrophotometry for measuring reflectance of optical laser components," *Opt. Express,* vol. 21, no. 22, pp. 26735-26741, 2013.

[14] D. Iesan and A. Scalia, *Thermoelastic deformations*. Kluwer, 1996.

[15] Y. Aoyagi, T. Taira, and I. Shoji, "Thermal analysis simulation using depolarization loss in solid-state microchip laser," *SICE 2003 Annual Conference,* vol. 2, pp. 2195-2200, 2003.

[16] V. Mitrofanov *et al.*, "Technology for the next gravitational wave detectors," *Science China Physics, Mechanics & Astronomy,* vol. 58, no. 12, pp. 1-26, 2015.

[17] Z. Yu *et al.*, "Damage threshold influenced by the high absorption defect at the film–substrate interface under ultraviolet laser irradiation," *Opt. Lett.,* vol. 38, no. 21, pp. 4308-4311, 2013.

[18] L. Anghinolfi *et al.*, "Optical properties of uniform, porous, amorphous Ta2O5 coatings on silica: temperature effects," *Journal of Physics D: Applied Physics,* vol. 46(45), p. 455301, 2013.

[19] H. Waechter, D. Munzke, A. Jang, and H.-P. Loock, "Simultaneous and Continuous Multiple Wavelength Absorption Spectroscopy on Nanoliter Volumes Based on Frequency-Division Multiplexing Fiber-Loop Cavity Ring-Down Spectroscopy," *Analytical Chemistry,* vol. 83(7), p. 2719, 2011.

[20] C. Clark *et al.*, "Comparison of single-layer and double-layer anti-reflection coatings using laser-induced damage threshold and photothermal common-path interferometry," *Coatings,* vol. 6, no. 2, 2016.

[21] J. Sancho-Parramon, J. Ferré-Borrull, S. Bosch, A. Krasilnikova, and J. Bulir, "New calibration method for UV–VIS photothermal deflection spectroscopy set-up," *Applied Surface Science,* vol. 253(1), pp. 158-162, 2006.

[22] A. A. Maradudin, *Light Scattering and Nanoscale Surface Roughness*. New York: Springer, 2007.

[23] H. Wolfram and T. Wriedt, *The Mie Theory: Basics and Applications*. Berlin: Springer, 2012.

[24] G. Harry, T. P. Bodiya, and R. DeSalvo, "Optical scatter," in *Optical Coatings and Thermal Noise in Precision Measurement*. Cambridge: Cambridge University Press, 2012, p. 168.

[25] C. K. Carniglia, "Scalar Scattering Theory for Multilayer Optical Coatings," *Optical Engineering,* vol. 18, no. 2, pp. 104-115, 12, 1979.

[26] L. L. Service. "Total integrated scattering (TIS)." http://lidaris.com/glossary-2/total-integrated-scattering-tis/ (accessed.

[27] S. Schröder, S. Gliech, and A. Duparré, "Measurement system to determine the total and angle-resolved light scattering of optical components in the deep-ultraviolet and vacuum-ultraviolet spectral regions," *Applied Optics,* vol. 44, no. 29, pp. 6093-6107, 2005.

[28] L. Mazule, S. Liukaityte, R. C. Eckardt, A. Melninkaitis, O. Balachninaite, and V. Sirutkaitis, "A system for measuring surface roughness by total integrated scattering," *Journal of Physics D: Applied Physics,* vol. 44, no. 50, p. 505103, 2011.

[29] P. Kadkhoda *et al.*, "International round-robin experiment to test the International Organization for Standardization total-scattering draft standard," *Applied Optics,* vol. 39, no. 19, pp. 3321-3332, 2000.

[30] *ISO 21254-1:2011: Lasers and laser-related equipment - Test methods for laser-induced damage threshold - Part 1: Definitions and general principles*, I. O. f. Standardization, Geneva, Switzerland, 2011.

[31] T. Tolenis *et al.*, "Next generation highly resistant mirrors featuring all-silica layers," *Scientific Reports,* vol. 7, no. 1, p. 10898, 2017.

[32] C. Xu, Y. Zhao, Y. Qiang, Y. Zhu, L. Guo, and J. Shao, "Comparison of laser-induced damage in Ta2O5 and Nb2O5 single-layer films and high reflectors," *Chin. Opt. Lett.,* vol. 9, no. 1, p. 013102, 2011.

[33] S. Xu *et al.*, "Ultrafast Electronic Excitation in CaF2Crystals," *Japanese Journal of Applied Physics,* vol. 44, no. 11, pp. 8201-8203, 2005.

[34] *ISO 21254-2:2011: Lasers and laser-related equipment - Test methods for laser-induced damage threshold - Part 2: Threshold determination.*, I. O. f. Standardization, Geneva, Switzerland, 2011.

CHAPTER 4–CONCAVE MULTILAYER DIELECTRIC MIRRORS

In this chapter, the fabrication steps of curved mirrors for Fabry-Perot cavities are described. The protocol of preparation and fabrication of curved glass substrates using CO_2 laser ablation are presented. The curved substrates were coated with a multilayer high reflectance quarterwave coating of either IAD E-beam evaporated ZrO_2/SiO_2 or TiO_2/SiO_2. The surface profile, curvature and surface roughness of the concave mirrors were characterised using AFM and confocal microscopy. The fabrication and the characterisation of curved mirrors were completed during a research secondment in the Nano-Photonics group at University of Basel in Switzerland.

4.1 Curved mirrors for Fabry-Perot cavities

4.1.1 Concave templates fabrication methods

The most common fabrication methods of curved mirror for high finesse cavities are Focused Ion Beam or FIB milling(Figure 3.1a)[1-4] and CO_2 laser ablation[5, 6]. While both methods allow the fabrication of curved glass templates with radii of curvature ranging from several hundreds of microns to less than a micron and have a subnanometer surface roughness, FIB milling requires substantial capital investment. Other methods reported in the literature such as femtosecond laser wet etching[7, 8] applied to the fabrication of curved MicroLens Arrays or MLA (Figure 4.1.b) have the potential to realise ultralarge area fabrication, as shown in [9]. However, the surface roughness of the fabricated curved glass substrates was evaluated to be approximately several nanometers, which is incompatible with low loss dielectric mirrors for high finesse cavities. Therefore, CO_2 laser ablation is generally retained as a low-cost fabrication method fulfilling micron sized and near-gaussian shaped craters with low surface roughness.

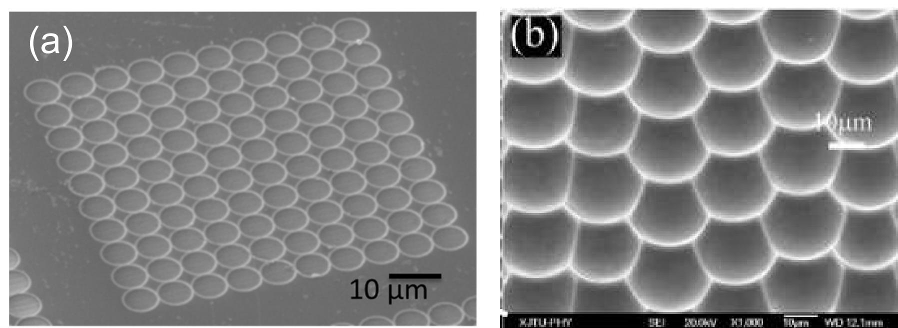

Figure 4.1: *Examples of curved substrates realised by two different fabrication methods. a) SEM scan of an array of curved templates for open microcavities realised by Oxford High-Q using focused ion beam (FIB) milling from [10]. b) 25° tilted-view scanning electron micrograph of quasi-periodic microlens arrays (MLA) fabricated using single-pulsed femtosecond laser wet etch from [9].*

CO_2 laser ablation allows a controlled fusion of a thin layer of the glass substrate using a laser pulse with a determined length and power. The penetration depth of the CO_2 laser ablation was estimated to 30 µm[11] which limits the heating of the substrate. The heated layer of the substrate melts and evaporates. The remaining fused material is pulled by

surface tension resulting in a smooth and gaussian shaped crater before the material solidifies again[12].

4.1.2 Design of curved mirrors

The fabrication protocol of curved mirrors for plano-concave Fabry-Perot cavities is shown in Figure 4.2. The protocol starts from a planar quartz substrate(a) where a mesa pattern is formed creating a step like pattern (b). A crater is created within the mesa using CO_2 laser ablation(c). The crater is finally coated with a multilayer dielectric coating(d). The fabrication steps of curved substrates are detailed in Section 4.2.

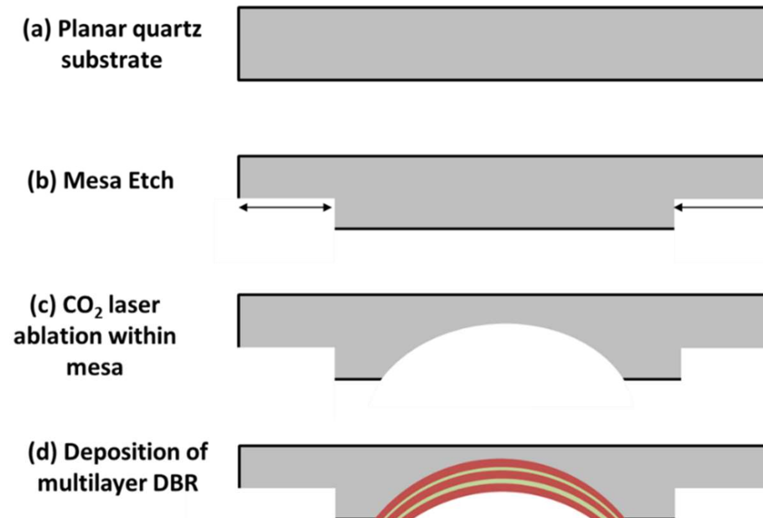

Figure 4.2: *Process steps for high reflectance curved mirrors fabrication.*

4.2 Fabrication of spherical substrates

4.2.1 Substrate cleaning and preparation

Curved mirror substrates are made from amorphous quartz 2-inch wafers provided by Planoptik. The wafers are 200 ± 10 μm thick and double side polished. The vendor specified a roughness of below 1 nm. A photoresist is spincoated on the wafers to protect the surface during the cleaving process. Quartz wafers were cleaved into 5 mm × 5 mm size samples. The photoresist is washed off from the cleaved samples using solvents. Each sample was cleaned separately on a spin coater at a speed of 1700 rpm and for 80 s by introducing gradually and in the following order acetone, isopropanol and ethanol. The cleaned samples were dried for two minutes on a hot plate set at 105 °C.

4.2.2 *Mesa pattern*

Dust particles and contaminants are a major concern during the alignment of plano-concave microcavities. Contaminants between the top and bottom mirrors of the cavity can increase the cavity length and consequently the cavity mode volume. Etching a small area on the quartz substrate allows an optimum alignment of the cavity mirrors by avoiding any increase of the cavity length. A round mesa structure was etched into the quartz substrate prior to CO_2 laser ablation and the deposition of the coating according to Figure 4.3:

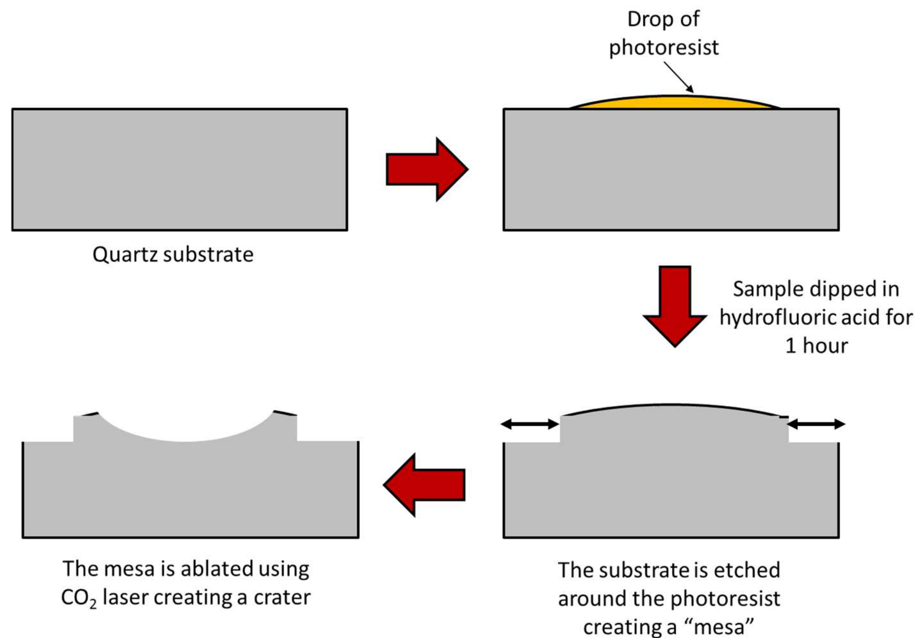

Figure 4.3: *Processing steps for a mesa pattern and curved templates fabrication. Quartz substrate must be cleaned before proceeding with the mesa etch; a drop of the photoresist is applied to the surface of the coating. After an immersion of the substrate in hydrofluoric acid solution for an hour, a mesa pattern is formed. After the mesa etch, the sample is carved using CO_2 laser ablation.*

A mesa pattern can be achieved by two different methods. The first method consisted of etching a circular mesa in the glass substrate as shown in Figure 4.4. A small amount of ma-N 415 photoresist was applied in the centre of the substrate using a toothpick. The photoresist was set afterwards on a hot plate at 105 °C for few seconds until the photoresist was hard. The sample was then transferred to a suitable holder to prepare for the acid etching step. The samples were dipped for an hour in a solution mixture of hydrofluoric acid. The etching rate of the solution was around 3 nm/s. Consequently, the height of the mesa is estimated to 10.8 µm after an hour of chemical reaction. The sample was successively rinsed in three volumes of water to eliminate any acid residue and left overnight in water.

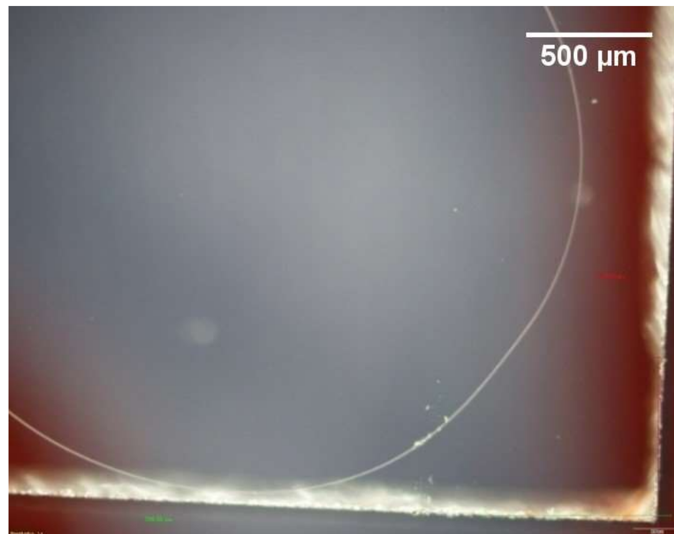

Figure 4.4: *Circular mesa etched in a quartz substrate.*

The second method relied on photolithography. Multiple square mesas were etched in the substrate as represented in Figure 4.5.

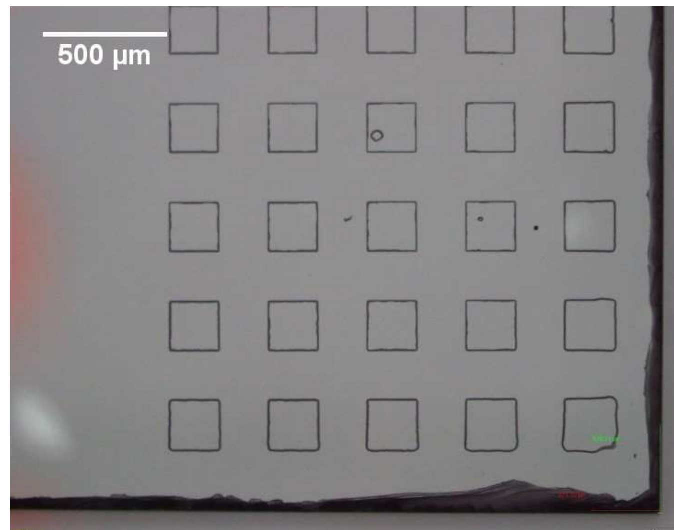

Figure 4.5: *Square mesas etched in a quartz substrate using photolithography.*

The quartz sample is dehydrated on a hot plate at 150 °C for 10 to 20 minutes. A primer of the photoresist is applied at a spin speed of 1500 rpm for 35 seconds. The photoresist (ma-N 415) was spin coated at 6000 rpm for 40 seconds. After the spin coating, a photoresist thickness of around 2 μm is expected from the constructor datasheet. The sample was then baked on hot plate for 90 seconds at 95 °C. Afterwards, the sample was aligned with an ohmic pattern on the photolithography mask. The sample was exposed for 15 seconds to a light power of 30 W. After exposure, the sample was placed in maD-332s developer for 3 minutes while stirring. Finally, the sample was rinsed in distilled water for 60 seconds and dried using compressed nitrogen. The chemical etching in hydrofluoric acid mix was similar to the procedure described for the round mesa sample.

While the first patterning method allowed a faster mesa etching with less process steps, the second method allowed the production of mesas of regular size and shape which facilitates the location of curved templates within the mesa and an easier alignment of the

top curved mirror and the bottom plane mirror during the assembling of the cavity. Some process defects that can be noted in Figure 4.5 are caused by the presence of contaminants on the aligning mask. The contaminated areas are not developed properly creating holes in the mesa pattern.

4.2.3 CO_2 laser ablation

The CO_2 laser ablation setup used for curved template fabrication is shown in Figure 4.6. This setup allows a controlled melting of the substrate surface using a CO_2 laser pulse. The operational wavelength of the CO_2 laser is 10.6 µm which is compatible with glass substrates due to the strong absorption of glass in this wavelength range[11].

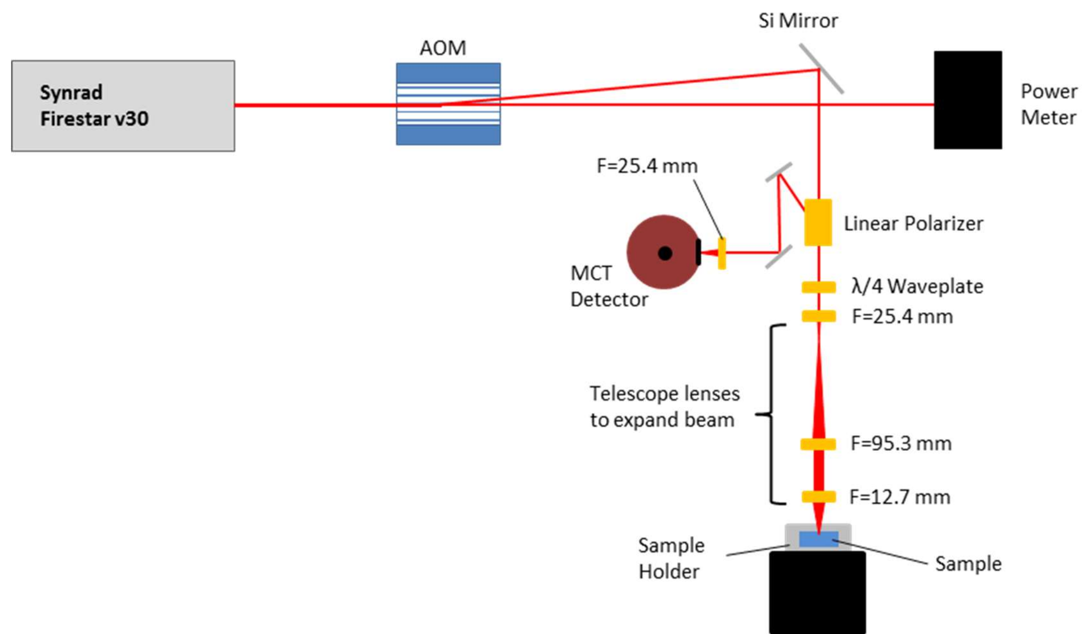

Figure 4.6: *CO_2 laser ablation setup developed by the Nano-photonics group at University of Basel. Setup diagram extracted from[13].*

In this setup, a Synrad Inc., Firestar v30 laser is used. The pulse frequency of the laser is of 20 kHz and the pulse length is 20 µs. A Brimrose Corporation, GEM40-1-10.6 acousto optical modulator (AOM) allowed the control of the incident power of the laser and hence the exposure time of the substrate to laser ablation. A quarterwave plate (II-VI infrared, WPM-10.6-.35-90-U) along with a linear polarizer (Thorlabs Inc., PHB-7) are inserted into the beam path to avoid back reflections and assure a long-term stability to the laser power. The Brewster plates in the polarizer reflect the vertically polarized light, which was then directed towards a nitrogen cooled mercury-cadmium-telluride or MCT photodetector (Hamamatsu Photonics K.K., P9697-01). Two ZnSe lenses of focal lengths of 25.4 mm and 95.3 mm (ULO Optics Ltd.) inserted after the quarterwave plate act as telescope lenses to expand the beam diameter. Finally, the beam was focused on the sample using a lens with a focal length F equal to 12.7 mm. The geometry distribution of the curved templates is presented in Figure 4.7 for three focal lengths values (12.7, 25

and 150 mm). A large range of craters was produced by varying the pulse power from 270 mW to 320 mW.

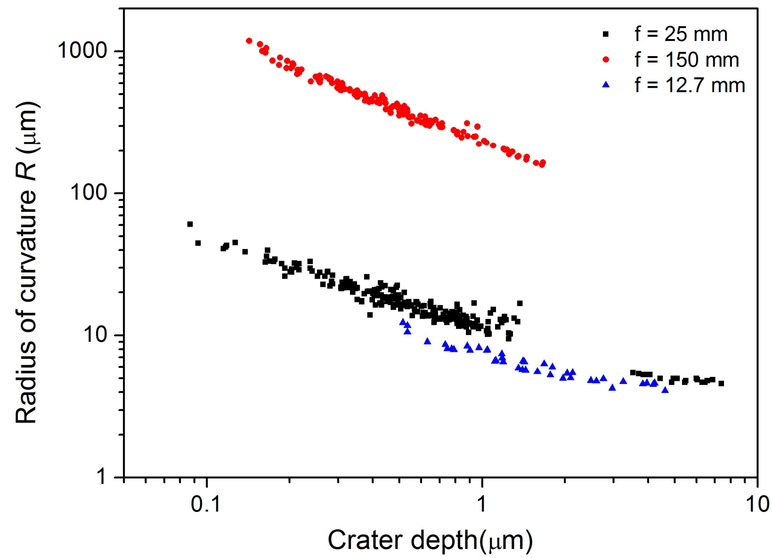

Figure 4.7: *Geometry parameters of curved templates fabricated by CO_2 laser ablation using different focal lengths. Reproduced with permission from the Nano-Photonics group at University of Basel.*

A strong correlation between the crater depth and the radius of curvature for the curved fabricated mirrors was noted previously[14]. Using a focal length of 150 mm, the radius of curvature of the fabricated templates varied between 100 µm and 1 mm and the crater depth between 0.1 µm and 1 µm. A long focal length increased the size of the focussed spot and slowed the melting of the glass substrate leading to wide and shallow craters. Achieving smaller size craters is possible using a shorter focal length lens. With a focal length of 25 mm or 12.7 mm, the radius of curvature can be reduced to 5 µm; the corresponding crater depth is 8 µm. This geometry is however unsuitable for microcavity operation as the cavity resonance becomes unstable for cavity lengths superior to the radius of curvature R (or 2R) in a plano-concave geometry[14, 15]. A post-processing method proposed in [15] allowed the reduction of the crater depth to 1.4 µm for a radius of curvature of 5 µm by coating the ablated crater with a photoresist and consuming it with two reactive ion etching steps while maintaining the original surface smoothness. In the same work, craters of smaller radii of curvature of 1.2 µm and shallow depths of 1 µm have been also achieved using a pre-etching of the glass substrate before the CO_2 laser ablation. In this study, a lower laser power range is used (from 220 mW to 250 mW) to produce shallow craters with low radii of curvature.

During the fabrication process, the sample was mounted on an xyz stage motor from Physik Instrumente GmbH, M (112.12S). The reflected radiation of the laser focused on the MCT detector allowed positioning the sample. The stage motor and the fabrication parameters were controlled by a LabVIEW interface as represented in Figure 4.8.

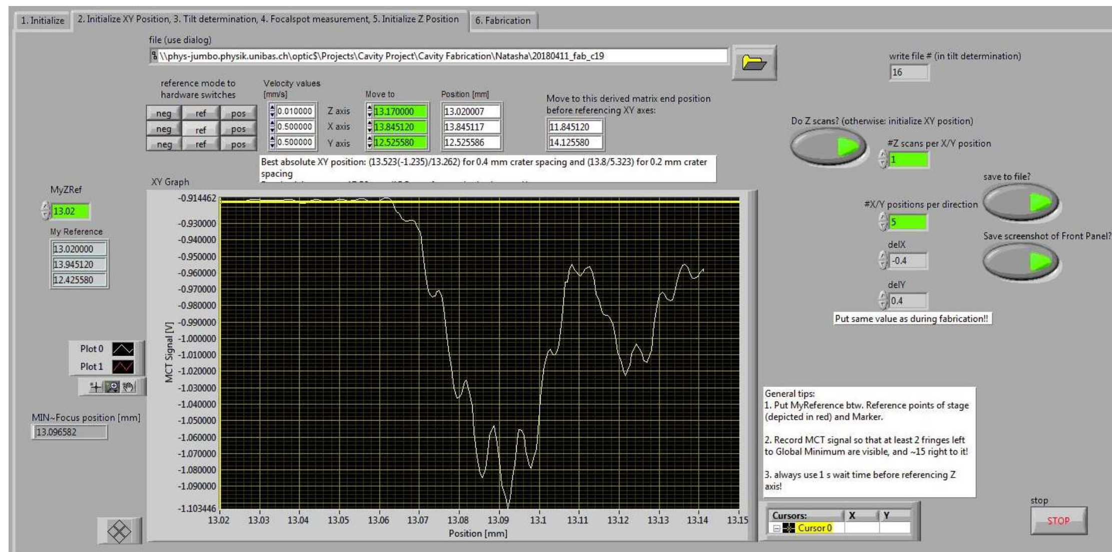

Figure 4.8: *LabVIEW user interface controlling the xyz stage motor and allowing the setting of the (x,y) coordinates origin and the tilt of the z position. The setup interface was developed by the Nano-Photonics group at University of Basel.*

At a given z reference, the MCT signal was recorded until a global minimum was visible with at least two fringes to the left of the minimum (Figure 4.8). The position of the signal at the minimum is used during the fabrication step as a focus set for the CO_2 laser.

The fabrication parameters are also entered in the same LabVIEW interface. The pulse length was set to 0.5 s. The laser power is indirectly monitored in the user interface using the AOM voltage. The AOM is driven at 40 MHz by a modulator driver modulated by an external voltage varying between 0 and 1 V. The laser power is proportional to the modulation voltage. Further details about laser power characterisation and AOM calibration are available in [13]. A repetition matrix of 5×5 was set in the fabrication tab, allowing the ablation of 25 templates per sample. The AOM voltage was set to decrement after each ablated spot resulting in a distribution of radii of curvature and craters depths.

4.3 Coating of spherical mirrors

The curved glass substrates were coated with 29 layers of IAD E-beam evaporated ZrO_2/SiO_2 and TiO_2/SiO_2, corresponding to a $(HL)^{14}$ H structure. At 640 nm wavelength, the respective quarterwave physical thicknesses of ZrO_2, TiO_2 and SiO_2 are of 78 nm, 72 nm and 110 nm. The deposition parameters are summarised in Table 4-1.

Material	Method	Source material	Process pressure(mbar)	Deposition rate(Å/s)	Backfill gas(sccm)	Substrate heating(°C)
TiO_2	IAD E-beam	TiO_2 pellets	1.8×10^{-4}	1	O_2: 35	110
ZrO_2	IAD E-beam	Zr tablets	1.7×10^{-4}	2	O_2:50	110
SiO_2	IAD E-beam	SiO_2 pellets	9.6×10^{-5}	2	none	110

Table 4-1: *Deposition parameters of TiO_2, SiO_2 and ZrO_2 by IAD E-beam evaporation used for high reflectance curved mirrors coatings.*

Two examples of ZrO_2/SiO_2 curved mirrors are provided in Figure 4.9 and 4.10. The ablated structures can be identified within the square and round mesas patterned in the glass substrates before CO_2 laser ablation.

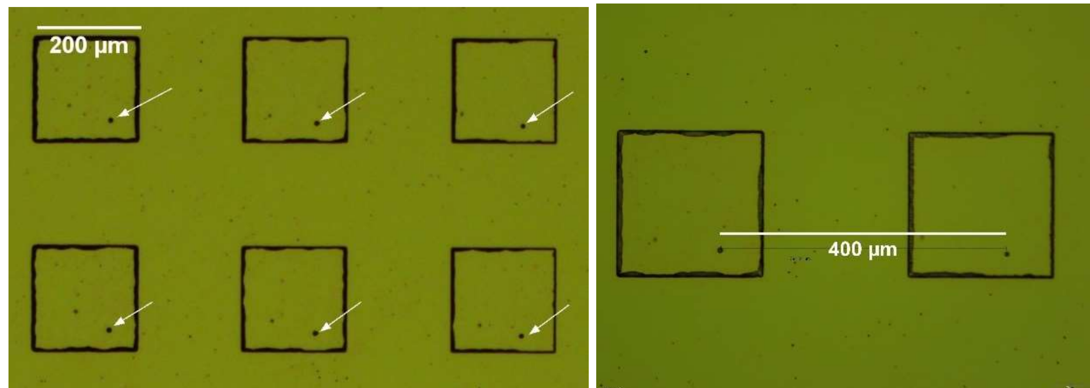

Figure 4.9: *curved mirrors within square mesa templates coated with a 29-layer E-beam evaporated ZrO_2/SiO_2.*

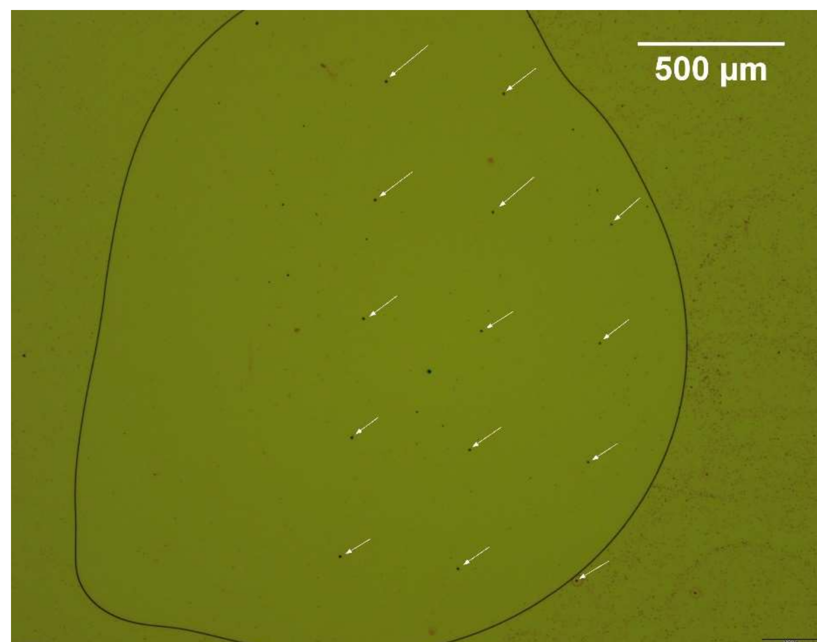

Figure 4.10: *Curved mirrors within a circular mesa coated with a 29-layer E-beam evaporated ZrO_2/SiO_2.*

4.4 Characterisation of curved mirrors

4.4.1 Confocal microscopy

After coating, the curved mirror's curvature and geometry are determined using a 3D confocal laser scanning microscope (Keyence,VK–x200). The height resolution is of 1 nm and the lateral resolution is 5 nm. Optical and height profiles of a curved mirror obtained using Keyence confocal microscope are given in Figure 4.11. The mirror was coated with a 29-layer E-beam evaporated ZrO_2/SiO_2. A radius of curvature of 5.8 µm and a crater depth of 1.4 µm were obtained for the curved mirror.

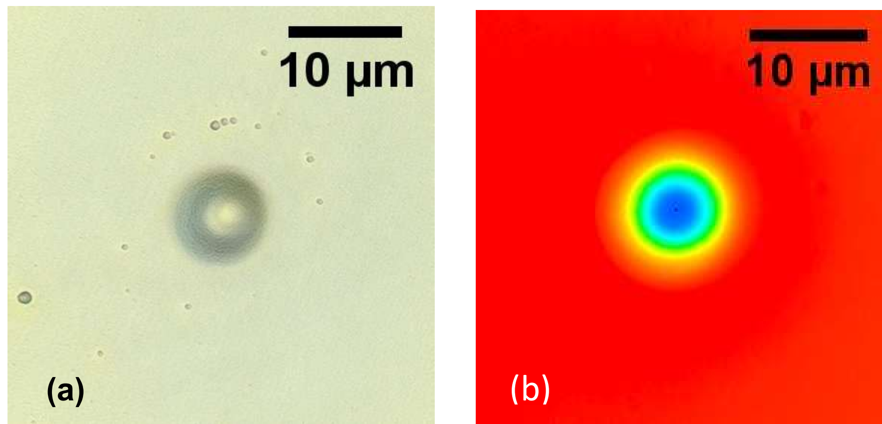

Figure 4.11: *(a) Optical and (b) height profiles of curved mirror using Keyence VK–x200 confocal microscope and VK-H1XAE analysis application. The mirror is coated with a 29-layer E-beam evaporated ZrO_2/SiO_2. The radius of curvature of the crater is of 5.8 µm corresponding to a depth of 1.4 µm.*

The geometry of the curved mirrors was determined using VK-H1XAE analysis application of the confocal microscope as shown in Figure 4.12. The depth of the curved mirrors was determined from the cross-section of the crater. A tilt correction is hence necessary to assure the flatness of the surface. The radius of curvature is obtained by a 3-segment circular fit 2 µm around the centre of the mirror.

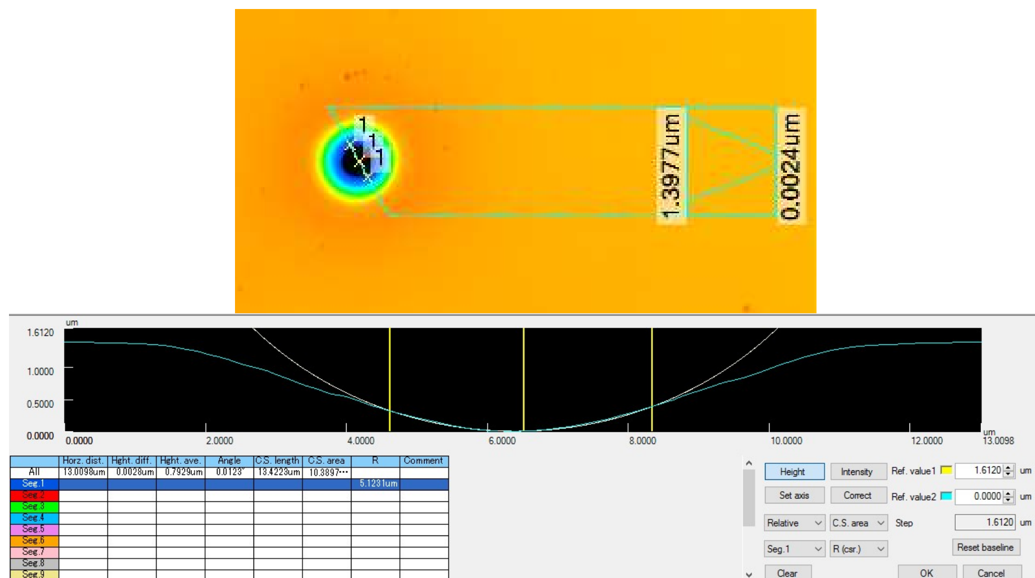

Figure 4.12: *Fit operation of curved template fabricated by CO_2 laser ablation using a VK-H1XAE Keyence analysis application. The program performs a correction of the tilt of the sample and extracts the geometry of the crater. The depth of the crater is calculated from its cross-section profile and the radius of curvature is determined using a circular fit 2 µm around the centre of the crater.*

By varying the ablation power from 220 mW to 250 mW with a pulse length of 0.5 s, a controlled range of curved mirrors is obtained with radii of curvature varying from 22 µm down to 5 µm and corresponding to craters depth from 0.1 µm to 1.4 µm (Figure 4.13). In this case, a logarithmic correlation can be noted between the crater depth and the radius of curvature.

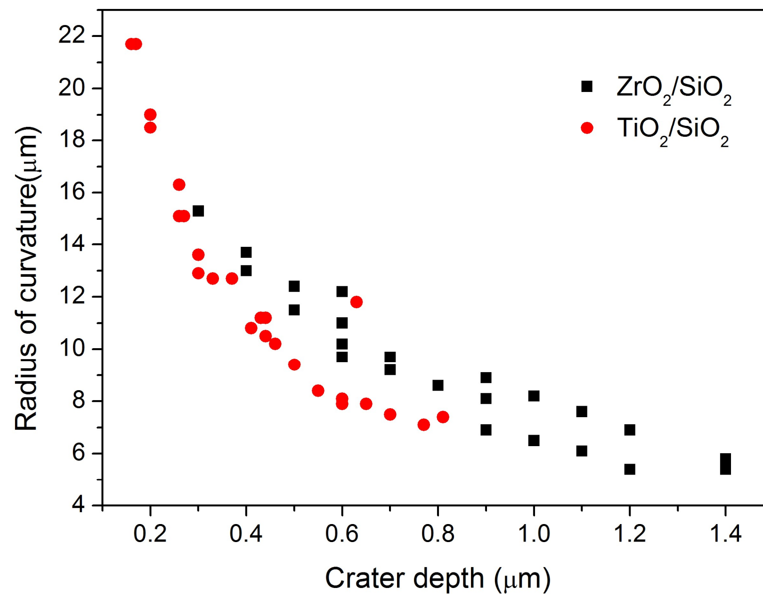

Figure 4.13: *Distribution of radius of curvature according to crater depth for 29-layer IAD E-beam evaporated ZrO_2/SiO_2 and TiO_2/SiO_2 curved mirrors. Datapoints are obtained using VK-H1XAE Keyence analysis application for 25 curved mirrors.*

Both ZrO_2/SiO_2 and TiO_2/SiO_2 curved mirrors follow the same distribution. However, datapoints are slightly shifted, which show slight variations during the ablation of the glass substrates and can be also justified by fitting errors of the craters using the confocal microscope analysis application.

4.4.2 Atomic force microscopy

AFM measurements have been performed in tapping mode on a set of curved mirrors of both ZrO_2/SiO_2 and TiO_2/SiO_2 coatings using Veeco Dimensions 3100 system and Bruker silicon tips. AFM profiles illustrating the mirrors geometry distribution presented are shown in Figure 4.14 and 4.15.

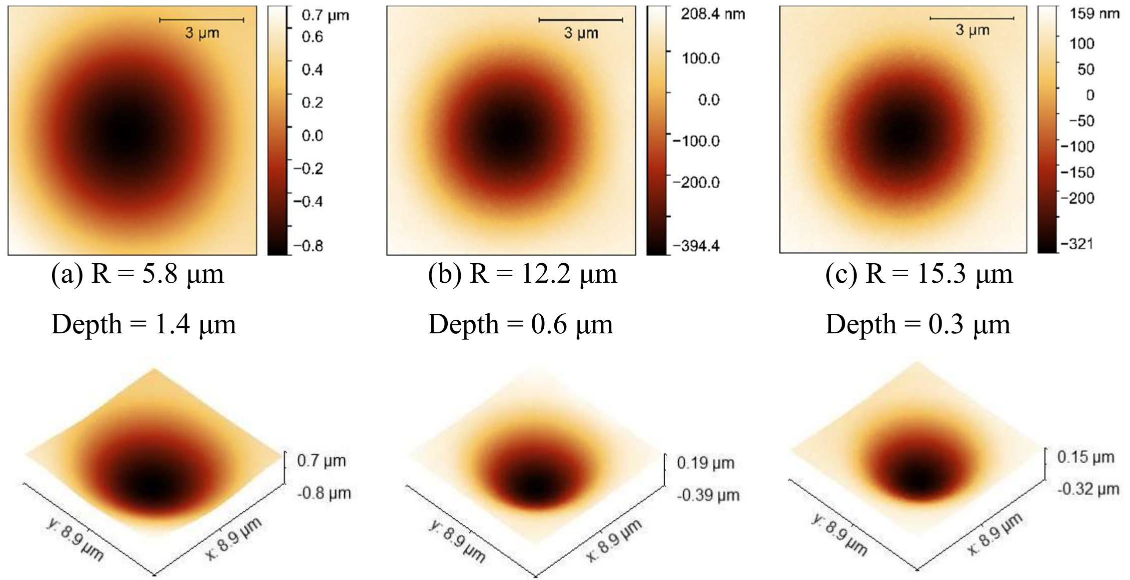

Figure 4.14: *Two dimensional and three-dimensional AFM height profiles of curved mirror templates. The templates have been coated with 29-layer IAD E-beam deposited ZrO_2/SiO_2 coating. AFM scans were performed on an area of 9 µm × 9 µm using a scan speed of 0.5 Hz and a sampling matrix of 512 × 512.*

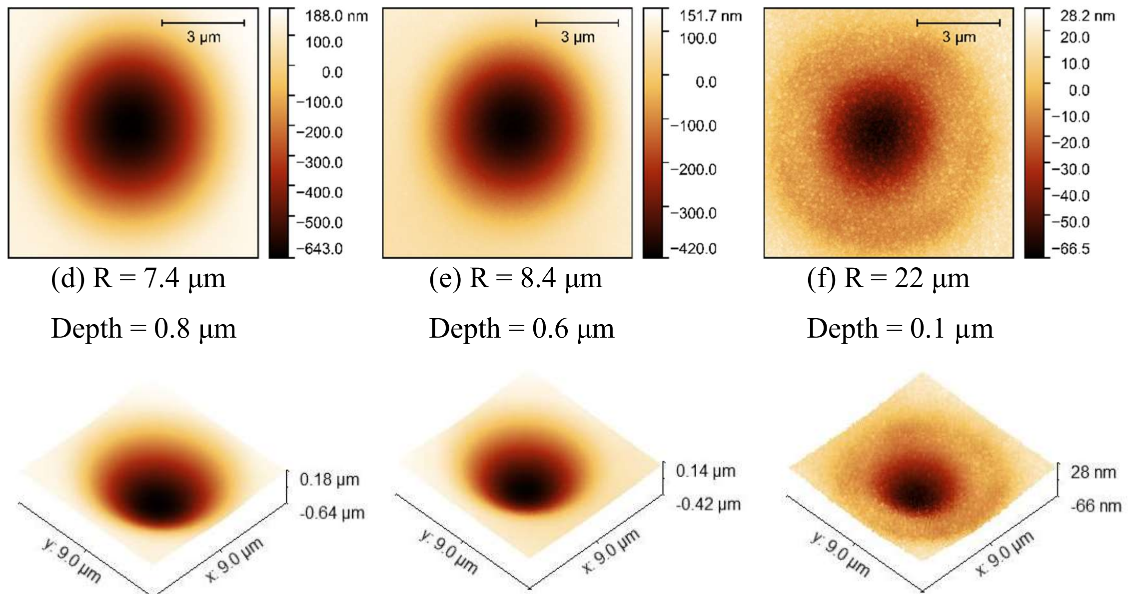

Figure 4.15: *Two dimensional and three-dimensional AFM height profiles of curved mirror templates. The templates have been coated with 29-layer IAD E-beam deposited TiO_2/SiO_2 coating. AFM scans were performed on an area of 9 µm × 9 µm using a scan speed of 0.5 Hz and a sampling matrix of 512 × 512.*

Figure 4.16 shows the AFM profiles for curved mirrors annotated as per Figure 4.14 and 4.15. The mirrors have nearly parabolic smooth profiles which allow the calculation of the radii of curvature using an appropriate fitting tool.

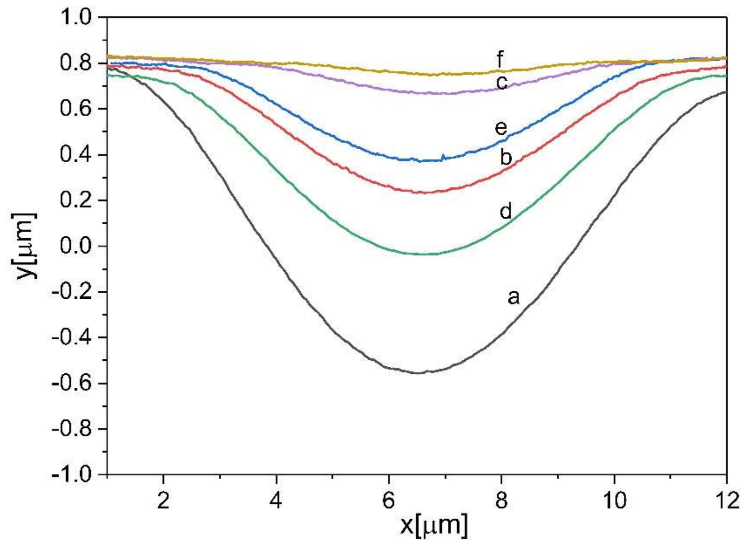

Figure 4.16: *AFM height profiles for curved mirrors presented in Figures 4.14 and 4.15.*

Using the curvature data processing tool of Gwyddion software[16] presented in Figure 4.17, the radius of curvature can be determined from the AFM scan by tracing two cross-section lines intersecting in the centre of the crater. The corresponding profiles are plotted and the radii of curvature are calculated below the graph. Both profiles overlap up to 1 µm around the centre. Beyond this range, the profiles split because the crater is not symmetrical over the whole crater area.

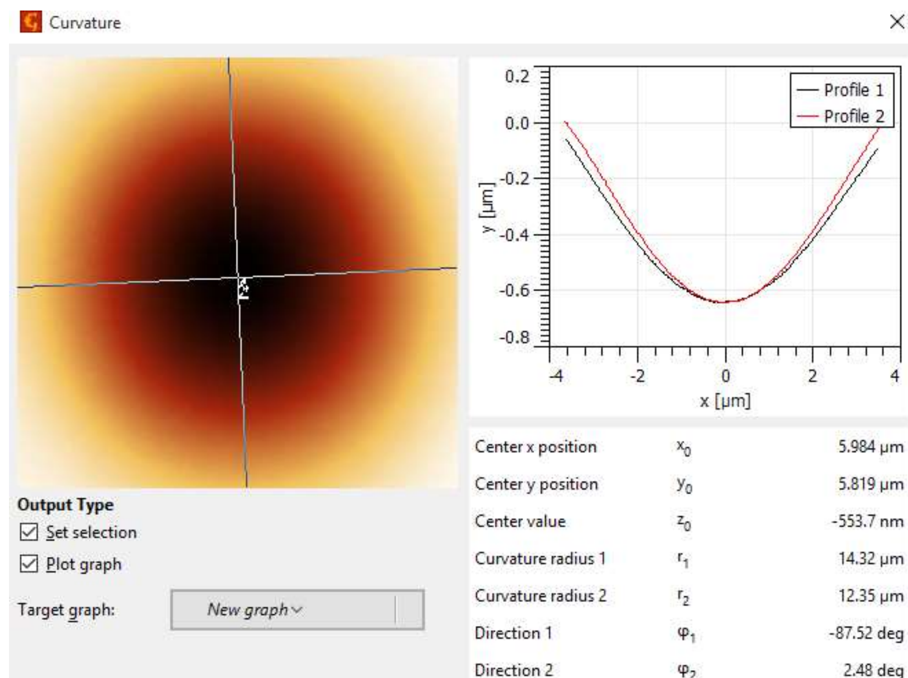

Figure 4.17: *Curvature fit module of Gwyddion[16] software allowing the calculation of the radius of curvature. The analysis tool calculates the radius of curvature from the profile of the crater. Because the crater is not symmetrical, the surface profiles are not identical leading to two different radii of curvature.*

The centre of the AFM profiles presented in Figure 4.16 is fitted 2 µm around the centre using a Boltzmann step filter[17]. Fitting results are shown in Figure 4.18.

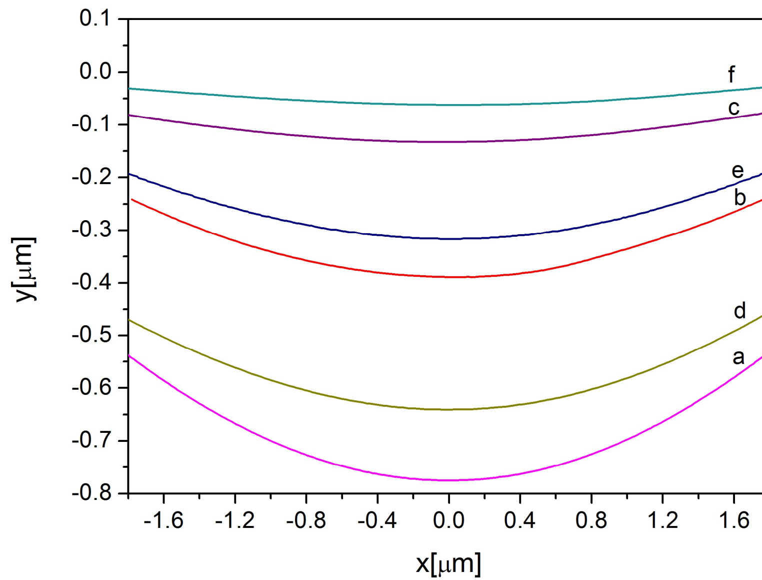

Figure 4.18: *Fitted AFM profiles of craters presented in Figure 4.14 and 4.15 using the curvature module of Gwyddion software for curved mirrors presented in Figures 4.14 and 4.15. The AFM profile has been fitted 2 µm around the centre of the mirror using a Boltzmann filter.*

After analysing the curved mirror by both AFM and confocal microscopy, the geometry distribution can be compared by both methods as shown in Figure 4.19 for 25 datapoints. The calculation of radii of curvature and mirror depth using AFM measurements is indeed very close to the one performed by Keyence confocal microscope. However, datapoints are not the same due to the difference between fitting methods. For Keyence datapoints, a 3-segment circular fit 2 µm around the centre of the mirror is used to determine the radius of curvature while a Boltzmann fit was used for AFM profiles in a narrower area of the crater (limited to 1 µm around the centre of the mirror). Data fitting using Keyence analysis application also induces a substantial error (up to 1 µm) in the radii of curvature calculation.

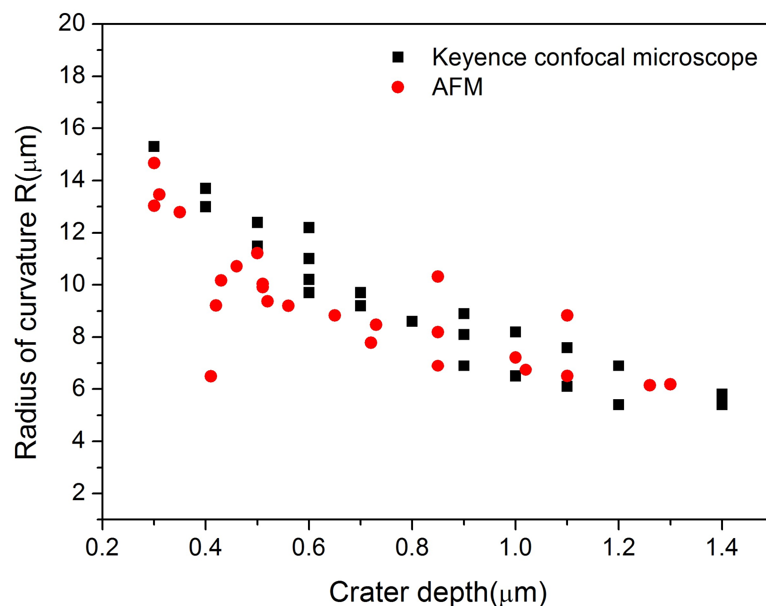

Figure 4.19: *Distribution of curved mirrors geometries using Keyence confocal microscope and AFM. Datapoints originate from the same sample and represent dimensions for 25 craters coated with a 29-layer IAD E-beam deposited ZrO_2/SiO_2.*

Furthermore, both AFM and Keyence profiles from the same curved mirror are plotted on the same graph in Figure 4.20. The mirror was coated with a 29-layer IAD E-beam deposited ZrO_2/SiO_2. The estimated radius of curvature and the mirror depth from Keyence profile are of 7.5 µm and 0.83 µm while the estimated radius of curvature and the crater depth from the AFM profile are of 7.96 µm and 0.8 µm. It can be noted indeed that both plots are nearly identical. However, the crater imaged using Keyence confocal microscope is slightly deeper.

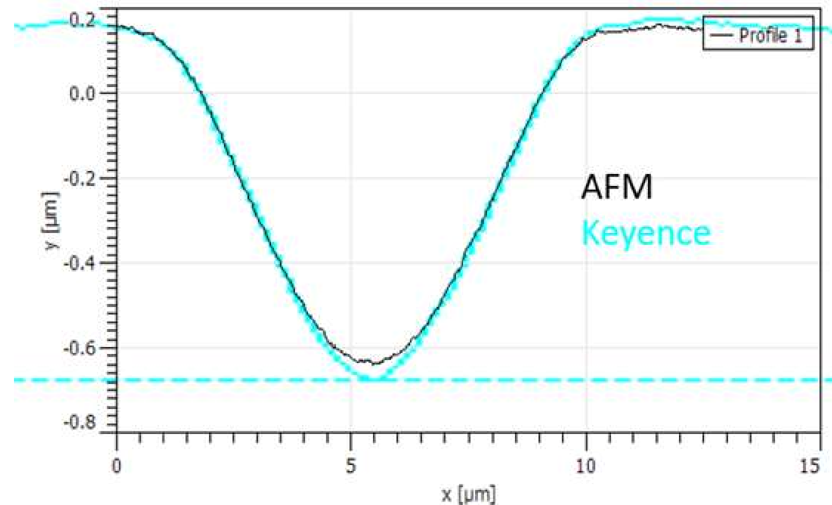

Figure 4.20: *Comparison between an AFM profile and confocal profile for the same curved mirror coated with 29-layer IAD E-beam deposited ZrO_2/SiO_2.*

Using AFM measurements of 25 curved mirrors from the same sample, a statistical study was performed for curved mirror roughness. The average root mean square surface roughness Rq is estimated as 2.2 nm using the calculation tool of Gwyddion application (Figure 4.21.a). However, the roughness does not show a correlation to the mirror's depth and radius of curvature according to Figure 4.21.b.

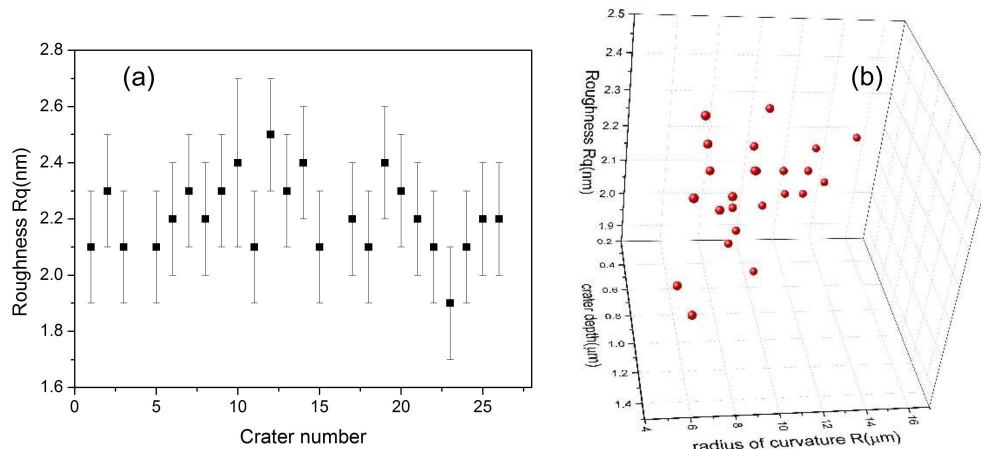

Figure 4.21: *a) Roughness measurements of curved mirrors using the roughness analysis tool of Gwyddion software. Datapoints originate from the same sample and represent roughness values for 25 mirrors coated with 29 layers of IAD E-beam deposited ZrO_2/SiO_2. b) Three-dimensional roughness plot as function of curved mirrors geometry.*

This roughness value is further confirmed on a smaller area of the coating (1 µm × 1 µm). A root mean square roughness of 2.3 ± 0.2 nm is obtained for scan area shown in

Figure 4.22. This high level of roughness is consistent with the grainy texture of the coating.

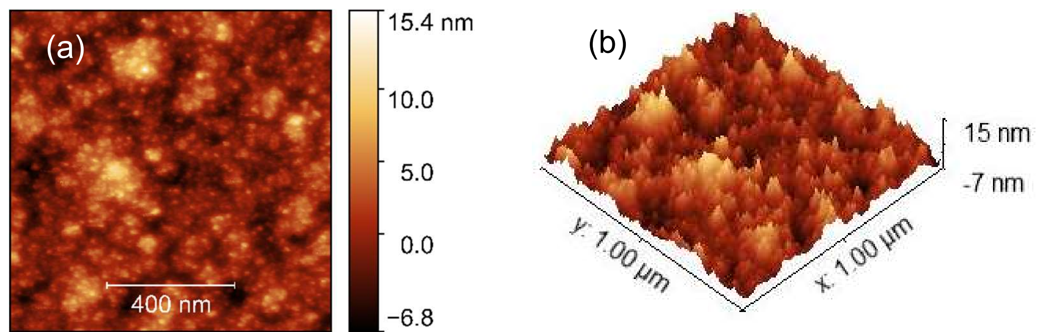

***Figure 4.22:** a) AFM height profile for a 29-layer IAD E-beam evaporated ZrO_2/SiO_2 curved mirror. The scan area is of 1 µm × 1 µm, the scan speed of 0.5 Hz and the sampling matrix of 512 × 512. b) Three-dimensional AFM profile of the same curved mirror.*

Despite a regular crater shape as shown in the previous AFM and confocal microscope characterisation and a suitable curved mirror geometry for cavity resonance, the surface roughness is still too high for the micro-cavity application as it will significantly increase the scatter losses. Surface roughness as low as 0.2 nm has been previously reported in [14, 15] for ion beam sputtered TiO_2/SiO_2 and Ta_2O_5/SiO_2 mirrors deposited on CO_2 laser ablated silica with micron-sized radii of curvature. Further process improvement is therefore required in order to reduce the surface roughness of the coating and limit the optical losses of the Fabry-Perot cavity.

4.5 Summary and conclusion

Concave mirror templates were fabricated using CO_2 laser ablation. The fabrication parameters were characterised. The curved glass substrates were coated with high reflectance quarterwave stacks of IAD E-beam evaporated ZrO_2/SiO_2 and TiO_2/SiO_2 centred at 640 nm wavelength. The coated mirrors were characterised using confocal microscopy and AFM. The mirrors radius of curvature ranges between 5 µm and 22 µm and the mirror depth between 0.2 µm and 1.4 µm. The geometry of the curved mirror was suitable for cavity resonance mode. The estimated roughness of the curved mirrors was 2.2 nm. This level of coating roughness was too high for the micro-cavity application as it would significantly increase the optical losses of the Fabry-Perot cavity. Opportunities for fabricating curved mirrors with lower surface roughness will be explored in future work, in order to achieve high-finesse Fabry-Perot cavities. IAD E-beam evaporated ZrO_2/SiO_2 and TiO_2/SiO_2 high reflectance coatings deposition conditions will be further optimised to reduce the final roughness of the coating.

4.6 Acknowledgments

The fabrication of curved glass templates was performed at the University of Basel with technical assistance of Dr. B. Petrak, Ms N. Tomm and Mr D. Najer during a secondment to the Nano-Photonics group. The characterisation of curved mirrors using AFM and

confocal microscopy was performed at the University of Basel. Access to characterisation facilities was kindly permitted by Dr. M. Schoenenberger and Prof. R. Warburton.

REFERENCES

[1] S. Dufferwiel *et al.*, "Valley-addressable polaritons in atomically thin semiconductors," *Nature Photonics,* vol. 11, p. 497, 2017.

[2] A. A. P. Trichet, P. R. Dolan, D. James, G. M. Hughes, C. Vallance, and J. M. Smith, "Nanoparticle trapping and characterization using open microcavities," *Nano Letters,* vol. 16, no. 10, pp. 6172-6177, 2016.

[3] S. Dufferwiel *et al.*, "Spin textures of exciton-polaritons in a tunable microcavity with large TE-TM splitting," *Physical Review Letters,* vol. 115, no. 24, p. 246401, 2015.

[4] S. Johnson *et al.*, "Tunable cavity coupling of the zero phonon line of a nitrogen-vacancy defect in diamond," *New Journal of Physics,* vol. 17, no. 12, p. 122003, 2015.

[5] D. Najer, M. Renggli, D. Riedel, S. Starosielec, and R. J. Warburton, "Fabrication of mirror templates in silica with micron-sized radii of curvature," *Applied Physics Letters,* vol. 110, no. 1, p. 011101, 2017.

[6] S. Bogdanovic *et al.*, "Design and low-temperature characterization of a tunable microcavity for diamond-based quantum networks," *Applied Physics Letters,* vol. 110, no. 17, 2017.

[7] M. He, X. Yuan, J. Bu, and W. C. Cheong, "Fabrication of concave refractive microlens arrays in solgel glass by a simple proximity-effect-assisted reflow technique," *Opt. Lett.,* vol. 29, no. 9, pp. 1007-1009, 2004.

[8] Z. Deng *et al.*, "Fabrication of large-area concave microlens array on silicon by femtosecond laser micromachining," *Opt. Lett.,* vol. 40, no. 9, pp. 1928-1931, 2015.

[9] F. Chen *et al.*, "Rapid fabrication of a large-area close-packed quasi-periodic microlens array on BK7 glass," *Opt. Lett.,* vol. 39, no. 3, pp. 606-609, 2014.

[10] L. C. F. A. Trichet, P. Dolan and J. M. Smith, "Topographic induced mode-coupling: Beyond FIB-milled single open microcavities," in *Nanophotonics and Micro/Nano Optics International Conference 2016*, Paris, 2016,

[11] R. J. Barbour, "A tunable microcavity for semiconductor quantum dots," P. R. Warburton, Ed., ed: Heriot-Watt University, 2010.

[12] D. Hunger, C. Deutsch, R. J. Barbour, R. J. Warburton, and J. Reichel, "Laser micro-fabrication of concave, low-roughness features in silica," *AIP Advances,* vol. 2, no. 1, pp. 012119-012119-6, 2012.

[13] L. E. Greuter, "self-assembled quantum dots in a fully tunable microcavity," Doctor of Philosophy, Departement Physik, University of Basel, Basel, 2015.

[14] L. Greuter *et al.*, "A small mode volume tunable microcavity: Development and characterization," *Applied Physics Letters,* vol. 105, no. 12, 2014.

[15] D. Najer, M. Renggli, D. Riedel, S. Starosielec, and R. J. Warburton, "Fabrication of mirror templates in silica with micron-sized radii of curvature," *Applied Physics Letters,* vol. 110, no. 1, 2017.

[16] D. Nečas and P. Klapetek, "Gwyddion, Free SPM data analysis software," ed.

[17] C. Zhuo and C. Zhong, "Filter-matrix lattice Boltzmann model for microchannel gas flows," *Physical review. E, Statistical, nonlinear, and soft matter physics,* vol. 88, no. 5, p. 053311, 2013.

CHAPTER 5–CONCLUSION AND FUTURE RESEARCH WORK

5.1 Summary

The fabrication of low loss multilayer dielectric mirrors requires a deep understanding of thin film deposition processes and of dielectric materials structural and optical properties. In Chapter 1, the physics of cavity QED and Fabry-Perot interferometer were presented. The advantage of using multilayer Bragg reflectors in high finesse microcavities over metal coatings have been also explained.

In Chapter 2, the fabrication and the characterisation of dielectric materials for high reflectance mirrors was presented. A selection of low index and high index materials was proposed. Materials studied represent the state of the art of dielectric materials for high finesse Fabry-Perot microcavities and were selected from common metal oxides, sulphides, selenides and fluorides. The main deposition methods employed were E-beam, ion assisted deposition, plasma assisted deposition and several sputtering methods. Common metal oxides such as hafnium dioxide, zirconium dioxide and niobium pentoxide were deposited by several evaporation and sputtering methods. Single layers of 500 nm thickness were deposited on glass substrates. The optical constants of the coatings were determined from fitted transmittance and reflectance data using Optichar fitting module. The surface roughness of the studied materials was measured using atomic force microscopy. Surface roughness obtained from AFM topography allowed a first estimation of scatter losses for single layer coatings. The structural and optical study of dielectric materials has shown very mitigated results. While some materials like thermally evaporated magnesium fluoride, lithium fluoride, lanthanum titanate were transparent in the studied wavelength range and have a low refractive index, their surface roughness (4 to 6 nm) is not acceptable for the desired application. Other materials such as zinc selenide showed a very high refractive index and a low surface roughness but suffer from a very high absorption. A good compromise between optical properties and surface roughness was found for PIAD E-beam niobium pentoxide, P-DC sputtered tantalum pentoxide, IAD E-beam titanium dioxide and zirconium dioxide as high index dielectrics and IAD E-Beam silicon dioxide as low index dielectric. Microwave assisted plasma sputtered (Microdyn) niobia high index in the studied wavelength range presents a very interesting possibility for high reflectance mirrors. However, the deposition process requires further optimisation in order to reduce the coating defects and high absorption. A bespoke stress apparatus was built to determine the intrinsic stress of single layer dielectrics. Single materials were deposited on 100 µm thick (100) silicon strips. Using the curvature method and Stoney's equation, the internal stress of thin film coatings was calculated. The studied materials showed overall very low stress values.

In Chapter 3, the design, fabrication and characterisation of high reflectance mirrors were presented. High reflectance mirrors were designed using Essential Macleod software. TiO_2/SiO_2, ZrO_2/SiO_2 and Nb_2O_5/SiO_2 mirrors were grown using IAD E-beam, plasma

assisted magnetron sputtering and microwave assisted magnetron sputtering deposition methods. Reflectance and transmittance were measured using optical spectroscopy. Spectral reflectance measurements did not allow to determine which mirror is the best as they are not sufficiently accurate. A cavity ring down spectroscopy experiment was presented to determine the reflectance and the optical losses of the mirrors with a higher accuracy. Total optical losses were deduced from transmittance and reflectance spectral measurement. The optical losses determined by this method were subject to large errors. Plasmacoat ZrO_2/SiO_2 and Nb_2O_5/SiO_2 and Microdyn Nb_2O_5/SiO_2 exhibited a high defect density caused by debris and contaminants ejected during the sputtering process.

The effect of increasing layers on the surface roughness of a multilayer coating was studied for IAD E-beam TiO_2/SiO_2 and ZrO_2/SiO_2 mirrors deposited on microscope slides using atomic force microscopy. AFM scans indicated that surface roughness of the top layer is influenced by the previously grown layers and showed a grain coalescence with increasing layers. The surface roughness of IAD E-beam TiO_2/SiO_2 and ZrO_2/SiO_2 mirrors was approximately of 2 nm which is too high for low loss Fabry-Perot cavities. In order to establish the effect of the substrate roughness on the mirror roughness, some mirrors were grown on superpolished etalons. The surface roughness was not reduced in the case of IAD E-beam TiO_2/SiO_2 which had a roughness of 1.8 ± 0.5 nm that was similar to roughness measured on microscope slides. The roughness of Plasmacoat Nb_2O_5/SiO_2 deposited on superpolished substrate was of 2.0 ± 0.5 nm. This high surface roughness is explained by an island growth mode. Smooth surfaces were obtained for Microdyn Nb_2O_5/SiO_2 and Plasmacoat ZrO_2/SiO_2 mirrors with a rms roughness of 0.3 ± 0.02 nm and 0.5 ± 0.02 nm respectively, which are more convenient for low loss Fabry-Perot cavities [1].

Roughness measurements allowed a first estimation of scatter losses at the reference wavelength. Estimated scatter for Microdyn Nb_2O_5/SiO_2 and Plasmacoat ZrO_2/SiO_2 mirrors were of 30 ppm and 90 ppm at 640 nm wavelength respectively. Total integrated scatter measurements were performed on IAD E-beam TiO_2/SiO_2, Plasmacoat Nb_2O_5/SiO_2 and ZrO_2/SiO_2 and Microdyn Nb_2O_5/SiO_2 mirrors grown on superpolished substrates using a normal incidence Ulbricht sphere setup. Low scattering losses were obtained for IAD E-beam TiO_2/SiO_2 mirror and are approximately equal to 200 ppm. The scatter losses for Microdyn Nb_2O_5/SiO_2 mirror are of 0.15 %. The highest scatter losses were obtained for Plasmacoat ZrO_2/SiO_2 and Nb_2O_5/SiO_2 mirrors and were approximately of 0.3 % to 0.8 %. The latest values are hundred times higher than scatter estimated from surface roughness. This great disparity can be explained by the multiple surface defects, craters and contaminants noted on the coating surface. Measured scatter losses for the studied mirrors are generally too high for the present application and further process optimisation is required to reduce the roughness and the defect density of the coatings.

A laser-induced damage study was performed on IAD E-beam TiO_2/SiO_2, Plasmacoat Nb_2O_5/SiO_2 and ZrO_2/SiO_2 and Microdyn Nb_2O_5/SiO_2 mirrors deposited on superpolished substrates using an S-on-1 test procedure. Laser-induced damage thresholds were determined by fitting experimental damage probability data with a Poisson derived model. The lowest LIDT values were reported for Microdyn and

Plasmacoat Nb_2O_5/SiO_2 mirrors which can be explained by the high defect density of the coating. Many damage morphologies were observed and were mainly induced by defects absorption, mechanical stress or overheating of the coating after applying a laser fluence exceeding the damage threshold. Typical morphologies included pin-point damage in the case of IAD E-beam TiO_2/SiO_2 at a fluence 1.66 J/cm^2 after 66 pulses and at 0.590 J/cm^2 after the 1000th- on -1 pulse. Other defect induced damages included a coating delamination for Microdyn Nb_2O_5/SiO_2 mirror at a fluence of 1.19 J/cm^2 after the 40th- on -1 pulse. Crater damage observed for Plasmacoat ZrO_2/SiO_2 mirror is caused by surface overheating. Finally, a typical absorption induced melting damage was reported for Plasmacoat Nb_2O_5/SiO_2 mirror after the 24th pulse at a fluence of 1.17 J/cm^2.

In Chapter 4, micron-sized radii concave mirror templates were fabricated using CO_2 laser ablation. The curved glass substrates were coated with high reflectance quarterwave stacks of IAD E-beam evaporated ZrO_2/SiO_2 and TiO_2/SiO_2 centred at 640 nm. The coated mirrors were characterised using confocal microscopy and AFM. Mirror dimensions determined by confocal microscopy agreed with dimensions determined by AFM. The mirrors radii of curvature varied between 5 μm and 22 μm and the mirror depth between 0.2 μm and 1.4 μm. The geometry of the curved mirrors is suitable for cavity resonance mode[2, 3]. The estimated roughness of the curved mirrors was of 2.2 nm. This level of coating roughness is too high as it would significantly increase the optical losses of the Fabry-Perot cavity.

5.2 Conclusions

The following conclusions can be drawn from the single layer study presented in Chapter 2:

- Using high energy processes such as ion assisted or plasma assisted depositions allow increased refractive index but could result in a higher absorption as demonstrated for hafnia, niobia, zirconia and silica layers.

- With the exception of hafnium dioxide, the lowest surface roughness was generally obtained for metal oxides deposited by IAD E-beam and magnetron sputtering.

- Many thermally evaporated materials are unsuitable for low loss mirrors due to either high absorption or high scatter.

In Chapter 3, multilayer mirrors were grown using IAD E-beam, plasma assisted sputtering and microwave assisted sputtering. The following conclusions can be made:

- The reflectance and the transmittance of multilayer mirrors can be determined with 0.5 % and 0.1 % accuracy respectively using optical spectroscopy.

- For IAD E-beam process, the surface roughness of the top layer depends on the previously deposited layer. The surface roughness of the coating is increased by increasing the number of layers due to a grain coalescence and nuclei growth as demonstrated for IAD E-beam ZrO_2/SiO_2 and TiO_2/SiO_2.

- Surface roughness of multilayer coatings is not necessarily improved by the use superpolished substrates as demonstrated for TiO_2/SiO_2 and Plasmacoat Nb_2O_5/SiO_2 mirrors.

- It is possible to achieve low surface roughness as required for cavity applications using plasma assisted and microwave assisted magnetron sputtering as demonstrated for Plamacoat ZrO_2/SiO_2 and Microdyn Nb_2O_5/SiO_2 mirrors. These late deposition systems demonstrated a high potential in producing smooth surfaces and consist a new thin film deposition alternative for multilayer dielectric quarterwave mirrors in the visible region.

- Estimating scatter losses from surface roughness measurements can be misleading as it does not consider surface contaminants and defects. A more accurate scatter measurement is provided by total integrated scattering measurement thanks to data reduction method explained in section 3.4.4.

- The lower optical losses were obtained for TiO_2/SiO_2 deposited by IAD E-beam and can be estimated to 0.12 %. However, a more accurate measurement of absorption losses is required to confirm this statement.

In Chapter 4, curved glass templates were fabricated using CO_2 laser ablation and coated with multilayer TiO_2/SiO_2 and ZrO_2/SiO_2 deposited by IAD E-beam. This study allows to make the following conclusions:

- IAD E-beam deposition allows the fabrication of micron sized spherical mirrors as previously achieved by ion beam sputtering[2, 4, 5]

- The geometry of curved mirrors fabricated by IAD E-beam is suitable for cavity resonance mode[2, 3].

- A logarithmic correlation has been demonstrated between the radius of curvature and the depth of mirrors fabricated by IAD E-beam deposition for ZrO_2/SiO_2 and TiO_2/SiO_2 mirrors.

- The mirrors geometry can be either determined by AFM or confocal microscope as both methods lead to similar results.

- The surface roughness obtained of mirrors deposited by IAD E-beam is too high for high finesse Fabry-Perot cavities.

5.3 Future research work

5.3.1 High reflectance and optical losses measurements

In Chapter 3, reflectance of dielectric mirrors was determined using optical spectrometry. However, the accuracy of this measurement method is not sufficient for mirrors with a reflectance above 99.9 %. A cavity ring down spectroscopy experiment was presented to determine the total optical losses of the studied mirrors. The reflectance is deduced from the cavity losses with a high accuracy[6]. Future research steps include building a CRDS setup for high reflectance measurements.

While CRDS allows the measurement of total optical losses on a high finesse cavity with a high accuracy, it is fundamental to determine the absorption contribution in the optical losses. Many techniques such as the photothermal deflection technique[7], the photothermal common path interferometry[8, 9] and lock-in detection[10] allow the accurate measurement of very small absorption losses. Absorption can also change during the life of the mirror due to contamination, air humidity and temperature. A further study of the mirrors environmental resistance will be required to ensure the mirrors stability for cavity applications.

One point of concern for single and multilayer coatings was their high surface roughness. The coating roughness ranges between 1 to 2 nm in the case of IAD E-beam dielectric oxides due to the nuclei growth and grain coalescence for multilayer mirrors. In Section 3.4.3, Microdyn Nb_2O_5/SiO_2 and Plasmacoat ZrO_2/SiO_2 mirrors showed promising results with a surface roughness of 0.3 ± 0.02 nm and 0.5 ± 0.02 nm respectively. Measured scatter losses were, however, dramatically increased by the high defect density on the coating surface. The same defects contributed to a low laser damage resistance. Further coating runs will be performed in order to reduce defects and optical losses for the coatings and improve the laser damage resistance.

Total optical losses of the mirrors may be further reduced by annealing the mirrors as demonstrated for IBS Ta_2O_5/SiO_2 mirrors in [5] and TiO_2/SiO_2 mirrors in [11]. An experimental study will be carried to investigate the effect of the annealing temperature and duration on the optical losses of mirrors presented in Chapter 3.

5.3.2 Finesse and Q-factor measurements

Finesse and quality measurement can be achieved using a compact cavity setup as described in [4]. The diagram presents a mechanical setup of a plano-concave Fabry-Perot cavity used by the Nano-Photonics group at University of Basel. The top mirror is a quarterwave curved mirror fabricated using CO_2 laser ablation as previously described in Chapter 4. The bottom mirror is a quarterwave planar mirror. The mirrors are separated by a wavelength sized air gap, forming a high finesse Fabry-Perot cavity. The bottom

mirror is mounted on a three-axis piezoelectric nanopositioner and the transmission signal exiting the cavity is measured by a silicon photodiode placed below the bottom mirror. The finesse is deduced from the transmission peaks of the cavity. The cavity Q-factor is deduced from the finesse of the cavity. A Finesse measurement also allows an estimation of the reflectance of the mirrors. The cavity setup can operate at both room and cryogenic temperatures.

5.3.3 Plasma assisted E-beam TiO_2/SiO_2 mirrors

Future coating experiments include the deposition of multilayer high reflectance TiO_2/SiO_2 mirrors by plasma assisted E-beam deposition method described in Section 2.1.4 in Chapter 2. Promising optical properties such as high film packing density and low extinction coefficient determined at 550 nm wavelength have been recently demonstrated in [12] for rutile titanium dioxide layers produced using plasma assisted E-beam deposition. In future coating runs, multilayer mirrors will be deposited on several substrate types for structural and optical characterisation purposes. The mirrors will be deposited on curved templates produced by the Nano-Photonics group at University of Basel for finesse measurement and low temperature NV-centres experiments. Several glass and silicon wafers will be included in the same run to determine the mechanical stress of multilayer coatings (see Section 5.3.4). Other coated substrates include superpolished etalons for TIS, LIDT, SEM, AFM, reflectance and absorptance measurements.

5.3.4 Mechanical stress measurements

The mechanical behaviour of multilayer coatings consists a very important characterisation aspect which can affect the durability of thin film Fabry-Perot cavities. Indeed, intrinsic compressive or tensile stresses alter the structure of multilayer coatings leading to modified light-matter interactions within the cavity. A stress study will be performed for multilayer plasma assisted E-beam TiO_2/SiO_2 coatings grown on silicon and glass wafers. An experiment plan is set to study the effect of increasing layers and plasma source current and voltage on intrinsic stress in multilayer coatings.

Stress measurements of multilayer dielectric mirrors deposited on silicon and glass wafers will be performed using a KLA tencor P16 stylus profilometer. The profilometer has a dedicated stage for 2D and 3D stress measurements. The stage is provided with a pin geometry which eliminates undesired placement stresses as described in [13]. The pins placement is adapted to the wafer size and allows extending its capacity to an 8-inch wafer. Four scans will be performed on the front and back sides of the wafer using both x and y directions. The front-back subtraction is needed to eliminate the deformation that is caused by gravity. The stress on the wafers is calculated by comparing the bow before and after coating.

REFERENCES

[1] T. Klaassen, M. P. van Exter, and J. P. Woerdman, "Characterization of scattering in an optical Fabry-Perot resonator," *Applied optics,* vol. 46, no. 22, p. 5210, 2007.

[2] L. Greuter *et al.*, "A small mode volume tunable microcavity: Development and characterization," *Applied Physics Letters,* vol. 105, no. 12, 2014.

[3] D. Najer, M. Renggli, D. Riedel, S. Starosielec, and R. J. Warburton, "Fabrication of mirror templates in silica with micron-sized radii of curvature," *Applied Physics Letters,* vol. 110, no. 1, 2017.

[4] L. E. Greuter, "self-assembled quantum dots in a fully tunable microcavity," Doctor of Philosophy, Departement Physik, University of Basel, Basel, 2015.

[5] S. Bogdanovic, "Diamond-based Fabry-Perot microcavities for quantum networks," PhD Doctoral thesis, Delft University of Technology, Delft, Netherlands, 2017.

[6] H. Zu, B. Li, Y. Han, and L. Gao, "Combined cavity ring-down and spectrophotometry for measuring reflectance of optical laser components," *Opt. Express,* vol. 21, no. 22, pp. 26735-26741, 2013.

[7] J. Sancho-Parramon, J. Ferré-Borrull, S. Bosch, A. Krasilnikova, and J. Bulir, "New calibration method for UV–VIS photothermal deflection spectroscopy set-up," *Applied Surface Science,* vol. 253(1), pp. 158-162, 2006.

[8] L. Anghinolfi *et al.*, "Optical properties of uniform, porous, amorphous Ta2O5 coatings on silica: temperature effects," *Journal of Physics D: Applied Physics,* vol. 46(45), p. 455301, 2013.

[9] C. Clark *et al.*, "Comparison of single-layer and double-layer anti-reflection coatings using laser-induced damage threshold and photothermal common-path interferometry," *Coatings,* vol. 6, no. 2, 2016.

[10] H. Waechter, D. Munzke, A. Jang, and H.-P. Loock, "Simultaneous and Continuous Multiple Wavelength Absorption Spectroscopy on Nanoliter Volumes Based on Frequency-Division Multiplexing Fiber-Loop Cavity Ring-Down Spectroscopy," *Analytical Chemistry,* vol. 83(7), p. 2719, 2011.

[11] S. Chao, W.-H. Wang, and C.-C. Lee, "Low-loss dielectric mirror with ion-beam-sputtered TiO2–SiO2 mixed films," *Applied Optics,* vol. 40, no. 13, pp. 2177-2182, 2001.

[12] B. Hui *et al.*, "Automated Control of Plasma Ion-Assisted Electron Beam-Deposited TiO2 Optical Thin Films," *Coatings,* vol. 8, no. 8, 2018.

[13] R. Mays, "The Measurement of Residual Film Stress in Deposited Thin Films Using the KLA-Tencor 2D/3D P7 Surface Profilometer," University of Pennsylvania, 2017.